Title
SCANNING TUNNELING MICROSCOPY OF METALS ON GRAPHITE

Author
Ganz, E.D.

Publication Date
1988-08-01

Center for Advanced Materials

CAM

Scanning Tunneling Microscopy of Metals on Graphite

E.D. Ganz
(Ph.D. Thesis)

August 1988

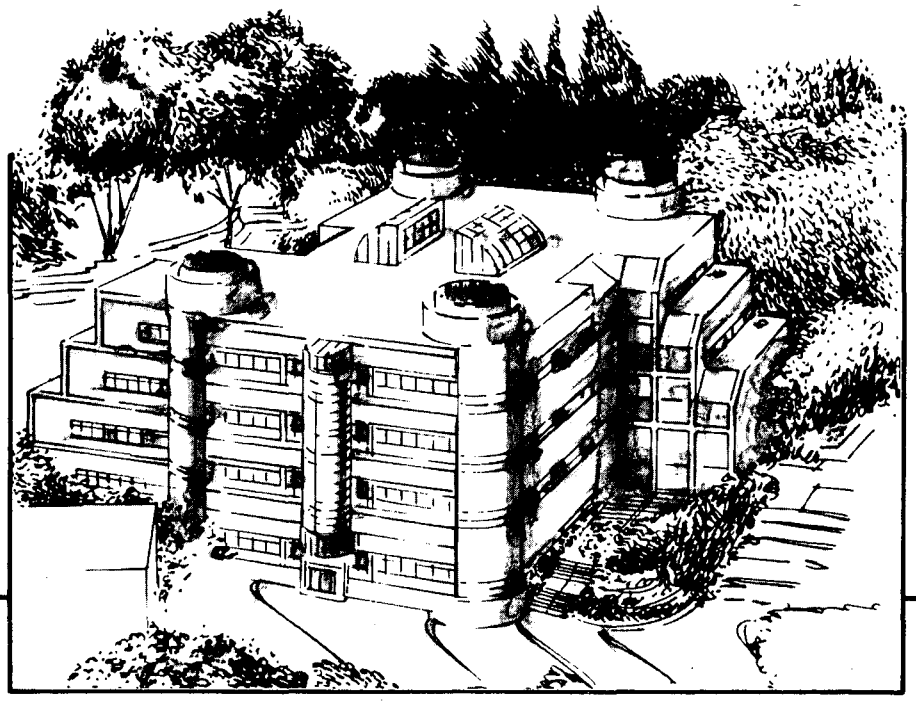

Materials and Chemical Sciences Division

Lawrence Berkeley Laboratory • University of California

ONE CYCLOTRON ROAD, BERKELEY, CA 94720 • (415) 486-4755

Prepared for the U.S. Department of Energy under Contract DE-AC03-76SF00098

DISCLAIMER

LBL-25323

Scanning Tunneling Microscopy of Metals on Graphite

Eric David Ganz
(Ph.D. Thesis)

Physics Department
University of California
and
Center for Advanced Materials
Materials and Chemical Sciences Division
Lawrence Berkeley Laboratory
1 Cyclotron Road
Berkeley, California 94720

August 1988

ACKNOWLEDGMENTS

This has been an interesting project, and over the years I have worked with many stimulating people. I would particularly like to thank my advisor John Clarke. He introduced me to the STM, funded the research, improved the papers, and directed the project all these years. I have enjoyed these years in the Clarke group, and I am grateful to John for all that he has done for me.

I started this project with another student, John Mamin, and a post-doc, David Abraham. The three of us built the microscope and the electronics to run it, and designed the necessary computer programs (which I wrote). We worked well together. Later, Klaus Sattler joined us with expertise on clusters and many fresh ideas. I am indebted to all three of these close friends for years of inspiration, instruction, cameraderie, and elbow grease.

Thanks are due to Gerd Binnig and Heinrich Rohrer, for first inventing the microscope, and then sharing it with the rest of the world. They set the tone for the STM community, and so the field has grown in an unusually open and non-competitive fashion. They spent many hours with us discussing the STM possible experiments, and we are grateful to them for it.

I also want to thank Christophe Gerber, Paul Hansma, and Calvin Quate for many discussions on STM construction. The Stanford group pioneered the fast 'current imaging' mode and the magnetic walkers which we have used so much.

I want to thank Jene Golovchenko and Miguel Salmeron for many helpful suggestions, experimental hints, and also for providing

samples. In our STM group I also want to thank Ruth Ellen Thomson, Sue Whitfield, and Tim Sharpe for general assistance, and tip making.

I have enjoyed working in the Clarke group, and thank Fred Wellstood, John Pelz, Mike Heaney, Non Fan, Dan Seligson, Mats Gustafson, Mark Johnson, John Martinis, Claude Hilbert, Cristian Urbina, and the rest for making this group dynamic, fun, and also interesting to work in.

I would like to thank the administrators at the Center for Advanced Materials, especially Rebecca Hunt who made the bureaucracy seem so simple for the years that she took care of us. I thank Randy Michelson at the Real Time Systems Group who spent many invaluable (although billable) hours leading me through the thick jungles of RT-11, and Wolf Schaefer at Tektronix who generously helped me set up the 6130 computer.

Thanks are due to Frank Ogletree for advice on LEED and Auger, to Winnie Heppler for polishing gold samples, and to David Tomanek, Steven Louie, Neil Bartlett, and Marvin Cohen for helpful discussions. I also want to thank Steven Louie and Neil Bartlett for carefully reading the manuscript.

The hundred or so photographs in this thesis were processed by the technicians at the photo lab at LBL, and I greatly appreciate their high quality, reliable turnaround, and polite service. Thanks are due to Rita Jones for help on bureaucratic rules of the game, hints on BRIT, for sending out reprints (eventually), and for her wonderful papercutter (actually Ron Shen's).

I built most of my electronics myself, and this was only possible due to the assistance of John Davis and Ken Grove in the electronics

shop. John was always available for circuit advice, and Ken was always quick to help find parts, make boards, or lend out equipment. I also thank Ken for the use of his Macintosh for several of the figures in this thesis. Some of the electronics was built by Levern Gardner, and I thank him for his careful work.

My girlfriend, Nina Bacaner, has been very patient and supportive about the late nights, and I would like to thank my family and friends for their support all these years.

I am indebted to IBM for a most generous three year pre-doctoral fellowship. This paid my salary, and also provided money for books and travel to conferences. They also flew me to Yorktown for a meeting, which was a very stimulating experience. As a symptom of the general good will on both sides, both John Mamin and David Abraham now work for IBM (at Almaden and Yorktown, respectively).

I also thank the Director, Office of Energy Research, Office of Basic Energy Science, Materials Science Division of the U. S. Department of Energy for funding under contract number DE-AC03-76SF00098.

TABLE OF CONTENTS

CHAPTER I

INTRODUCTION

When I started this project five years ago, the STM had recently been invented by G. Binnig and H. Rohrer[1], and only a few STM's had been built (at IBM Zurich, Stanford, and Bell Labs). In 1983, they published[2] an atomic resolution image of the 7 X 7 reconstruction of Si(111), and suddenly the physics community realized the potential of this new instrument. Binnig and Rohrer travelled widely giving talks on the STM and the many possible applications they saw for it. More importantly, they encouraged others to build STMs, and shared ideas and techniques freely. Many instruments were built, and a small STM community was born. Today, there are hundreds of STMs in operation, and large international meetings every year. Commercial STMs are now available at moderate cost for operation in air or in ultra high vacuum, and the range of applications continues to grow from surface science to micromachining to biology.

The principle of the STM is relatively simple. A metal tip is brought to within a few angstroms of a conducting surface (see Figure 1-1). A small voltage is applied between the tip and sample, encouraging electrons to jump across the gap. For clean surfaces in vacuum, the electron needs typically 4eV to escape from the surface (the work function), and so if we keep the bias voltage smaller than a few volts, the electrons will be forced to quantum mechanically tunnel across the gap. If we use a simple one dimensional tunneling barrier approximation[1], we find that the tunneling current $J \propto \exp(-A\phi^{1/2}s)$ where $A = 1.0\ \text{Å}^{-1}\ \text{eV}^{-1/2}$, ϕ is the barrier height (or effective work

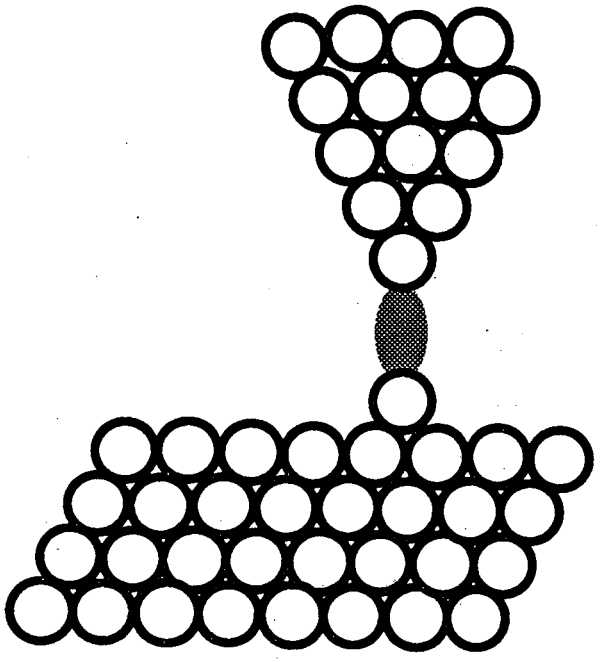

Fig. 1-1 Most of the tunneling current flows from the tip to the nearest atom on the surface.

function), and s is the gap spacing. For a typical barrier of 4 eV, we find that the current changes by a factor of ten when the gap changes by 1 Å.

The atomic resolution of the STM is due to this very strong dependence of the tunneling current on the gap. The current will flow primarily from the part of the tip that is nearest (on a scale of 1 Å) to the sample, and this will typically be one atom. Then, most of the current will flow to the parts of the surface nearest to this single atom. An image can be formed by rastering the tip across the surface (in the X and Y plane), while moving the tip in the Z direction (perpendicular to the surface) to maintain a constant tunneling current. This is called the topographic imaging mode and is shown schematically in Figure 1-2(a).

An alternative method of image formation is to raster the tip rapidly across the surface at a constant average height[3] [see Figure 1-2(b)]. This is called the current imaging mode because changes in the tunneling current constitute the image. The advantage of the topographic mode is that it directly gives the topography of the surface (neglecting electronic effects), and one can track rough surfaces or large structures. For a flat surface, the current imaging mode has the advantage of higher speed, and lower noise.

The STM can operate in a wide variety of environments and conditions. Images have been obtained in air, water, ultrahigh vacuum, and liquid nitrogen[4] and even in grease[5]. Microscopes have been operated at temperatures as high as 600K[2] and as low as millikelvins[6]. Virtually any conducting sample seems to work, and tips have been made from W, Au, and even pencil lead[7]. The bias voltage can range from

REFERENCES

1 G. Binnig, H. Rohrer, Ch. Gerber, and E. Weibel, Phys. Rev. Lett. 49, 57 (1982).

2 G. Binnig, H. Rohrer, Ch. Gerber, and E. Weibel, Phys. Rev. Lett. 50, 120 (1983).

3 D. P. E. Smith and S. Elrod, Rev. Sci. Inst. 56, 1970 (1985).

4 P. K. Hansma and J. Tersoff, J. Appl. Phys. 61, R1 (1987).

5 J. Schneir, R. Sonnenfeld, O. Marti, P. K. Hansma, J. E. Demuth, and R. J. Hamers, J. Appl. Phys. 63, 717 (1988).

6 K. W. Ng and A. L. De Lozanne, presented at the March meeting of the APS, New Orleans, Louisiana, March 1988.

7 R. J. Colton, S. M. Baker, J. D. Baldeschwieler, and W. J. Kaiser, Appl. Phys. Lett. 51, 305 (1987).

8 Proceedings of the Workshop on Scanning Tunneling Microscopy, Oberlech, Austria, July 1985, IBM Journal of Research and Development 30, 350 - 553 (1986).

9 Proceedings of the First International Conference on Scanning Tunneling Microscopy, Santiago de Compostela, Spain, July 1986. Surf. Sci. 181 (1987).

10 Proceedings of the Second International Conference on Scanning Tunneling Microscopy, Oxnard, California, July 1987, J. Vac. Sci. Tech. A6, (1988).

11 J. Golovchenko, Science 232, 48 (1986).

12 C. Quate, Physics Today p. 26, Aug. 1986.

CHAPTER II

EQUIPMENT

a) UHV SYSTEM

Most of the experiments described here were performed in ultra high vacuum (UHV). By operating in UHV, we are able to control the surface composition of our samples, and prevent contamination. This is of critical importance, because the STM is inherently surface sensitive.

Our criteria for the design of the vacuum system were to provide good vacuum (10^{-10} torr range), sample preparation and characterization facilities, sample transfer to the STM, rapid sample introduction from outside the system, and reliable operation. Overall, the design has been quite successful and easily adapted to many applications.

Figure 2-1 shows the layout of the vacuum system. The basic system consists of a Varian surface science bell jar and VT112 pumping station with five 40 liter/sec ion pumps, a titanium sublimation pump, a poppet valve, and a cold trap. The system is roughed out with dual vacsorb pumps, and can also be pumped by a 50 l/s turbo pump. By using the turbo pump for the first hour after pump out, we avoid exposure of the ion pumps to pressures above 10^{-6} torr. We bake the system using heating tapes which warm the surface to 180-210°C; this brings the interior to 120°C. Typically we bake for 24-48 hours, and then cool for a day before we begin the experiment. The temperature of the bakeout is limited by the torr seal epoxy used in microscope which is rated only to 125°C. This procedure produces a vacuum of 1-3 X 10^{-10} torr.

To insert a sample into the vacuum system, we put the sample into the sample introduction system via the sample loading port. Two

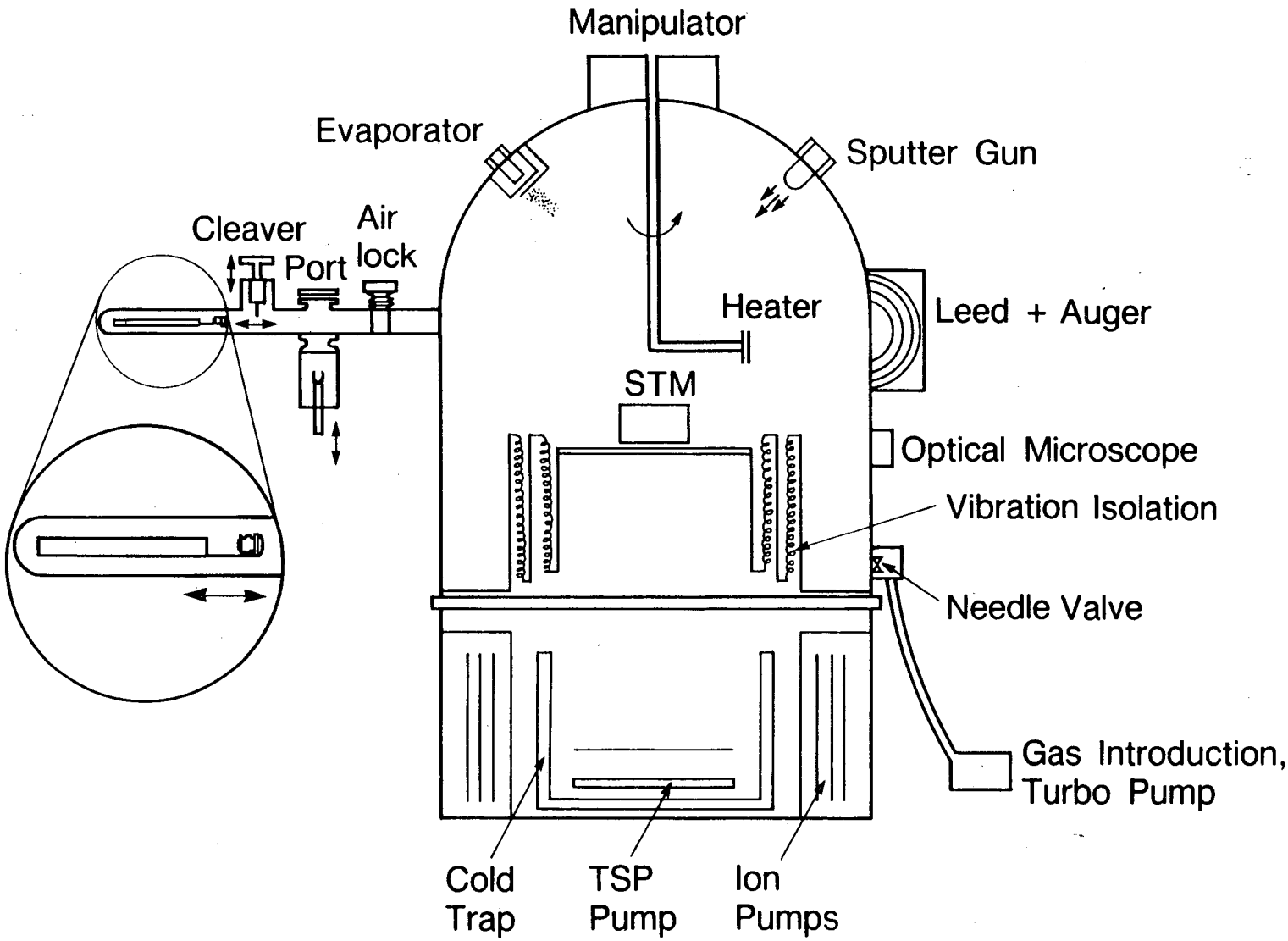

Fig. 2-1 Schematic of ultra-high vacuum system.

samples can be loaded, one into a sample holder and the other on the sample transfer piece. The system is roughed out with the vacsorb pumps, and then pumped by a small 30 l/s ion pump. After several hours, or overnight, the pressure in the introduction system is in the 10^{-7} to 10^{-8} torr range. We then open the air lock to the main system, and the pressure drops into the low 10^{-8} torr range. At this point, we can also use the cleaver (a razor blade mounted on a linear motion feedthrough) to cleave the sample in vacuum if necessary. We then use the sample transfer tube to transfer samples to the manipulator.

The manipulator (See Figure 2-2) has accomodation for two samples: one on a holder, and the other on the heater. These positions are located 6.2 cm out from the central axis of the manipulator. The manipulator can swing to position the samples for evaporation, sputtering, or LEED and Auger analysis. A wobble stick is used to transfer the samples to a gripper mounted on the central axis of the manipulator. We use the gripper to drop samples onto and remove samples from the STM.

The STM is mounted on a two stage spring system with eddy current damping. This system has been described by Mamin[1], and is effective above 2Hz. We use a long working distance optical microscope (Aus Jena 212 OPM with a 400mm working distance objective) to observe the coarse approach of the sample towards the tip.

A mass spectrometer is available for residual gas analysis, and we have found this especially useful during sputtering to ensure the purity of the Ar gas. The Ar (or any other gas) is let in via a gas introduction system, with a needle valve which allows a controlled

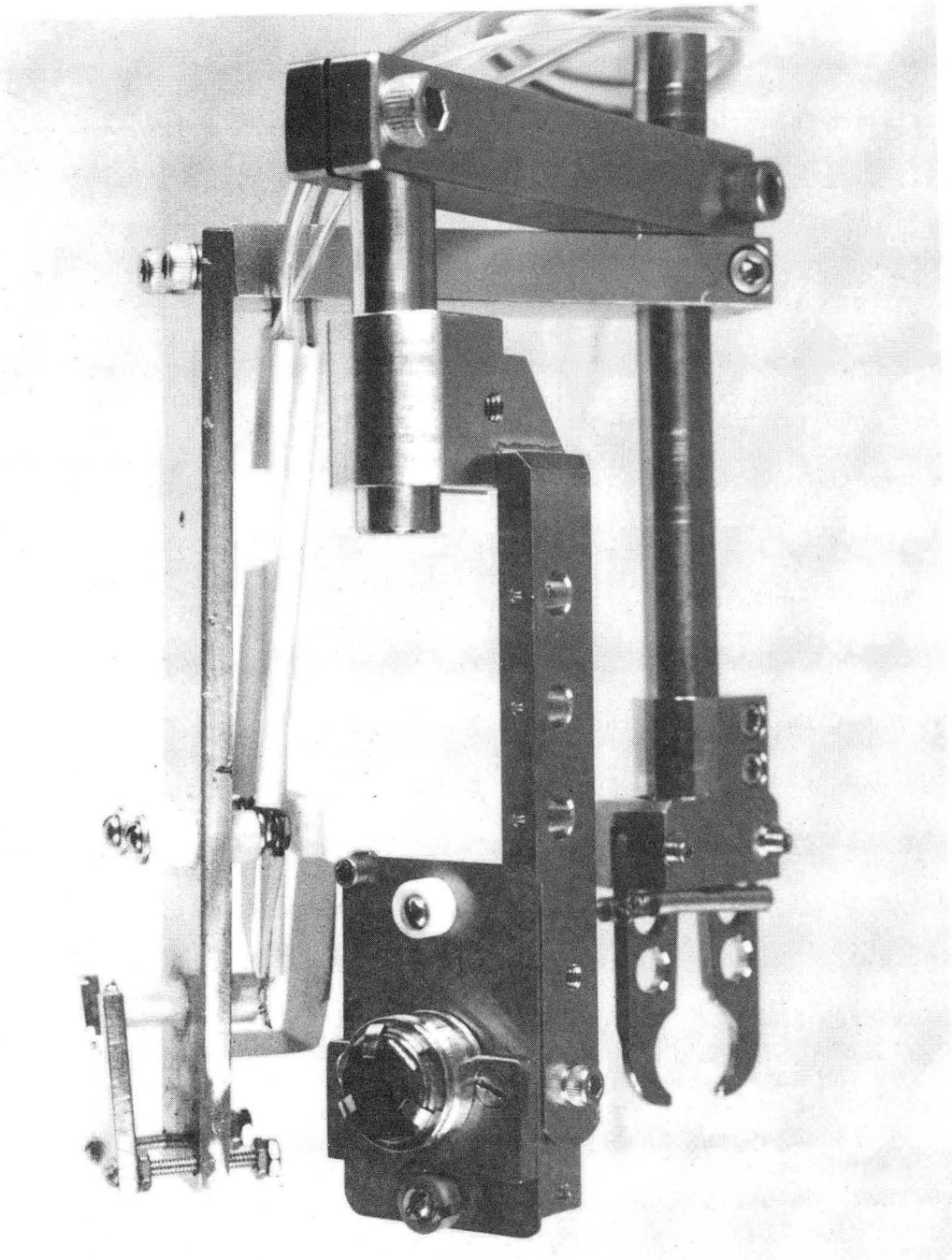

Fig. 2-2 Picture of the manipulator showing the holder, the heater, and the gripper.

XBB 874-3501

leak. We use the 50 l/s turbo pump to remove the bulk of the Ar gas during flow through sputtering.

Figure 2-3 (a) shows the two types of molybdenum sample holders we have used. The samples are transferred to the STM using a gripper shown in Figures 2-2 and 2-3(b). Samples to be heated are held by three moly clips, while samples to be cleaved are epoxied directly to the moly holder. For metallic samples, it is not feasible to use resistive heating, so we heat them from the back using an electron beam. Electrons are emitted from a small coated can (Spectra-Mat standard 134 emitter with potted heater) situated directly behind the sample (as shown on the left of Figure 2-2). The can is heated to 1000-1200° C by an internal coil, and then biased at -1000 volts relative to the sample. This arrangement provides 25 to 50 watts of power into the sample. The heater must be extensively outgassed to prevent sample contamination, and also must be quite close to the sample in order to achieve reasonable electron currents, but is reliable and clean.

We have used very simple evaporators in these experiments. Typical sources are shown in Figure 2-4. The metal to be evaporated is placed in a boat made from Ta sheet [Figures 2-4 (a) and (b)], or in a coil made from Ta or W wire [Figure 2-4 (c)]. This source is attached to a high current feedthrough, and heated resistively by 5 to 15 amps. The source is enclosed in a shield, which contains a crystal monitor and a shutter. Unfortunately, the crystal monitor is too close to the source, and therefore thermal drift overwhelms the deposition signal, especially for light metals like Al or Cu. We have therefore installed a second crystal monitor on the manipulator 10cm away from the source.

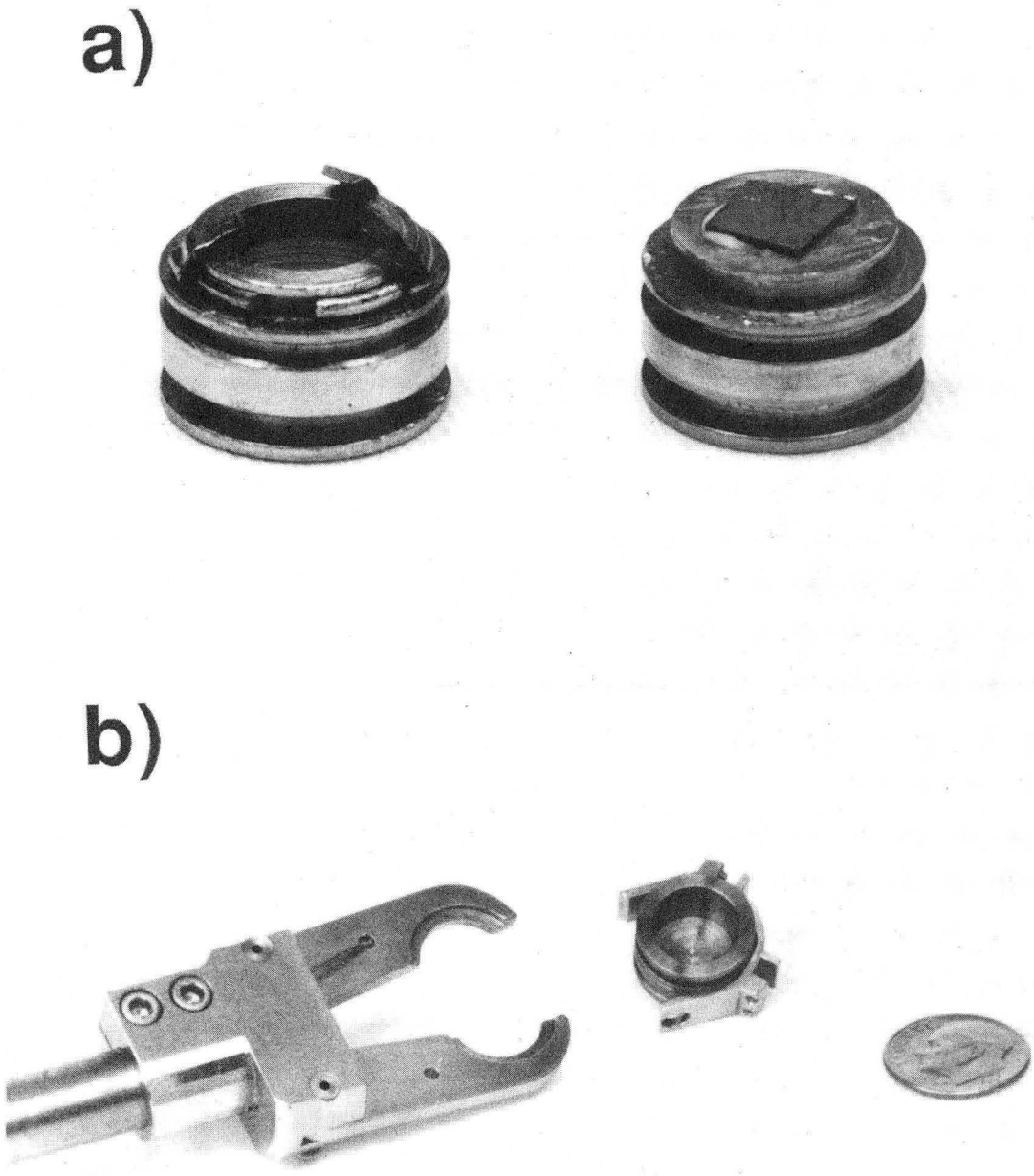

Fig. 2-3 (a) Molybdenum sample holders, and (b) gripper. XBB 885-5657A

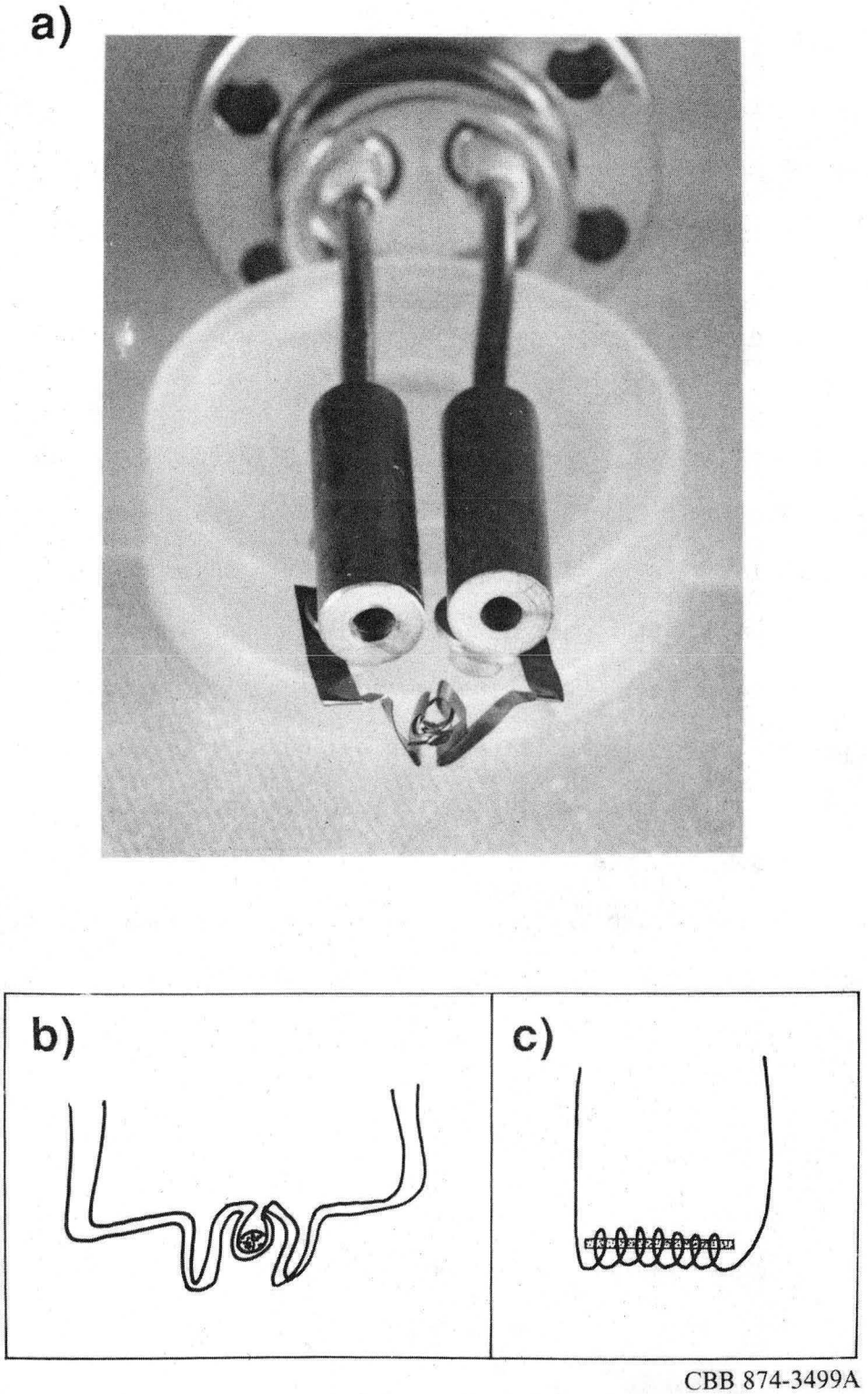

Fig. 2-4 (a) Photograph of the evaporator. The metal is evaporated from either a boat (b) or a coil (c).

Ultimately the source should be replaced with a Knudsen cell with a liquid nitrogren cooled baffle to provide reliable, clean, and uniform slow deposition rates. The existing setup does allow small amounts of material to be deposited (typically we put down 0.1% of a monolayer), but the actual coverage in any given run is quite variable. Again, we have found it necessary to degas the source extensively to prevent contamination during deposition.

Unfortunately, the UHV system is very large and spread out, and so has strong low frequency resonances. This can produce vibration problems in the STM. Ideally the UHV system would be more compact, or else at least better damped. Furthermore, one could isolate the entire system from floor vibration using isolation mounts. A second source of vibrational noise in the microscope at 500Hz is due to resonaces in the stainless steel springs used in the spring system. This frequency is not damped by the viton standoffs used to hold the springs. We have reduced the Q of the springs by installing small Macor blocks 2 cm below the top of the spring and just touching it. When it vibrates, the spring hits blocks and is damped out.

b) STM CONSTRUCTION

We have built several different types of scanning tunneling microscope in the last few years. Two old designs are shown in Figure 2-5. These two microscopes were based on thin film louses which have been discussed previously[1,2]. In the microscope shown in Figure 2-5(a) the sample was scanned in the X and Y directions, while the tip and Z drive were mounted on the louse. This decoupling of the XY drives from the Z drive aliowed large dynamic range in X and Y, without

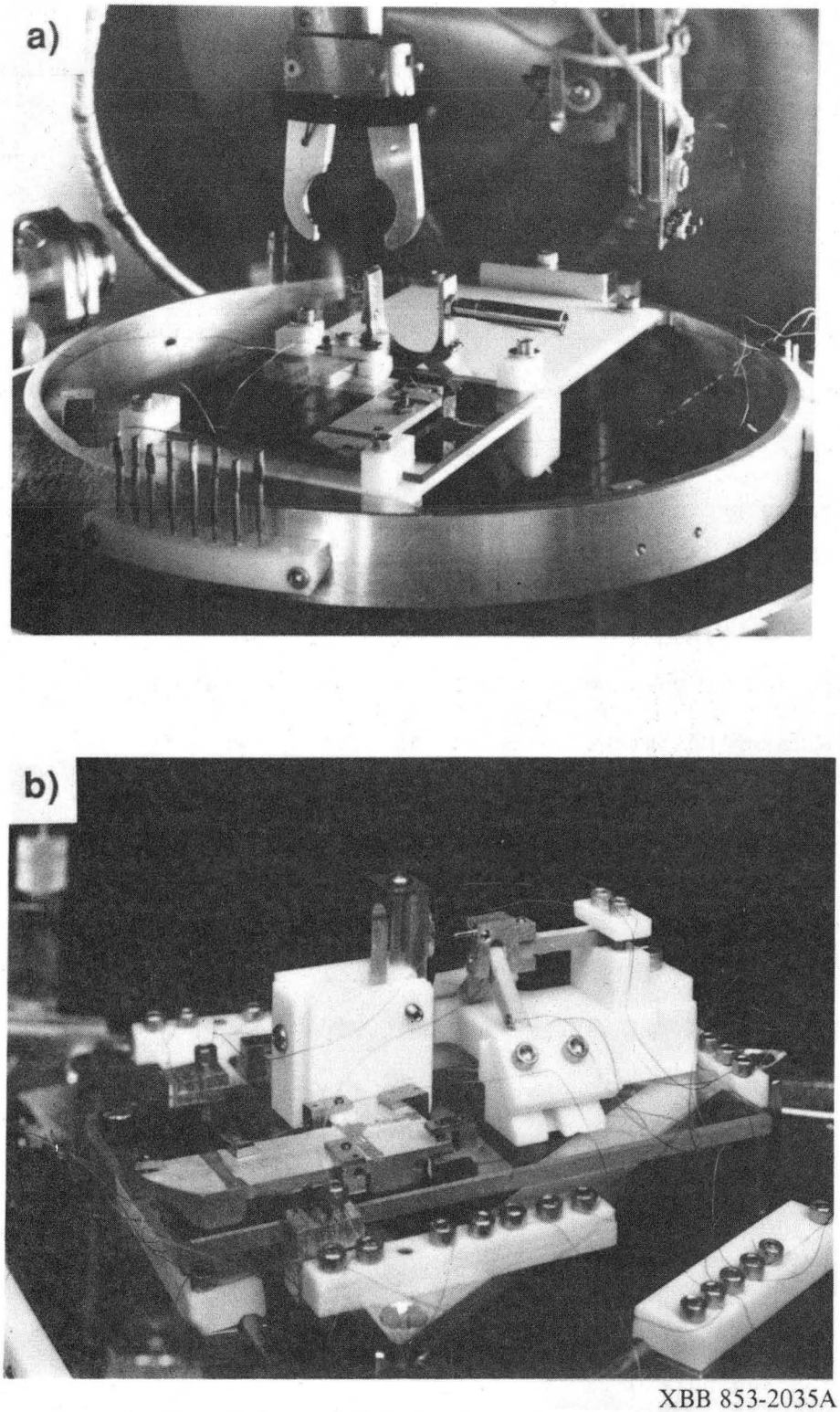

XBB 853-2035A

Fig. 2-5 Two old STM designs based on louses.

compromising the high frequency performance of the Z drive. The gripper which transfers samples down onto the microscope is visible at the top of Figure 2-5(a). The second microscope [shown in Figure 2-5 (b)] used the more standard XYZ tripod scanner, with the louse bringing up the sample. Unfortunately, although the louses could be made to work in air, they often stuck to the substrate when used in UHV after a bakeout, and so we switched to magnetic walkers.

Figure 2-6 shows the microscope used for the bulk of the experiments presented in this thesis. The microscope consists of a coil, a walker, and a scanner all mounted on a large thick quartz plate. The walker can move forward and back to bring the sample up to the tip, and is based on a design used by Smith and Elrod[3]. These walkers take 100Å steps quite reliably, are simple to build, and are reliable in UHV. The walker itself is just a quartz plate with three stainless steel ball bearings glued to the bottom. This assembly slides on the polished quartz surface. The coil is pulsed with 30 to 60 V (roughly 3 amps) for 50 to 200 μsec. This produces an impulse on the magnet which then pushes the walker forward or backward. The walker is constrained to move between two rails which prevent it from falling off the substrate, but allow a few mm of lateral play. To get to a new location on the sample, we move the sample back several μm to several mm, and then forward again: there is generally some small lateral motion. Of course, one can also push the walker laterally using the manipulator.

Most of the experiments were performed using the simple tripod scanner[4] shown in Figure 2-6. This has 3 piezoelectric elements mounted orthogonally, and moves 10Å per volt. One advantage of PZT

a)

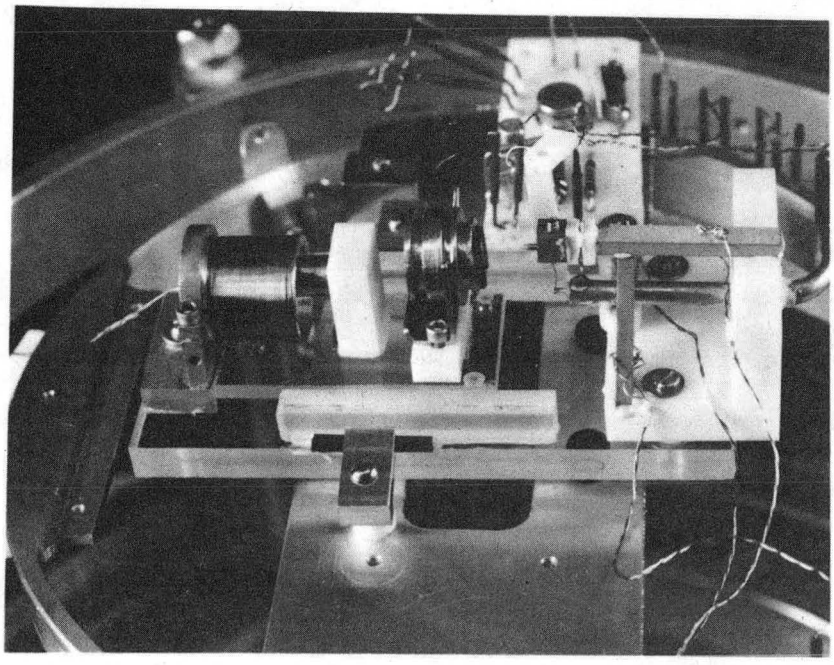

b)

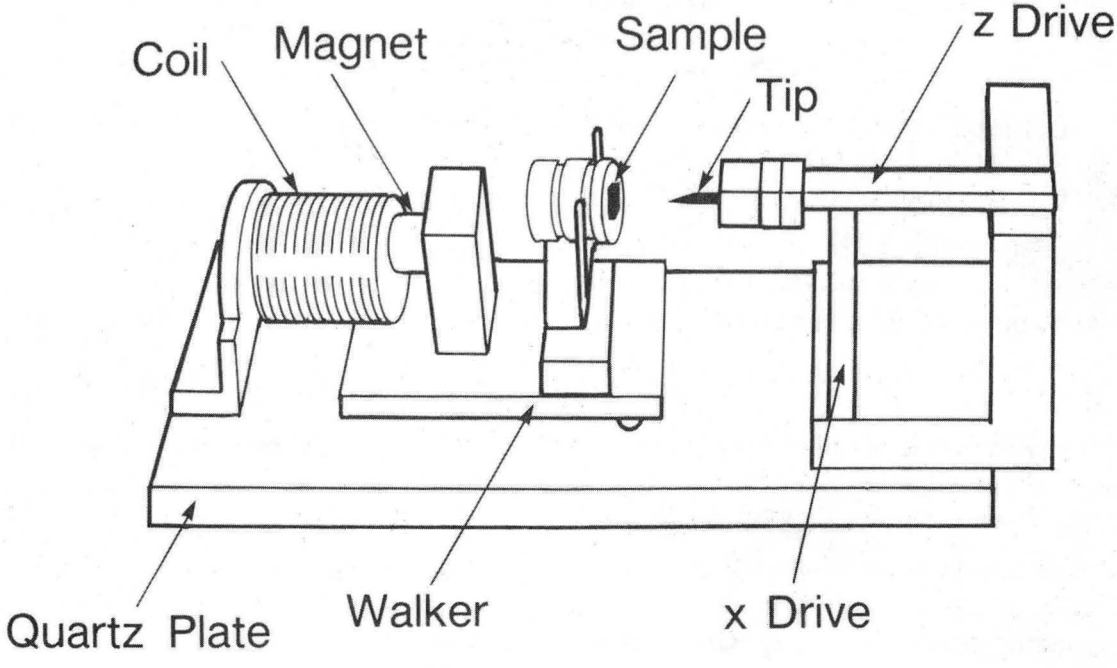

Fig. 2-6 (a) STM design used for the bulk of the experiments. (b) Schematic diagram of the STM.

XBB 886-5515

plates is that a separate voltage can be applied to each side, and the motion is proportional to the difference between the two applied voltages. Thus we used a slow, low noise, high voltage amplifier (a KEPCO BOP 500M, ±500 V range) to provide a large dynamic range, and a fast, low noise, ±15 V OP AMP to provide rapid response. Unfortunately, the BOP high voltage amplifier has 25 mV line synched 60 Hz spikes on its output, and so we needed to add a 10 Hz low pass filter to attenuate the line syncronized spikes on the output. This system allowed us to run the scanners at frequencies up to their mechanical resonances which were typically around 1 to 2 kHz. With the slow stage filtered, and the fast stage for correction, this setup provided less than 2 mV noise peak to peak in a 10 kHz bandwidth.

Recently we have replaced the tripod with a tube scanner. This idea was first introduced by Binnig[5]. Figure 2-7 shows the layout of this scanner. We start with a small PZT tube with Ni electrodes on the inside and outside. We then cut the outer electrode into four sections. The Z voltage is applied to the inner electrode, while the X and Y voltages are applied to the outer quadrants. By applying +X to one quadrant and -X to the opposite quadrant, the tube will bend symmetrically, producing a motion in the X direction with very low coupling to the Y or Z directions. The tip is mounted along the central axis of the tube. Using a 12 mm tube of 8 mm diameter and 0.75 mm thick we obtain roughly 50 Å per volt. We use a KAMAN measurement system to calibrate the motion of the tubes on a large scale, and use images graphite to obtain a small scale calibration in the X and Y directions.

These tubes have a capacitance of 2.5 nF per quadrant, and we can

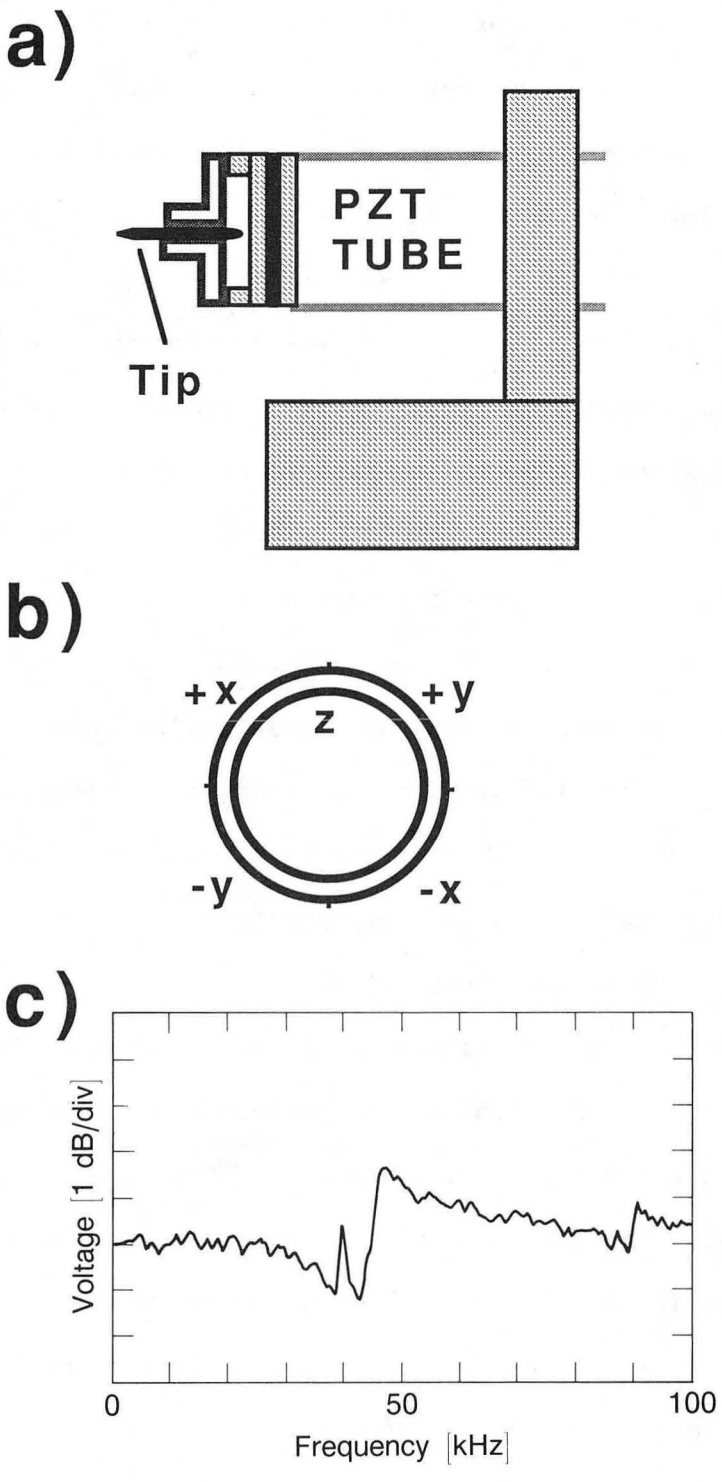

Fig. 2-7 (a) The latest STM has a tube scanner. (b) Schematic showing how voltages are applied to the tube. (c) Differential impedance of the tube as a function of frequency shows the first resonance is near 40 kHz.

use this capacitance to measure the mechanical resonances of the tube electrically. For an ideal capacitor, the impedance $Z = 1/i\omega C$, where $i=(-1)^{1/2}$. We can measure this impedance with a spectrum analyzer by supplying periodic white current noise (i.e. periodic white voltage noise through a 1 MΩ resistor). We measure the voltage across the tube using the spectrum analyzer. By differentiating the spectrum, we can remove the $1/\omega$ dependance. This result is shown in Figure 2-7 (c) and shows that the first mechanical resonance of this tube is near 40 kHz.

We scan with 1 mm W tips that have been electrochemically etched at 7 V DC in 2 M NaOH. There are many recipes, varying the concentration of NaOH, the voltage (AC or DC), and the thickness of wire. We show scanning electron micrographs of a typical tip in Figure 2-8. Generally, the tips we used had a radius of curvature of 0.5 μm or less. (See ref. 6 for a technique which produces single atom tips). One drawback with W is the presence of surface oxide or contamination. To combat these problems, we briefly tried gold plating the tips, but did not observe a significant improvement (We were also concerned that the gold might be transferred onto the sample). We find that tip preparation (by field emission at 1000 V, 1 to 100 μA to a silicon surface, or momentary 5 to 20 V spikes while tunneling) in vacuum was sufficient to clean the tips and remove most of the contamination (see chapter 4). We have also tried etched 0.25 mm tips, which should be sharper, but we found them to have high Q resonances, and thus generally give noisy results.

Figure 2-9 shows a tip before and after use on a gold surface. This shows the consequences of crashing a tip into the surface: Gold has been transferred onto the tip. Figure 2-10 shows another tip after

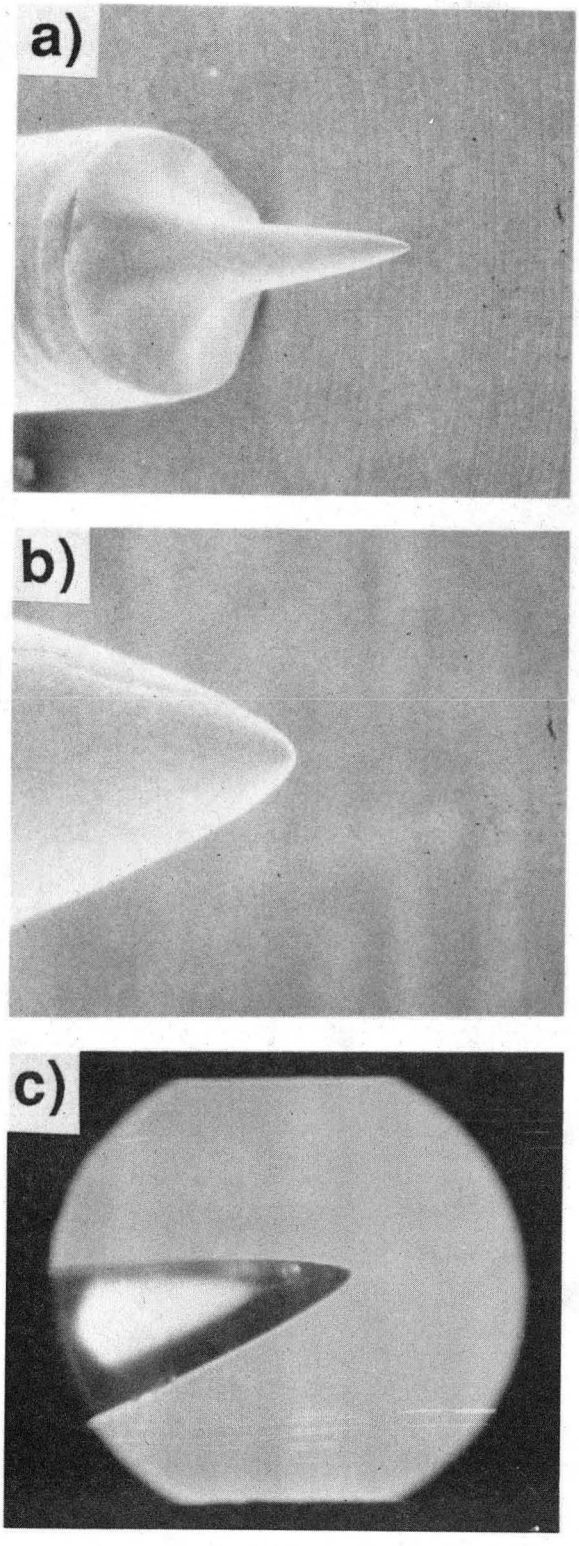

Fig. 2-8 Scanning electron micrographs of a W tip at (a) 40X, and (b) 800X magnification. An optical microscope image at 400X is shown in (c).

XBB 887-6957

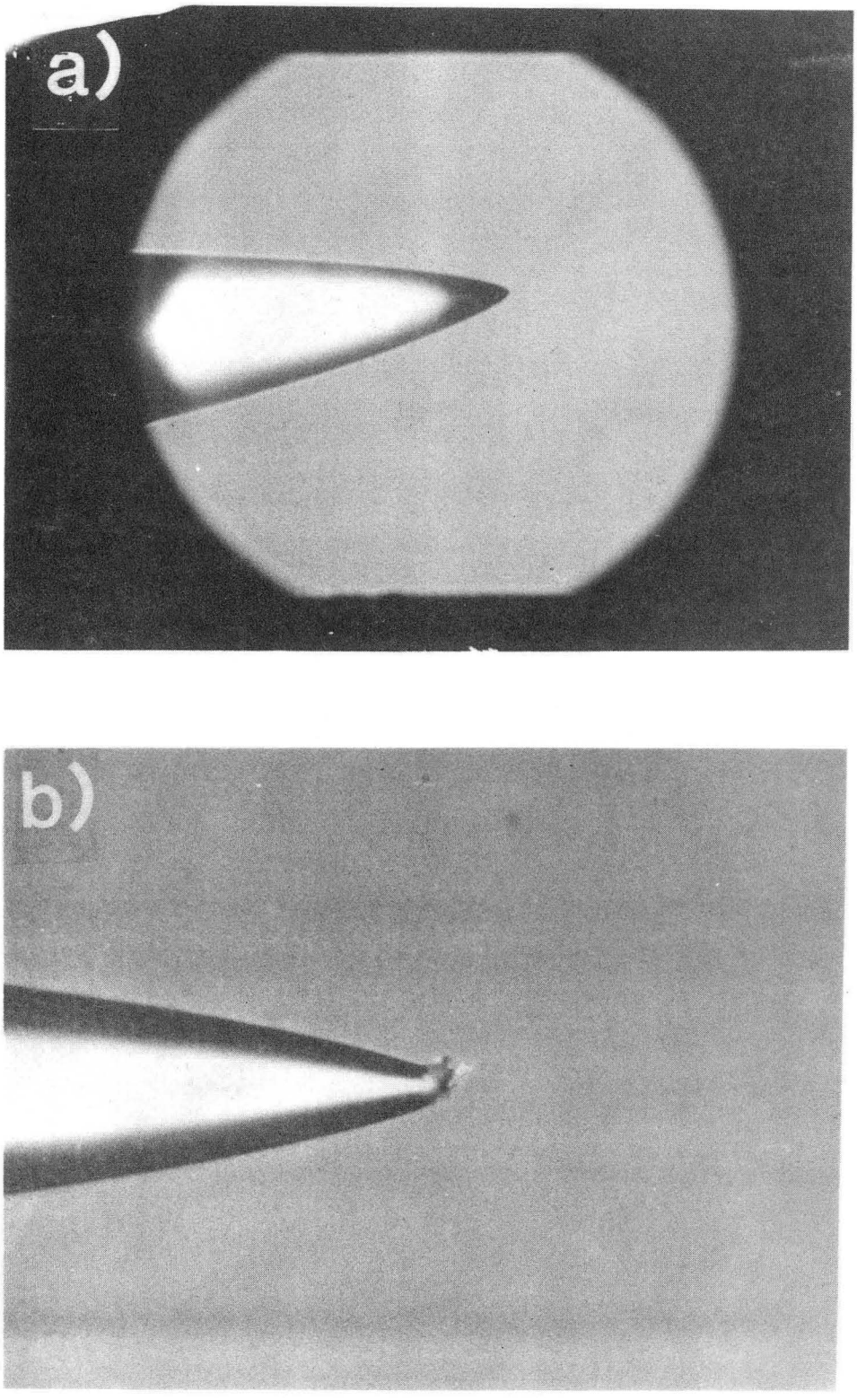

Fig. 2-9 Optical microscope image of a W tip at 400X magnification (a) before, and (b) after crashing into a Au surface. XBB 884-4470

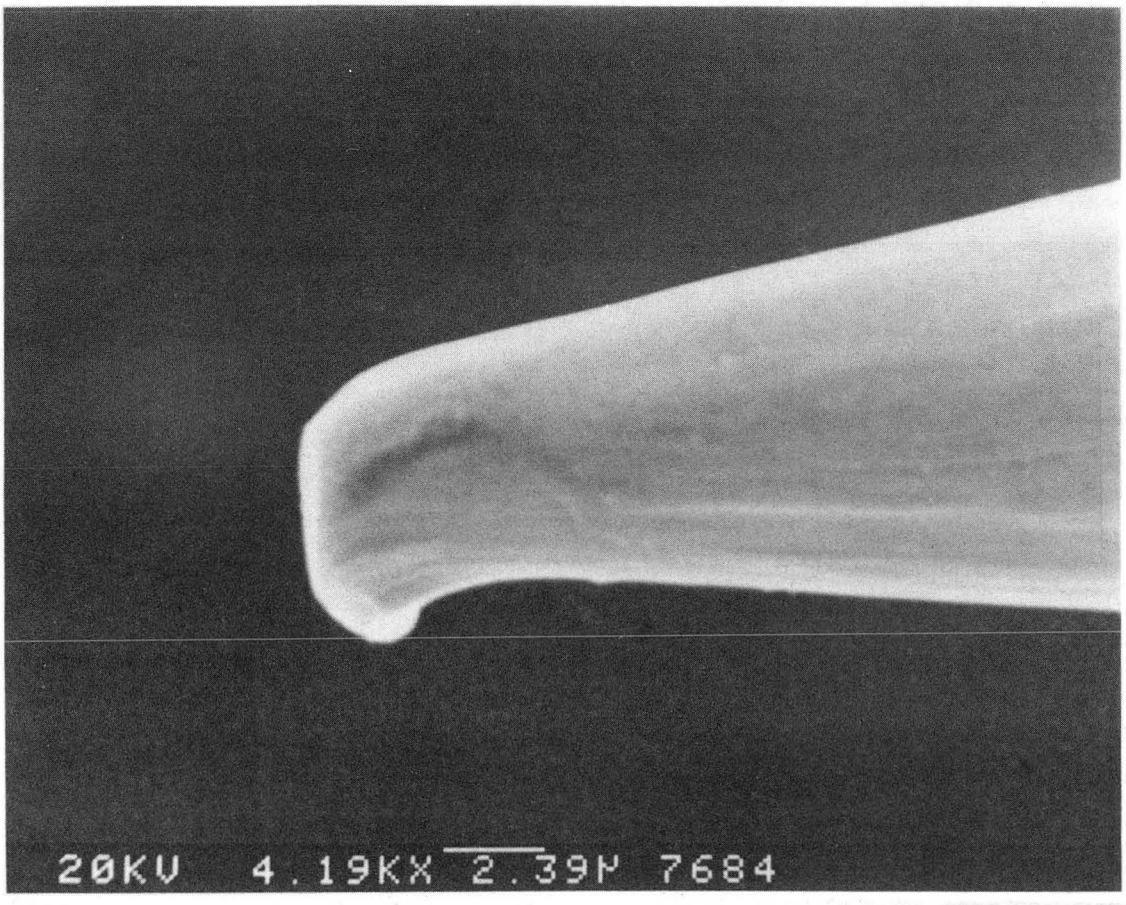

XBB 885-4480

Fig. 2-10 Scanning electron micrograph of a W tip after crashing into a Au surface.

it was crashed into a gold surface: Here the end of the tip has been blunted. R. Wilson has suggested that even when the tips are not crashed, material can be tranfered to the tip. Thus it is important not to crash the tips, and to be aware of tip condition and tip contamination effects in the interpretation of STM data.

c) CONTROL ELECTRONICS

Figure 2-11 shows an overview of the data acquisition system. We will discuss each section separately.

The preamplifier used in air consists of a current to voltage converter followed by an instrumentation amp with a gain of 20 [see Figure 2-12(a)]. The back to back transistors at the input protect the circuit against high voltage inputs up to 1000 V. We found it important to locate the preamplifier as close as possible to the tunneling gap. Therefore, in UHV we use a leak tested (MIL SPEC 883B) Burr Brown 106 VM operational amplifier [see Figure 2-12(b)]. A small Macor plate holds the operational amplifier, a few uncoated resistors, and a potted capacitor. The second stage is directly outside of the UHV system. Figures 2-12(c) and (d) show the response of the preamplifier to white noise and square wave inputs, respectively, and we see that the response rolls off smoothly above 20 kHz. We apply the bias voltage to the sample and measure the current into the tip to allow better shielding and reduce capactive pickup.

The design of the feedback circuit is shown in Figure 2-13. We have found that a logarithmic amplifier is not necessary for most applications, and complicates circuit analysis and design. A logarithmic amplifier can be useful, however, in topographic mode, for

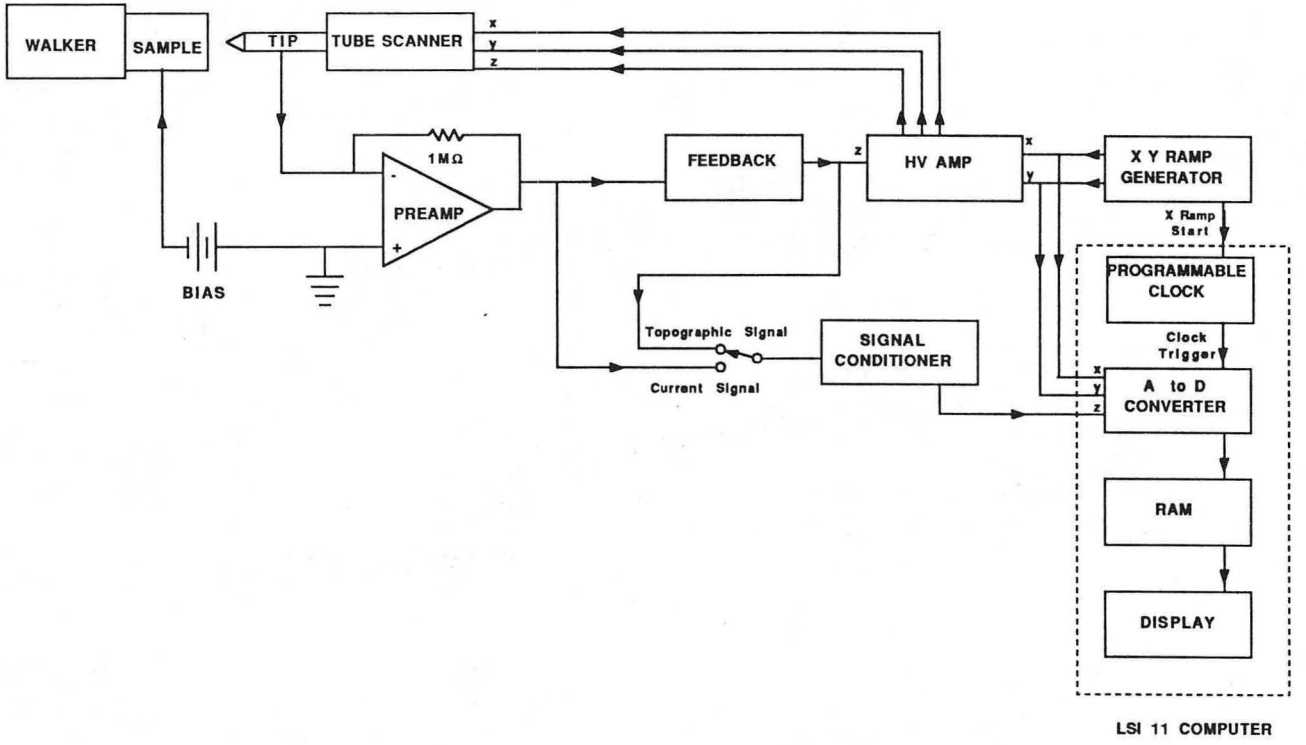

Fig. 2-11 Overview of the data acquisition system.

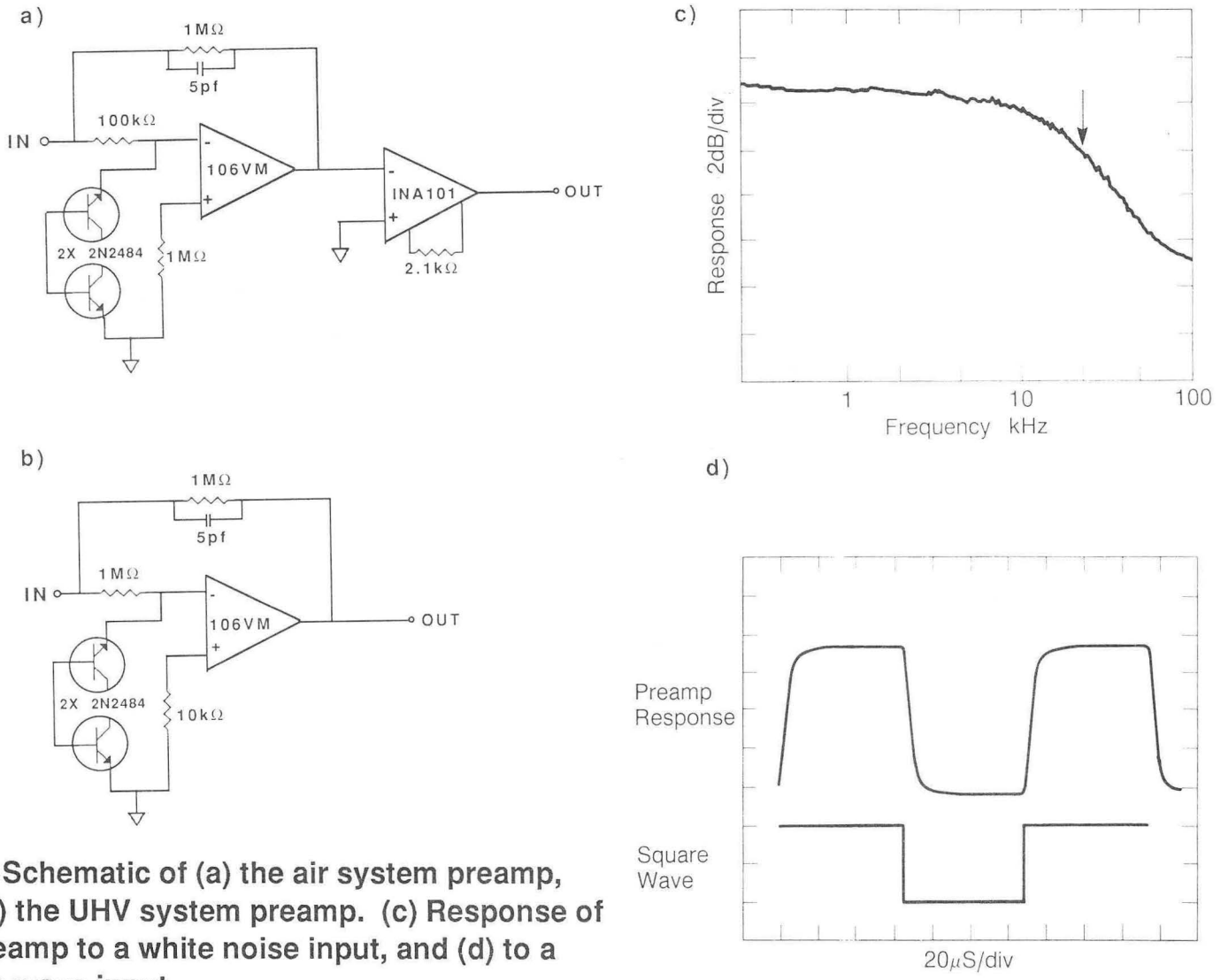

Fig. 2-12 Schematic of (a) the air system preamp, and (b) the UHV system preamp. (c) Response of the preamp to a white noise input, and (d) to a square wave input.

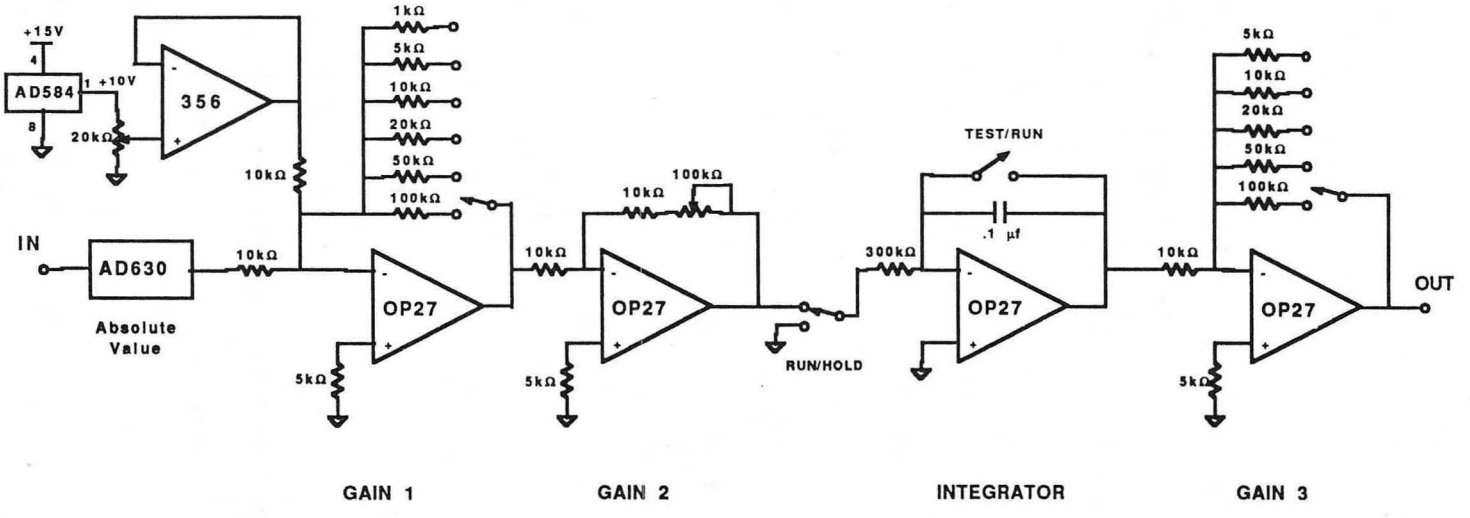

Fig. 2-13 Schematic of the feedback circuit.

it equalizes the slew rate for tip motion towards and away from the surface when the tip is not tracking the surface well (i.e. either too close or not tunneling).

Note that the positive input on the integrator is connected directly to ground. It is important that this input sees a low impedance to ground at high frequencies to reduce the noise at the output of the integrator[7].

To operate in current mode, we turn the gain of the feedback loop down to minimize noise induced by the feedback loop. Of course, some feedback is necessary to prevent drift and low frequency noise, but since the changes in tunneling current form the image, the feedback must be slow enough to allow changes in current as the tip is scanned. For topographic imaging, we use the maximum gain available without driving the system into oscillation. Further discussion of this feedback circuit can be found in Mamin's thesis[1]. Two useful features are the test switch (which zeros the integrator) which allows us to pull the tip back out of the way, and the hold switch (which zeros the input to the integrator) which removes the feedback loop from operation while fixing the tip in position. Finally, since we bring up the sample with a pulsed magnetic walker, to avoid crashing, we use a testing mode: after each step forward, the tip is ramped forward to test for tunneling current. If current is detected, the tip is immediately retracted, and the computer is notified to halt the approach.

The high voltage amplifiers used to control the tripod scanners were described above. For the tube scanners, we use five Burr Brown 3582 300 V operational amplifiers [see Figure 2-14]. These are

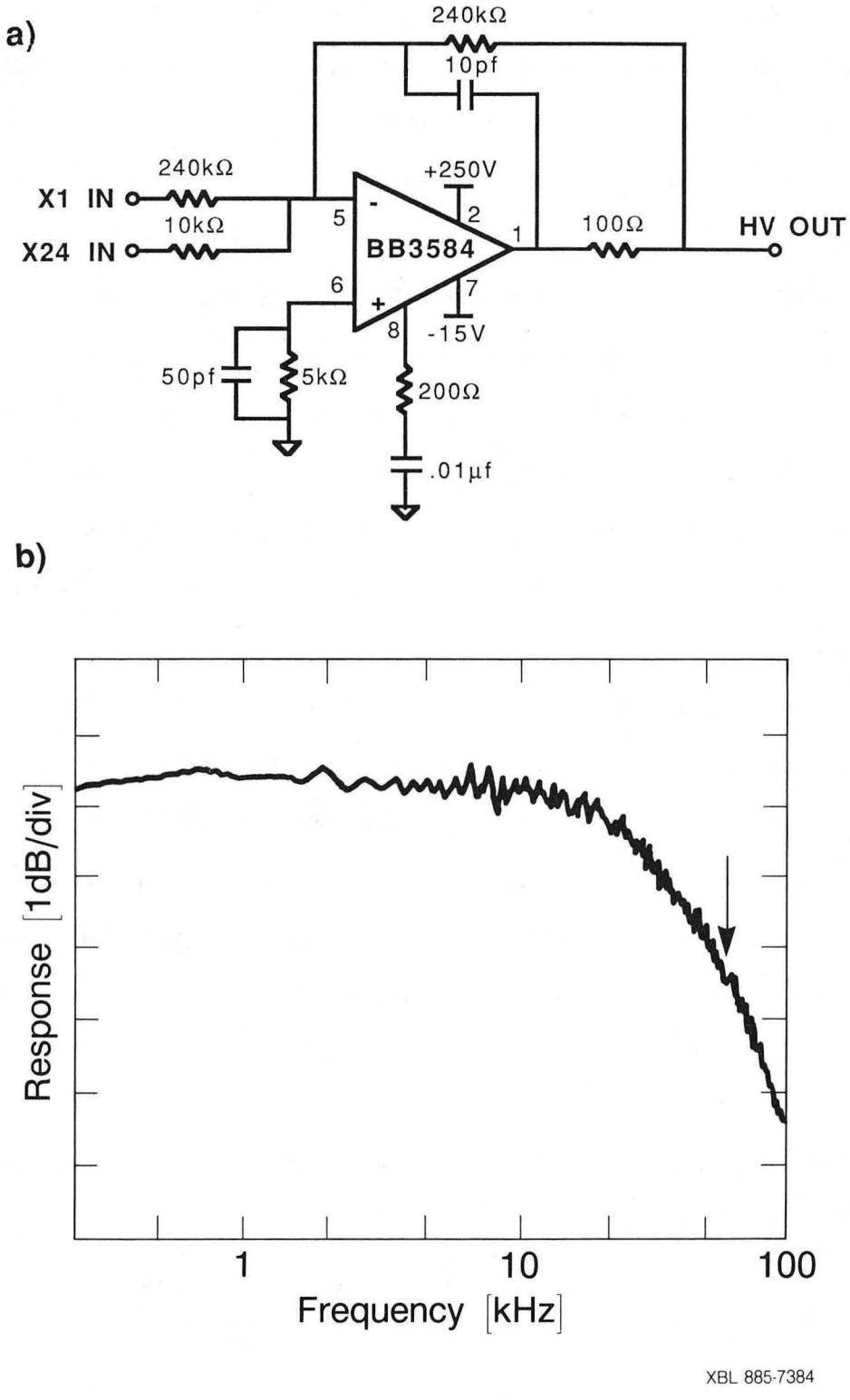

Fig. 2-14 (a) Schematic of the 3584 high voltage amplifier, with (b) the white noise response.

marvelous amplifiers, combining speed, low power, low noise, and low profile. We typically operate these amplifiers at a gain of 24, where they have a 3 dB rolloff at 60 kHz, and 1 to 2mV of noise rms at the output. One can now buy a similar 450 V operational amplifier (the APEX μTech PA88) which would provide twice the dynamic range.

We use analog ramps controlled by the computer to generate the X and Y raster for scanning. Typically we use 0.1 to 10 V ramps. For large topographic scanning, we multiply these ramps by 25 in the high voltage amplifier box. We usually leave the X ramp running all the time, the ramp box provides an 'X Start' pulse to trigger each scan line of the data acquiition. The computer controls Y ramp, starting and stopping it for each image.

We chose to build analog ramps for several reasons. They are very quiet, easy to set up, provide a smooth linear ramp, and it is simple to change parameters with knobs. Furthermore, computer generated ramps may be quite noisy. Also, the LSI 11/73 computer is not fast to both generate the ramps, and do the data acquisition at the speeds we required. On the other hand, it would be convenient to be able to change the speed, size of scan, or position of the scan from the computer.

Recently, I designed a new digital ramp box with Mats Gustafson, and he built it with assistance from John Davis and LeVern Gardner. This box has three main knobs: one each for size, speed, and rotation angle. The box generates the necessary clock pulses so that the data acquisition is almost completely controlled by the digital ramp box. This should provide a new level of convenience and reliability in data acquisition, and further simplify the computing.

We do limited analog signal processing before the computer A to D converter. For current imaging, we apply a 0.1 to 1.0 Hz high pass filter, a 20 kHz low pass filter, an offset, and then a gain of 10 to 1000. This provides a high quality signal for the A to D converter, and allows the user to easily manipulate the image as it is displayed in real time on the screen. For topographic imaging mode, we may use a 0.1 Hz high pass filter, and a 1 to 10 kHz low pass filter followed by a gain of 100 to 1000. Of course, these parameters depend on the scan speed as well as the type of sample being imaged, and so it is very useful to be able to control them during the experiment.

We use a battery to provide the DC bias for tunneling. This avoids 60 Hz noise, and with a resistive divider it is simple to provide 1 mV to 1 V for general use. For larger bias voltages, we use an HP power supply.

d) COMPUTING

The microscope is controlled, and data are acquired with a DEC LSI 11/73 computer. We bought this many years ago, and it has been upgraded over the years. The system consists of an LSI 11/73 central processing unit, 768 kBytes of random access memory, a dual 8"floppy disk, 2 RL02 10 Mbyte removable hard disk drives, a Parallax Q600 graphics card (480 by 640 screen with 256 gray levels or colors and RS-170 output for connection to a video tape recorder), a Grant Technology Systems analog to digital converter with direct memory access (150 kHz maximum data acquisition rate), a Grant Technology Systems programmable clock, and parallel and serial ports. When the data acqisition rate is below 50 kHz, the computer can read a scan line

and display it in real time. Above 50 kHz, the computer stores the entire image at rates up to 120 kHz, and then displays it. In normal operation, the images are shown as they are digitized, and the screen display is saved on video tape. With 128 X 128 data points per image, images can be acquired at rates up to 1 Hz. There is also a frame grabber which allows us to digitize images back off of the videotape when necessary.

For topographic imaging, the program ACQUIR is used. This program will acquire up to 120 lines of 256 points of XYZA data (where the fourth coordinate A might be work function or dI/dV). This is primarily used for slow data taking, with one to thirty minutes per image. As each scan line is taken, it is displayed X vs Z, and then when the image is complete, the data set is drawn in projection. The program can substract baselines, subtract an average z drift, rotate images to an average flatness, show single scans, and show top views.

For more rapid data acquisition, we use the program FASTD. This program was designed for current imaging, but will also work for fast topographic imaging. This program provides 1 Hz image rates with 128 X 128 points per image, and 0.25 Hz rates with 256 X 256 points per image. The images are then sent to the Tektronix computer for post-processing.

We currently use a Tektronix 6130 CPU with a 4129 Display to do the image processing. This system started as a 4115 Standalone display, and then has been upgraded over the years. The 6130 provides a UNIX operating system, with 3 MB RAM, a 26 MB hard disk, and a streaming tape backup. The 4129 provides 256 grays, 1024 X 1280 pixel screen, internal 3D manipulation hardware, and lightsourcing firmware.

For publication, we photograph the screen with a 4 X 5 Camera. The programs were written in FORTRAN and made extensive use of the graphics firmware of the 4129.

One of the most common data manipulation tasks is to filter the data. This is done by the FFT program, named for the main routine: the fast Fourier Transform. Figure 2-15 shows a typical image of graphite and its Fourier transform, before and after filtering using a butterworth filter. This just attenuates the high frequency components of the Fourier transform (the zero is plotted in the middle of the square), and so is roughly equivalent to a defocussing of the image.

Another common task is the correction of distortions in the image. This is performed by the CALIB program. To correct for thermal drift, non-orthogonality of the drives, or errors in the calibration of the X and Y drives, we use the graphite lattice as a calibration. In Figure 2-16 we show an example of this process. The graphite lattice is input by specifying sets of points along the lattice directions. We use several points per line, and two lines per direction for improved accuracy. The computer then calculates a mean direction and distance for each of the three lattice directions. A 2 X 2 linear transform is generated to map two of these vectors to the same length and 60° angle. The third vector is used as a consistency check. Using this we can measure distances to 0.1 Å, angles to better than 1°. Figure 2-17 shows the result of mapping the image using the linear transform. When there are adatoms in the image, we digitize the outline of the observed adatoms, and the computer can produce a model showing the positions of the adatoms relative to the substrate lattice (see Figure 2-18 and chapters VII and VIII). We can use the model to

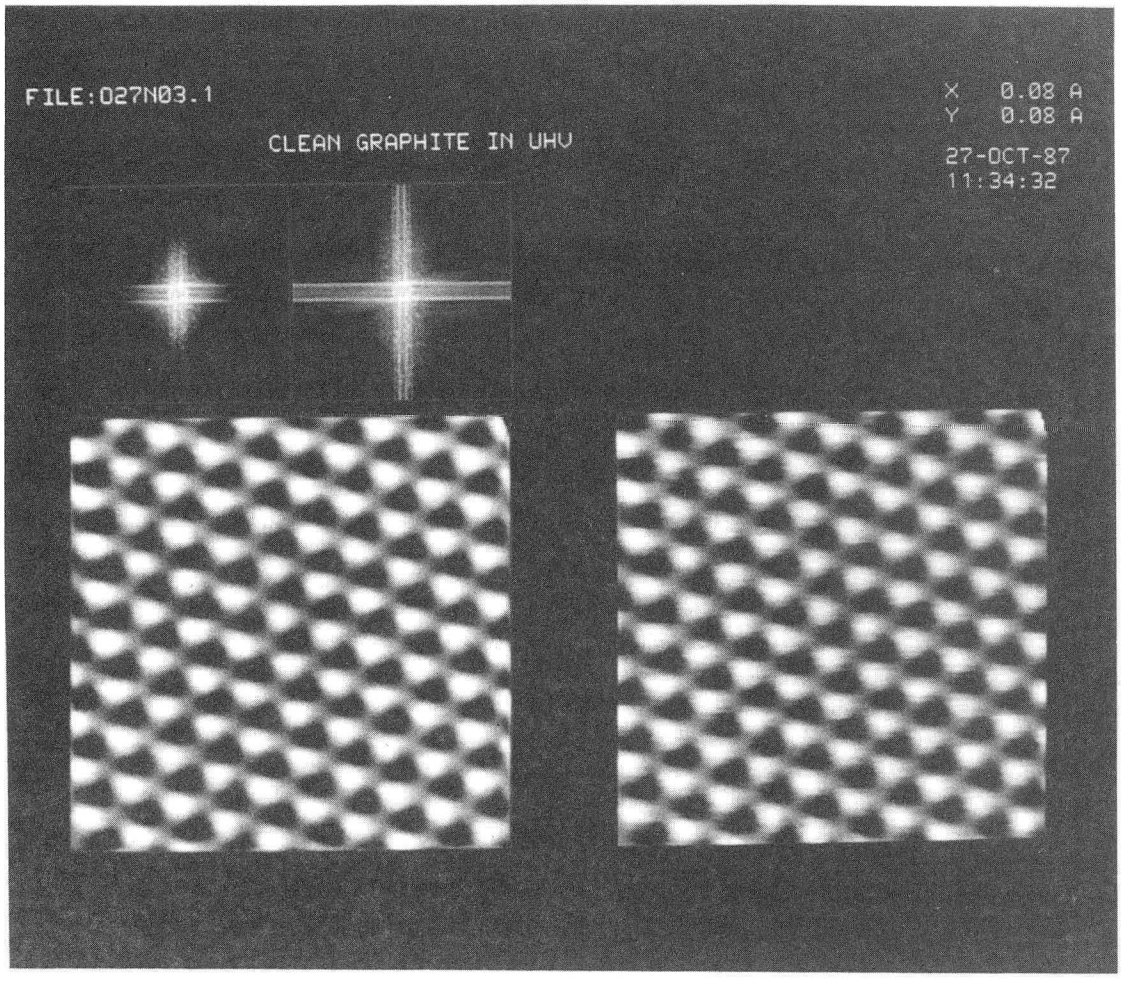

CBB 885-4495

Fig. 2-15 The lower boxes show the data before (right) and after (left) filtering, the upper boxes the 2D Fourier transform before and after filtering.

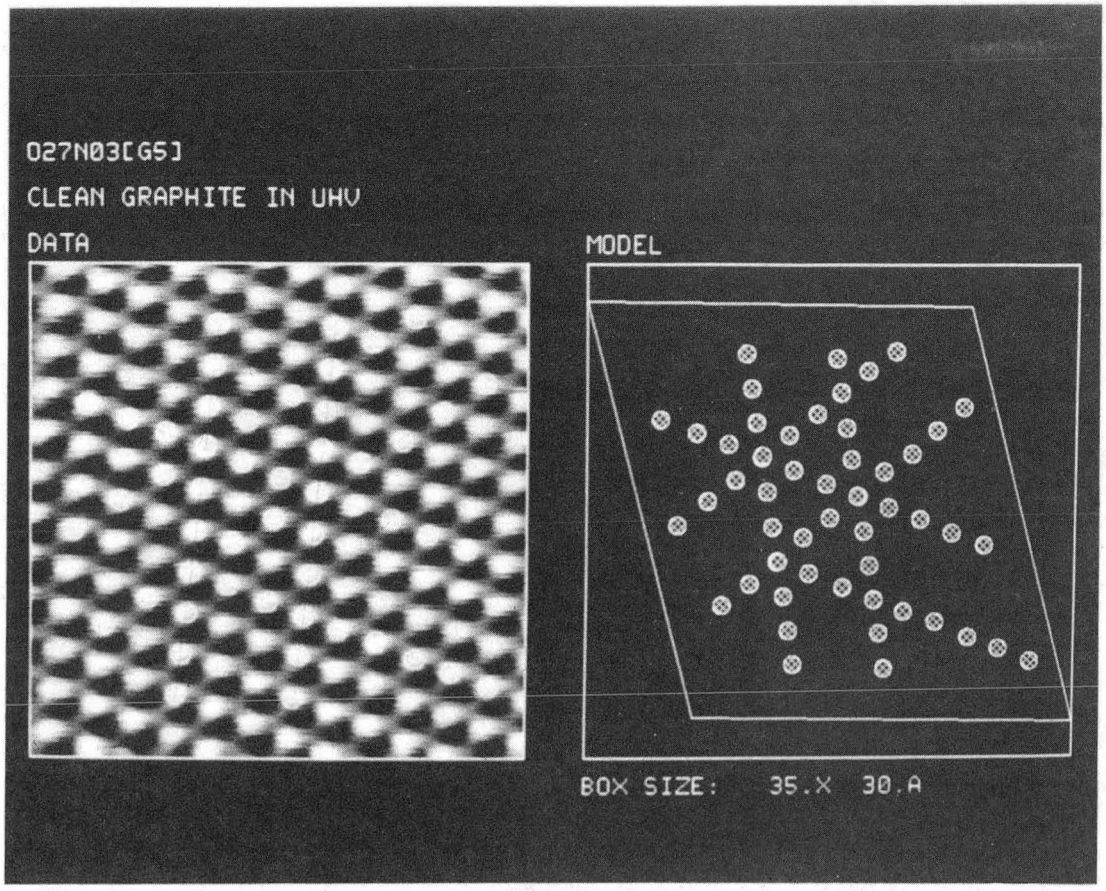

CBB 885-4481

Fig. 2-16 We input the locations of the graphite spots to generate a model.

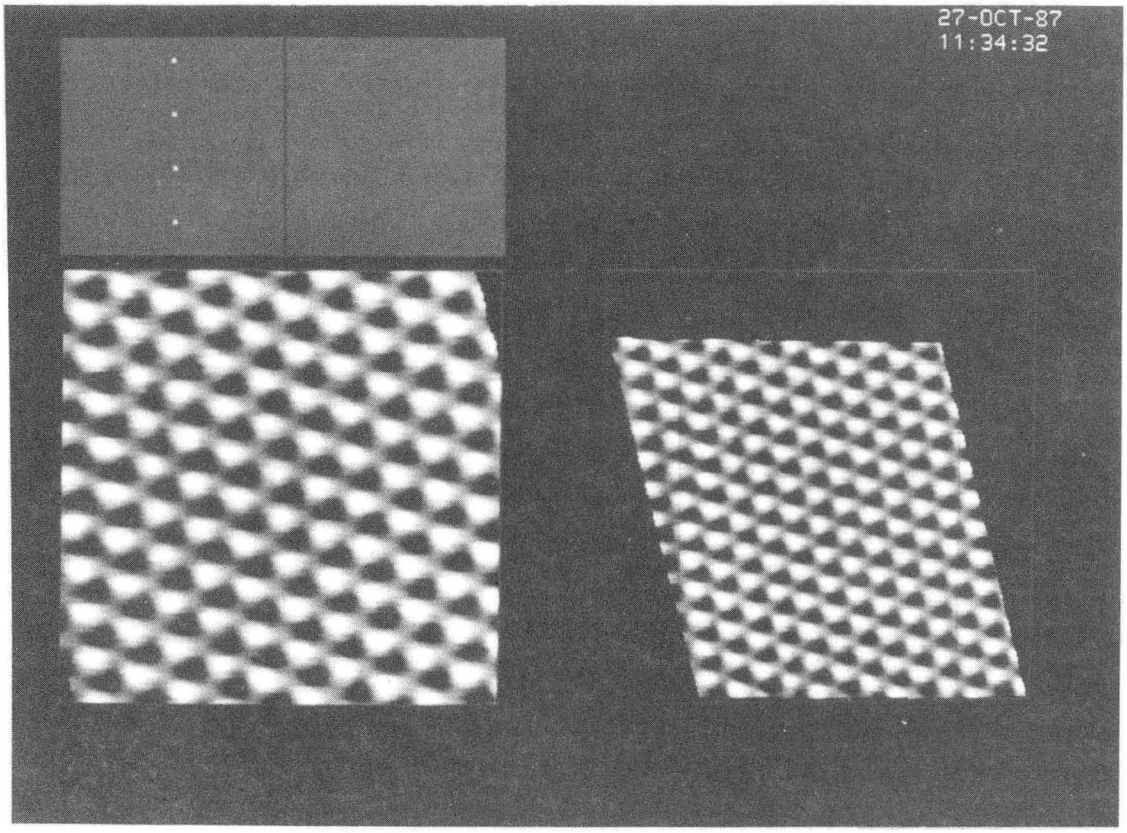

CBB 885-4493

Fig. 2-17 We can use the model to transform the data.

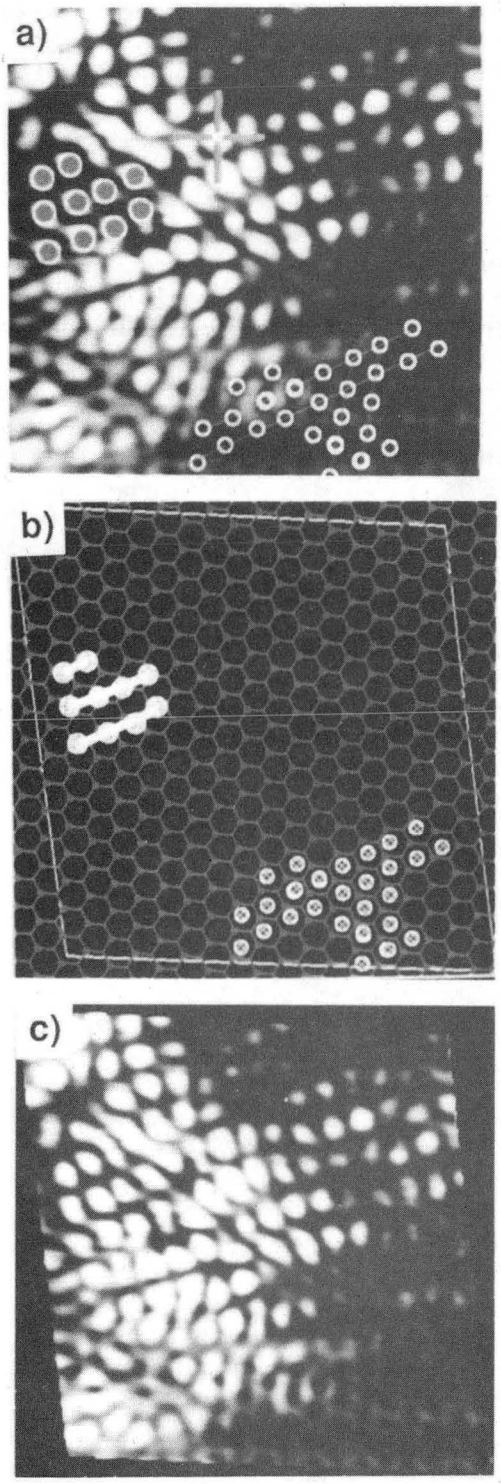

Fig. 2-18 (a) Image of Ag on graphite showing graphite lattice spots (small circles) and adatom locations (large circles) used for transformation. (b) Computer model. (c) Transformed image.

XBB 888-7413

make accurate determinations of adsorption sites and spacings, since the graphite surface has an accurately known honeycomb lattice spacing[8] of 2.46 Å.

We can also use the FFT program to do lattice averaging in Fourier space. In Figure 2-19(a) we show an image of a charge density wave in TaS_2 (see ref. 9). In Figure 2-20(a) we show the Fourier transform. Both the charge density wave, and the atomic lattice are imaged simultaneously, but the CDW spacing is three times larger. Thus if we choose just those spots at the lattice periodicity [Figure 2-20(b)], and then transform back to real space [Figure 2-19(b)] we get a lattice averaged image of the atomic lattice. Alternatively, we can choose the spots corresponding to the CDW periodicity [Figure 2-20(c)], to produce an averaged image of the CDW lattice [Figure 2-19(c)]. Finally, if we keep both sets of spots [Figure 2-20(d)], then we can produce a model image with very low noise [Figure 2-19(d)].

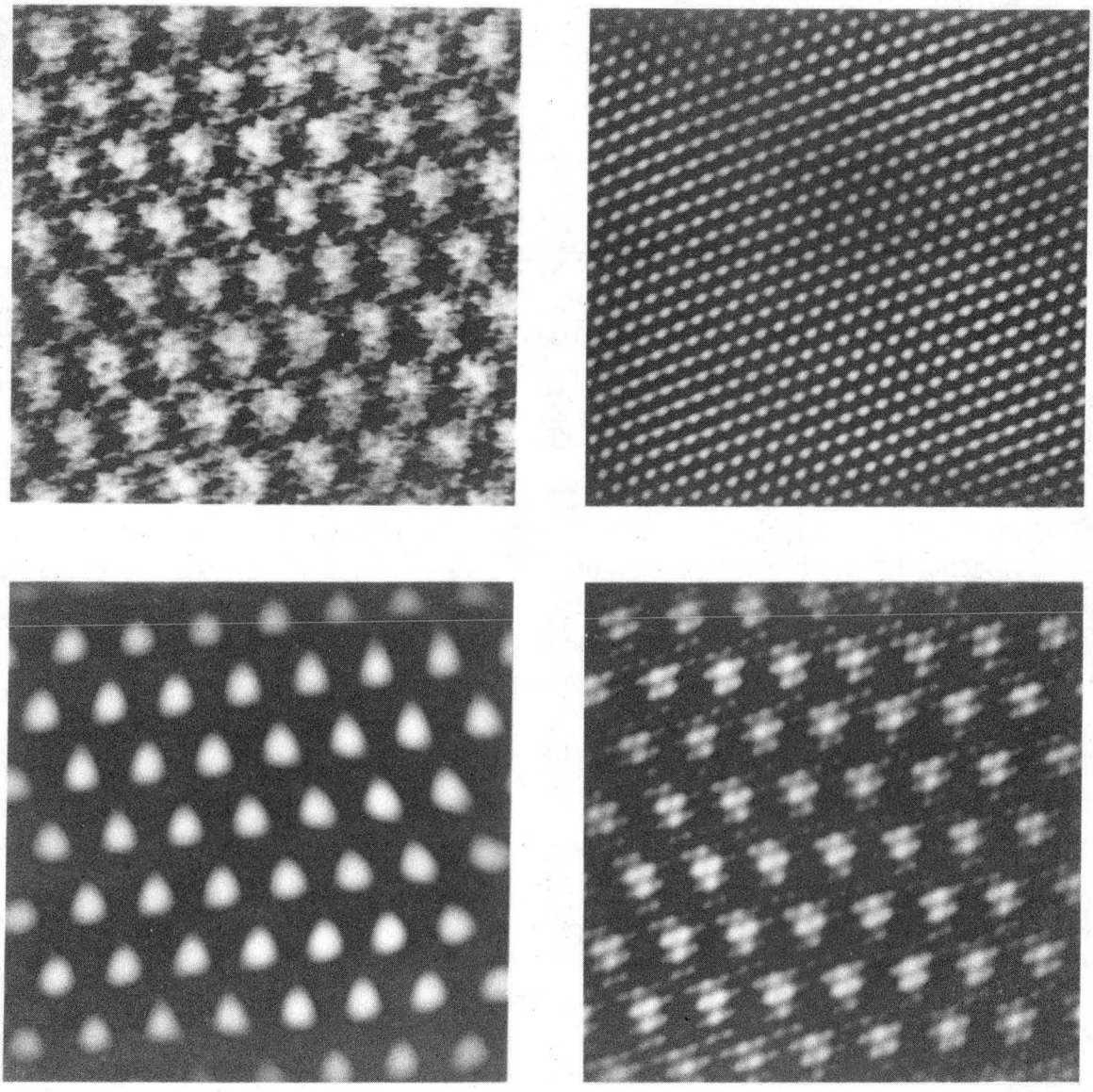

XBB 883-2139

Fig. 2-19 (a) Image of a charge density wave on TaS_2. By selecting set of Fourier components, we can observe just (b) the atomic lattice, (c) the CDW lattice, or (d) both lattices.

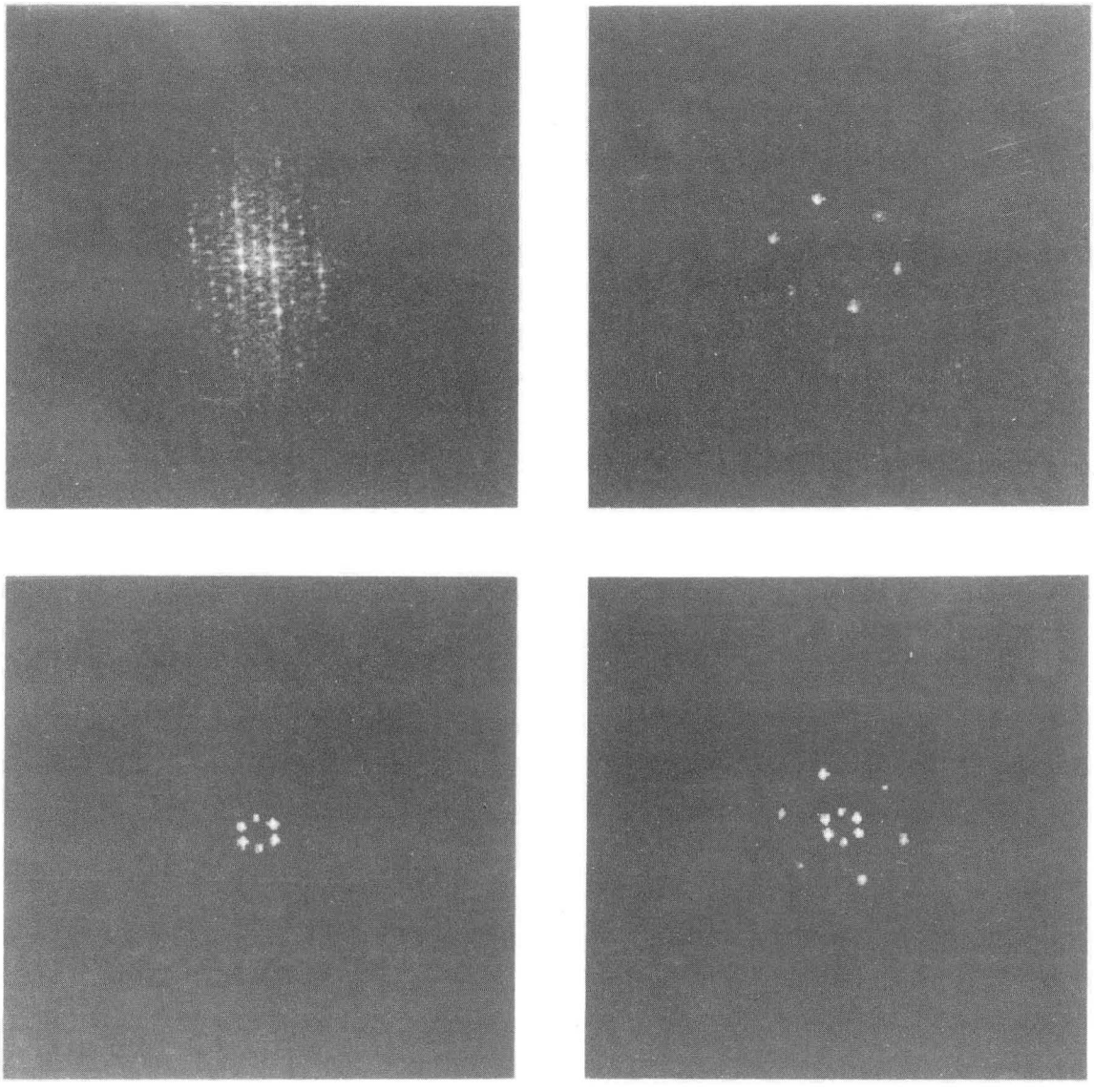

XBB 883-2140

Fig. 2-20 Fourier Transforms of the images in Fig. 2-19.

REFERENCES

1 H. J. Mamin, Ph. D. Thesis, University of California at Berkeley 1984.

2 H. J. Mamin, D. W. Abraham, E. Ganz, and J. Clarke, Rev. Sci. Inst. 56, 2168 (1985).

3 D. P. E. Smith and S. A. Elrod, Rev. Sci. Inst. 56, 1970 (1985).

4 G. Binnig, H. Rohrer, Ch. Gerber, and E. Weibel, Phys. Rev. Lett. 49, 57 (1982).

5 G. Binnig and D. P. E. Smith, Rev. Sci. Inst. 57, 1688 (1986).

6 H.-W. Fink, IBM J. Res. Dev. 30, 460 (1986).

7 D. E. Stout, pg. 3-18 "Handbook of Operational Amplifier Circuit Design" Ed: M. Kaufman (McGraw-Hill, New York 1976).

8 P. Trucano and R. Chen, Nature 258, 137 (1975).

9 R. E. Thomson, U. Walter, E. Ganz, J. Clarke, A. Zettl, P. Rauch, and F. J. DiSalvo, to be published in Phys. Rev. B (1988).

CHAPTER III

MODIFICATION OF A GOLD SURFACE

In our first set of experiments, we used the scanning tip to modify the surface under study. In principle, one should be able to transfer just one or a few atoms between the tip and the sample. On a larger scale, small holes or trenches can be dug. These techniques permit surface self-diffusion studies on the atomic scale by depositing a small group of atoms [as in the classic set of field ion microscope studies by Erlich and coworkers[1]], or by making a small scratch, and then observing the subsequent diffusion[2]. Other possible applications include the correction of errors in integrated circuits, or the fabrication of very high density storage units[3]. The unique combination of high resolution imaging and angstrom scale tip control will allow many new micromanipulation and microfabrication technologies based on scanning tunneling microscopes.

We decided to use gold in our experiments for several reasons: it is a good conductor, is readily available, and is relatively easily prepared. It also is a relatively soft material, and thus easily deformed. By using an inert material, which does not oxidize, we hoped to minimize the effects of contamination . The experiments were performed in 5×10^{-10} torr vacuum using mechanically ground 1mm diameter tungsten tips. These experiments were performed using the microscope of Figure 2-11(a). The tips were cleaned by field emission to the sample, and also by smashing them into the sample (thus presumably coating the end with gold). This work was published in 1986 with color photographs[4].

The first step was to prepare relatively flat and clean gold samples. We obtained a bulk single crystal gold sample with a polished (210) face. This sample was placed in the vacuum chamber, and then transfered to the STM. Figures 3-1(a) and (b) show typical images of this surface before cleaning. The surface is quite rough, with rolling hills of 100 Å to 200 Å diameter. Clearly, further sample preparation is necessary. We therefore heated the sample to approximately 850°C for three minutes *in situ*. During the heating, the pressure remained below 10^{-9} torr. This produced cleaner and flatter samples. The following data were then acquired over the next several days. We found the heated samples to be adequate for demonstration purposes, but certainly a more elaborate sample preparation could provide flatter and cleaner samples. Recent experiments by other groups have used very flat samples with excellent results[5,6,7].

In Figure 3-2, we show an image of the heated Au sample. The microscope was operating at relatively high resolution here, and the noise level in the z-direction is seen to be only 0.1 Å to 0.2 Å peak-to-peak in a measurement bandwidth of several hundred hertz, although individual atoms are not resolved. This image clearly shows atomic terraces formed by the annealing procedure. The step heights are roughly 2 Å, just half of the 4.1 Å gold lattice spacing as we expect. The small feature on the bottom left terrace may be due to contamination, or may be a small cluster of Au. Large, atomically flat areas with occasional terraces would provide the ideal substrate for deposition and manipulation experiments, since they provide both the flat areas to work on, and the steps for markers and calibation.

Unfortunately, for the experiments discussed here, we were not

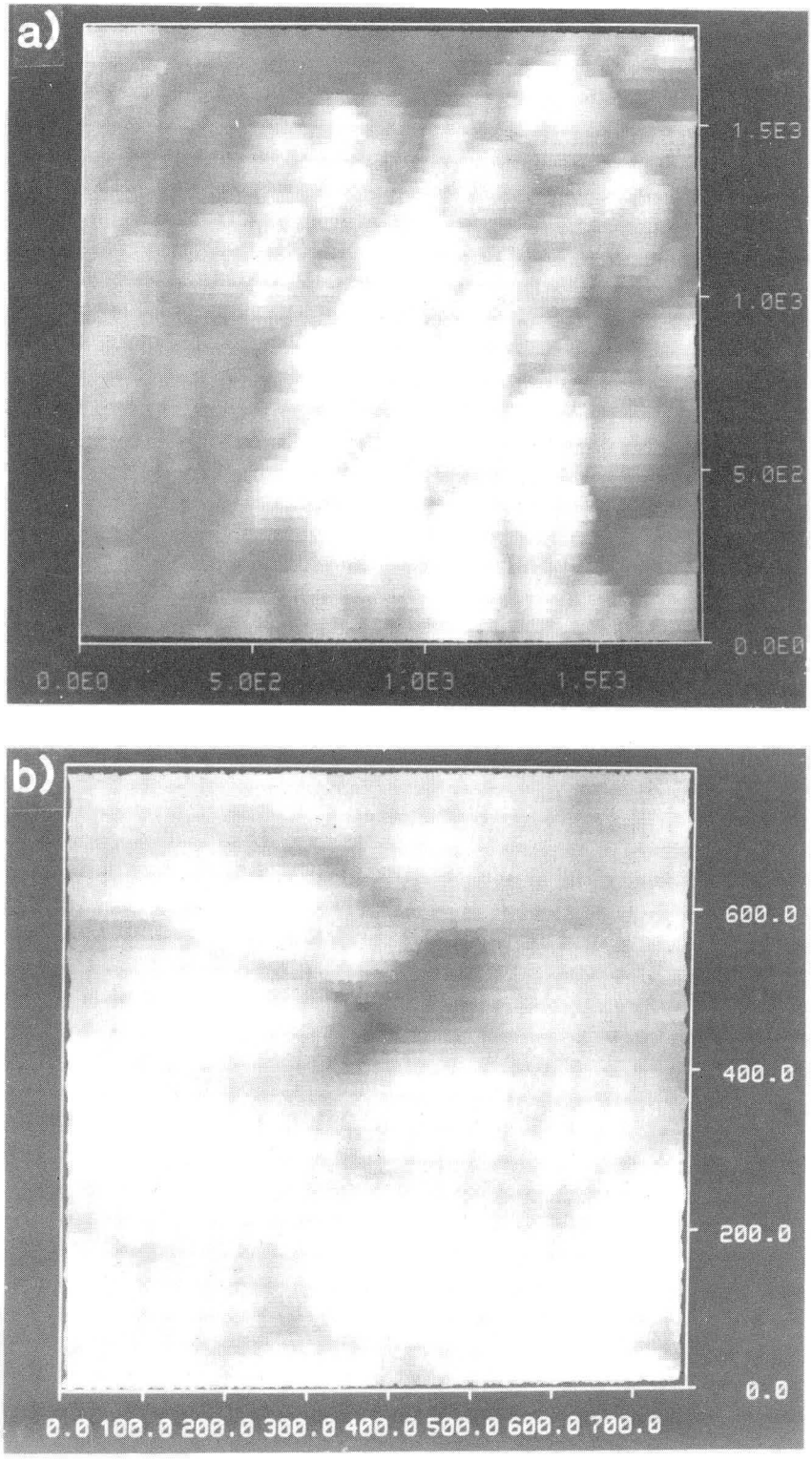

Fig. 3-1 Au sample in vacuum before annealing treatment. We observe rolling hills composed of roughly 100 Å grains. (a) 1800 Å X 1800 Å topographic image, with 130 Å Z range. (b) 750 Å X 750 Å topographic image with 26 Å Z range.

XBB 885-4566

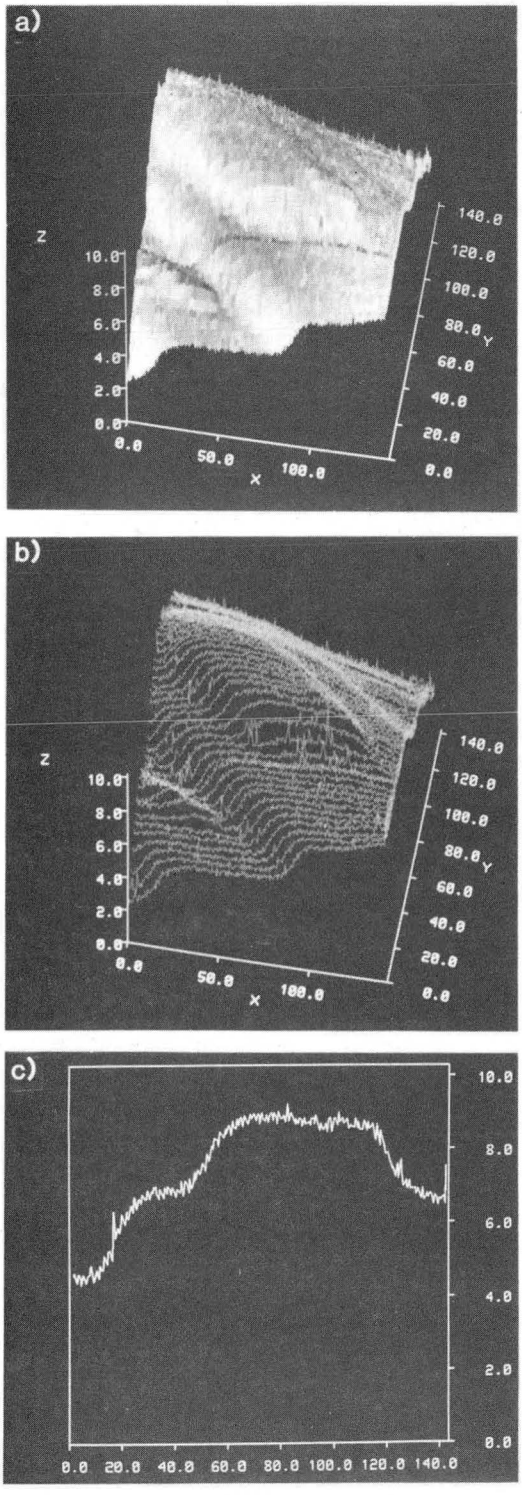

Fig. 3-2 140 Å X 140 Å topographic image of the Au sample after annealing. Atomic plateaus are visible. (a) Projected, illuminated image, (b) line trace, and (c) single scan showing 2 Å step height. XBB 885-4568

able to find large flat terraced areas consistently. The annealed sample was found to be quite flat, but with shallow rolling hills. A typical image is shown in Figure 3-3(a). This level of flatness was judged sufficient for demonstration purposes. But first, in a further effort to characterize our samples, we decided to map the effective barrier height as a function of position.

At low bias voltages and currents, typically mV and nA, the STM operates in the tunneling regime. It has been suggested[8] that the tunneling current can be predicted by a simple WKB model of single-electron tunneling through a trapezoidal barrier. Such a picture predicts an exponential dependance of tunneling on tip-to-sample separation s. In this model, the tunneling current density j is given by

$$j = (e/\hbar)^2 (V/s) \sqrt{2m\Phi}\; e^{-(2/\hbar)\sqrt{2m\Phi}\, s} \qquad (3.1)$$

for a fixed bias voltage V (with $eV << \Phi$), where m is the electron mass, $\hbar$ is Planck's constant, and Φ is the average work function of the tip and sample. If we neglect the image potential[8,9], Φ is also the tunnel barrier height. For small variations in s, we can then estimate the barrier height from $\partial(\ln I)/\partial s \approx 1.025\Phi^{1/2}$, with Φ in eV and s in Å, where I is the total tunneling current.

We have produced maps of this model or 'effective' barrier height by sinusoidally modulating the tip-to-sample distance at a frequency higher than the roll-off frequency of the feedback loop, and detecting the modulation in the tunneling current with a lock-in amplifier[10]. Thus, by recording both the voltage applied to the z-drive and the

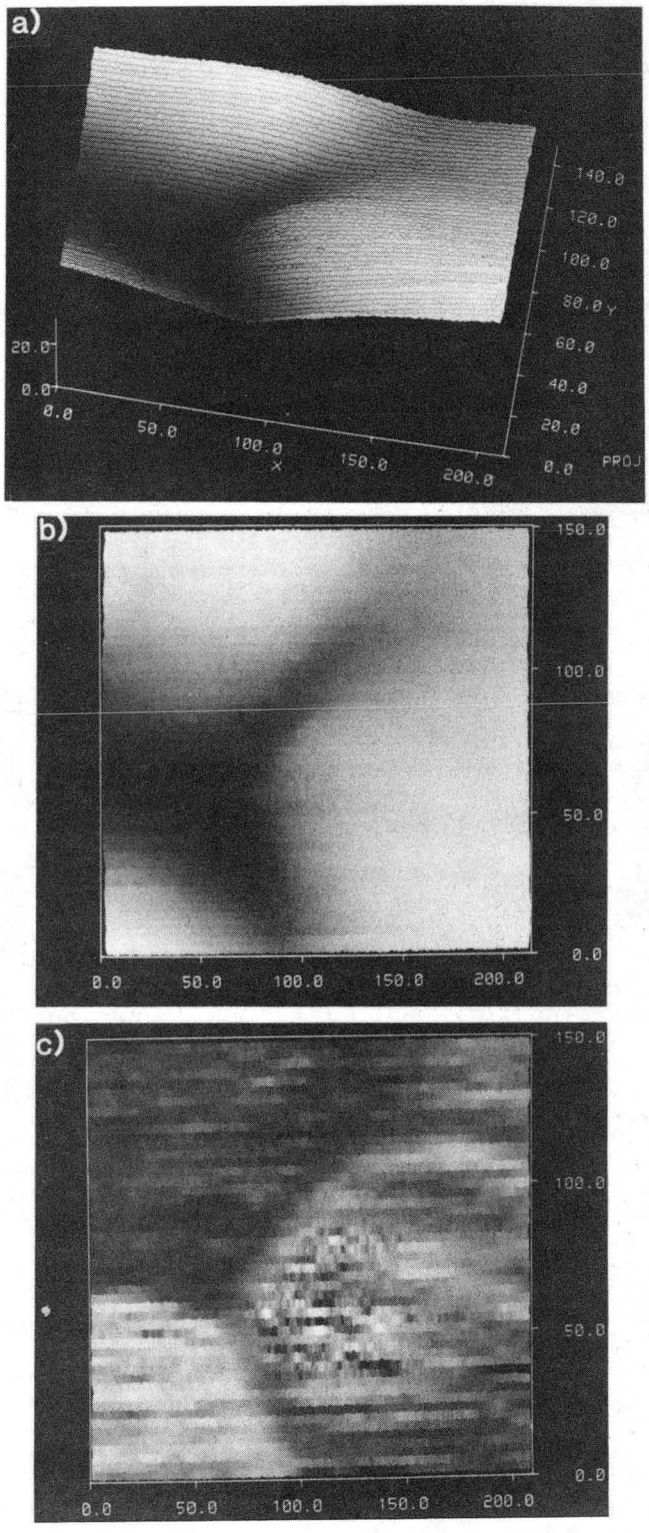

Fig. 3-3 (a) Projected view of 210 Å X 150 Å topographic image showing the tripartite boundary between three Au grains. (b) Top view, and (c) effective barrier height plot (dark to light range is 0.5 eV to 1.1 eV). XBB 885-4570

output of the lock-in detector while the surface is scanned, we are able to obtain a "topographic" image, and an "effective barrier height" image simultaneously. Figures 3-3(a) and (b) show topographic images obtained at a bias of 50 mV for a 100 Å X 100 Å region of the annealed gold sample. Figure 3-3(c) shows the effective barrier height map, obtained with a modulation frequency and peak-to-peak amplitude of 1 kHz and 0.4 Å respectively. The gray scale in Figure 3-3(c) corresponds to an average barrier height that varies from 0.6 eV (upper left grain) to 1.1 eV (lower left grain).

We see that the image is centered at the junction of three gold grains. The grain boundary has a characteristic tripartite structure, with three equal angles[11]. The two grains on the left of the image appear quite flat, while the grain on the right has a small rounded mound on it. When we examine the effective barrier height plot, we notice several facts. First of all, the grain boundary is well delineated, showing that barrier height is relatively constant for each individual grain. Secondly, the round mound on the right hand grain corresponds to an area of low and quite noisy barrier height. We expect that this area is contaminated. Finally, we note that all of these values are significantly lower than the 5 eV expected for a clean gold surface. This discrepancy is not due to the measuring technique, as we have also measured the current vs position using a DC technique, and obtained similar results. There are several possible explanations for these low barrier heights. First of all, the entire sample may be contaminated. On the uncleaned gold surface we typically measured[12] barrier heights of 0.1 eV. Alternatively, the tip may be somewhat contaminated, or have a thin oxide layer. Finally, the simple WKB

approximation we have used may not be accurate under these conditions. We have neglected the effects of image potentials[13], but recent calculations by Coombs *et al.*[14] indicate that dI/ds may not be significantly affected by the presence of an image potential. However, recent experiments[15] and calculations[16] indicate that for sample separations smaller than roughly 4 Å the tunnel barrier may collapse.

Thus, on the one hand, we have seen that the measure of the local barrier height is not straightforward, and many factors can produce low effective barrier heights. In chapter IV, we will see that sample deformation can also produce very low effective barrier heights for certain samples. On the other hand, we have demonstrated the capability of making barrier height measurements using an AC lock-in technique while scanning. The AC detection can give good signal to noise, and recently there has been some interest in applying these techniques to biological materials[17]. In hindsight, we can see that our annealing step was not sufficient to provide completely clean samples. By now, several groups have prepared clean metal samples and measured reasonable barrier heights[18,19] of 3 to 5 eV. At the time, we decided it was most important to demonstrate the potential of surface modification, leaving more careful sample preparation for later. Therefore, although we were working in reasonable vacuum, with annealed samples and field emitted tips, we must keep in mind the possibility that contamination played a role in the modification experiments that follow.

We used two simple techniques to modify the surface. First, we touched the tip to the sample to produce scratches and indentations. Generally, the resulting features were roughly 100 Å in size, although

there was usually some deformation of the surface at distances of 500 Å or more from the primary indentation. Sometimes, however, we found that the tip had changed, so that the microscope was scanning a completely new section of the sample. In fact, these tip changes pose a serious problem, and a potential limitation for this technique. The second method actually deposited material onto the surface. This was accomplished by working at high currents and small tip-to-sample separations, but without touching the tip to the sample. Typically, small hillocks were formed on the surface roughly 200 Å across. In both cases, we have observed surface diffusion (i.e. healing) in the period following the initial formation. After the modification step, we reduced the tunneling current to 10 nA, thus increasing the spacing, s, to prevent the scanning from affecting the diffusion process.

In Figure 3-4 we show a scratch we made in the surface. We located a steep hill with a flat spot at the bottom, set the feedback circuit for slow response, and then moved the tip in the -X direction by turning an offset control by hand. The feedback circuit was not able to pull the tip back quickly enough, and so the tip was dragged across the hill. Figure 3-4(b) clearly shows the resulting trench dug into the hillside. This trench is roughly 100 Å wide and 20 Å deep. This type of surface scratching was studied by Gane and Bowden[20] in the 1960's using a scanning electron microscope. They were able to form 1000 Å scratches by dragging a needle across a gold surface. With the STM, we are now able to operate on a much smaller size scale.

Figure 3-5 shows a series of trenches dug into a relatively flat sample. Figure 3-5 (a) shows an area with recognizable features, as well as a large flat area. To make the scratches, we increased the

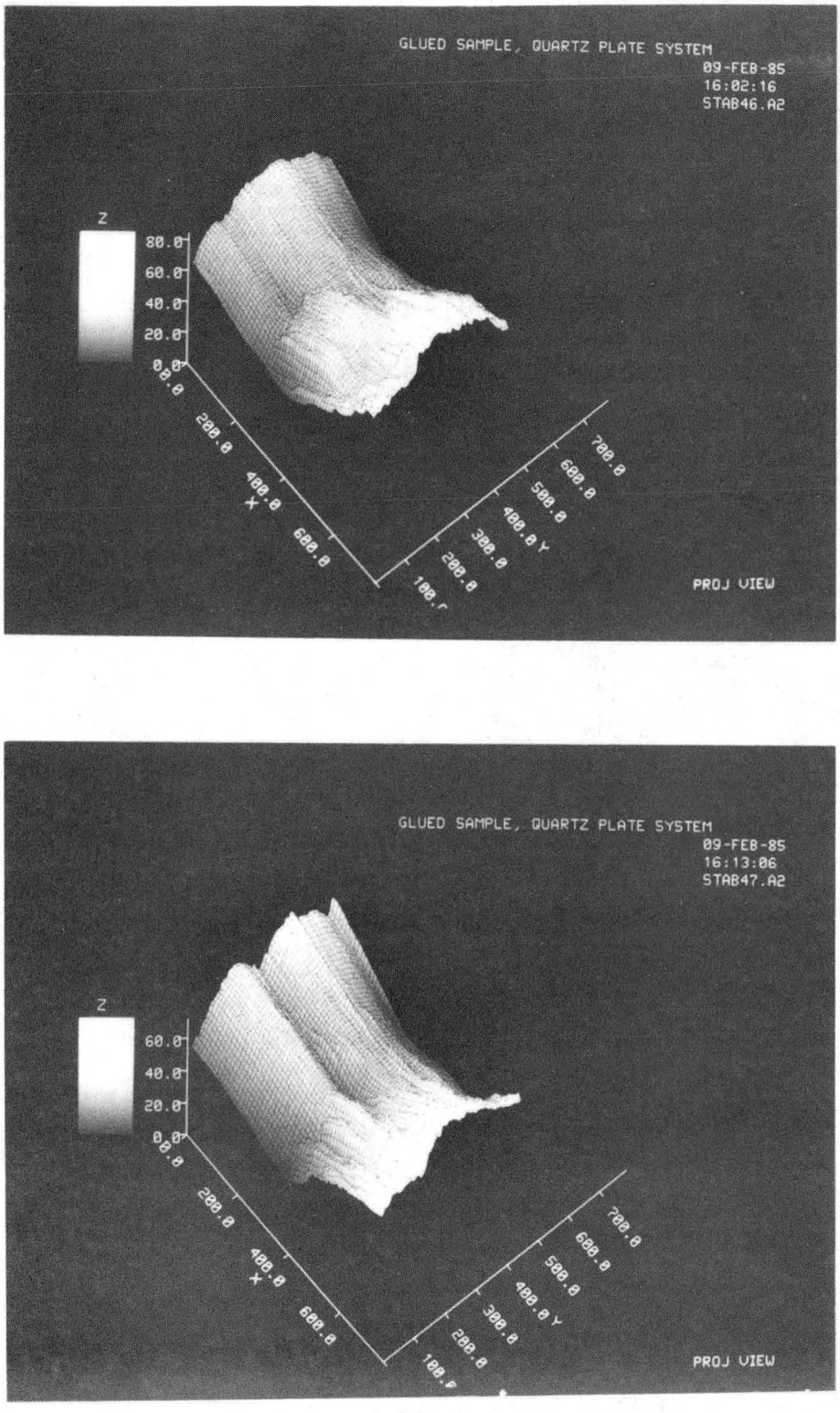

Fig. 3-4 (a) Topographic image of a Au surface before, and (b) after scratching the surface with the tip.

XBB 853-2202

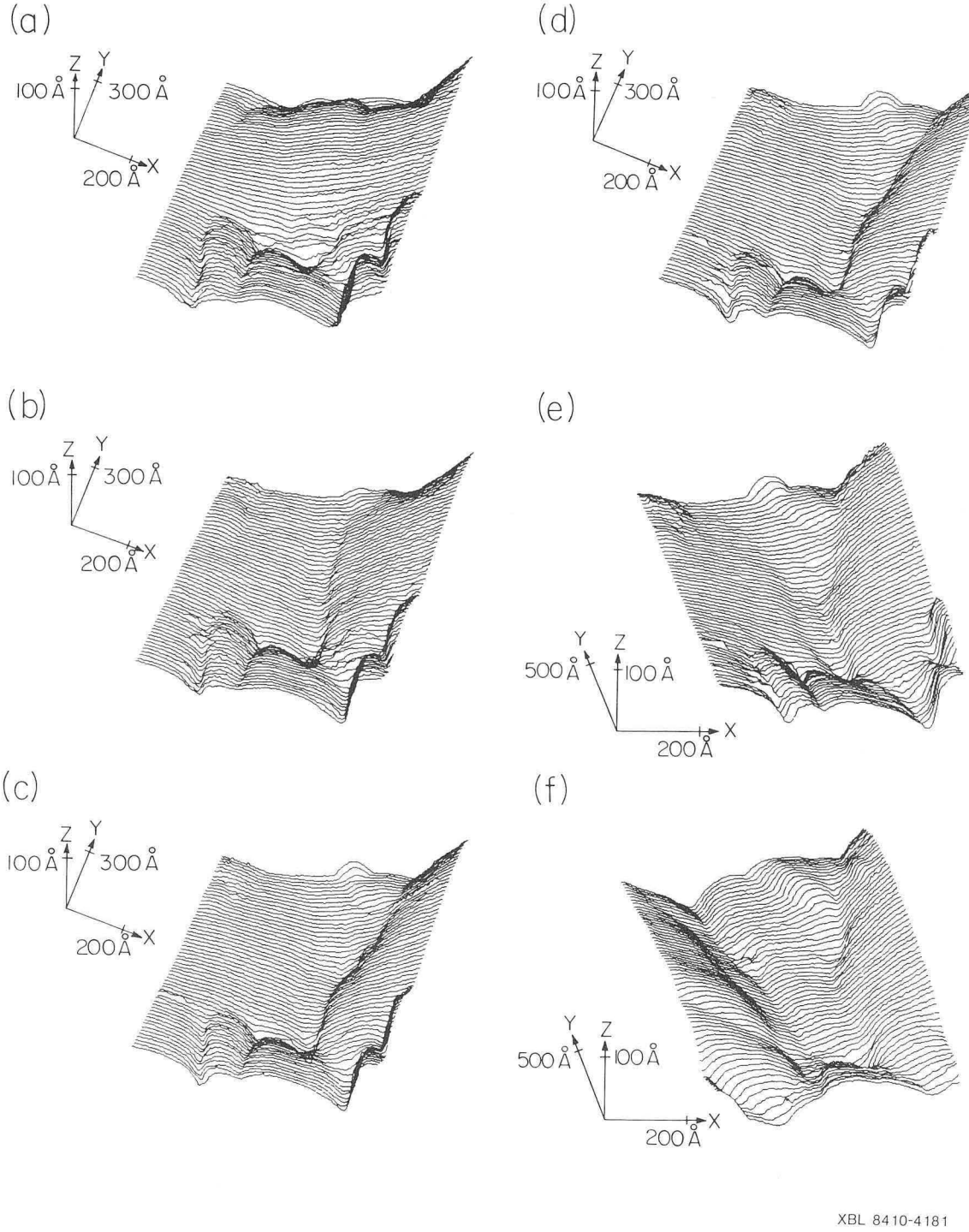

Fig. 3-5 Series of topographic images showing the effects of scratching the Au surface.

tunneling current to 1 μA (corresponding to a gap resistance of 10^4 Ω), and then moved the X or Y drive in the desired direction. Figure 3-5(b) shows the result of a vertical scratch (Y direction) down the center of the image. A trench roughly 50 Å wide and 30 Å deep was dug into the surface. Figure 3-5(c) shows the result of a horizontal scratch (X direction) across the center of the area. This did not cut a trench, but did put a dent into the hill at the right hand side. Figure 3-5(d) was made 8 minutes after (c), and shows the same area (a hidden line algorithm was applied here to improve the visibility of the surface features). The image has drifted roughly 30 Å in eight minutes. Figure 3-5(e) shows the same data as (d) but rotated to a different viewing angle. Finally, Figure 3-5(f) shows the result of a second vertical scratch which produced a second trench to the left of the first one. With the introduction of the atomic force microscope, it should now be possible to drag a tip across a surface with a specific, small load.

The effect of lowering the tip onto the sample is show in Figure 3-6. Initially the surface was featureless as shown in Figure 3-6(a). The images were made with 3 mV bias voltage, and 10 nA current giving a gap resistance of $3X10^5$ Ω. To crash the tip into the surface, the X and Y drives were offset to move the tip to the middle of the imaging area, and then the current setting was momentarily raised to 1000 nA (3000 Ω). To raise the tunneling current, the feedback loop forced the tip forward, smashing it gently into the surface. Figures 3-6 (b), (c), and (d) are subsequent scans made over a period of forty minutes. The imaged area was moving slowly to the left due to thermal drift. We see that a relatively small dent has been pressed into the surface.

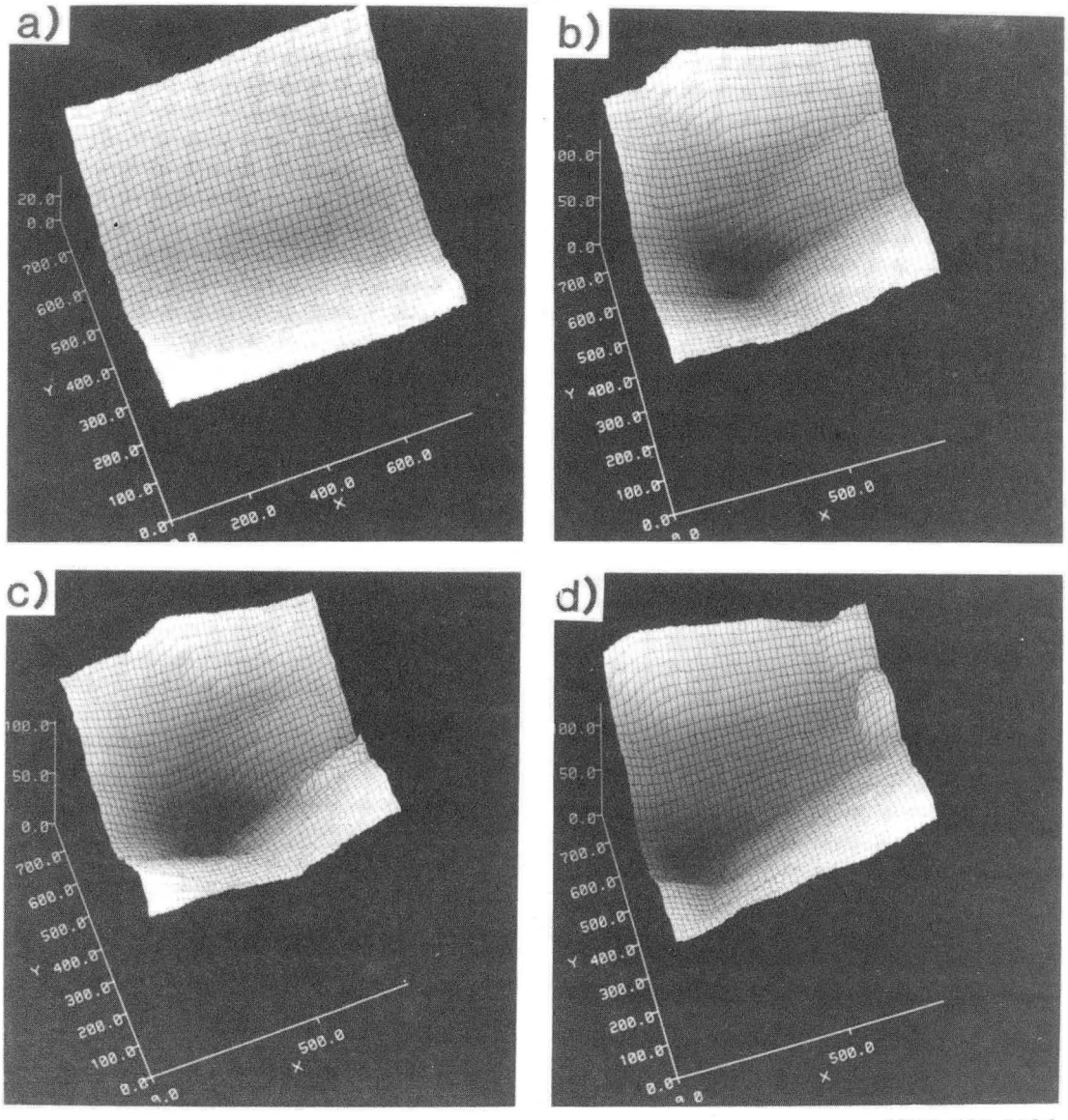

XBB 885-5496

Fig. 3-6 Topographic images showing (a) a flat region of a Au surface, (b) result of poking the tip into the surface, (c) and (d) subsequent images.

The dent is roughly 500 Å across and 100 Å deep. A small amount of surface healing is observed by the end of the 40 minutes. We found that the recipe for making these small dents varied greatly depending on tip and sample condition: Our usual method was to start delicately, and then bring the tip in closer and closer (by lowering the bias voltage) until we got a result.

In Figure 3-7(a) we show another dent created by crashing the tip into the surface. The initial surface was flat like that in Figure 3-6(a). In this case, the tunneling resistance was lowered to 200 Ω for several seconds. This 200 Ω is presumably due to contact resistance, and roughly agrees with an estimate based on the observed contact area. The center portion of the resulting hole was more or less axial in shape and was approximately 150 Å across and 30 Å deep. In addition, we found that the surface was deformed to some extent over a region roughly 700 Å across. After 3¾ minutes had elapsed, some of these latter irregularities had annealed out [Figure 3-7(b)]; after a further 13¾ minutes the stable configuration shown in Figure 3-7(c) was reached. Subsequent images showed no significant changes in the structure.

The final result is a very well-defined Y-shaped pattern roughly 10 Å deep, and is very similar to the naturally occurring grain boundary observed in Figure 3-3. We speculate that this pattern may be caused by stress relief in the gold surface (we note that the lowest energy configuration of a boundary between three grains is threefold symmetric[11]). The total spatial extent of this process seems to be at least 500 Å square, even for extremely delicate contact. I note that in recent experiments on flat gold films[6,7] similar diffusion on gold

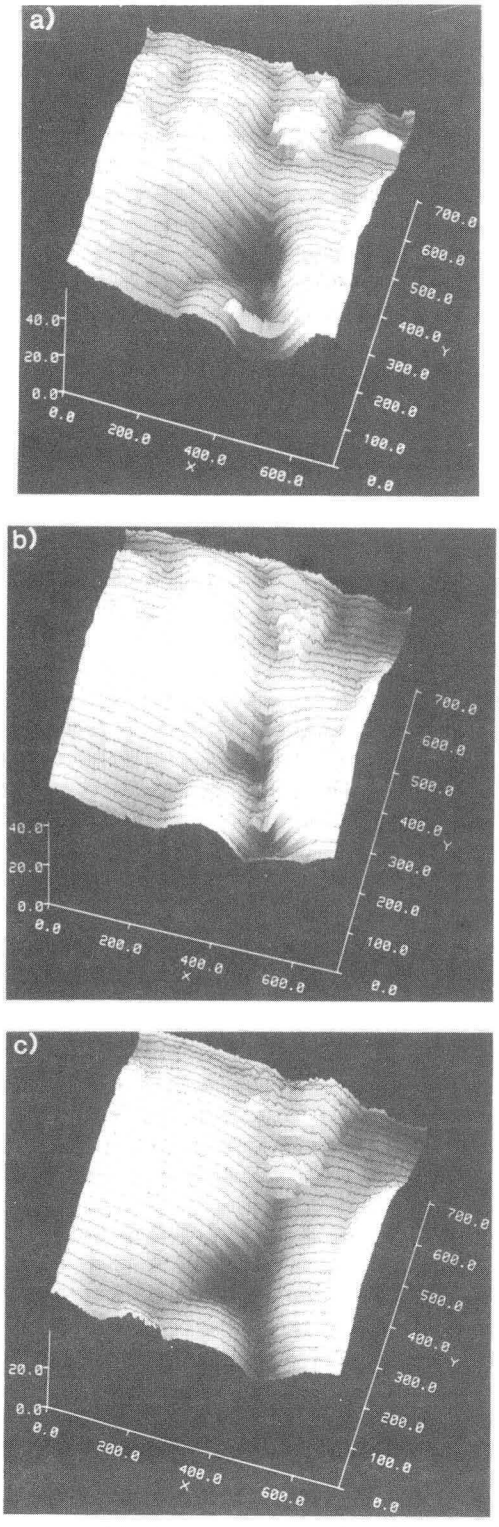

Fig. 3-7 Topographic images of the Au surface after crashing the tip into a flat region. (a) Image made right after the crash, (b) 3.5 min later. (c) 17 min after the crash the surface has healed significantly. XBB 884-4472

surfaces over periods of hours was observed. Unfortunately, the observed healing rates are faster than the canonical numbers for surface self-diffusion on bulk gold; perhaps the initial impact creates a strained state, which contains dislocations or interstitials thus driving an enhanced annealing rate.

To apply these techniques to microdeformation experiments, it would be necessary to measure the force exerted by the tip on the surface during modification. This can now be done with an atomic force microscope[21]. The results of Gane and Bowden[20] suggest that plasic deformation will occur in gold when the applied shear stress exceeds ~1/20 of the bulk shear modulus. This corresponds to roughly 10^9 N/m^2 in gold. Thus for a 500 Å tip, we expect that we must apply a force of roughly 10^{-8} N to make a 10 Å deep mark. Forces of this magnitude can be measured and controlled using an atomic force microscope.

In Figure 3-8 we see two small mounds formed by a deposition of material from the tip. Initially, the sample area was relatively flat, with a sharply rising feature at the right rear of the image [Figure 3-8(a)]. We used this marker to confirm that subsequent scans were made over exactly the same region. We then moved the tip to each of the two locations specified by the arrows on Figure 3-8(a), and momentarily increased the tunneling current to 1 μA with the tip biased at +5 mV (5000 Ω). We were also able to form similar mounds with the tip negative. Initially, the mounds were rounded in shape and were 200 Å to 250 Å wide and 20 Å high.

While there are several possibilities, we think that these mounds were formed by the deposition of material from the tip to the surface. In its previous history, the tungsten tip had come into contact with

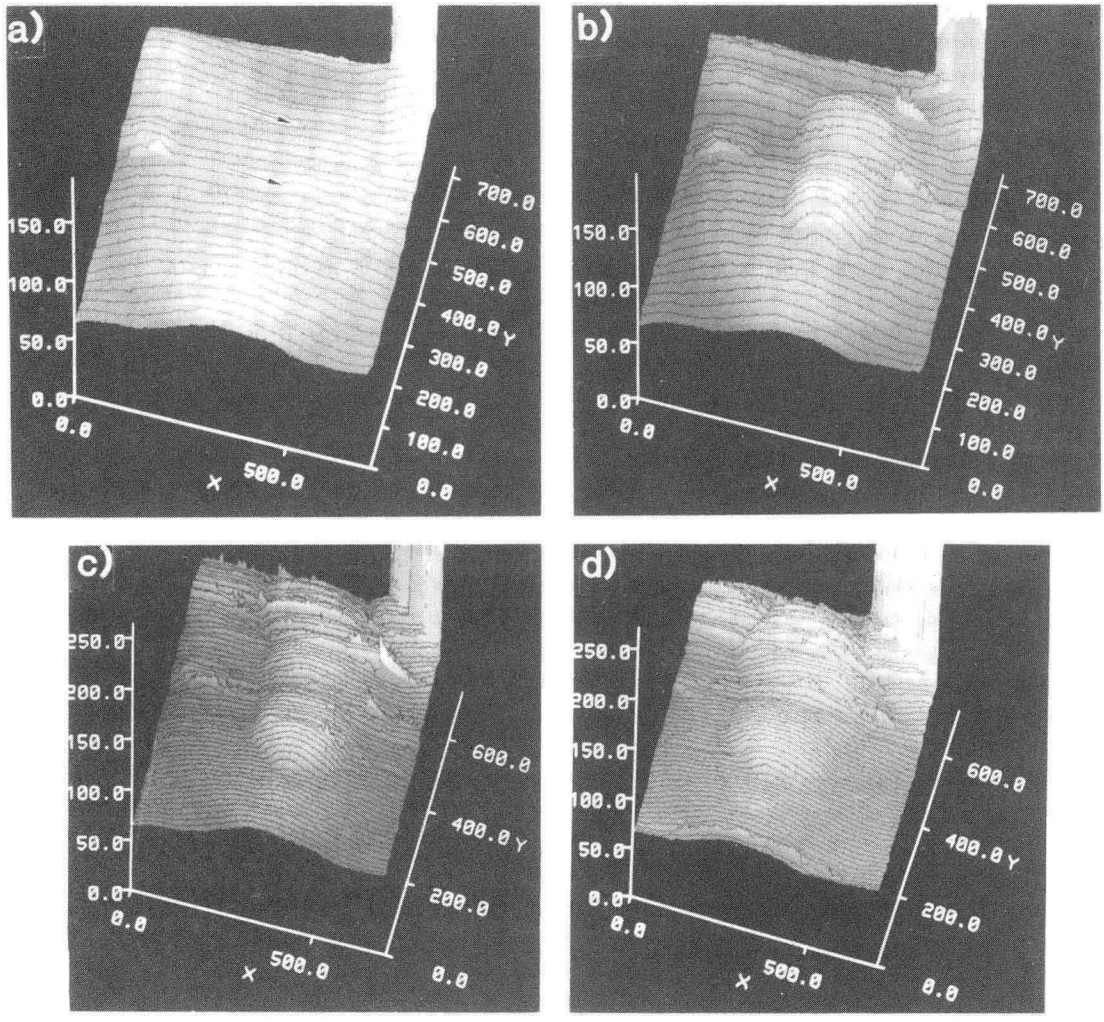

XBB 885-4564

Fig. 3-8 Topographic images of (a) a flat area of the Au surface with a hill at the right rear which we use as a marker. (b) Two mounds are formed by deposition of material from the tip. (c) Subsequent image, and (d) image made 12 min after the deposition.

the gold surface many times, and it seems likely that a small amount of gold was transferred to the tip. The mechanism for the transfer of gold back to the surface during deposition is unclear. Simple estimates based on the power dissipated in the junction between tip and sample suggest that significant heating did not occur (if we assume that the incoming electrons travel a mean free path before dissipating their energy, then the few nanowatts of power are rapidly dissipated by the mass of gold near the junction). Thus, it seems likely that material was transferred due to the close proximity of tip and sample.

In contrast to the deformation experiments illustrated in Figures 3-6 and 3-7, the deposition process appears to be very local, and not to disturb a larger surrounding area: For example, in Figure 3-8 the small feature roughly 250 Å to the left of the mounds was not affected by the deposition process. Subsequent images showed that the mounds diffused laterally. In Figure 3-8 (c) the mounds have developed flat tops and are now roughly 300 Å to 400 Å across and 12 Å high. This suggests that the mounds have increased in volume. This may be due to further gold atoms collecting onto the freshly deposited gold, or it may arise from contamination of the gold. It might be interesting to measure the barrier height of such deposited areas.

There is another possibility for the apparent increase in the volume of the gold mounds: The tip may be changing. When the gold is deposited onto the surface, it may leave a sharp tip. During the subsequent scanning, gold on the tip might diffuse to round off the tip. A blunt tip would make the deposited mounds appear to be larger than they really are. This effect is shown graphically in Figure 3-9. As the tip moves over a large feature, the tunneling current will move

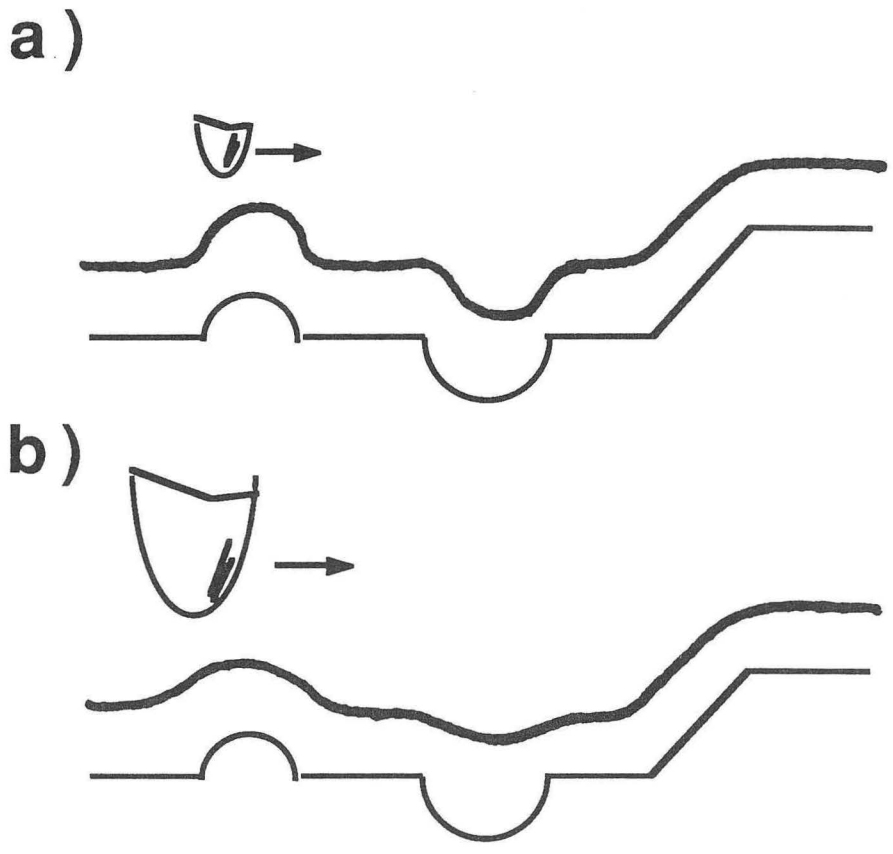

Fig. 3-9 The STM image is strongly affected by the shape of the tunneling tip. In (a) we see that a small tip reproduces the surface topography better than (b) a larger tip. In general, the heights of steps and protrusions are maintained, but the width of a protrusion will be increased, while both the depth and width of a depression will be reduced.

from one side of the tip to the other, thus making a protrusion appear wider but not taller than it really is. On the other hand, a depression on the surface will appear narrower and perhaps also shallower. Thus, for quantitative measurements of macroscopic objects, the tip shape will need to be well defined.

These experiments have wide-ranging implications in the study of surface diffusion, hardness measurements on a nanometer scale, and micro-machining. In addition, the techniques outlines are potentially useful as a mechanism for high-density memory storage[3]. Finally, it would be particularly interesting to observe these processes with atomic resolution. The recent observation of atomic features on thin film gold (111) samples epitaxially grown on mica[21] with very large corrugations should spur further experiments in this area. It might be interesting to watch a small gold mound diffuse away into a flat substrate as the substrate temperature was raised.

REFERENCES

1 K. Stolt, W. R. Graham, and G. Erlich, J. Chem. Phys. 65, 3206, (1976).

2 J. M. Blakely and H. Mykura, Acta Metal. 9, 23 (1976).

3 C. Quate, private communication.

4 D. W. Abraham, H. J. Mamin, E. Ganz, and J. Clarke, IBM J. Res. Devel. 30, 492 (1986).

5 R. S. Becker, J. A. Golovchenko, and B. S. Swartzentruber, Nature 325, 419 (1987).

6 J. Scheir, R. Sonnenfeld, O. Marti, P. K. Hansma, J. E. Demuth, and R. J. Hamers, J. Appl. Phys. 63, 717 (1988).

7 R. C. Jaklevic and L. Elie, Phys. Rev. Lett. 60, 120 (1988).

8 J. G. Simmons, J. Appl. Phys. 34, 1793 (1963).

9 J. G. Simmons, J. Appl. Phys. 35, 2472 (1964).

10 G. Binnig, H. Rohrer, Ch. Gerber, and E. Weibel, Phys. Rev. Lett. 49, 57 (1982).

11 D. P. Woodruff, "The Solid-Liquid Interface", (Cambridge University Press, London 1973), p. 12.

12 H. J. Mamin, PhD thesis, University of California at Berkeley, Center for Advanced Materials, Lawrence Berkeley Laboratory, California (1984).

13 S. Elrod, PhD. Thesis, Stanford University, Stanford, California (1985).

14 J. H. Coombs, M. E. Welland, and J. B. Pethica, Surf. Sci. 198, L353 (1988).

15 J. K. Gimzewski and R. Moller, Phys. Rev. B36, 1286 (1987).

16 N. D. Lang 1988, "The apparent barrier height in STM" Preprint

17 G. Travaglini, H. Rohrer, M. Amrein, and H. Gross, Surf. Sci. 181, 380 (1987).

18 J. K. Gimzewski, E. Stoll, and R. R. Schlittler, Surf. Sci. 181, 267 (1987).

19 W. J. Kaiser and R. C. Jacklevic, Surf. Sci. 181, 55 (1987).

20 N. Gane and F. P. Bowden, J. Appl. Phys. 39, 1432 (1968).

21 G. Binnig, C. F. Quate, and CH. Gerber, Phys. Rev. Lett. 56, 930 (1986).

22 V. M. Hallmark, S. Chiang, J. F. Rabolt, J. D. Swalen, and R. J. Wilson, Phys. Rev. Lett. 59, 2879 (1987).

CHAPTER IV

DEFORMATION OF A GRAPHITE SURFACE

Graphite has become an increasingly popular substrate for use with the scanning tunneling microscope. It is readily cleaved to give a flat surface that can be imaged in air with atomic resolution[1], and that exhibits a perfect lattice over thousands of angstroms[2]. A typical 'current' image is shown in Figure 4-1. A detailed explanation of the imaging of graphite will be given in chapter V. In this chapter, we will discuss the observation that for graphite in air, the tunneling current is very weakly dependent on the position of the tip in the z-direction (normal to the surface). In fact, we have obtained atomically resolved images of graphite with the tip progressively displaced over a range of as much as 100 Å. More strikingly, we have observed topographic images in air with a corrugation, i.e. peak-to-peak amplitude, of up to 24 Å. Following Soler and coworkers[3], we explain the large corrugations in terms of an amplification of the tip motion arising from surface deformation. However, in an analysis of the profile of the deformation we show that the tip must press on the surface over a region of several thousand square angstroms. To reconcile the large area over which the force is exerted with the atomic resolution of the images, we propose that the force is mediated by a layer of surface contamination, and that the tunneling is to a 'mini' tip protruding through the contamination. We demonstrate that progressive cleaning of the surface and tip in ultra-high vacuum can eliminate the deformation, confirming the important role of surface contamination[4].

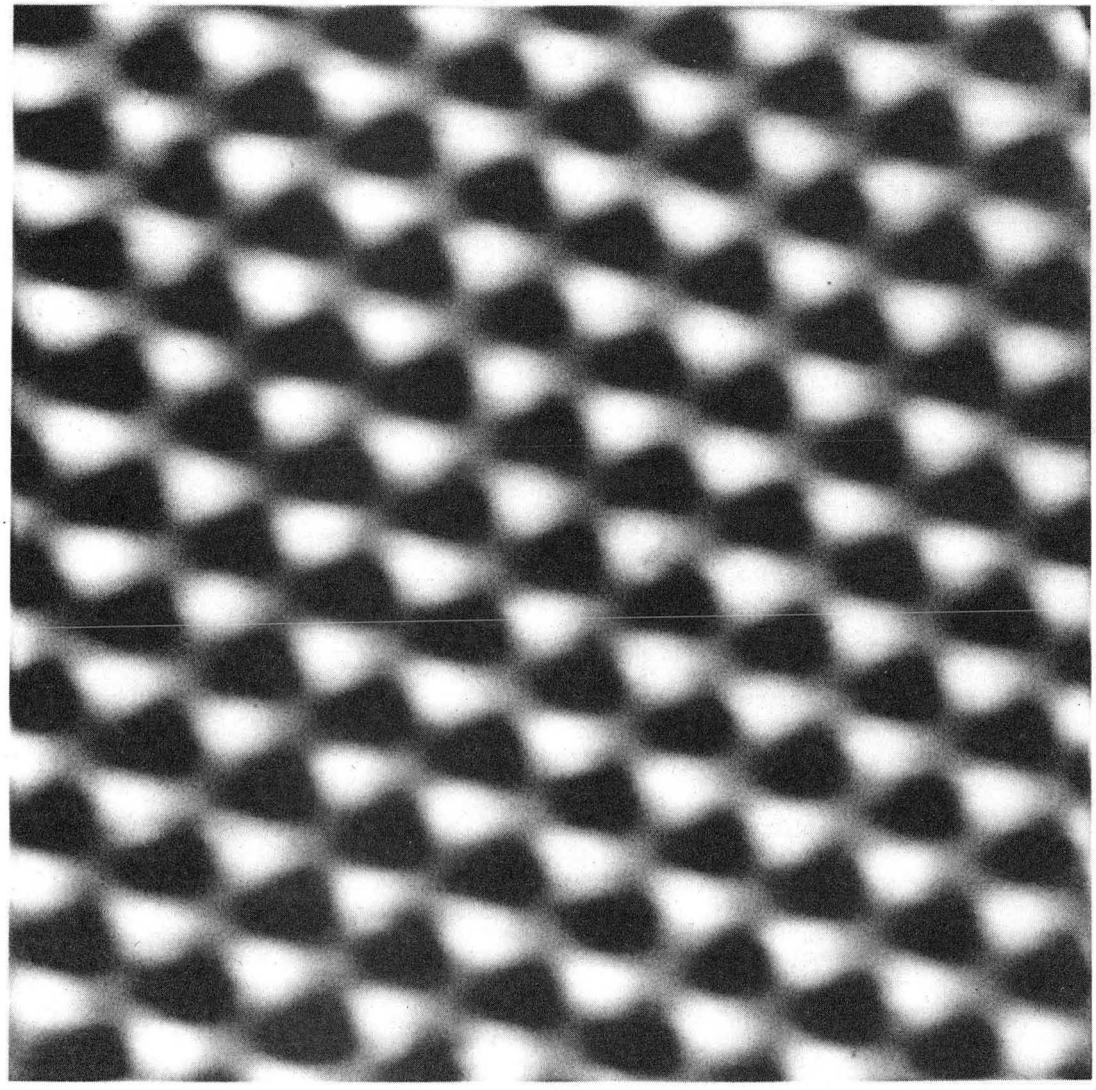

XBB 884-4477

Fig. 4-1 23 Å X 23 Å current image of graphite.

There has been some effort to explain why the corrugation of graphite observed in the STM[2,3,5,6] is much greater than the hard sphere estimate of 0.2 Å obtained from helium scattering experiments[7]. Selloni *et al.*[5] have suggested that variations in the local density of states could account for a corrugation up to 1 Å. Tersoff has pointed out that the unusual electronic band structure of graphite can lead to a corrugation which, depending on tip shape and operating conditions, may be as high as a few angstroms. Following the earlier suggestion of Coombs and Pethica[8], Soler *et al.*[2] have proposed that the tip elastically deforms the surface to produce an amplification of the corrugation, which they observe to be up to 8 Å on graphite in air. In their model, they propose that the deformation results from a force acting locally over atomic distances.

We have made extensive studies of freshly cleaved highly oriented pyrolitic graphite (Union Carbide, grade ZYB). We have used both the standard topographic mode, in which the tunneling current is maintained at a fixed value by a feedback loop as the tip is scanned, and the current imaging mode, in which the tip is scanned at constant height above the surface, and the variations in tunneling current constitute the image (see chapter I). We obtain atomically resolved images which, compared with the expected honeycomb structure of the graphite lattice, show a pattern with every other atom suppressed. This asymmetry between atomic sites will be discussed in chapter V. We typically operate at a bias voltage of 10 to 50 mV, but in air we have obtained atomically resolved images with a bias voltage of up to 1.5 V.

Figure 4-2 shows the peak-to-peak corrugation amplitude *vs.* tunneling resistance for three values of bias voltage. These data were

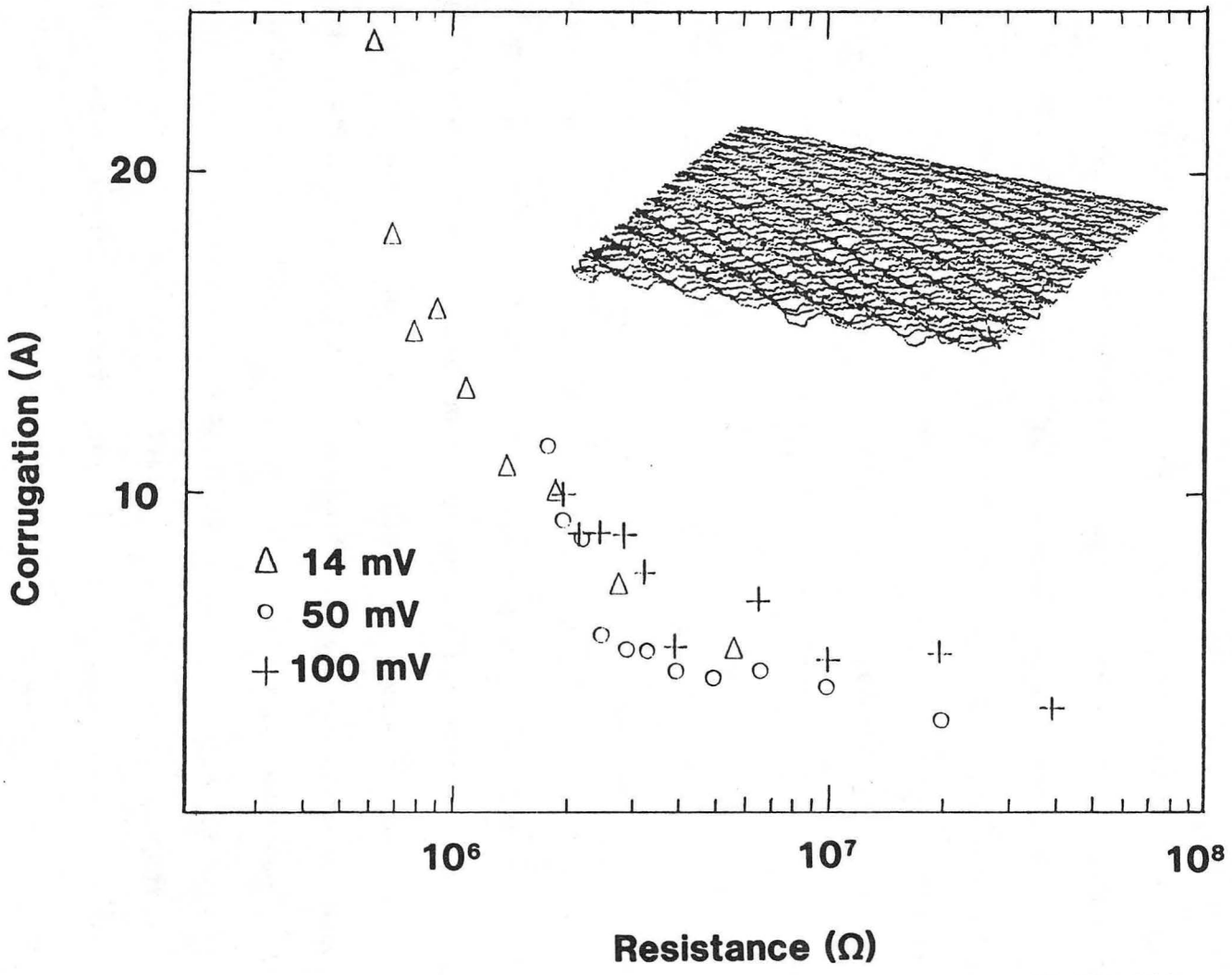

Fig. 4-2 Topographic corrugation *vs.* tip-to-sample resistance.

taken from two-dimensional topographic images obtained in air. The inset shows a typical image made by increasing the bias current after each set of five scans. We then determine the corrugation (i.e. the maximum distance the tip moves Δz as it moves from above an atom to above a hole site) from individual one-dimensional scans. Since the resistance decreases with decreasing separation, we see that the corrugation grows as the separation is reduced. At low resistance, the corrugation is as large as 24 Å, although maximum corrugation amplitudes of about 10 Å are more typical. Over the range of tunneling resistance shown in Figure 4-2, the tip moved over a distance of roughly 100 Å normal to the surface. For a clean surface with a work function in the range 5 to 10 eV, the tip should move by only a few angstroms when the resistance is changed over two decades. Thus, our observations provide strong evidence that the surface follows as the tip is retracted, thereby implying that the surface is deformed by the tip.

One can model the mechanism by which deformation leads to amplification as follows[8]. We represent the tip-surface interaction by a spring constant k_t and the restoring force of the graphite lattice by k_g. A change Δs in the tip position produces a change $\Delta d=\Delta s/(1+k_t/k_g)$ in the tip-sample separation. A given change Δd thus requires a correspondingly greater value of Δs, giving rise to an amplification of the corrugation as the tip is moved in and out to maintain a constant tunneling current. Thus, in this model, the increasing corrugation implies that the spring corresponding to the interaction between tip and surface becomes stiffer as it is compressed, that is, the spring is nonlinear.

We have also investigated the dependence of the current modulation on the mean tunneling current I in the current-imaging mode in air. Figure 4-3 shows the root mean square current modulation ΔI obtained from one-dimensional scans as a function of mean current. At the highest currents the one-dimensional scans show atomic features, although the two-dimensional images are of poor quality. At the peak current of 50 nA, the tip has been extended 70 Å towards the surface from its position at 0.5nA. Over this range, the ratio $\Delta I/I$ is constant, indicating that the relative modulation is independent of the resistance and hence of the tip-sample separation. This result is consistent with the surface deformation model: There is no amplification of the tip motion since the tip is scanned at constant height above the surface, and the compression of the springs is unchanged.

We now briefly discuss the forces required for the amplification process. The elastic deformation and stress distribution arising from a given load applied normal to the surface of an infinite halfspace of an anisotropic material have been calculated exactly[9,10] (the problem was originally solved by J. Boussinesq in 1885). For graphite[11], a force F in the z-direction (c-axis) applied uniformly over a disk of radius r produces a maximum deflection $u_o = 2.4 \times 10^{-11}$ F/r (MKS units). The related "rigid-die" problem of applying a given deformation (as opposed to a given force) to the surface has also been solved for an isotropic material[10]; we have extended this solution to cover the anisotropic case. We model our tip as a parabaloid of the form $\zeta = C\rho^2$, where ρ is the radial distance from the center axis of the tip. This shape has radius of curvature R = 1/2C at the center.

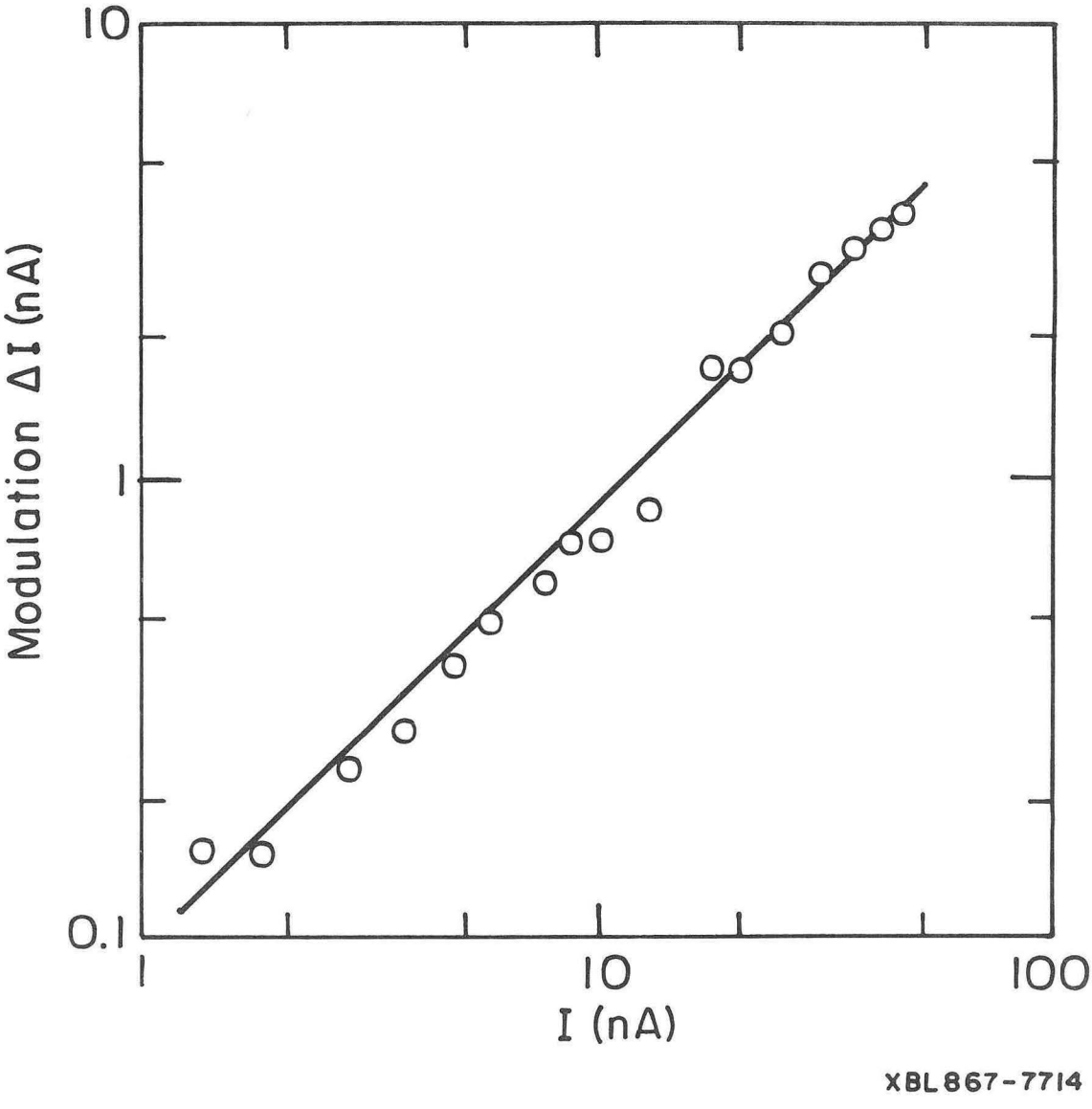

Fig. 4-3 RMS current modulation *vs.*current level in current imaging mode.

Scanning electron microscope pictures of our etched tungsten tips show that this choice is not unreasonable (see chapter II). We take the maximum deformation to be u_o, and assume that for small ρ the deformation profile has the shape of the tip, with no kinks. We find the following surface profile:

$$u(\rho) = u_o - C\rho^2 \qquad \rho<a,$$

$$u(\rho) = (2/\pi)\ [\ (u_o - C\rho^2)\sin^{-1}(a/\rho) + Ca(\rho^2 - a^2\ )^{1/2}\ ] \qquad \rho>a,$$

where $a = [u_o/(2C)]^{1/2} = (u_oR)^{1/2}$ is the radius over which the surface profile tracks the tip. The model predicts a slowly varying pressure distribution for $\rho \lesssim 0.8a$, with a maximum at $\rho = 0$ of $2\text{x}10^{10}\ (u_oC)^{1/2}$ N/m^2. Figures 4-4 (a) and (b) show the profiles for a 70 Å deformation, a value that we have achieved at low resistances. The tips shown have R = 2 Å and 500 Å respectively. In the first case, the tip was chosen to give an atomically small contact area between tip and sample. This tip has an unrealistically small cone angle of 15° over a length of 70 Å. Note that even for such a sharp tip, the contact radius is still 12 Å, and the surface has an unreasonably steep profile. The peak pressure is $1\text{x}10^{11}$ N/m^2 (1 Mbar), and the total force is $3\text{x}10^{-7}$ N, distributed over 300 $Å^2$. For such large stresses, Hooke's Law is not valid, so that the model breaks down and plastic deformation may occur. It has been demonstrated[12] that in gold, plastic deformation from a 6000 Å tip occurs when the applied shear stress exceeds ~1/20 of the bulk shear modulus. Examples of plastic deformation in gold were discussed in chapter III. In graphite, the equivalent shear stress would be roughly $2\text{x}10^{10}$ N/m^2. On the other hand for R=500 Å, a realistic value for our tips, the deformation profile and the pressure are much more reasonable. Here the total

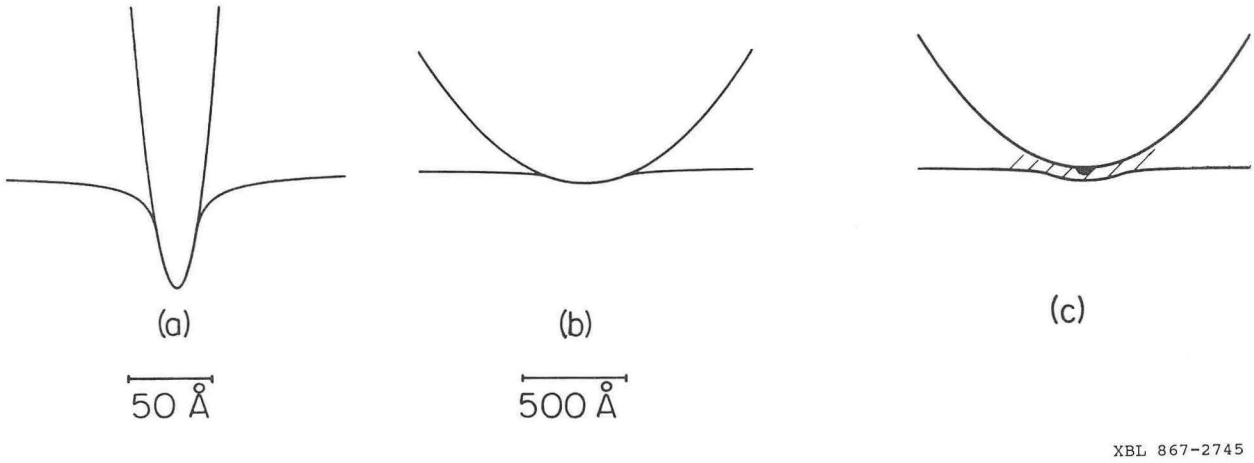

Fig. 4-4 Surface profile for a 70 Å deformation with force applied by tips with radii (a) R = 2 Å, and (b) R = 500 Å; (c) shows the contamination model, with a 'mini' tip providing the tunneling path. Under different conditions, the contamination could be on the tip, on the sample, or could be condensed in the capillary gap between tip and sample.

force of 5×10^{-6} N, distributed over an area of 10^5 Å^2, results in a peak pressure of 6×10^9 N/m^2. The peak pressure and the radius of contact vary only as $u_o^{1/2}$; thus for elastic deformations greater than a few angstroms, the force will be distributed over thousands of square angstroms.

Under a large deformation, one might expect a low tip-sample resistance due to the close electrical contact over a large area. This resistance would be dominated by spreading resistance, which we estimate for graphite by extending the analysis of Tinkham *et al.*[13] for point contacts to an anisotropic material. For a contact radius of 200 Å, as in Figure 4-4(b), we find a spreading resistance of less than 2 kΩ. This is significantly less than the 1 MΩ observed in air with the tip extended 70 Å.

To reconcile the large area of mechanical contact with the high observed resistance we propose that a layer of contamination acts to cushion the tip and transmit the force to the surface. To explain the atomic resolution images, we further propose that the tunneling occurs from a 'mini' tip protruding from the end of the tip through the contamination [Figure 4-4(c)]. Recent work[14] has shown that the STM can operate with atomic resolution on graphite in water, thus it is plausible that all images of graphite in air are obtained through a surface layer of water or other contaminant[15].

To investigate the role of surface contamination, we have measured the variation of the current I with tip position s under a variety of conditions. All the measurements were taken on a flat region on which we first obtained high quality images of the graphite structure. While scanning laterally to obtain a value of s averaged over several atomic

positions, we disengaged the feedback loop and ramped the voltage to the z-drive up and back. The voltage was kept constant, and the current was measured as a function of tip position s. Figure 4-5(a) shows I vs. s for graphite in air. We speculate that the strong hysteresis was due to an expulsion of material from the gap between tip and sample as they were pressed together. We obtained Figure 4-5(b) after transfering the sample into a vacuum of $3x10^{-10}$ torr, and Figure 4-5(c) after the sample was subsequently heated to 1000° C for 1 hour in the ultra-high vacuum system. Finally, to obtain Figure 4-5(d) we cleaned the tungsten tunneling tip by field emission at 500 V to a gold surface and scanned the cleaned graphite surface without breaking vacuum. The hysteresis disappeared as the sample was cleaned. Even more striking is the steepening of the I-s curves as the sample and tip became progressively cleaner. In (a), the current increased to 300 nA over roughly 100 Å, while in (d) it increased to 300 nA over only 1 Å. These results imply that both surface and tip are contaminated in air, and as the graphite surface and tungsten tip were progressively cleaned the tendency of the surface to follow the displacement of the tip was greatly reduced. Under clean conditions, we observed a topographic corrugation of 0.9 Å at 120 mV bias voltage and 20 nA tunneling current, in contrast to the 5 Å corrugation observed in air under the same bias conditions. These results provide strong evidence that significant distortion of the surface occurs only when there is a layer of contamination available to transmit the force from the tip.

In practice, we have found it difficult to reliably produce steep I vs. s curves even in UHV. Perhaps our cleaning procedure (field emission from the tip) is too delicate to completely remove surface

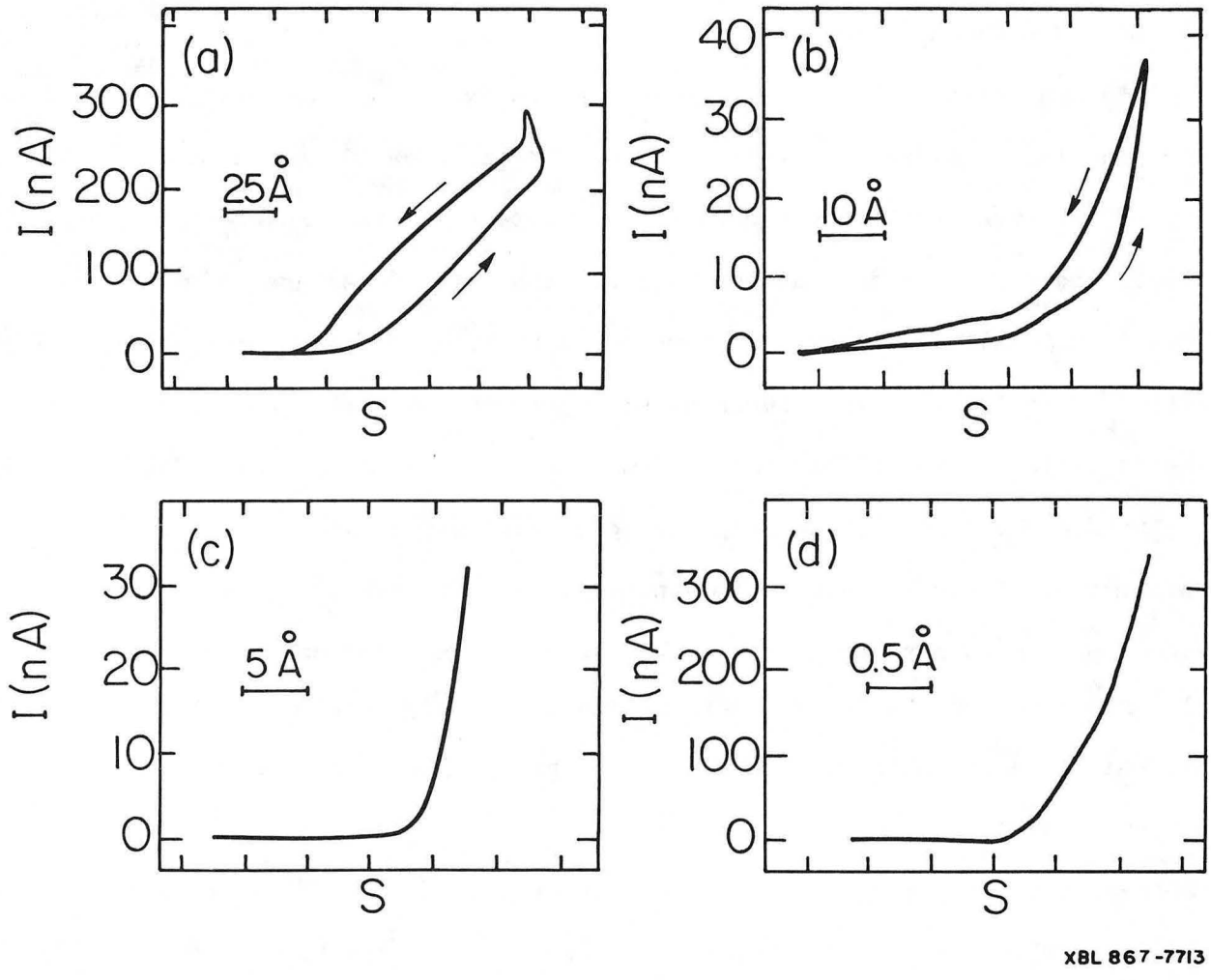

Fig. 4-5 Current, I, *vs.* tip position, s, for graphite (a) in air, (b) in UHV, (c) in UHV with heated sample, and (d) as in (c) with tip cleaned by field emission.

oxides. Furthermore, tips which do produce steep I vs. s curves are often unstable and short-lived. It is important to remember, therefore, that on graphite the STM may operate with a certain amount of surface deformation.

In conclusion, the fact that one can observe atomic corrugations when the tip is displaced over a distance as large as 100 Å provides strong evidence that the tip deforms the surface in air. However, a simple model for the deformation suggests that the forces are not localized to atomic dimensions as proposed by Soler *et al.*[3], but rather extend laterally over many hundreds of angstroms. In air, we believe the force is transmitted to the surface via a contamination layer; as the surface, and finally the tip, are progressively cleaned, the deformation of the surface becomes negligible. It is known that the graphite surface adsorbs a variety of gases, and must be baked or cleaved to remove them[16,17]. One implication of our results is in the determination of the effective barrier height ϕ from measurement of the current I as a function of position s from the well-known WKB expression[18] $I \propto \exp[-\phi^{1/2}s]$, with ϕ in eV and s in Å. Clearly, if the surface follows the tip position, an anomalously low value for barrier height will be obtained; this mechanism could thus explain the low barrier heights obtained for graphite and other layered materials in air, where contamination may be present. Finally, one might expect deformation of the surface by the STM tip to be an important problem for a variety of systems, especially biological materials.

Recently, several other groups have confirmed and extended our results. On Kish graphite, corrugations up to 175 Å have been observed[19]. This is almost certainly possible due to the very high

elastic limit of a graphic single crystal relative to the small grains of HOPG. The invention of the atomic force microscope (AFM) has allowed the direct measurement of applied force while scanning. Forces of 1×10^{-7} to 5×10^{-7} N have been observed[20,21] for tunneling currents of 0.1 to 10 nA. Erlandsson *et al.*[20] also present indirect evidence for the presence of a water layer trapped by capillary condensation as has been proposed by D. Pohl[21]. In cases of severe contamination (for example, a thick insulating adsorbed layer), the STM images will show severe distortions[22].

REFERENCES:

1 P.K. Hansma, Bull. Am. Phys. Soc. 30, 251 (1985).

2 G. Binnig, H. Fuchs, Ch. Gerber, E. Stoll, and E. Tosatti, Europhys. Lett. 1, 31 (1986).

3 J. Soler, A.M. Baro, N. Garcia, and H. Rohrer, Phys. Rev. Lett. 57, 444 (1986).

4 H. J. Mamin, E. Ganz, D. W. Abraham, R. E. Thomson, and J. Clarke, Phys. Rev. B34, 9015 (1986).

5 A. Selloni, P. Carnevali, E. Tosatti, and C.D. Chen, Phys. Rev. B31, 2602 (1985).

6 J. Tersoff, Phys. Rev. Lett 57, 440 (1986).

7 G. Boata, P. Cantini, and R. Tatarek, Phys. Rev. Lett. 40, 887 (1978).

8 J.H. Coombs and J.B. Pethica, IBM J. Res. Devel. 30, 455 (1986).

9 S.G. Lekhnitskii, "Theory of Elasticity of an Anisotropic Elastic Body", (Holden-Day, Inc., San Francisco 1963).

10 Isaac Todhunter, "A History of the Theory of Elasticity and of the Strength of Materials", (Cambridge University Press, Cambridge 1893).

11 R. Nicklow, N. Wakabayashi, and H.G. Smith, Phys. Rev. B 5, 4951 (1972).

12 N. Gane and F.P. Bowden, J. Appl. Phys. 39, 1432 (1968).

13 M. Tinkham, M. Octavio, and W.J. Skocpol, J. Appl. Phys. 48, 1311 (1977).

14 R. Sonnenfeld and P.K. Hansma, Science 232, 211 (1986).

15 P. Staszczuk, Mat. Chem. Phys. 12, 111 (1985).

16 A. Sen and J.E. Bercaw, J. Phys. Chem 84, 465 (1980).

17 J.J. Metois, J.C. Heyraud and Y. Takeda, Thin Solid Films 51, 105

(1978).

18 G. Binning, H. Rohrer, Ch. Gerber, and E. Weibel, Phys. Rev. Lett. 49, 57 (1982).

19 S. Morita, S. Tsukada, and N. Mikoshiba, J. Vac. Sci. Tech. A 6, 354 (1988).

20 R. Erlandsson, G. M. McClelland, C. M. Mate, and S. Chiang, J. Vac. Sci. Tech. A 6,266 (1988).

21 D. Pohl private communication.

22 D. P. E. Smith, G. Binnig, and C. F. Quate, Appl. Phys. Lett. 49, 1166 (1986).

CHAPTER V

INTERPRETATION OF STM IMAGES OF GRAPHITE

In this chapter we will discuss theoretical and practical aspects of STM on graphite. Graphite has become the standard calibration sample for STM, and also is the basis for the commercial manufacturer's claims of 'guaranteed atomic resolution'. In fact, graphite must be one of the simplest materials to image with the STM; one can readily obtain a piece of HOPG, cleave it in air using a piece of scotch tape, and then image the surface in air. As long as there is not an overwhelming amount of vibrational noise, the atomic signal will beam through and bandwidth limiting techniques can produce a lovely image (see Figure 5-1).

In fact, as we have already seen in the last chapter, there is more to the imaging process than one might naively imagine. The deformation we observe on graphite in air means that there is always a physical contact between the tip and the sample. This contact can act to stabilize the junction width, thus giving a relatively steady signal even in the presence of considerable applied vibration. But we shall see that there are other, more subtle, effects at work here, and these can obscure the actual atomic information on the surface. We will start with a theoretical calculation for the STM image of graphite, and then we will proceed to the diverse images actually observed when scanning graphite.

a) Theoretical calculations.

The following discussion is the result of a collaboration with

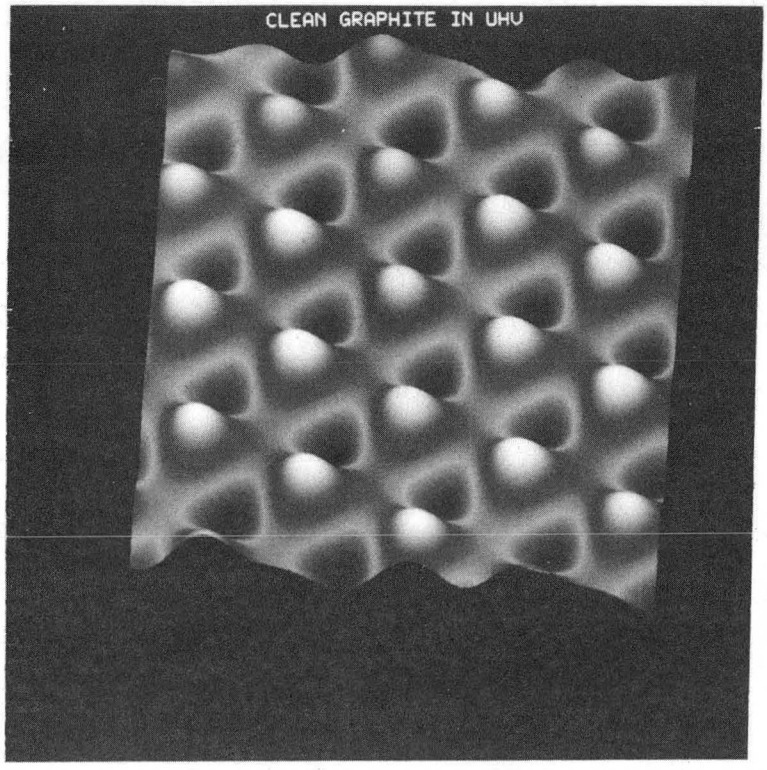

CBB 881-421

Fig. 5-1 Projected current image of clean graphite.

David Tomanek and Steven Louie. They are responsible for the calculations[1]. Work along similar lines was done concurrently by Batra *et al.*[2]. The calculations were motivated by the observation that there is a substantial asymmetry in the apparent heights of neighboring carbon atoms on the surface [see Figure 5-1(a)]. This cannot be understood if one assumes that the STM images total charge densities at the surface, since the weak interaction between the graphite layers should ensure that the total charge densities on both atoms are practically identical. Previous calculations on graphite slabs[3,4], revealed some asymmetry between these sites, but did not explain the main experimental findings of this section: The asymmetry is large at a low bias voltage, decreases with increasing voltage, and is independant of the bias polarity. All three experimental observations are well explained by the model outlined here, which demonstrates that the asymmetry is primarily a property of the bulk material. Using *ab initio* methods, we calculate STM current densities which lead to images closely resembling experimental observations (see Figure 5-2).

The graphite samples were prepared by cleaving highly oriented pyrolytic graphite in air. The STM was operated in the current-imaging mode. We emphasize that in this mode the deformation fo the graphite surface remains constant and amplification of the atomic heights therefore does not occur. Thus, even for a surface exposed to air, we expect the observed variations of the tunneling current to be the same as those on a clean surface. In contrast, the asymmetry observed in images obtained in the topographic mode, in which the tip-to-surface separation varies, depends strongly on the surface deformation, and hence on the level of contamination of the surface and the tunneling

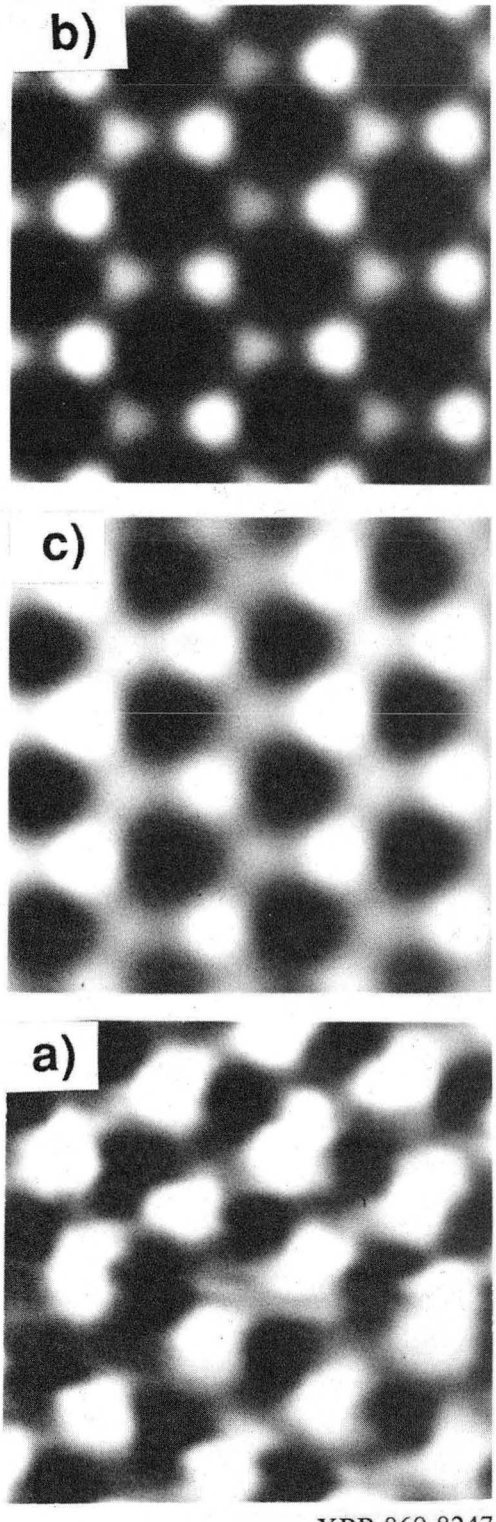

XBB 860-8247

Fig. 5-2 (a) Observed, and (b) calculated STM current densities for V = 0.1 volt. (c) Filtered version of (b).

tip as we have discussed in the previous chapter.

Figure 5-2(a) shows a typical current image of a 12 Å X 12 Å area of a graphite sample obtained in air at bias voltage V = 0.1 V. Figure 5-3(a) shows an image of graphite at 0.25 V. We see that the STM image does not reflect the expected honeycomb atomic arrangement, but instead shows only a sublattice with a hexagonal close-packed structure, which contains every second atom. The contrast between the neighboring sites in terms of the current asymmetry is very large. In hexagonal graphite (with ABAB stacking), the crystal is composed of an α sublattice consisting of atoms with neighbors directly above and below in adjacent layers, and a β sublattice consisting of sites without such neighbors (see Figure 5-4). The theory presented below predicts that the atoms visible in the STM image are of the β type.

For a given small positive bias voltage V, the tunneling current density $j(\mathbf{r})$ can be obtained from a simple extension of the expression derived by Tersoff and Hamann[4,5,6],

$$j(\mathbf{r},V) \propto \int_{E_f-eV}^{E_f} \rho(\mathbf{r},E)\, dE \quad , \tag{1a}$$

where

$$\rho(\mathbf{r},E) \equiv \sum_{n,\mathbf{k}} |\psi_{n\mathbf{k}}(\mathbf{r})|^2\, \delta(E_{n\mathbf{k}}-E). \tag{1b}$$

Here, $\rho(\mathbf{r},E)$ is the local density of states at the tip position $\mathbf{r} = (x,y,z)$, and the $\psi_{n\mathbf{k}}(\mathbf{r})$ are the eigenstates of the unperturbed surface with corresponding energy $E_{n\mathbf{k}}$. The implied assumptions are a constant matrix element for tunneling and the description of the relevant tip states by s waves with a constant density of states for the tip in the narrow (but nonzero) energy region $\{E_F-eV;E_F\}$. The explanation of the observed asymmetry in the STM current is crucially dependant on the

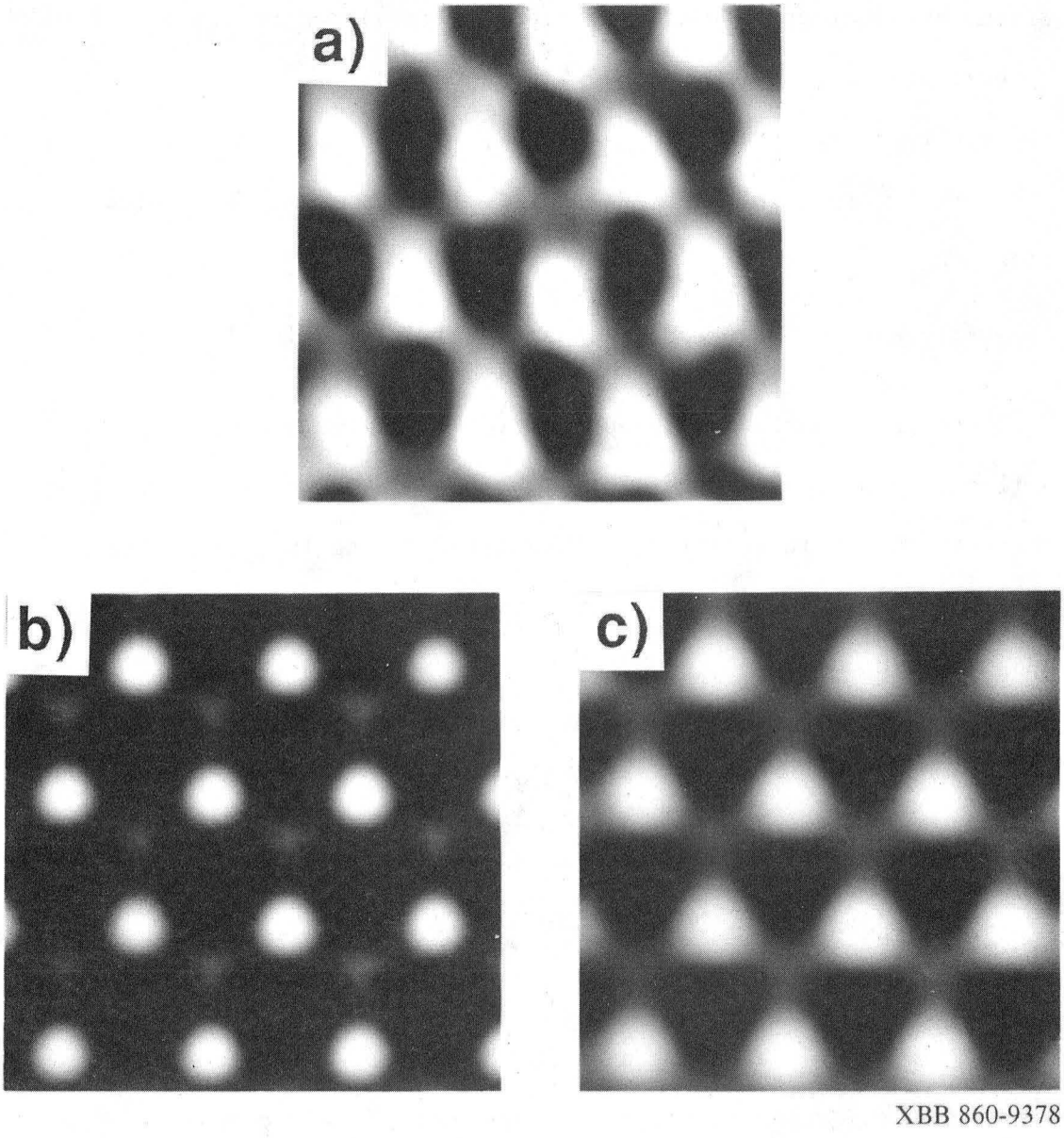

Fig. 5-3 (a) Observed, and (b) calculated STM current densities for V = 0.25 volt. (c) Filtered version of (b).

nature of the graphite eigenstates ψ_{nk} , which contribute to the tunneling current. They are p_z in character and can be written as a linear combination of Bloch functions Φ_j localized on the $\alpha,\alpha',\beta,\beta'$ sites in the unit cell shown in Figure 5-4(b),

$$\psi_{nk}(r) = c_{n\alpha}\Phi_\alpha(r,k) + c_{n\alpha'}\Phi_{\alpha'}(r,k) + c_{n\beta}\Phi_\beta(r,k) + c_{n\beta'}\Phi_{\beta'}(r,k) , \qquad (2a)$$

where

$$\Phi_j(r,k) = N^{-\frac{1}{2}} \sum_R e^{ik\cdot(R-\tau_j)} p_z(r-R+\tau_j) , \quad j=\alpha,\alpha',\beta,\beta' . \qquad (2b)$$

The Fermi surface of graphite lies close to the *P* line in the Brillouin zone [see Figure 5-5(a)], defined by $k = (1/3,1/3,\xi)$ (in units of the reciprocal lattice vectors). Along this line, the Hamilton matrix $H_{ij}(k) = \langle\Phi_i|H|\Phi_j\rangle$ is given in the nearest-neighbor approximation by

$$H(1/3,1/3,\xi) = \begin{array}{c} \\ \alpha \\ \alpha' \\ \beta \\ \beta' \end{array} \begin{array}{c} \begin{array}{cccc} \alpha & \alpha' & \beta & \beta' \end{array} \\ \begin{pmatrix} E_\alpha & t_\alpha(\xi) & 0 & 0 \\ t_\alpha^*(\xi) & E_\alpha & 0 & 0 \\ 0 & 0 & E_\beta & 0 \\ 0 & 0 & 0 & E_\beta \end{pmatrix} \end{array} . \qquad (3)$$

Because of the crystal symmetry, the phase factors in Equation (2b) add up in such a way that the states on the α atoms are decoupled from those on the β atoms in the whole crystal up to all orders of neighbor interactions. For the same reason, we obtain the *unexpected* result that the Bloch functions on β atoms do not interact with those on β atoms on neighboring planes, leading to a diagonal β submatrix. Since the atomic environment of the α and β sites is similar, we expect $E_\alpha \approx E_\beta$. Along the P line, this Hamiltonian then gives rise to a doubly degenerate band at $E = E_\beta$ near E_F, with wave functions localized on the

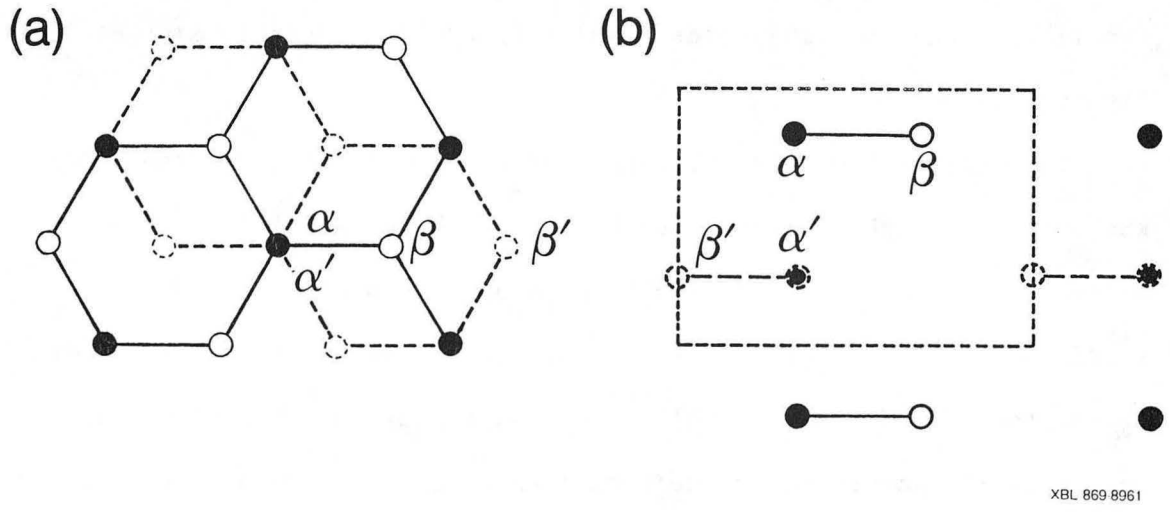

Fig. 5-4 Schematic diagram of two successive layers of hexagonal graphite in (a) top view, and (b) side view. The unit cell is enclosed by a dotted line in (b).

β sites, and to a dispersive band with wave functions localized on the α sites [see Figure 5-4(b), this splitting was previously discussed by Samuelson *et al.*[7]]. The STM, which scans a narrow energy region below E_F corresponding to k states near the P line, detects all β states and only a very small fraction of the α states. It is this "density of states" effect, rather than a different spatial extension of wave functions on neighboring sites[8], which causes the dramatic asymmetry in Figures 5-2 and 5-3.

The extension of the physical picture from the bulk to the (0001) surface is straightforward. The P line in the bulk Brillouin zone collapses to the point $\overline{K}$ in the surface Brillouin zone. The α band folds to a continuum of states spread over approximately 1.2 eV around E_F and the β band is essentially a δ function at E_F. The physical origin of the asymmetry in the tunneling current j between the α and β sites is unchanged. As the magnitude of the bias voltage is increased, the tunneling process samples states increasingly far from the P line (or $\overline{K}$ point), where α and β states are not completely decoupled. However, because of the large band dispersion near P or $\overline{K}$, the part of the Brillouin zone sampled by the STM is still very small, which causes a decrease, but not a disappearance, of the asymmetry for larger bias voltages V.

Tomanek and Louie have calculated the electronic structure of graphite quantitatively using the *ab initio* pseudopotential local-orbital method[9,10]. They used a Gaussian basis[11], norm-conserving ionic pseudopotentials of Hamann-Schluter-Chiang type[12], and the Hedin-Lundqvist[13] form of the exchange-correlation potential in the local-density approximation. The calculations were

performed fully self-consistently on graphite slabs with four layers. The irreducible part of the surface Brillouin zone is sampled by a fine mesh consisting of 61 k points. A $k_{||}$-resolved density of states is derived from the four-layer slab results by broadening energy levels using Gaussians with a half-width at half maximum of 0.2 eV. Calculations on bulk graphite yielded similar results, supporting our claim that the effect is a bulk, rather than a surface property. Since the α and the β densities of states are nearly symmetric around E_F [Figure 5-5 (b)], the tunneling current is expected *not* to depend on the polarity of the bias voltage. Only at large voltages is the tunneling current expected to be different for the two polarities.

Figure 5-2(b) shows a predicted tunneling current density image, obtained from Equation (1a) for V = 0.1 V and a tip-to-surface separation of 1 Å. When comparing this image with the experimental image in Figure 5-2(a), one should bear in mind that the relatively large size and irregular shape of the real STM tip limits the lateral resolution. We can mimic this effect by filtering out the high-frequency Fourier components from the calculated current density shown in Figure 5-2(b) to produce Figure 5-2(c), which shows a strong similarity to the data. Figure 5-3 shows a similar comparison at a bias voltage of 0.25 V.

To obtain a quantitative comparison between the experimental and calculated data, we define the asymmetry between the tunneling current j at the α and β sites by

$$A \equiv [j(\beta)-j(\alpha)]/[j(\beta)+j(\alpha)]. \qquad (4)$$

In the experiment, $j(\alpha)$ and $j(\beta)$ were extracted from a whole image by averaging over sites with the low and high current density,

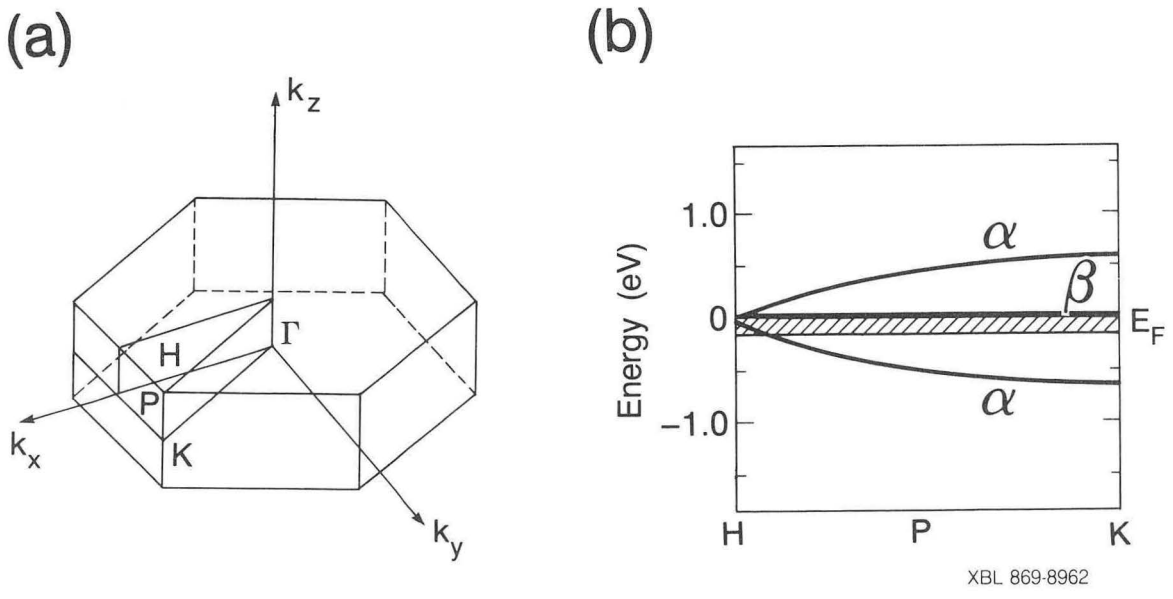

Fig. 5-5 (a) The Brillouin zone, and (b) schematic band structure of the π states of hexagonal graphite along the P line. States sampled by the STM are crosshatched.

respectively. (This approach neglects the effects of a position independant or 'offset' current which we will discuss below. For this discussion, we chose data with minimum offset). In general, we expect A to depend on the tunneling voltage V and the tip height h above the surface (the tip height h is related to the tunneling resistance). Figure 5-6 summarizes our results for this asymmetry as a function of the bias voltage V. Calculated values of A (from the unfiltered STM prediction) for h = 0.5 and 1.0 Å are given by the broken and solid lines, respectively. These results indicate that A decreases with increasing voltage and is almost independent of h in this height range. The experimental data, taken at a fixed but unknown height (perhaps 2 Å to 6 Å), show very similar trends, with A decreasing from roughly 0.2 at 0.05 V to roughly 0.1 at 0.5 V bias. The complete data set was obtained with the same tip and sample in one continuous run. The values of the asymmetry shown in Figure 5-6 were among the largest obtained; in some runs A was substantially smaller, probably due to multiple tip effects. Multiple tips, which can produce an offset current that reduces the measured value of A, will be discussed below. The filtered theoretical values for A are shown as the dotted curve in Figure 5-6. The same filter parameters have been used for all voltages in Figure 5-6 and correspond to those used in Figures 5-2(c) and 5-3(c). We note that h was certainly greater than 1 Å in the experiment; if so, A would be further reduced below the computed values. We can think of the low pass filtering as a naive way to extrapolate the theory out to larger h, since the higher order Fourier components of the electron density will be attenuated rapidly as h increases. Ideally, we want to calculate the STM current for larger

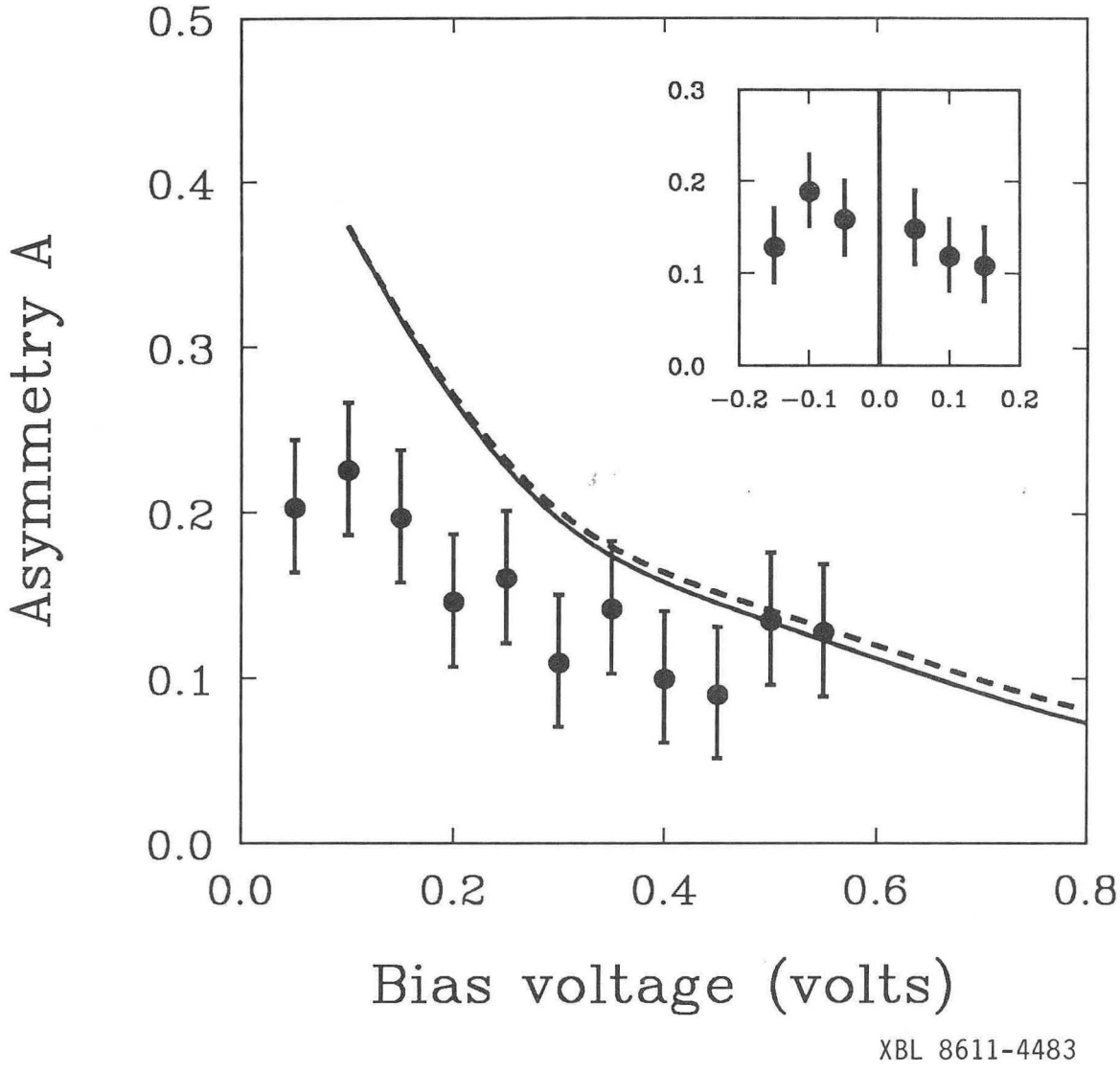

Fig. 5-6 Asymmetry, A, of the tunneling current as a function of bias voltage, V. The solid and broken lines represent calculated results at a tip-surface separation h = 1.0 Å and 0.5 Å respectively. The experimental points are constant resistance data corresponding to an unknown tip-surface separation. The inset shows the observed polarity dependence of A.

values of the height h. This would also give an absolute distance calibration for the measurements. Unfortunately, the electron densities become so small that the existing method is not accurate for h larger than 1 Å.

An important test of the theory is the dependence of A on the polarity of the bias voltage. Data in the inset of Figure 5-6, obtained by reversing the bias polarity in the middle of one scan, indicate that A is insensitive to the polarity. These results agree with our prediction and mitigate against surface states as the origin of the asymmetry.

b) Practical considerations.

Figure 5-7 shows several of the many different images we have obtained when scanning graphite. These patterns come and go, and can depend on the bias current or resistance in a reproducible manner for several minutes. Figure 5-8 shows a switching event between the two most common patterns which we call 'dots' and 'honeycombs'. As the tip was scanned up the image in the Y direction, the pattern changed from dots to honeycombs, and then back again 75 milliseconds later. Neglecting the suggestion of Batra[14] that the top layer of the graphite is displaced by one half a unit cell (the model as presented does not explain what would happen at a grain boundary, why the top layer only slides one half a unit cell and then stops, and finally why the top layer should slide at all), we can presume that changes in the scanning tip are responsible for the observed image changes.

Figure 5-9(a) shows a group of Ag atoms (bright spots) on a

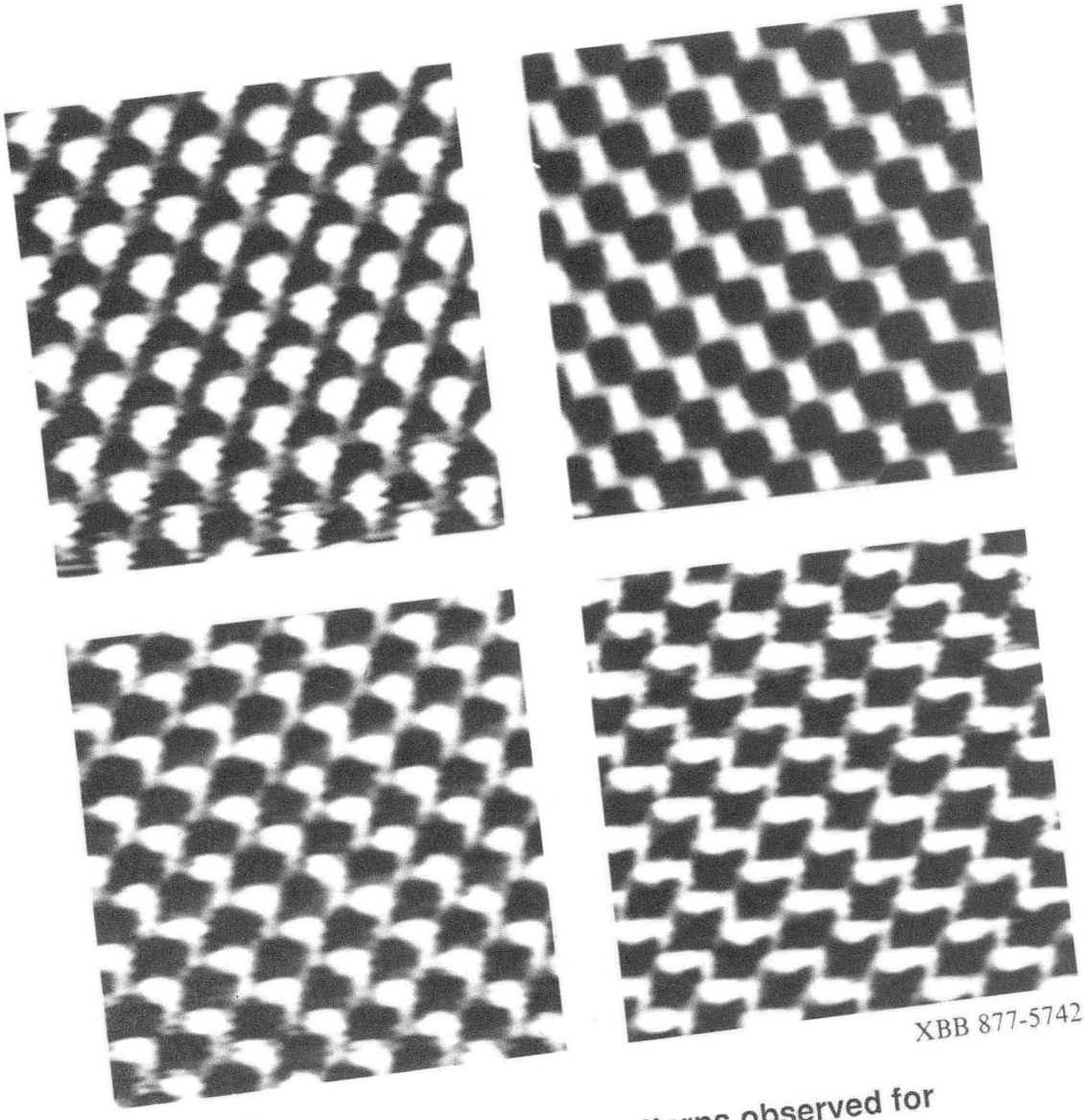

Fig. 5-7 Four of the many patterns observed for STM current images of graphite.

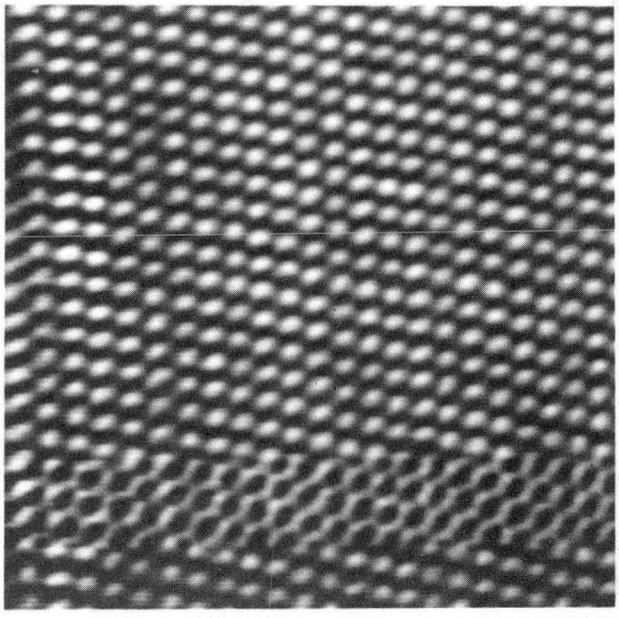

XBB 877-5741

Fig. 5-8 This 54 Å X 54 Å current image shows the graphite pattern switching from 'dots' to 'honeycombs' to 'dots' (as the tip scans in Y from bottom to top). The honeycomb pattern lasted for 54 msec.

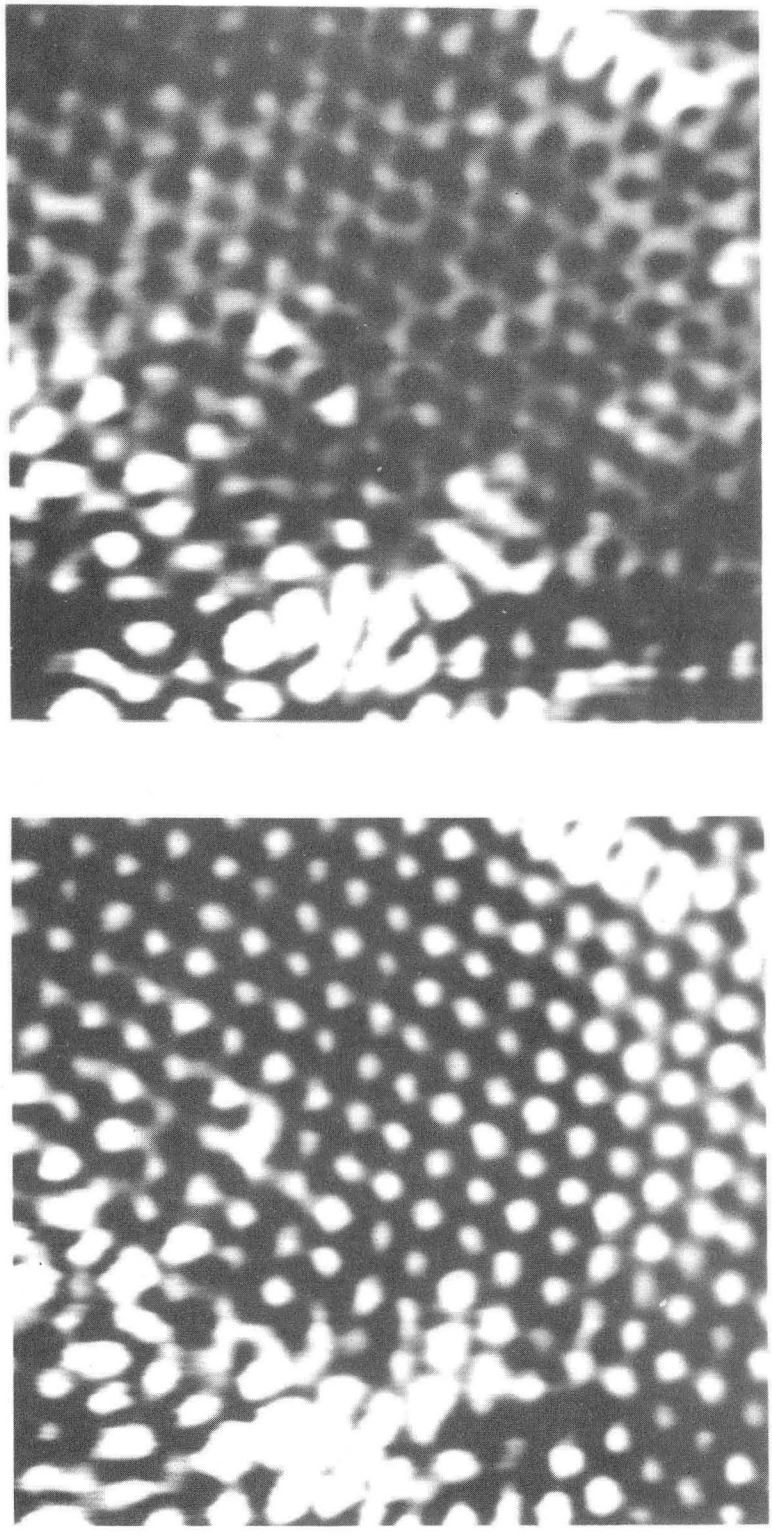

Fig. 5-9 (a) Image of Ag atoms on graphite, with the graphite lattice imaged as a honeycomb. (b) Several seconds later, the graphite is imaged as dots, but the Ag atoms appear unchanged. (c) Position of the dots relative to the honeycombs using the Ag atoms as a reference.

XBB 877-5737

graphite substrate which is imaged as a honeycomb lattice (Imaging of metals on graphite will be discussed in subsequent chapters). Eight seconds later, we obtained the image shown in Figure 5-9(b). The graphite substrate is now imaged as dots, but the Ag adatoms are still visible and are basically unchanged. The resolution of the microscope as tested by the imaging of Ag adatoms is unchanged. We can locate the relative positions of the dot and honeycomb lattices by using the Ag adatoms as a reference. The result is shown in Figure 5-9(c), and shows that the dots sit slightly offset in the hole of the honeycomb. At first glance, these results seem to contradict the careful calculations of the last section, unless multiple tips are operating simultaneously (or several atoms are active on one tip).

Mizes and Harrison have proposed a simple explanation for the many patterns observed in STM images of graphite[15]. They point out that in the vacuum, each Fourier component of the wavefunction

$$\psi_k \propto e^{ik\cdot r}\, e^{-k_z z} \qquad (5)$$

must satisfy

$$(k_z^2 - k_{||}^2) = 2m\phi/\hbar^2, \qquad (6)$$

where k_z is the magnitude of the imaginary wavevector perpendicular to the surface, $k_{||}$ is the wavevector parallel to the surface, and ϕ is the work function of the sample. Thus the higher transverse Fourier components of the wavefunction will decay more rapidly into the vacuum. Thus, at a sufficient distance from the surface, they suggest that one can ignore all higher order Fourier components. They therefore model the effects of multiple tips by adding together images composed of just three sine waves. The hexagonal symmetry of the surface then dictates that the three sine waves should be at 120°

angles in the plane. By adding together set of these sine waves (or equivalently by varying the amplitude and phase of these sine waves since

$$a\sin(x+\alpha) + b\sin(x+\beta) = c\sin(x+\gamma), \qquad (7)$$

they can produce most of the observed patterns. Figures 5-10(a) and (d) show two sums of three sine waves with equal intensity, but differing phase. Figure 5-10(a) closely resemble the three site or single tip images of Figures 5-2 and 5-3, while 5-10(d) resembles the dots image of Figure 5-8. The other images in Figure 5-10 are formed by adding an offset and attenuated version of (a) or (d) to itself. We see that Figure 5-10 (e) resembles the honeycomb pattern of Figure 5-8.

But there are several deficiencies with the Mizes model. We can simulate the tip switching event of Figure 5-8 by juxtaposing the bottom half of Figure 5-10(e) with the top half of 5-10(a). This is shown in Figure 5-11. But, in contrast to the offset observed in Figure 5-8, the black hole sites from each half line up in Figure 5-11. The tip switching event of Figure 5-9 also showed a similar disparity.

The Mizes model also fails to explain the relative abundance of the various graphite images. To obtain the honeycomb image of Figure 5-10(e), one must add two three site images with a precise offset and relative intensity. Even if one were adding dots images, one would then need two tips equally far from the sample and spaced at 0.7 Å (the carbon-carbon spacing in graphite). One might posit a carbon dimer on the end of the tip, but then it would need to be at exactly the correct orientation relative to the substrate lattice. Thus, in the Mizes

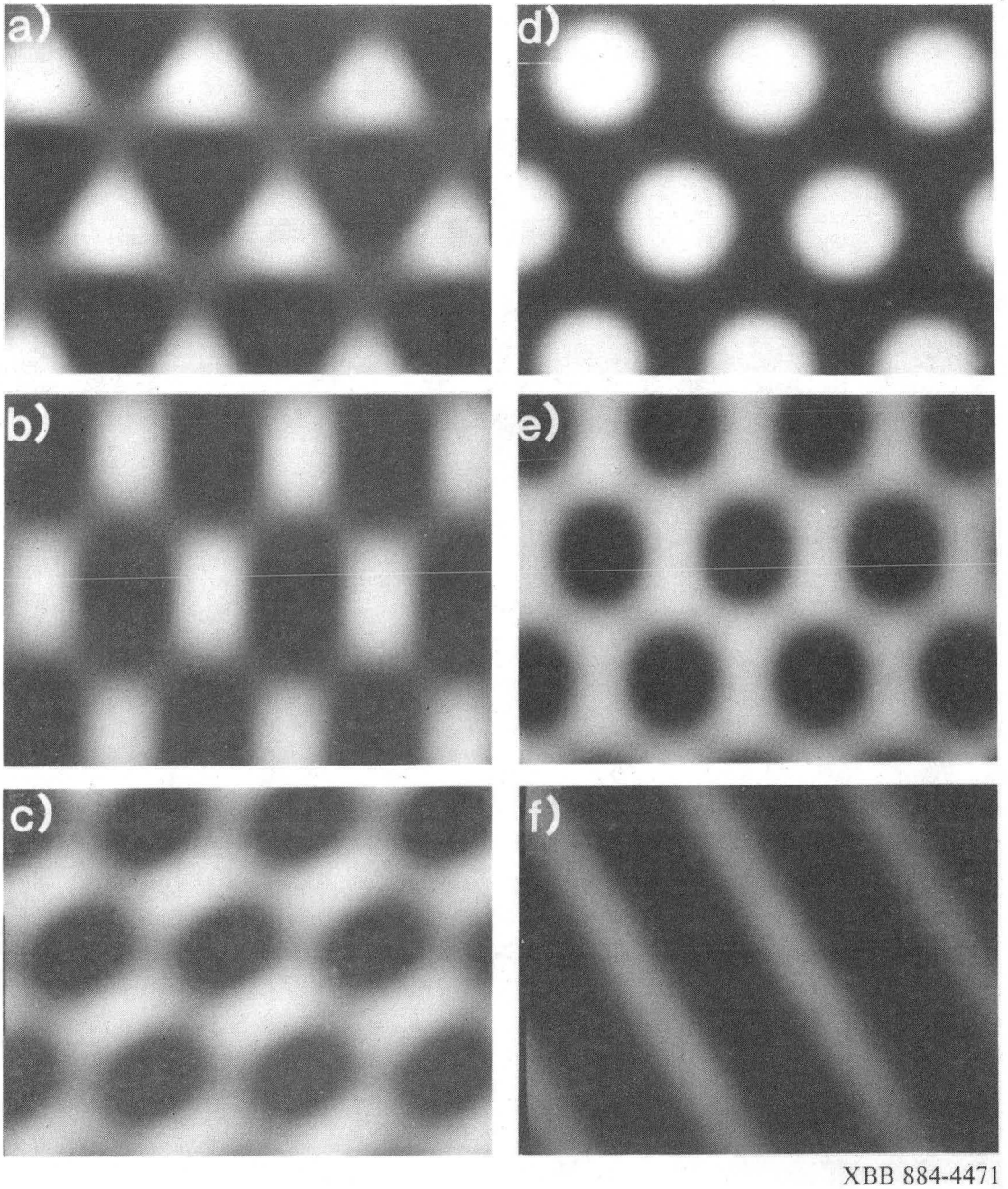

XBB 884-4471

Fig. 5-10 Patterns formed by the superposition of 3 sine waves.

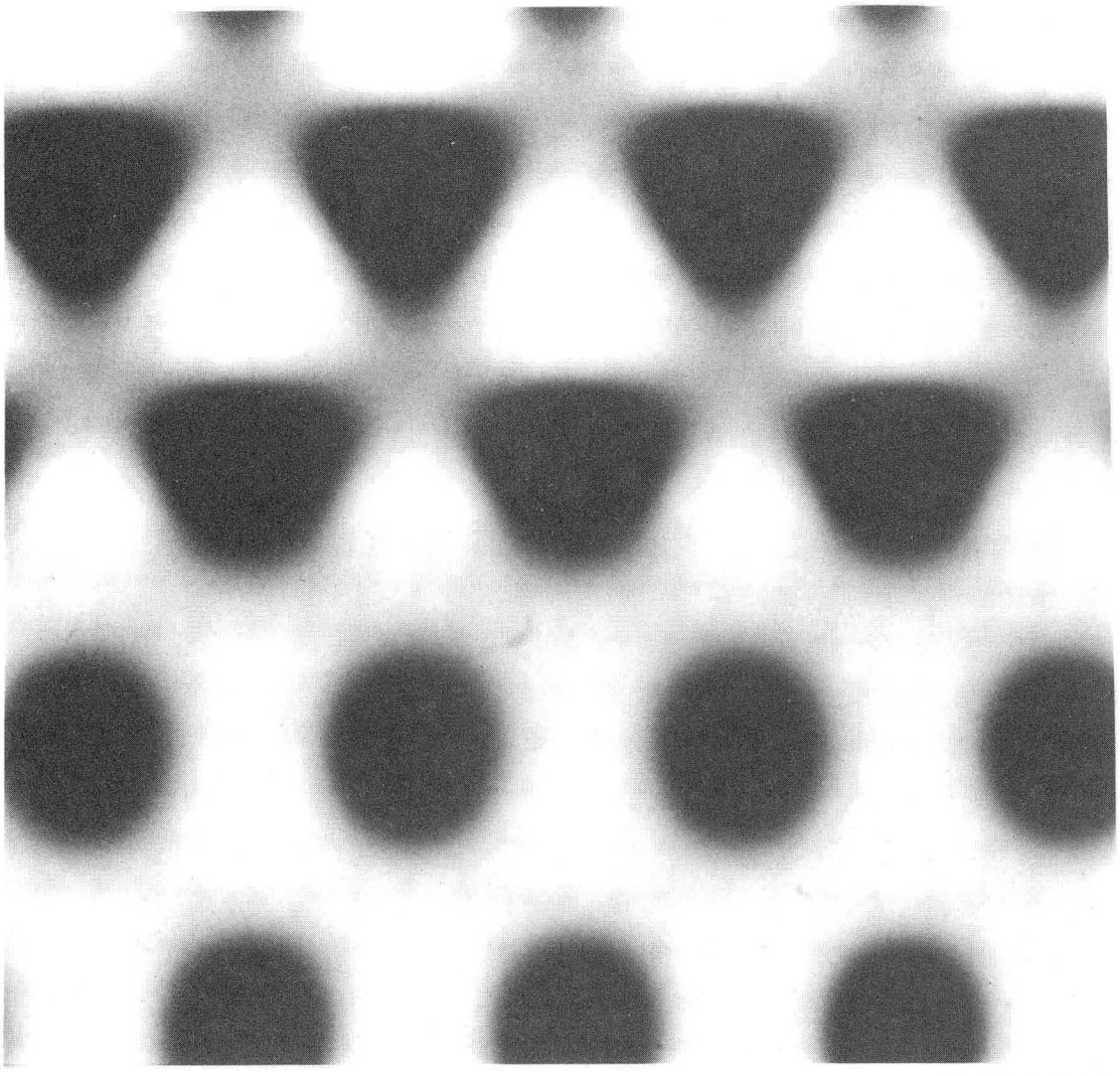

XBB 884-4479

Fig. 5-11 Model honeycomb pattern juxtaposed with a 3-site pattern for comparison with Figs. 5-8 and 5-9.

model, one might expect to observe the honeycomb pattern rather infrequently. Instead, it is a very common pattern. We feel that a complete model should be able to produce the observed image distribution naturally from an ensemble of generic tips.

Finally, the STM images we have obtained contain higher order Fourier components. With an accurate calculation for the single tip image at a reasonable gap spacing, one should be able to make accurate predictions for the effects of multiple tips.

A quite different model has been proposed by J. Chen[16]. He suggests that most of the observed images are due to a single atom tip, but that the state of the tip atom can affect the image. Thus, depending on the local environment of the tip atom, it might be scanning the surface with a p_x orbital, or a combination of p_x, p_y, and p_z orbitals. One can construct orbitals which act to effectively differentiate the surface charge density, and thus produce a whole new range of possible images. Figure 5-12 shows a candidate for an image produced by such a differential tip. This type of image is quite rare, and we have only one example.

If the adsorbate binds strongly to the graphite, it can modify the local electronic structure of the graphite. From a point source or defect, we expect a radially diminishing effect. We commonly observe these so called "superstructures" in our experiments on metals on graphite. A typical example of this effect is shown in Figure 5-13. Here, we observe a step on a graphite surface that had been coated with a fraction of a monolayer of aluminum. The superstructure is visible both as a linear modulation in the intensity running parallel to the step edge, and as periodic modulations of the β-site intensities. In

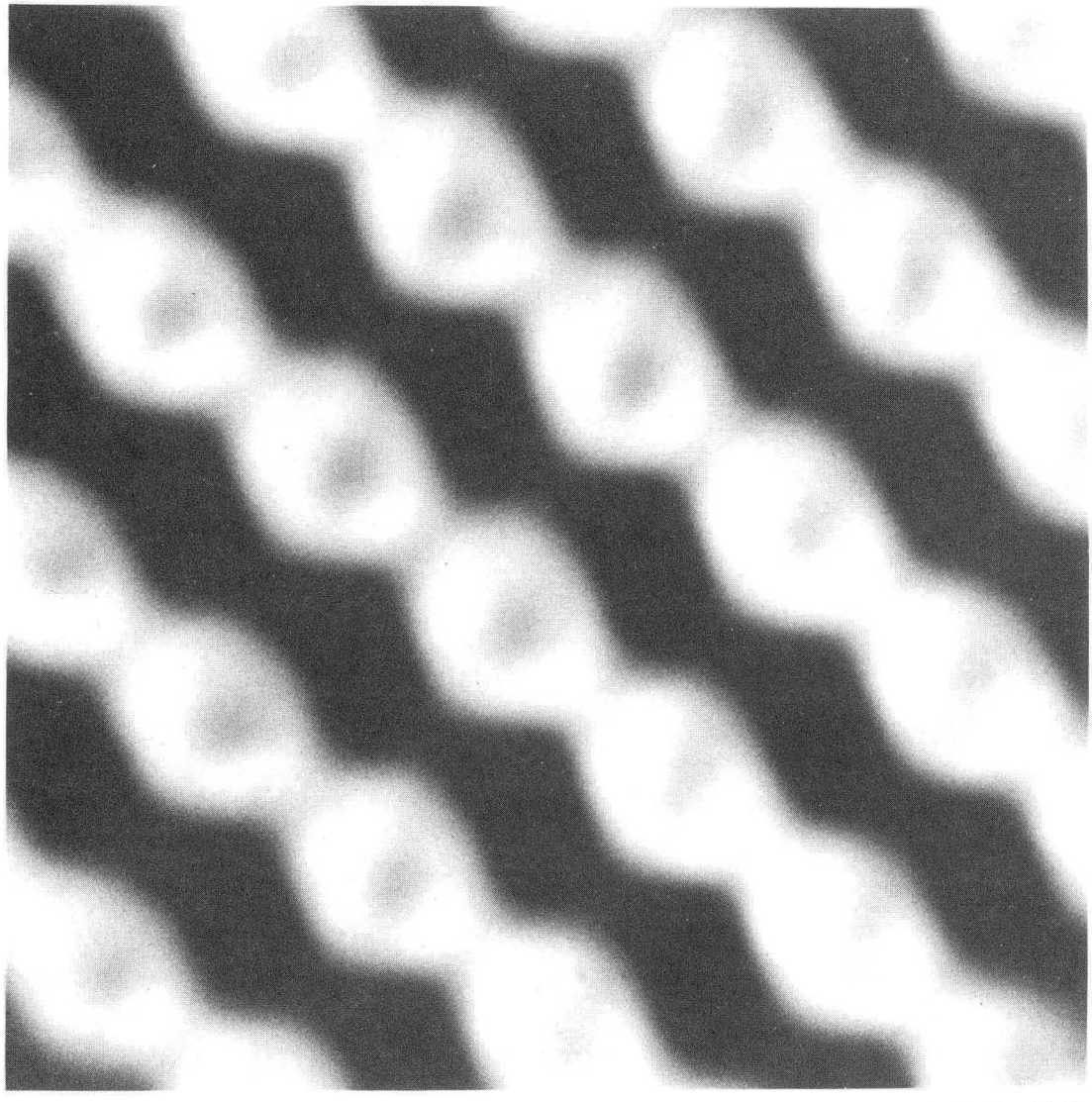

XBB 887-6958

Fig. 5-12 Donut-like image of graphite that may be due to a special tip configuration.

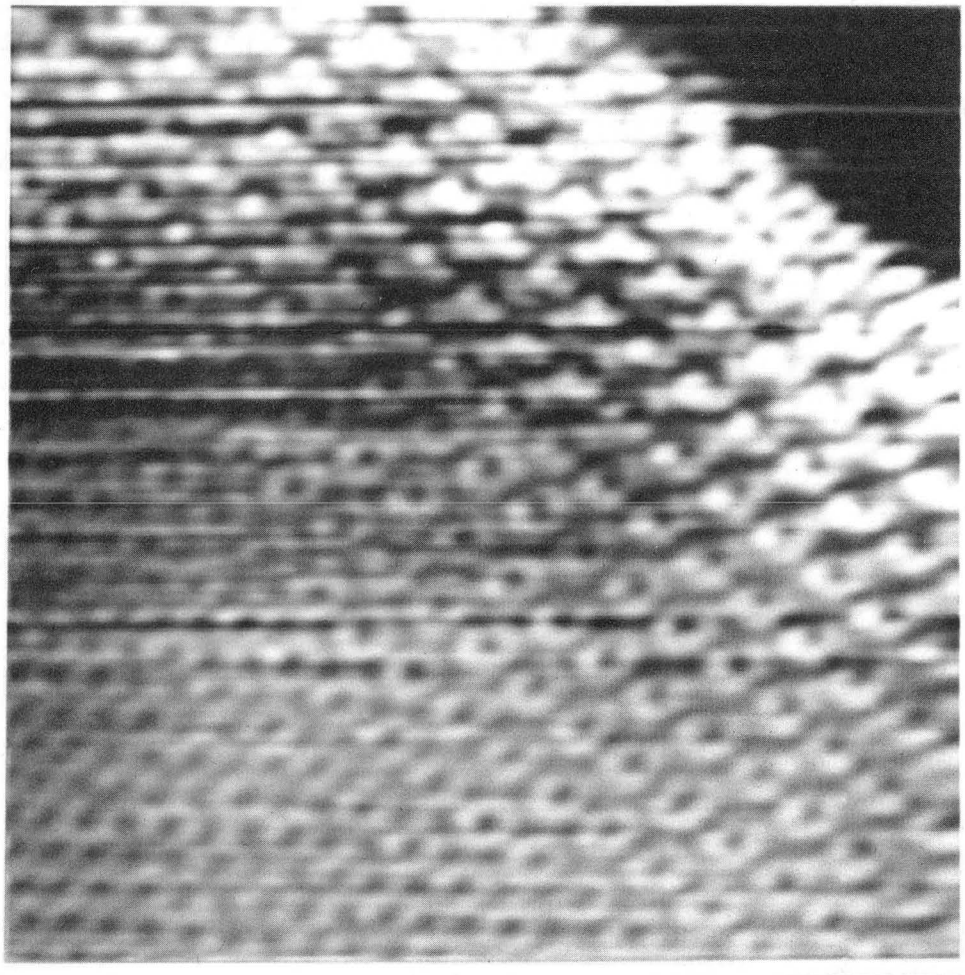

XBB 877-5736

Fig. 5-13 Image showing superstructure along a step edge.

Figure 5-14, we show a superstructure due to a small Ag island. Here, the periodic array of bright dots diminishes as we move away from the Ag island source. In this image, it appears that there are several generation sites, as the superstructure is split into several domains. A theory for the generation of superstructures has recently been developed by Mizes and Harrison[17].

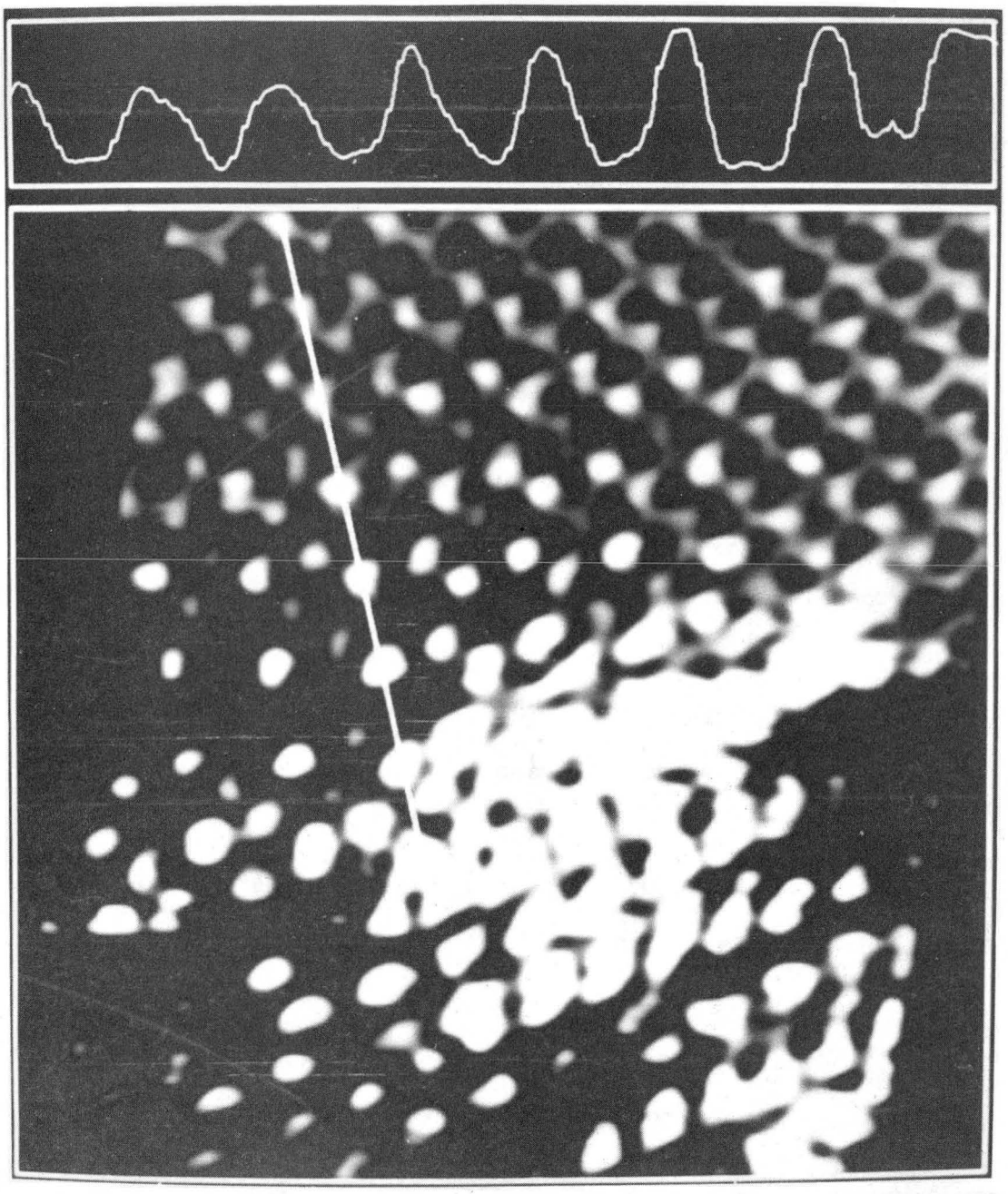

XBB 887-6966

Fig. 5-14 Image showing superstructure near a Ag island. A single scan line is shown at the top.

REFERENCES

1 D. Tomanek, S. G. Louie, H. J. Mamin, D. W. Abraham, R. E. Thomson, E. Ganz, and J. Clarke, Phys. Rev. B 35, 7790 (1987).

2 I. P. Batra, N. Garcia, H. Rohrer, H. Salemink, E. Stoll, and S. Ciraci, Surf. Sci. 181, 126 (1987).

3 G. Binnig, H. Fuchs, CH. Gerber, H. Rohrer, E. Stoll, and E. Tosatti, Europhys. Lett. 1, 31 (1986).

4 A. Selloni, P. Carnevali, E. Tosatti, and C. D. Chen, Phys. Rev. B 31, 2602 (1985).

5 J. Tersoff and D. R. Hamann, Phys. Rev. Lett. 50, 25 (1983).

6 J. Tersoff and D. R. Hamann, Phys. Rev. B31, 805 (1985).

7 L. Samuelson, I. P. Batra, and C. Roetti, Sol. St. Comm. 33, 817 (1980).

8 C. F. Quate, Physics Today 39, p. 26, Aug. (1986).

9 C. T. Chan, D. Vanderbilt, and S. G. Louie, Phys. Rev. B33, 2455 (1986).

10 C. T. Chan, D. Vanderbilt, S. G. Louie, and J. R. Chelikowsky, Phys. Rev. B33, 7941 (1986).

11 S. Fahy, S. G. Louie, and M. L. Cohen, Phys. Rev. B34, 1191 (1986).

12 D. R. Hamann, M. Schluter, and C. Chiang, Phys. Rev. Lett. 43, 1494 (1979).

13 L. Hedin and B. J. Lundqvist, J. Phys. C4, 2064 (1971).

14 I. P. Batra, N. Garcia, H. Rohrer, H. Salemink, E. Stoll, and S. Ciraci, Surf. Sci. 181, 126 (1987).

15 H. A. Mizes, S. Park, and W. A. Harrison, Phys. Rev. B36, 4491 (1987).

16 J. Chen, J. Vac. Sci. Tech. A6, 319 (1988), and private communication.

17 H. A. Mizes and W. A. Harrison, J. Vac. Sci. Tech. A6, 300 (1988).

CHAPTER VI

IMAGING OF METAL CLUSTERS ON GRAPHITE IN AIR

In this chapter, we will discuss some early results on the deposition of Ag and Au onto graphite. The imaging was done in air, but nevertheless, we were able to image small clusters and islands[1]. These early successes encouraged us to extend the experiment to ultrahigh vacuum, as will be discussed in the following chapters.

The graphite substrates were prepared by cleaving in air, and images obtained in air revealed a perfect lattice extending over thousands of angstroms[2]. To deposit the clusters, we placed the substrate in an evaporator with a base pressure of 10^{-6} torr. In the first series of experiments we evaporated approximately 3 Å of Ag (measured with a quartz crystal microbalance) onto the room temperature graphite in 2.2 torr of Ar. The Ar atmosphere causes the evaporated atoms to condense into clusters in flight. This technique is known to produce clusters with a log-normal size distribution[3], with mean size between 20 Å and 200 Å (the mean particle size depends on the deposition rate, path length, Ar pressure, and ambient temperature). We transferred the substrate to our STM and obtained pictures in air at atmospheric pressure. We studied five substrates prepared separately, in each case examining images from hundreds of different areas. We obtained a wide variety of pictures. In some we observed only the unadorned graphite lattice, while in others we observed clusters that were relatively stable, ranging in size from a few atoms to many thousands of atoms. In addition we often observed very small features that could perhaps have represented one or two adatoms, but that in

general were not stable in time. The examples presented here are thus representative of only a subset of the types of behavior that we have observed.

Figure 6-1 shows a topographic image of a large Ag cluster obtained with a bias voltage of 16 mV. The Ag cluster shown in Figure 6-1 has a cylindrical shape with a diameter of 350 Å and a height of about 30 Å. Closer inspection reveals that the cluster is composed of several smaller agglomerations each 30 to 100 Å in diameter. This structure was stable and reproducible during the 10 min period in which we made three images. Presumably, these smaller clusters were formed by condensation in the Ar during the deposition[3], and were mobile upon arrival on the substrate[4] and then collided to coalesce and form the large structure we observe in Figure 6-1. In fact, Ag particles 20 Å to 100 Å in diameter have been observed to move hundreds of angstroms using TEM[5].

We note that the lateral dimensions of the image in Figure 6-1 are, in fact, upper bounds on the true cluster size. Although tunneling probably occurred from a single atom on the tip, the structure supporting that atom may well have been relatively blunt. Thus, the apparent sizes of the convex features may have been increased to an extent depending on the height of the feature and the shape of the tip. This effect was discussed in chapter III with regard to the imaging of small gold mounds.

Although the topographic mode was useful for determining the general features of relatively large clusters, it was slow, requiring typically 3 min to obtain a single image (See chapter IX for fast topographic imaging using a tube scanner). To observe cluster motion

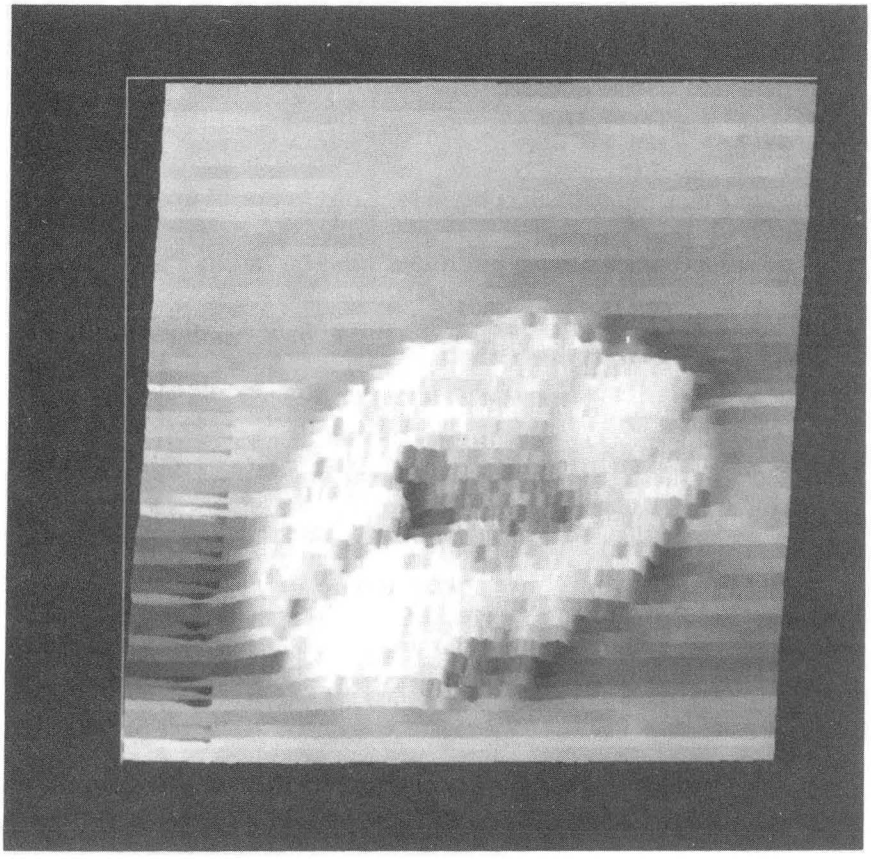

XBB 866-4979

Fig. 6-1 500 Å X 600 Å topographic image of a large three-dimensional Ag island on graphite in air shown in top view. The gray scale corresponds to a height variation of 40 Å.

on the time scale of a few seconds, we used the current imaging mode. Although limited to relatively flat samples, this technique allowed us to obtain a complete image every 2 seconds.

Figure 6-2 shows a series of five 24 Å × 24 Å current images. The pictures on the left are top views of the tunneling current as a function of position, while the pictures on the right are projected views of the same sets of data. Figures 6-2 (a) and (a') show the clean graphite surface. Figures 6-2 (b) and (b') show a Ag cluster roughly 15 Å long and 5 Å wide. The bare graphite to the right and left of the cluster appears lower than the graphite regions above and below the cluster due to the slow response of the feedback loop, which holds the tunneling current at a constant average value. This shadowing effect is a natural result of high pass filtering. The cluster appears to be made up of approximately seven groups of atoms. The feature at each end of the cluster could well be a single atom. Although the length of the inner five groups varies, the typical length of 4 to 5 Å is not inconsistent with the value expected for a Ag dimer, that is, two covalently-bonded Ag atoms. The bond length of a free Ag dimer has been calculated[6] to be 2.5 Å. Because the electron charge density between the two atoms is high, it is plausible that the STM would not resolve the individual atoms. If we assume that the dimers are weakly coupled in the cluster via van der Waals forces, we would expect the individual dimers to be resolved. We note that the dimers are roughly commensurate with the graphite lattice, suggesting that the substrate-cluster interaction is by no means negligible.

We emphasize that we have not proved that the observed structures are in fact Ag dimers. For example, motion of the Ag atoms during the

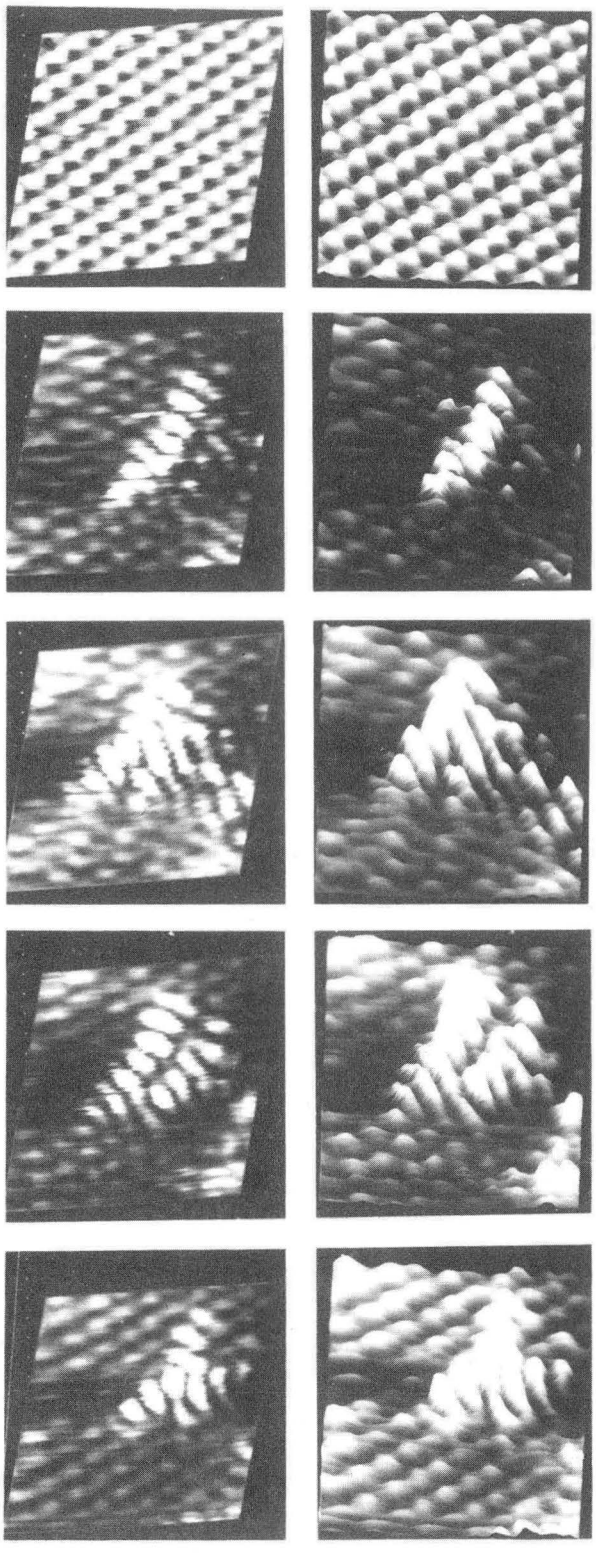

Fig. 6-2 24 Å X 24 Å current image of graphite in (a) top view, and (b) projected view; (b,b') through (e,e') illustrate the time evolution of a Ag cluster on graphite in air. XBB 867-5753

imaging time could seriously distort the shape of the image, conceivably causing a single atom to have an unusually large apparent length. In addition, we cannot rule out the possibility that some of the structure represents a trimer, for example, Ag_2O. We shall see in the next chapter that we do resolve Ag dimers in UHV. Thus the presence of air or water may contaminate the clusters and change the image.

The remaining pictures in Figure 6-2 were selected from a long series of scans. Figures 6-2 (c) and (c') show the same area as in Figures 6-2 (b) and (b') roughly 15 min later. It appears that more Ag atoms have diffused into the region to join with the original cluster. Two minutes later [Figures 6-2 (d) and (d')] the cluster changes again into two string-like features of comparable size in very close proximity. Five minutes later still [Figures 6-2 (e) and (e')], the cluster has taken on a Y shape which remained stable for 15 min.

In a second series of experiments, we evaporated Au onto the graphite surface at a base pressure of about 10^{-6} torr, with no Ar introduced into the chamber. This technique produces single atoms in the beam which then nucleate on the surface[7]. We found clean graphite regions as well as regions with clusters of very large size. At the boundaries between these regions, we occasionally found small clusters. Figure 6-3 shows a very small Au cluster of apparently six atoms with an average spacing of about 3 Å.

An important consideration in these experiments is the possible perturbation of the clusters by the tip during current imaging. In an extreme case, one could imagine that the tip would actually crash into the supported atoms, dramatically changing the structure of the

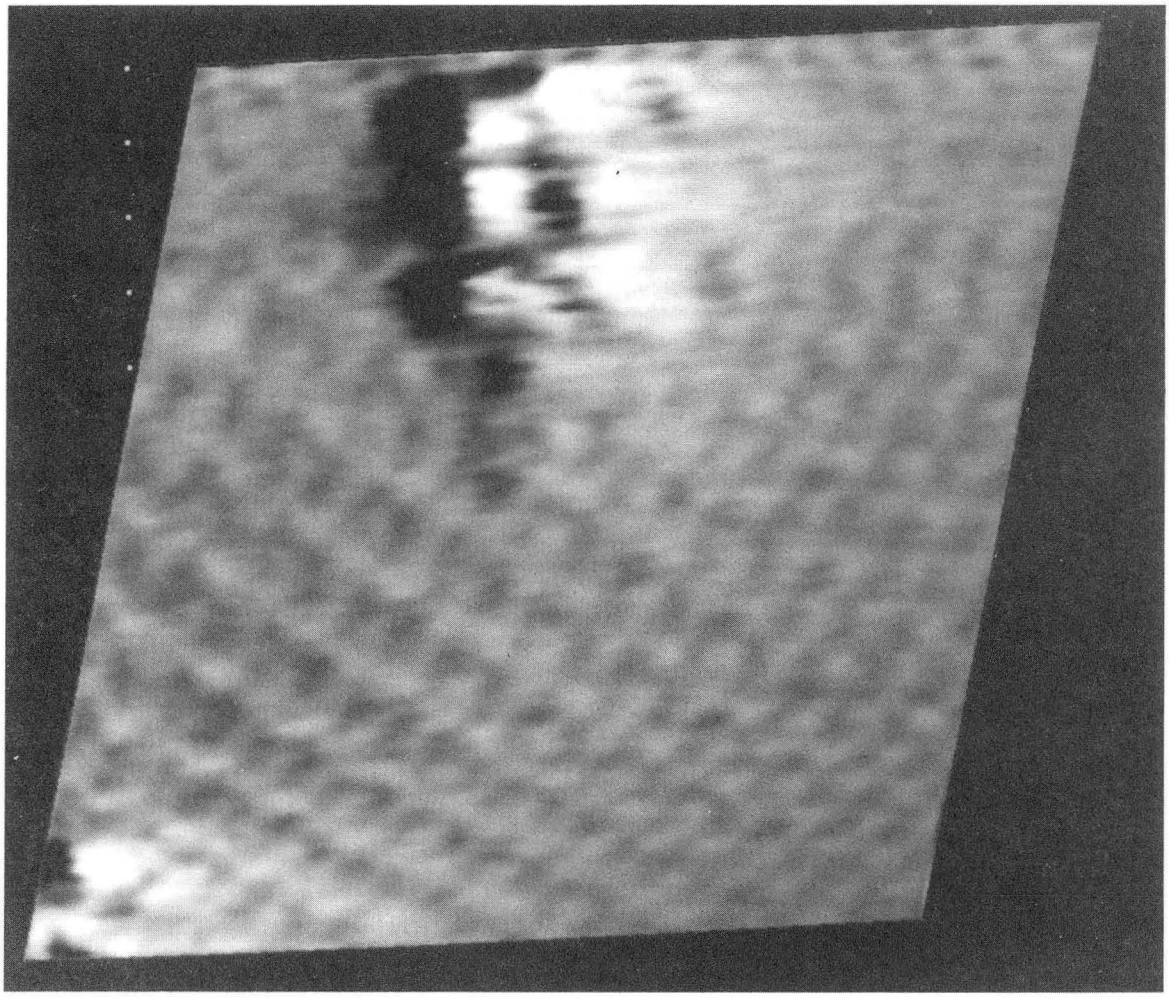

XBB 866-4977

Fig. 6-3 24 Å X 24 Å current image of a Au cluster on graphite in air.

cluster, or simply brushing it aside. The clusters shown in this chapter were observed for hundreds of scans during which time the structure was stable or underwent relatively slow, progressive changes. Thus, for these cases at least, we conclude that the effect of the tip on the observed structure was negligible.

Because we have imaged both the Ag and Au clusters in air, we must consider the possibility that adsorbed gases or surface defects would produce similar features. However, the images illustrated here were seen only when Au or Ag was deposited onto the graphite surface. In tests in which the graphite was taken through the same procedures except for the evaporation of the metal, and in extensive experiments on clean graphite in air, we have never observed features of the kind shown. Auger analysis of a representative Ag-deposited sample showed 10% surface coverage of Ag on graphite.

In conclusion, we shall avoid over-interpretation of these preliminary pictures. It is highly probable that the graphite surfaces are contaminated, for example, by water or oxygen. Such contaminants could have a profound influence on the binding of the adatoms to the substrate and hence on the structure and mobility of the clusters. Nevertheless, it is fascinating that under these presumably adverse conditions, we are still able to resolve individual metal atoms, and observe the merging of two clusters.

REFERENCES:

1 D. W. Abraham, K. Sattler, E. Ganz, H. J. Mamin, R. E. Thomson, and J. Clarke, Appl. Phys. Lett. 49, 853 (1986).

2 G. Binnig, H. Fuchs, Ch. Gerber, H. Rohrer, E. Stoll and E. Tosatti, Europhys. Lett. 1, 31 (1986).

3 C.G. Granquist and R.A. Buhrmann, J. Appl. Phys. 47, 2200 (1976).

4 R. Kern, J. J. Metois, and G. Lelay, Curr. Top. Mater. Sci. 3, 131 (1979).

5 J. S. Maa, J. I. Lee, and T. E. Hutchinson, Proc. 34th EMSA meeting, p. 648 (1976).

6 W. Andreoni and J.L. Martins, Surf. Sci. 156, 635 (1983).

7 J.A. Venables, G.D.T. Spiller, and M. Hanbucken, Rep. Prog. Phys. 47, 399 (1984).

CHAPTER VII

IMAGING OF SMALL METAL CLUSTERS ON GRAPHITE IN UHV

In the last ten years, new techniques for the production of clusters in beams have been developed that allow researchers to study free clusters for a wide variety of cluster materials[1,2]. As a result, many interesting differences have been found between the properties of bulk materials and those of free clusters, including dramatic changes in atomic spacing and electronic structure[3]. Studies of clusters are also technologically driven by the need for new and more specific catalysts. But, to use clusters in a catalytic environment, they must be supported on a substrate. The substrate can have a profound effect on the morphology and electronic structure of the ad-cluster, and thus change the catalytic activity of the system[4,5]. Thus, there is a need for fundamental studies of supported clusters.

Small clusters have been and continue to be extensively studied as tractable model systems for the study of larger clusters, and also as interesting systems in their own right. For example, Ag_4 has recently been shown to be an active catalyst in the formation of the latent image on photographic film[6]. Unfortunately, theoretical calculations on these systems are still very difficult, requiring large amounts of computer time to produce what is often only an approximate result. Thus, it is especially important to obtain reliable and precise experimental information about these systems.

In the previous chapter, we demonstrated the potential of the STM as a tool for the study of metal clusters on graphite in air. Here, we extend this work to ultrahigh vacuum, and demonstrate the capability of the STM to image, atom by atom, isolated monomers and small clusters of Ag, Al, and Au. This work was published in 1988[7].

We use graphite as a support for three reasons. First, graphite is easily cleaved, providing atomically flat planes over many square microns[8]. Second, graphite has been extensively studied with the STM, and can be reliably imaged with atomic resolution. Third, graphite is both a good conductor, and yet also relatively inert chemically. Thus, the graphite surface is particularly well suited to the study of supported metal clusters with the STM.

In the present experiment, we cleaved highly oriented pyrolytic graphite (Grade ZYB from Union Carbide) in a sample introduction chamber at 10^{-8} torr. The sample was then transferred to a UHV chamber at $2x10^{-10}$ torr without breaking vacuum. To prevent ion contamination, we turned off all ion gauges before the sample was cleaved and left then off for the duration of the experiment[9].

To prevent the STM from contaminating the surface, we found it necessary to clean the W tip *in situ* before scanning the sample. The tip was cleaned by field emission to a clean Si surface with a bias voltage of 900V and a current of 100 μA. For each run, after cleaning the tip and cleaving the sample, we searched $1\mu m^2$ with the STM. The STM images showed a perfect graphite lattice over the entire region, with no observable contamination. Furthermore, no grain boundaries, defects or steps were observed on the cleaved substrate. These two facts ensure that all features observed after deposition of the metal were due to adsorbed metal atoms. We used a new tip for each metal, and a freshly cleaved substrate for each run. The metal evaporation was done *in situ* in UHV to avoid contamination.

The Ag and Au atoms were evaporated from a resistively heated Ta boat 0.1m from the sample, while the Al was evaporated from a W coil. Both the Au and the Al eventually alloyed with the boat and coil, respectively,

preventing further evaporation, but only after several evaporation cycles. The evaporator was degassed prior to deposition. A quartz crystal microbalance was used to monitor the deposition rate, and a shutter was used to set the exposure time. We deposited approximately 1% of a monolayer of metal, as measured by the crystal monitor, in 0.5 sec. The work of Arthur and Cho[10] suggests that the sticking coefficient of Ag and Au on graphite might be less than 0.1 for clean graphite, so we would expect to find no more than 0.1% of a monolayer of metal on the surface. This corresponds roughly to what we observed in a survey performed with the STM: A survey of 10^8 Å^2 found 1.2×10^5 Å^2 covered with Ag adatoms distributed in small groups and islands. We were unable to measure the Al deposition rate accurately because of thermal drift in the crystal monitor. We chose the low coverage so that we could find isolated metal atoms surrounded by clean graphite. We then were able to image the graphite lattice and the metal adatoms simultaneously. Thus, the image of the graphite lattice provides an internal calibration for each image and allows us to determine adsorption sites by direct observation.

The STM was operated in the current imaging mode. A bias voltage of 5 mV and a tunneling current of 10 nA were typical and were chosen to optimize image quality and stability. When we brought the tip closer to the surface (higher current) the tip-sample interaction was increased, rendering the tip less stable and breaking up the metal islands. When we retracted the tip (lower current) the image resolution was reduced and the system noise was increased. Images were acquired at rates of 1 to 4 seconds per frame.

In the figures that follow, we have used a computer to generate a model showing the observed position of the adatoms. This has been discussed in chapter II in the section on the CALIB program. We can use the model to make

accurate determinations of adsorption sites and spacings based on the well known honeycomb lattice spacing of 2.46 Å for the graphite surface.

During the metal deposition, individual atoms arrive at the surface, where they are mobile until they re-evaporate or are captured into an island[10]. Surveys of large areas showed most of the substrate to be clean, with small areas containing groups of metal islands and clusters. By extensive searching, we were able to find several examples of stable isolated monomers, but always within 10 Å of a large island or cluster. In this chapter we will give representative examples of a few of the many monomers and small clusters that we have observed.

Figures 7-1(a) and Fig. 7-2 show single Ag adatoms on a clean graphite substrate. The Ag atoms are clearly visible as sites of enhanced current. The gray scale ranges from 5 nA in black regions to 10 nA in white areas. These isolated Ag monomers are observed on or near the bright spots of the graphite lattice which correspond to the carbon β-sites of the graphite honeycomb lattice: A β-site has no atom directly below in the next layer [see chapter V for further discussion of the graphite structure]. The adatom in Figure 7-1(a) [also shown in Figure 7-2(a)] was imaged at the same spot for several seconds, while that in Figure 7-2(b) was imaged only for a single scan before moving away.

Figure 7-1(b) shows a single isolated Au adatom on a clean graphite background. This Au monomer was quite stable, and was observed at the same spot for ten minutes. In contrast to the Ag atoms, the Au monomer is not located above a β-site. Unfortunately, we only have this one example of a single isolated Au monomer, and the background lattice is quite distorted in these images due to nonlinearities in the STM scanner. Thus, we cannot draw firm conclusions about the positions of isolated Au atoms on graphite.

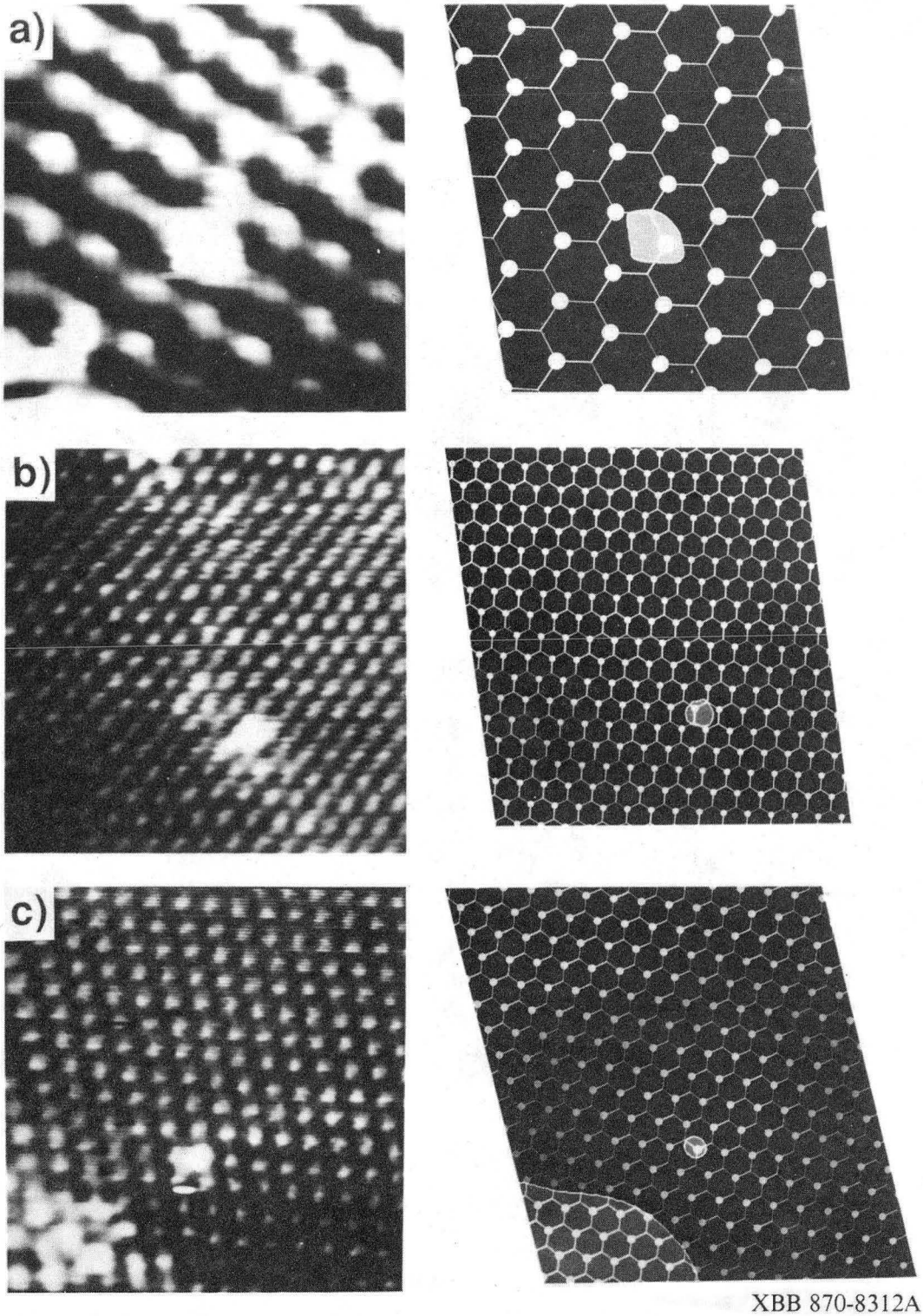

Fig. 7-1 (a) 14 Å X 16 Å current image of an isolated Ag monomer, (b) 37 Å X 39 Å current image of an isolated Au monomer, and (c) 33 Å X 37 Å current image of an isolated Al monomer near an Al island on graphite. To the right of each image is a computer generated model showing lattice positions.

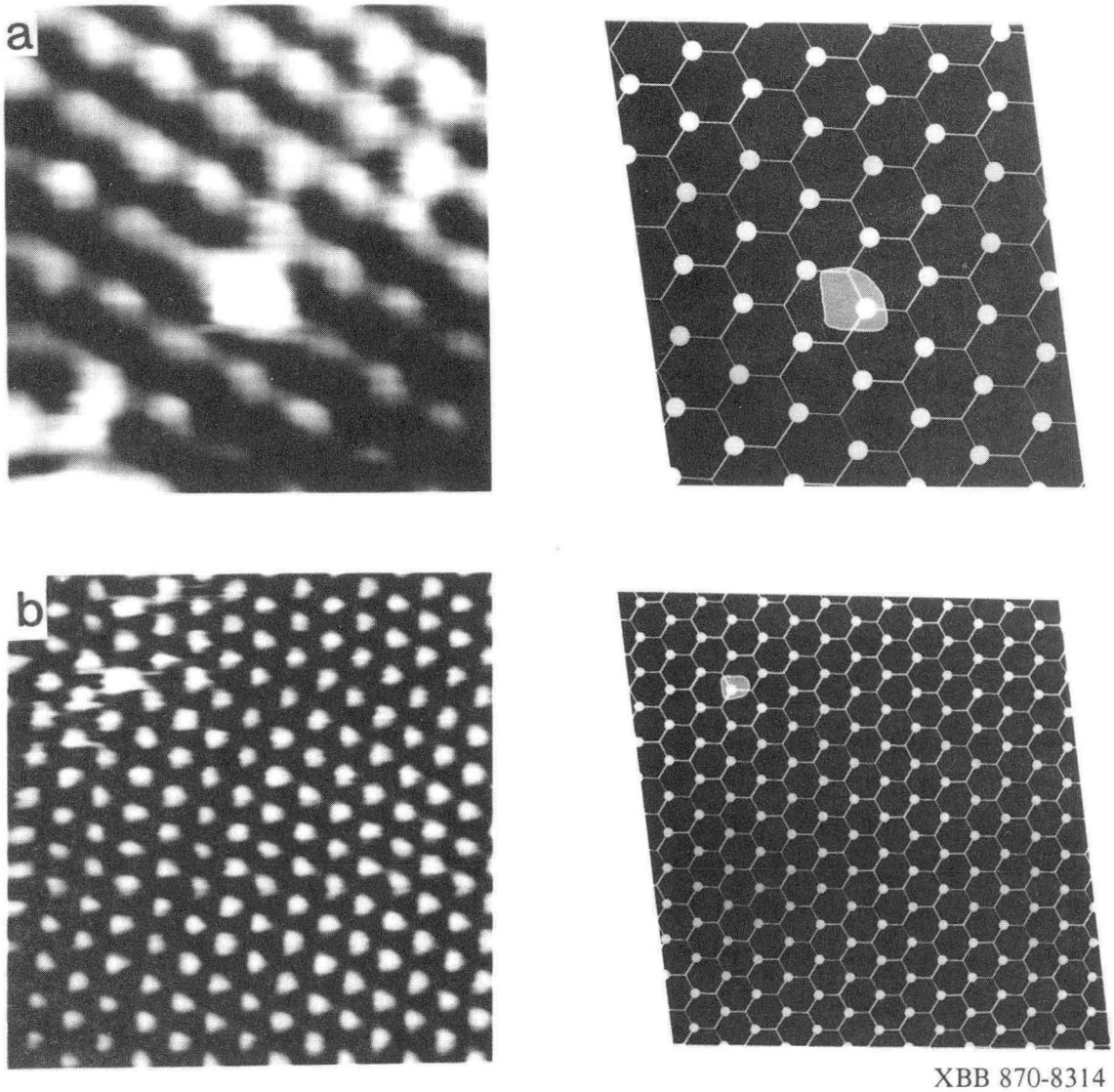

XBB 870-8314

Fig. 7-2 (a) 14 Å X 16 Å and (b) 31 Å X 32 Å current images of isolated Ag monomers on graphite.

Figure 7-1(c) shows a current image of an isolated Al monomer at a β-site. The adatom is roughly 2 Å in diameter. This provides a rigorous upper limit on the resolution of the STM[12,13,14]. As shown schematically in Figure 7-3, a periodic substrate will produce an image with the same periodicity independent of the resolution. The effect of lower resolution is a reduction in the amplitude of the modulation. Kuk *et al.*[15] have used a field ion microscope to compare the tip shape with the observed modulation of a metal surface, and showed that larger tips do give smaller modulation. Thus, without a model for the expected modulation, or independent information about the tip shape, we cannot infer the instrumental resolution. On the other hand, the observed diameter of a single adsorbed atom is the sum of the intrinsic size of the atom and the resolution of the measurement. Thus Figure 7-1(c) demonstrates (without knowledge of the tip shape) that the resolution of the STM is better than 2 Å.

The fact that a single metal adatom can be reproducibly imaged for several seconds in one spot demonstrates that it is relatively strongly bound to the substrate. Metois and Heyraud estimated a binding energy of 0.26 eV/atom for large Au islands on graphite[16,17], but this energy is too small to explain the lifetimes that we observe (this point is discussed further in chapter X). The strong binding may be due to the presence of defects on the surface, but we note that no defects were imaged by the STM before deposition of the metal. An alternative explanation is that the proximity of the metal islands [as in Figure 7-1(c)] may perturb the structure of the graphite sufficiently to enhance the binding of monomers. We do not understand why the adatoms should be observed preferentially at graphite β-sites.

In Figure 7-4 we show current images of (a) a Ag dimer, and (b) a Au dimer on graphite. The adatoms are clearly resolved, and are at or near

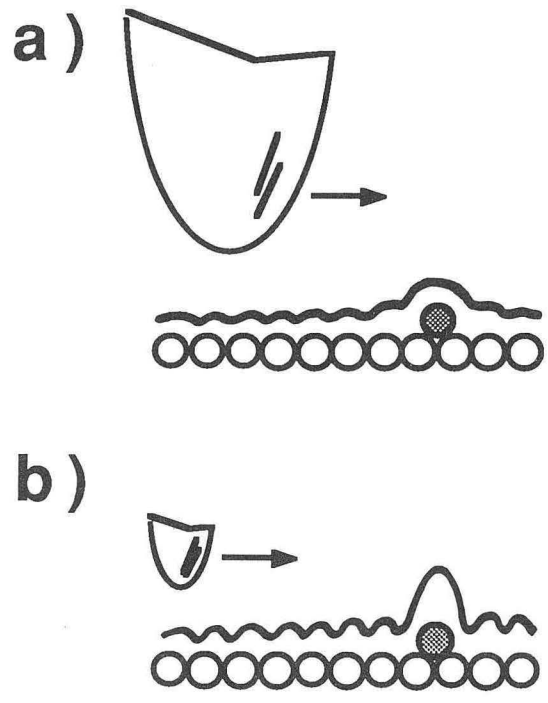

Fig. 7-3 With low resolution, (a), the adatom is not clearly resolved, although the lattice periodicity is still evident. At high resolution, (b), both the lattice and the adatom are resolved.

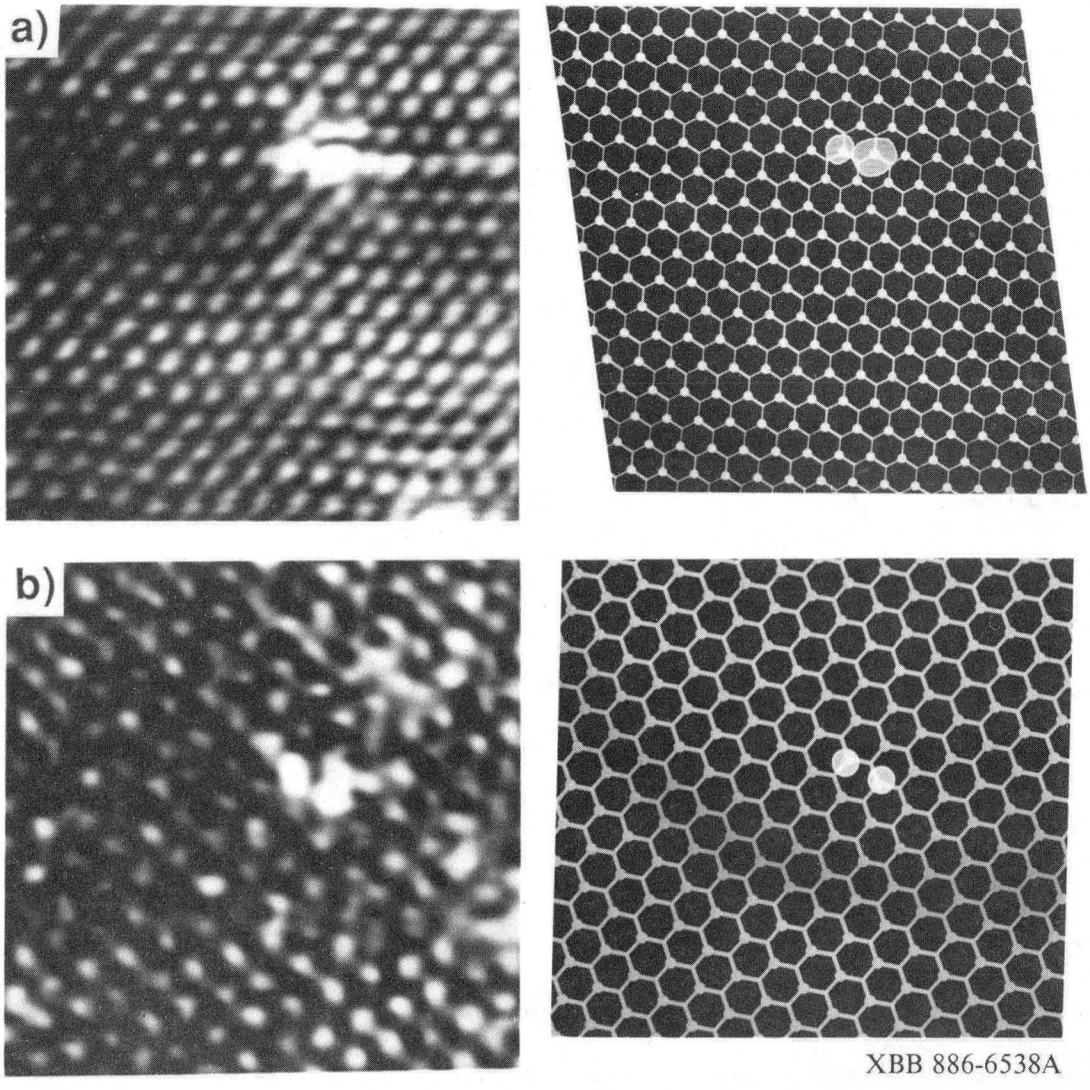

Fig. 7-4 (a) 36 Å X 40 Å current image of a Au dimer, and (b) 32 Å X 32 Å current image of a Ag dimer.

β-sites. The observed Ag dimer bond length is (2.5 ± 0.05) Å, which is smaller than the bulk nearest neighbor spacing[19] of 2.89 Å, but close to the free dimer bond length[20] of 2.50 Å. The observed Au dimer bond length is (2.7 ± 0.1) Å, which is between the bulk spacing[19] of 2.88 Å, and the free dimer bond length[21] of 2.47 Å. It is surprising that the STM is able to resolve the atoms in a dimer, since the STM images the electronic charge density at the Fermi level, and we would expect a significant charge density in the dimer bond. Perhaps charge transfer to the substrate (or some more subtle Au-C interaction), weakens the Au-Au and Ag-Ag bond and localizes the electrons.

In Figure 7-5(a) we show a current image of a Ag trimer. Again, the atoms are above β-sites, and the spacing is roughly 2.5 Å. The linear form is probably not the equilibrium form for a free cluster. The presence of the substrate may stabilize or induce different structures. This effect has been observed in FIM studies of Re on W[22]. Above the image, the line trace shows the variation of current along a line between the two arrows.

In Figure 7-5(b) we show a current image of an Al trimer with several monomers grouped around it. We obtained 10 images of this group over a period of 10 seconds before the tip changed. Figure 7-6 shows two subsequent images of this trimer. The relative positions of the adatoms remained constant during the period of observation. The monomers are above β-sites. The three-lobed trimer has one corner above a β-site, and is slightly rotated relative to the graphite substrate. The trimer has a compact triangular structure. The measured spacings from the center of each lobe to the others is roughly 2.5 Å, close to the recent theoretical result of Upton[23], who found spacings of 2.61 Å and 2.63 Å for the Al trimer and 2.51 Å for the dimer, respectively. Of course, the apparent size in the STM image depends

on the details of the tunneling process and also on the gray scale used for presentation. It is also possible that the presence of the graphite substrate has compressed the adsorbed trimer.

Figure 7-5(c) shows a current image of an array of four silver atoms. The graphite image is quite poor, and so the observed positions of the adatoms (on bridge sites) may not be correct. This array was only visible for a single image. We note that like the Ag dimer and the Ag trimer shown in Figs. 7-5(a) and 7-6(a), the individual atoms are commensurate with the underlying substrate. Although the poor resolution of the graphite prevents us from accurately specifying the position of the adatoms, we can clearly resolve the Ag atoms and the morphology of the particle. We see that the particle is flat on the substrate and not in the compact pyramidal form we might expect for a free particle.

Figure 7-7 shows a series of current images of the linear Ag trimer shown in Figure 7-5(a). These images were obtained at 40 mV bias and at a series of increasing tunneling currents. Although the absolute scale is not determined, the tip to sample distance (gap spacing) decreases as the tunneling current increases. We see that at the largest gap (Figure 7-7(a) at 3.2nA), the trimer is not visible, and only the graphite is imaged. As the gap is progressively reduced (Figs. 7-7(b) through 7-7(f) at 4.4, 5.4, 6.5, 7.3, and 8.0 nA respectively) the current density at the trimer sites is increased. This behaviour was commonly observed for adsorbed atoms and clusters, and shows that the charge density from the adatoms is attenuated more rapidly away from the surface than that of the graphite.

In Figure 7-8, we show a series of topographic images of a Ag dimer. These images were obtained at a bias of 40 mV and at a series of decreasing tunneling currents. In this case, as the current is reduced from 17 nA

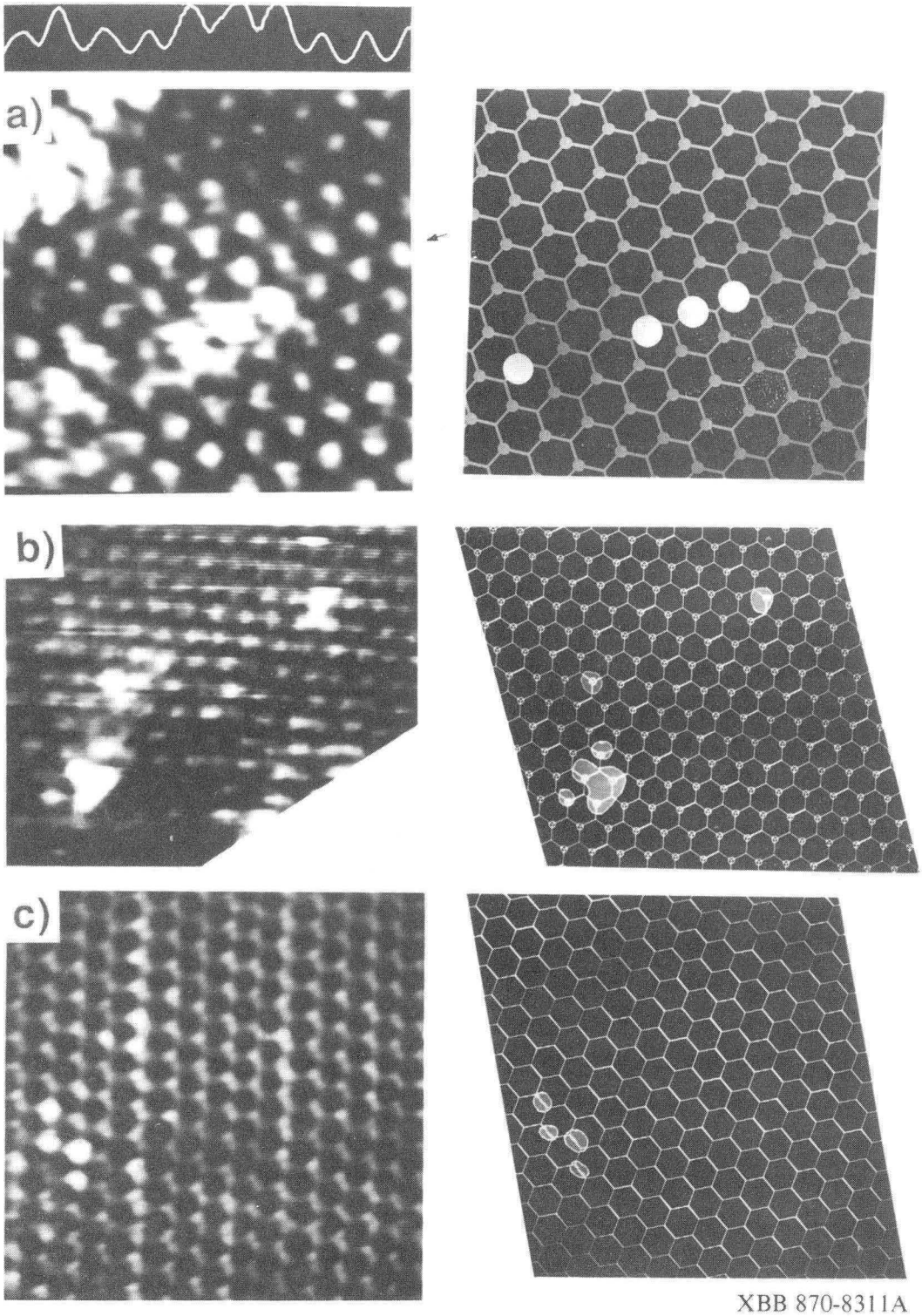

Fig. 7-5 (a) 20 Å X 18 Å current image of a Ag trimer showing a linear form. Above the image, we plot the current *vs.* position along the line between the two arrows. (b) 34 Å X 30 Å current image of an Al trimer, with several monomers nearby. (c) 31 Å X 34 Å current image showing a group of 4 Ag atoms.

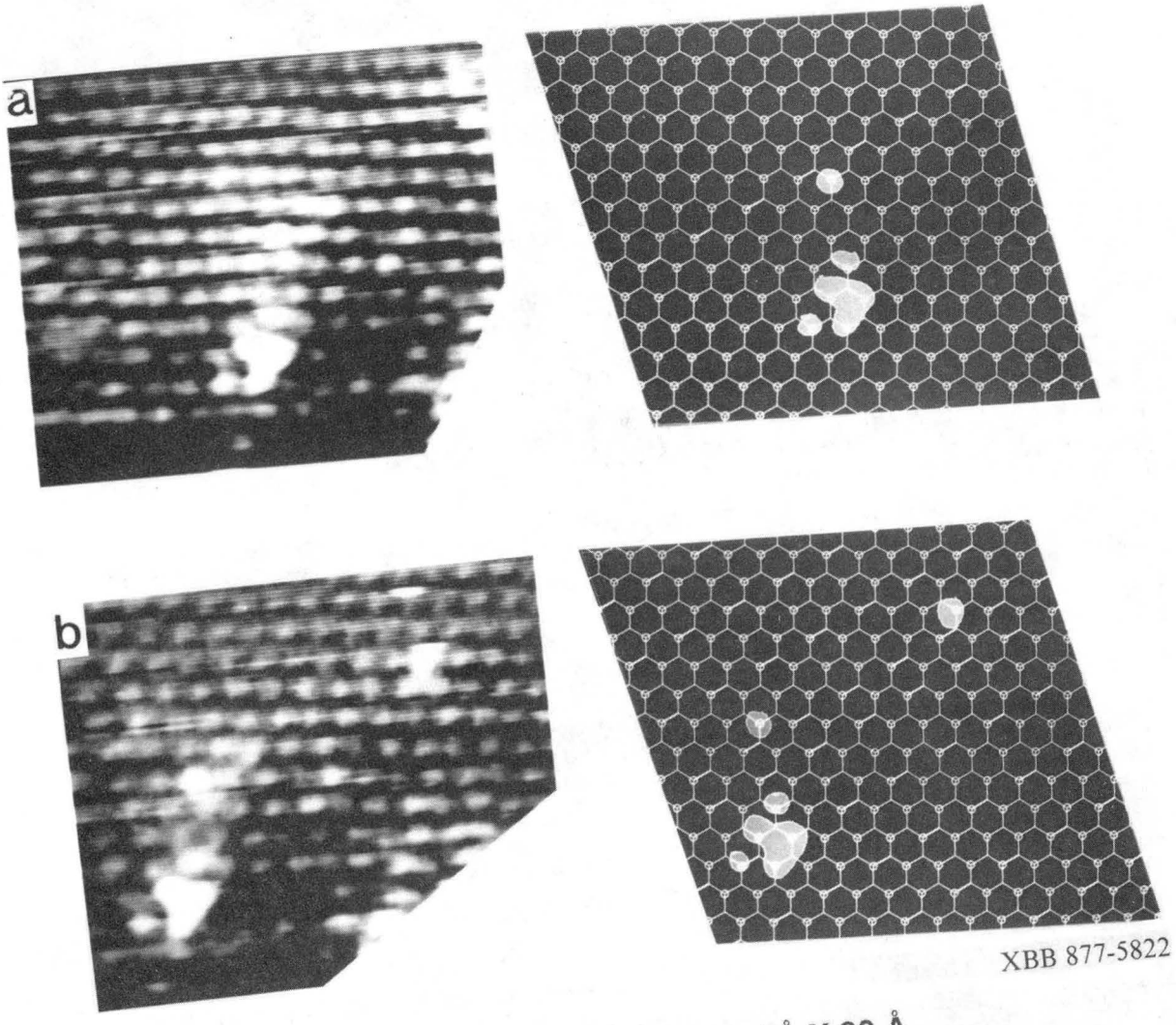

Fig. 7-6 (a) and (b) show sequential 34 Å X 30 Å current images 1 sec apart of an Al trimer, with several monomers nearby.

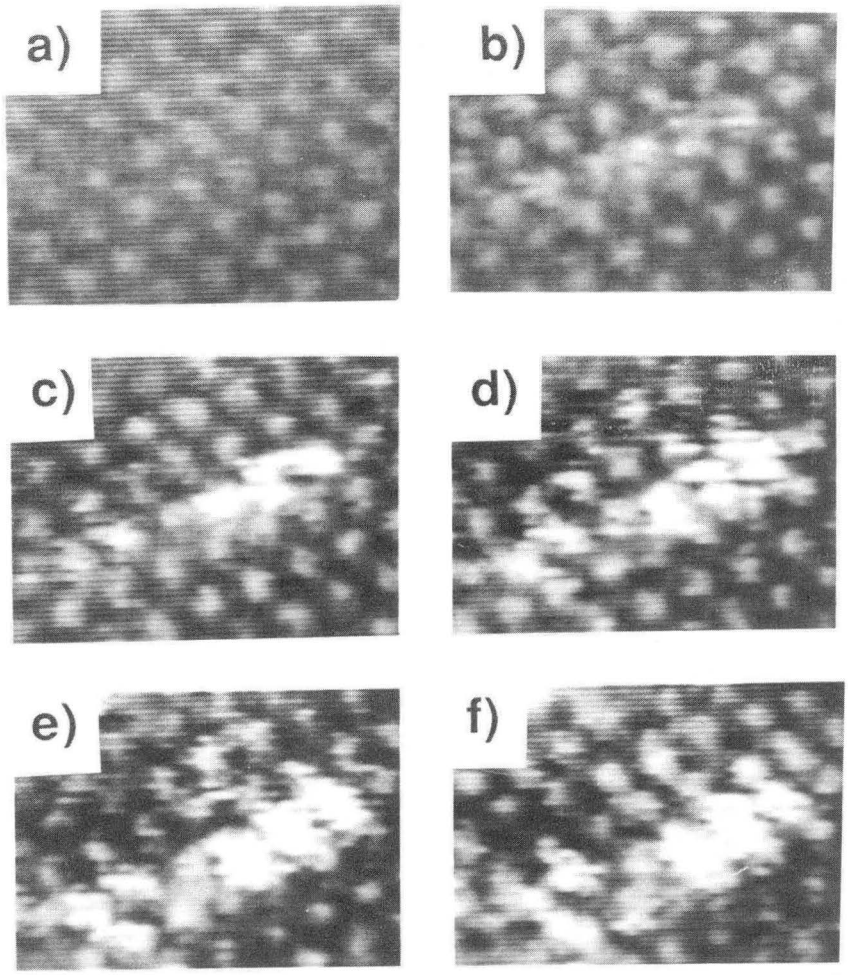

XBB 886-5516

Fig. 7-7 Current images of the Ag trimer of Fig. 7-5(a) at current of (a) 3.2 nA, (b) 4.4 nA, (c) 5.4 nA, (d) 6.5 nA, (e) 7.3 nA, and (f) 8 nA. The bias voltage was 40 mV. At lower tunneling currents (larger gap spacing), the trimer is not visible.

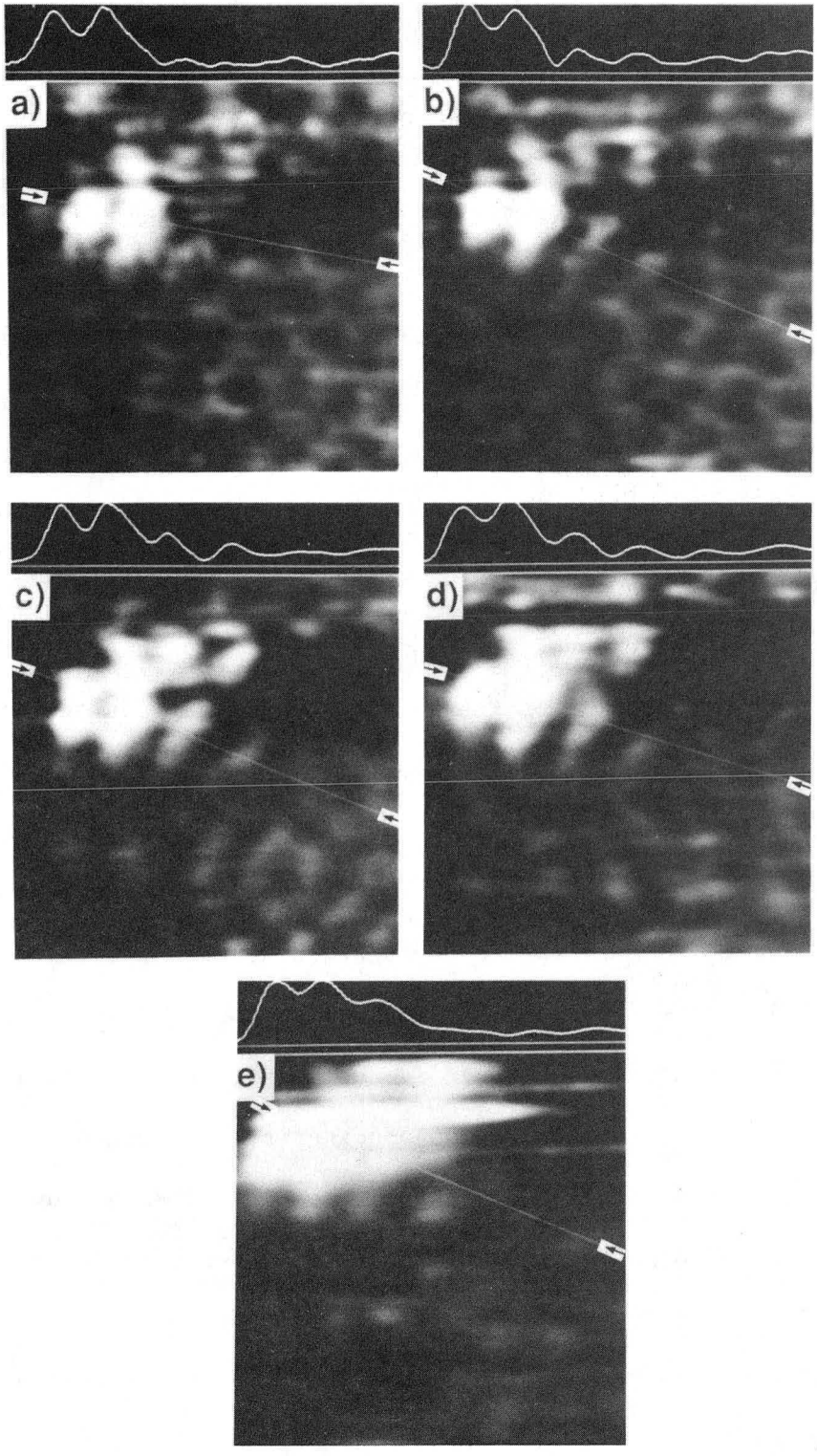

Fig. 7-8 15 Å X 15 Å topographic images of a Ag dimer at currents of (a) 17 nA, (b) 15 nA, (c) 12.5 nA, (d) 7.5 nA, and (e) 5 nA. The bias voltage was 40 mV. The profile in the box above each image was obtained along the line between the two arrows. The heights of the boxes are 18 Å, 16 Å, 17 Å, 18 Å, and 23 Å respectively (see text). At lower tunneling currents (larger gap spacing), the dimer appears larger.

XBB 885-5663A

(Figure 7-8(a)) to 5 nA (Figure 7-8(e)), the size of the adatoms increases. The effect was reproducible for this dimer, and compares qualitatively with predictions by Lang[24], and Doyen *et al.*[25]. Thus, the current imaging technique and the topographic imaging technique can give very different results. Qualitatively, one can understand this behaviour as follows: The contours of constant tunneling current expand spherically around the adsorbate, while a sweep at a fixed height will show smaller and smaller areas with a certain minimum current.

We can measure the heights and areas of the adatoms in Figure 7-8. But the heights are unusually large and range from 12 Å to 18 Å. This is presumably due to deformation of the graphite caused by contamination or oxide on the tip[26] (see chapter IV). We can, however, use the observed corrugation of the graphite to correct for the deformation. The graphite corrugation varies from 2.5 Å to 2.8 Å in the five images. With no deformation, we expect the graphite corrugation to be approximately 0.9 Å (see chapter IV). If we thus apply a scaling factor of 0.35 to reduce the observed heights, we find the average adatom heights range from 4.0 Å to 6.3 Å. To find the observed volume of the constant current contours for each image, we multiply the corrected height by the area of each atom. We estimate the volume to be 4, 9, 10, 12, and 45 $Å^3$ per atom for tunneling currents of 17, 15, 12.5, 7.5, and 5 nA respectively.

On occasion we see groups of several adatoms in which the individual atoms are not resolved. Figure 7-9 shows a complex structure which we interpret as two Ag clusters (of two to five atoms each) with several monomers or dimers grouped nearby. This identification is still tentative because of our limited theoretical understanding of the STM imaging process for metal on graphite. This group was very stable, and we were able to study

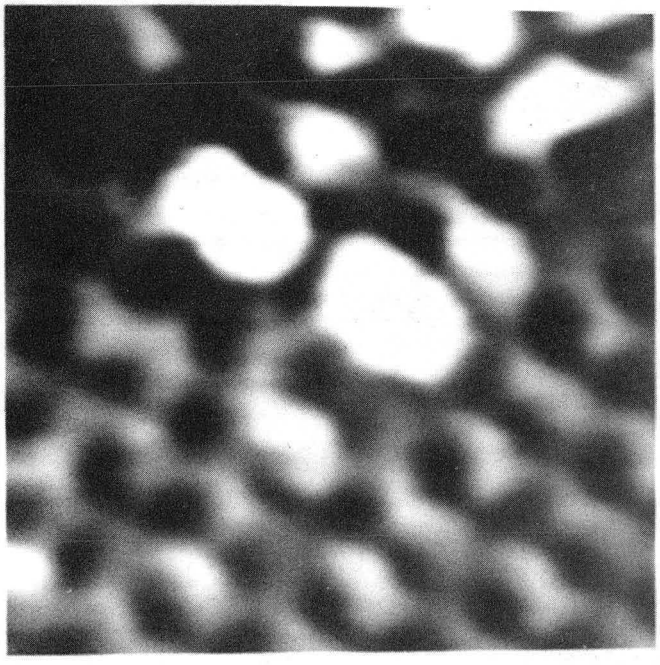

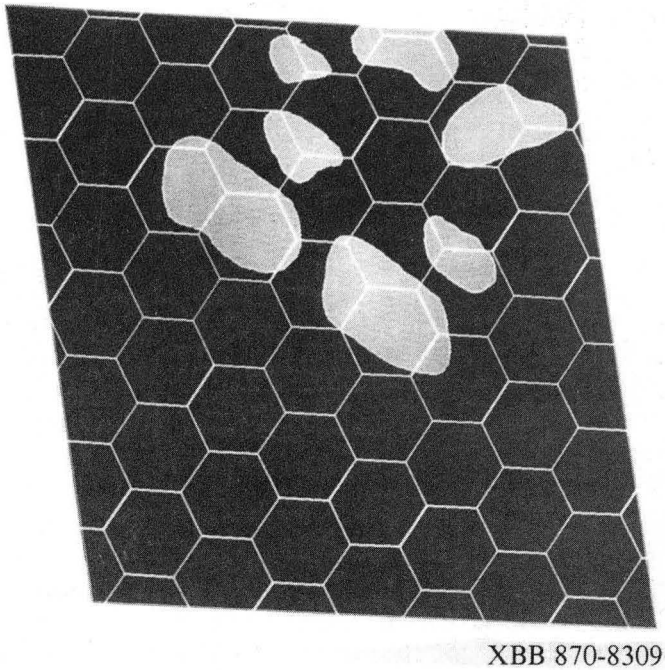

XBB 870-8309

Fig. 7-9 16 Å X 16 Å current image of a group of Ag clusters.

it for 20 minutes without any change in morphology. The two large clusters produced an unusually large tunneling current, 120 nA, much larger than the 5nA produced by the background lattice. This high current is presumably due to the large size of these clusters, approximately 2.7 Å X 4.5 Å, which we can compare to the bulk Ag nearest neighbor distance[19] of 2.89 Å, and the free Ag dimer bond length[20] of 2.50 Å. It is also conceivable that one or two atoms form a second layer on the clusters.

Figure 7-10 shows a 16 atom Al cluster adsorbed at a step edge. The graphite shows superstructure, presumably from the presence of the edge and the adsorbed cluster. The cluster is clearly resolved, and shows a rectangular lattice.

None of our images show isolated metal atoms above hole sites. This result is very different from the adsorption of noble gas atoms. For low coverages, noble gases physisorbed on graphite at low temperatures form registered patterns, with atoms located above the hole sites. These results for noble gases have been modelled with Lennard-Jones potentials, which encourage the adatoms to sink down into the graphite hole sites[27]. The stability and location of metal adatoms atop β-sites or bridge-sites suggest that the details of the graphite-metal bonding are not explained by a simple Lennard-Jones model.

Presumably, all of these clusters are trapped at defects in the surface. As we will see below, we would expect a cluster on a perfect graphite substrate to move quite rapidly. The presence of a defect may influence the structure of the adsorbed clusters due to the large binding energy to the defect. Nevertheless, we find these results interesting for two reasons: we are observing the very beginnings of nucleation and growth on a relatively non-interacting substrate, and we are able to resolve the

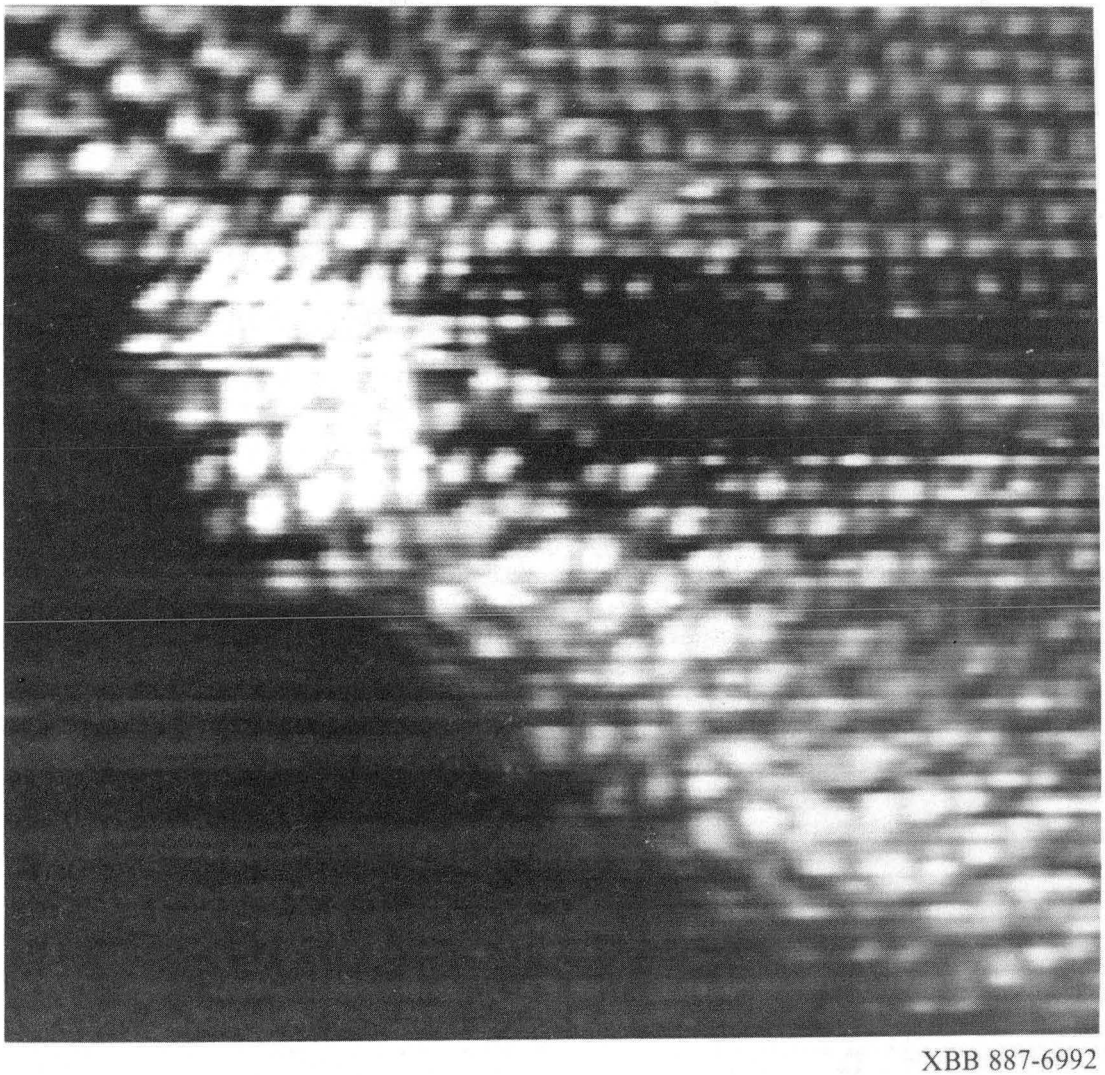

XBB 887-6992

Fig. 7-10 Current image of a 16 atom Al cluster at a step edge.

atomic structures and spacings of very small clusters on a substrate.

In summary, we have observed metal monomers, and clusters of two to four atoms adsorbed onto the basal plane of graphite substrates in UHV. These adatoms and small clusters were stable enough to be imaged reproducibly for periods of several seconds to many minutes. Single adatoms were only observed within 10 Å of an island: The fact that these single adatoms did not move is surprising, perhaps indicating bonding to defect sites or the stabilizing influence of the nearby island. The Ag and Al monomers were more usually observed at graphite β-sites, while the one Au monomer we observed was not. We observed clusters that were resolved into individual atoms usually above β-sites as well as compact clusters which were not atomically resolved. We conclude that for monomers and very small clusters, the effects of substrate-adsorbate interaction are important even for the relatively inert graphite substrate.

REFERENCES

1 F. Trager and G. zu Putlitz Eds: "Metal Clusters", (Springer Verlag, New York 1986).

2 S. Sugano, Y. Nishina, and S. Ohnishi Eds: "Microclusters" (Springer Verlag, New York 1986).

3 G. Apai, J.F. Hamilton, J. Stohr and A. Thompson, Phys. Rev. Lett. 43, 165 (1979).

4 M.G. Mason 1983, Phys. Rev. B27, 748 (1983).

5 M. de Crescenzi, P. Picozzi and S. Santucci, Surf. Sci. 156, 352 (1985).

6 P. Fayet, F. Granzer, G. Hegenbart, E. Moiser, B. Pischel and L. Woste, "Metal Clusters", p. 199 (Springer Verlag, New York 1986).

7 E. Ganz, K. Sattler and J. Clarke, J. Vac. Sci. Tech. A6, 419 (1988).

8 N. J. Ignatiev and A. Wu, Phys. Rev. B25, 2983 (1982).

9 J. J. Metois, J. C. Heyraud and Y. Takeda, Thin Solid Films 51, 105 (1978).

10 J. R. Arthur and A. Y. Cho, Surf. Sci. 36, 641 (1973).

11 P. Trucano and R. Chen, Nature 258, 137 (1975).

12 J. Tersoff and D. R. Hamann, Phys. Rev. Lett. 50, 25 (1983).

13 J. Tersoff and D. R. Hamann, Phys. Rev. B 31, 2 (1985).

14 J. Tersoff, Phys. Rev. Lett. 57, 440 (1986).

15 Y. Kuk, P. J. Silverman, and H. Q. Nguyen, J. Vac. Sci. Tech A6, 524 (1988).

16 J. C. Heyraud and J. J. Metois, Acta Metall. 28, 1789 (1980).

17 J. C. Heyraud and J. J. Metois, J. Crystal Growth 50, 571 (1980).

18 P. J. Feibelman, Phys: Rev. Lett. 58, 2766 (1987).

19 C. Kittel, "Introduction to Solid State Physics", 5th Ed., p. 32 (John Wiley and Sons, New York 1976).

20 W. Andreoni and J. L. Martins, Surf. Sci. 156, 635 (1985).

21 K.S. Krasnov *et al.*, Handbook of Molecular constants of Inorganic Compounds, (Israel program for scientific translations, Jerusalem 1970).

22 H.-W. Fink and G. Erlich, J. Chem. Phys. 81, 4657 (1984).

23 T.H. Upton, Phys. Rev. Lett. 56, 2168 (1986).

24 N. D. Lang, Phys. Rev. Lett. 56, 1164 (1986).

25 G. Doyen, D. Drakova, E. Kopatzki, and R. J. Behm, J. Vac. Sci. Tech. A6, 327 (1988).

26 H. J. Mamin, E. Ganz, D. W. Abraham, R. E. Thomson, and J. Clarke, Phys. Rev. B34, 9015 (1986).

27 R. J. Gooding, B. Joos and B. Bergersen, Phys. Rev. B27, 7669 (1983).

CHAPTER VIII

IMAGING OF SMALL TWO-DIMENSIONAL METAL ISLANDS ON GRAPHITE

Three-dimensional crystals of Ag or Au have a close-packed structure, namely face-centered cubic. However, very little is known about the structure of these metals in two dimensions or for small particles. In the case of small clusters, the electronic structure and chemical reactivity have been extensively studied, but the morphology has remained open to debate[1]. For systems containing only a few atoms, the local environment of each atom may be unique, and it is thus desirable to study these systems on an atomic scale, since the morphology forms the basis for predictions of the behavior of these systems. In this chapter, we will use the STM to observe the local atomic structure of small monolayer metal islands on highly oriented pyrolytic graphite. Islands form the first stage of the growth of metal films on graphite[2]. In striking contrast to the bulk case, we find the lattice to be rectangular, rather than close-packed.

The sample preparation technique was described in chapter VII. After depositing approximately 1% of a monolayer of Ag or Au. we find that most of the sample remains unadorned, with the metal adatoms distributed in small groups of flat islands. In this chapter we show a few representative examples of the large number of islands we have imaged.

Metois, Heyraud, and coworkers[3-7] have used transmission electron microscopy to study the morphology and distribution of gold islands formed by gold decoration of cleaved graphite. They followed the technique of Darby and Wayman[8], who found that the gold formed large

flat dendritic particles. Typically, before annealing, the islands studied were several thousands of angstroms across, yet only 20-40Å high, and were oriented with the (111) face against the substrate. The island shapes are kinetically determined, and depend on the deposition rate and substrate temperature[9]. Islands grown on room temperature substrates showed dendritic structure (see Figure 8-1), while those grown on substrates at 70° C were more nearly triangular[6]. By annealing the samples at successively higher temperatures, they were able to measure two-dimensional surface self-diffusion at the edges of these flat islands (Figure 8-1)[6,7]. At 500° C, the islands grew into round three-dimensional crystals (see Figure 8-2), and, after extensive annealing, they reached the equilibrium form: a hemispherical cap with flat facets. By measuring the equilibrium contact angle between the Au island and the graphite substrate, they estimated the Au-C interaction energy at 0.26 eV per Au atom[4,5].

Figure 8-3 shows two consecutive 35 Å X 35 Å current images of a small Ag island. The island is quite disordered, with just a few areas where the silver atoms form roughly rectangular arrays. Two 3 X 3 arrays are visible with lattice spacings of (2.41 ± 0.1) Å X (3.36 ± 0.1) Å and (2.58 ± 0.1) Å X (3.12 ± 0.1) Å. These arrays are neither commensurate with nor aligned with the substrate lattice.

The atoms in Figure 8-3 are imaged as individual spots with unique shapes that remain constant from image to image. The spot shape may be due to variations in the local electronic structure, which presumably depends on the local environment. It is also possible that vibration of a Ag atom about its equilibrium position produces an asymmetric shape. It is known that surface atoms have larger vibrational

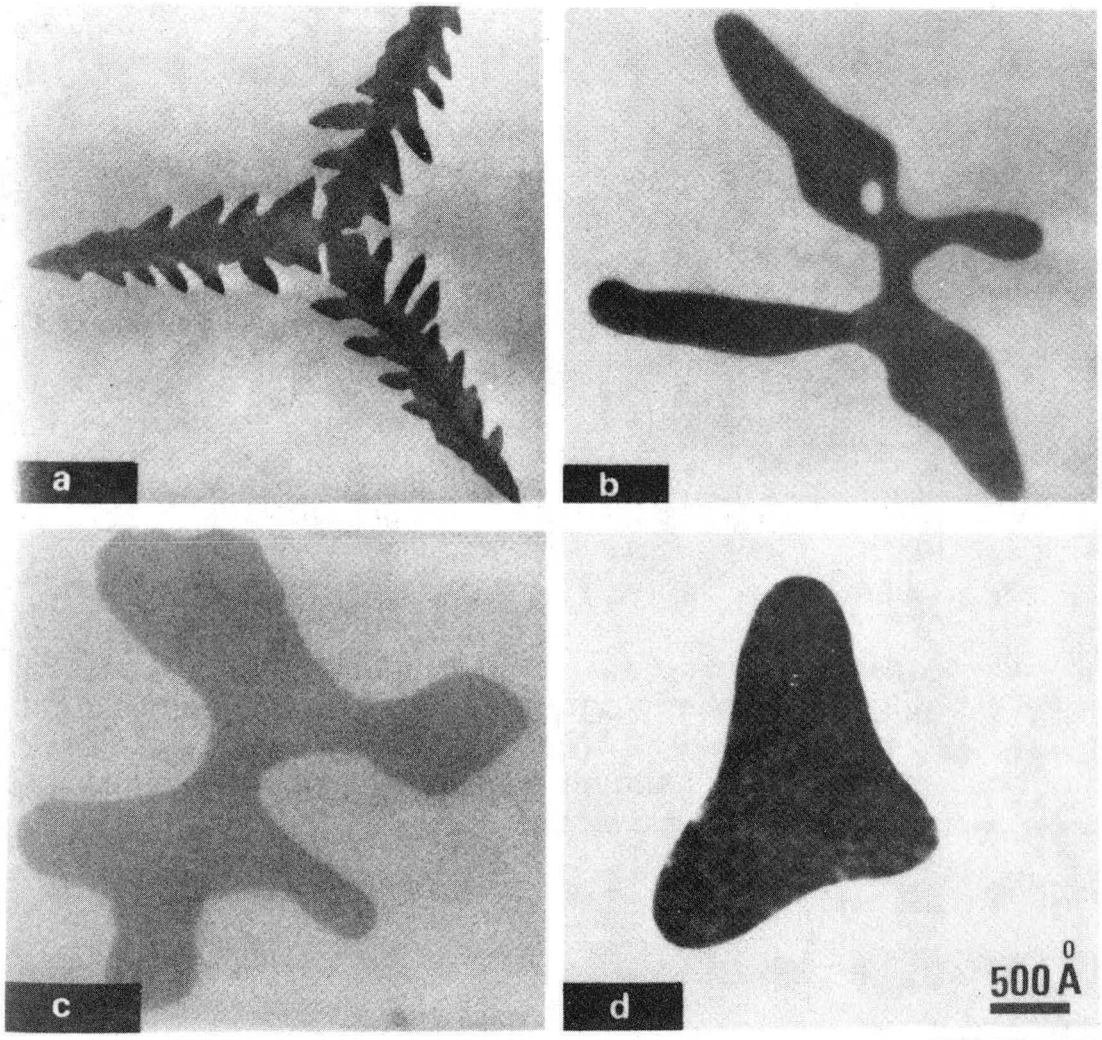

ZBB 888-7487

Fig. 8-1 TEM micrographs of the evolution of Au crystallites on graphite after heating in UHV. (a) Dendritic crystal obtained by deposition of Au on graphite at room temperature. Typical crystallites after heating for 1 h at (b) 100° C, (c) 200° C, and (d) 350° C. (Reproduced from ref. 6 courtesy of J.J. Metois and North-Holland Physics Publishing, Amsterdam, The Netherlands)

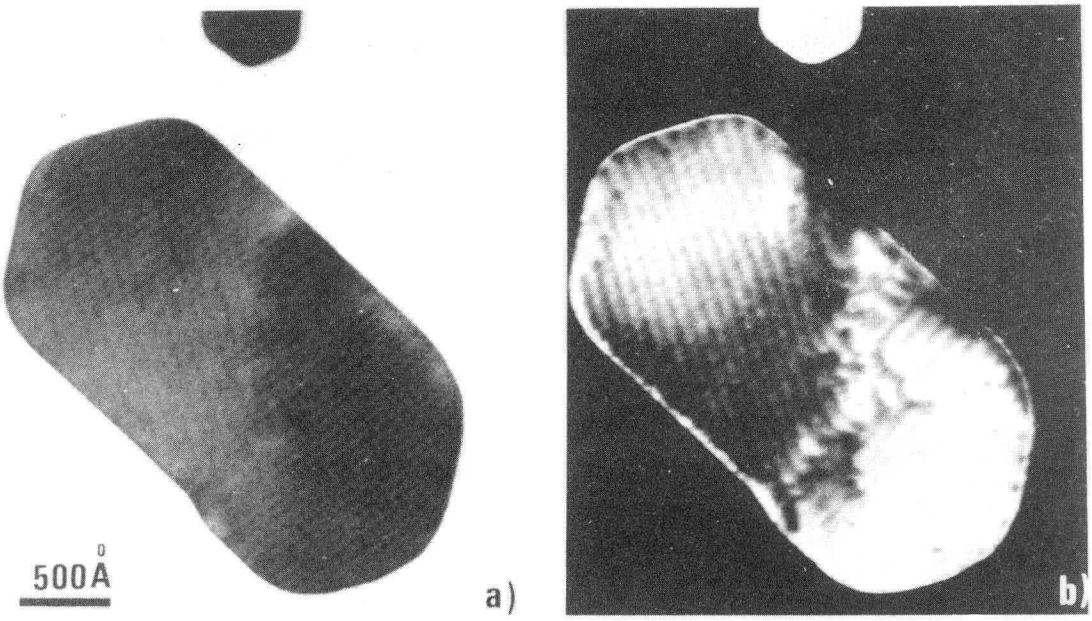

ZBB 888 7488

Fig. 8-2 TEM micrographs of Au crystallite on graphite after heating 500° C. (Reproduced from ref. 7 courtesy of J.J. Metois and permission of Elsevier Sequoia S.A., Lausanne 1, Switzerland)

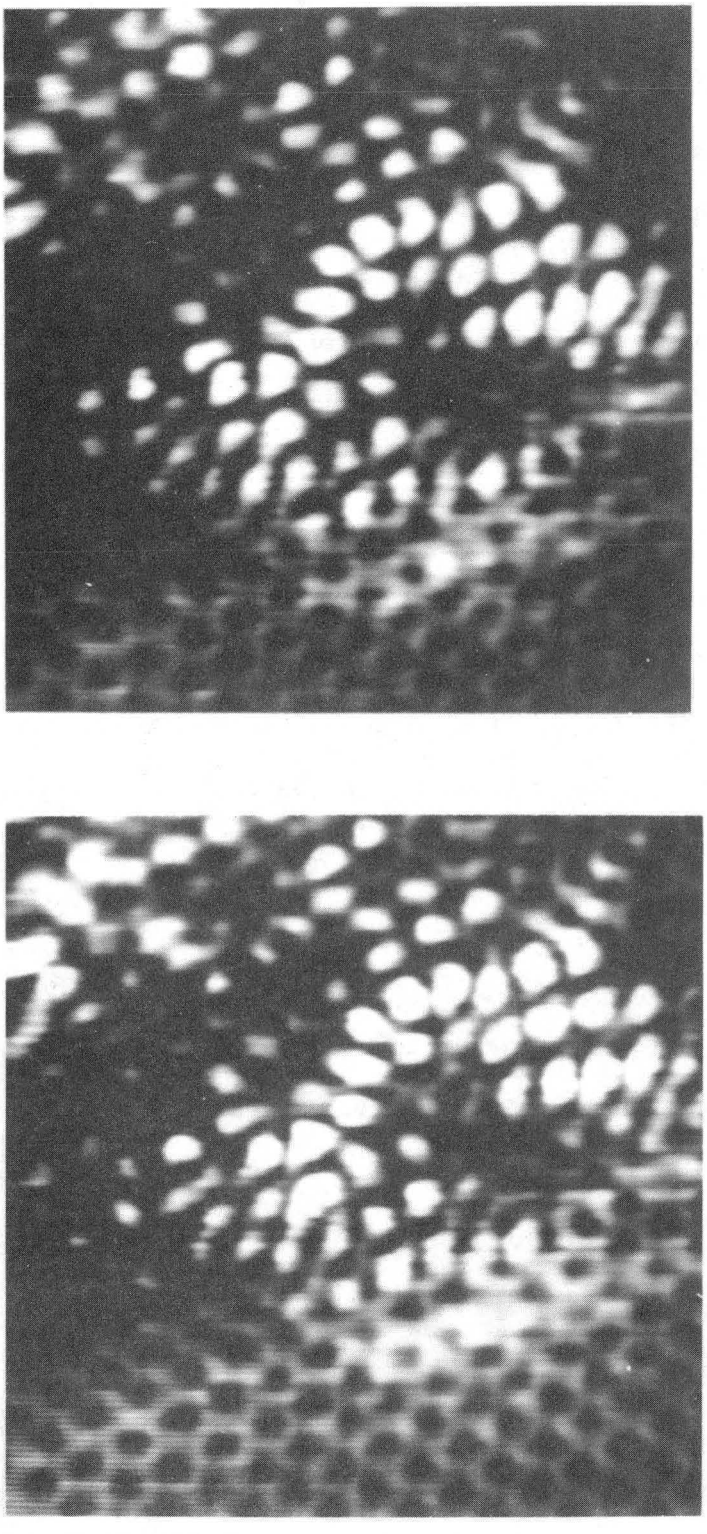

Fig. 8-3 Two consecutive 35 Å X 35 Å current images of a small disordered Ag island on graphite.

XBB 877 5738

amplitudes than in the bulk[10], and presumably the atoms in a loosely bound two dimensional overlayer would also have large vibrational amplitudes.

Figure 8-4 shows two subsequent 35 Å X 35 Å current images of part of a 40 Å diameter monolayer Ag island. In Figure 8-5 we show a projected view, and in Figure 8-6 a lightsourced image of the same data. In Figure 8-7 we show a computer model (see chapter II for a description of model construction). In the model, we have outlined two rectangular lattices. These lattices are neither commensurate with the substrate, nor close-packed. A grain boundary is visible in the center of the island. The shapes of the atoms at the boundary are unusual, and were reproduced from image to image. At the top right of the image, we observe a buckling of the chains of silver atoms in the rectangular array to form a six-fold ring. We have observed similar rings in other islands.

Within this one island there are several ordered regions each with its own lattice parameter. By averaging measurements from four images, we find the rectangular lattice parameters are (2.58$\pm$0.06) Å X (3.33$\pm$0.1) Å on the left, and (2.44$\pm$0.08) Å X (3.37$\pm$0.1) Å on the right. In subsequent images of the same island, a third ordered region was also observed with an almost square lattice (2.72$\pm$0.06) Å X (2.79$\pm$0.08) Å.

The morphology of the Ag islands was very stable. In Figure 8-3, the positions of the atoms are basically unchanged in the four seconds between the images. The island of Figure 8-4 was observed for several minutes. Again, no significant changes were observed in the positions of the individual atoms. This suggests that the atoms are pinned to

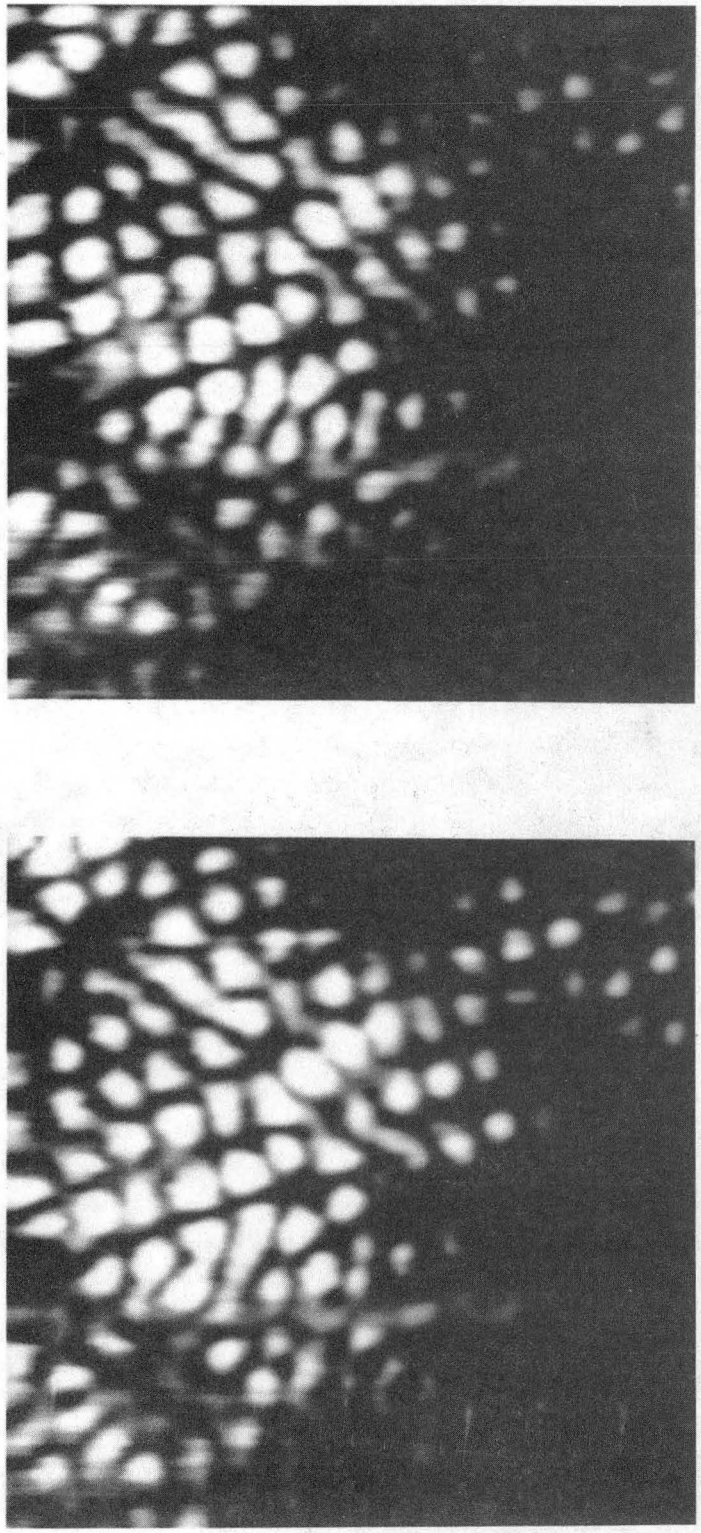

Fig. 8-4 Two consecutive 35 Å X 35 Å current images of part of a monolayer Ag island on graphite.

XBB 877 5739

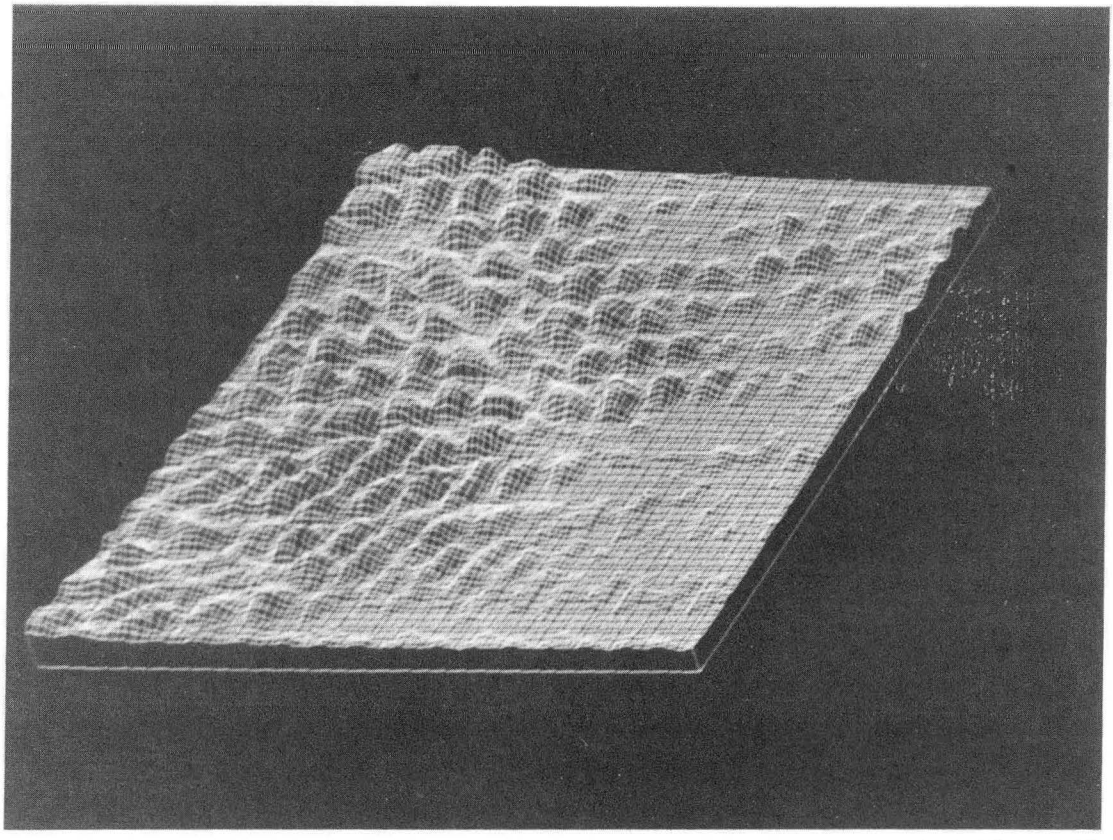

CBB 885-4489

Fig. 8-5 Projected line plot of Fig. 8-4.

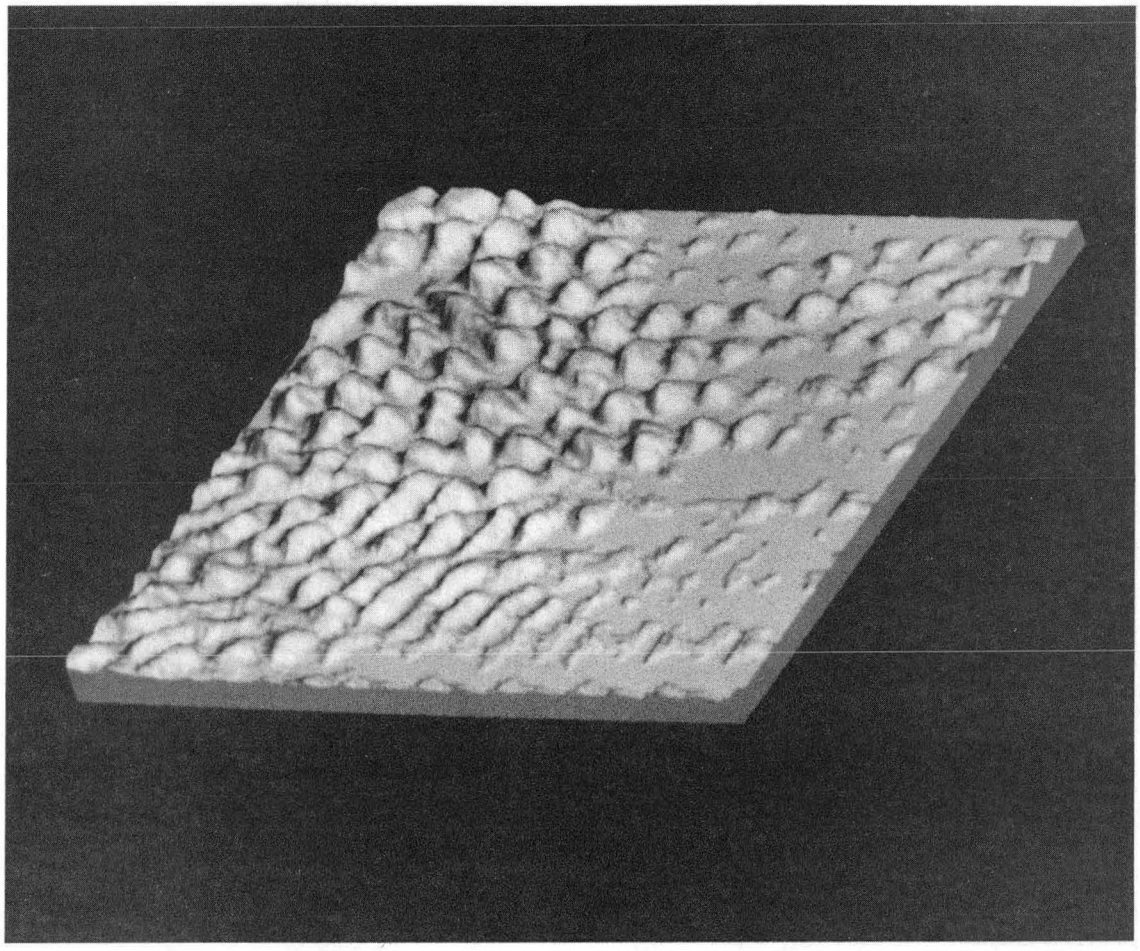

XBB 883 2220

Fig. 8-6 Projected, illuminated image of Fig. 8-4 (arbitrary height).

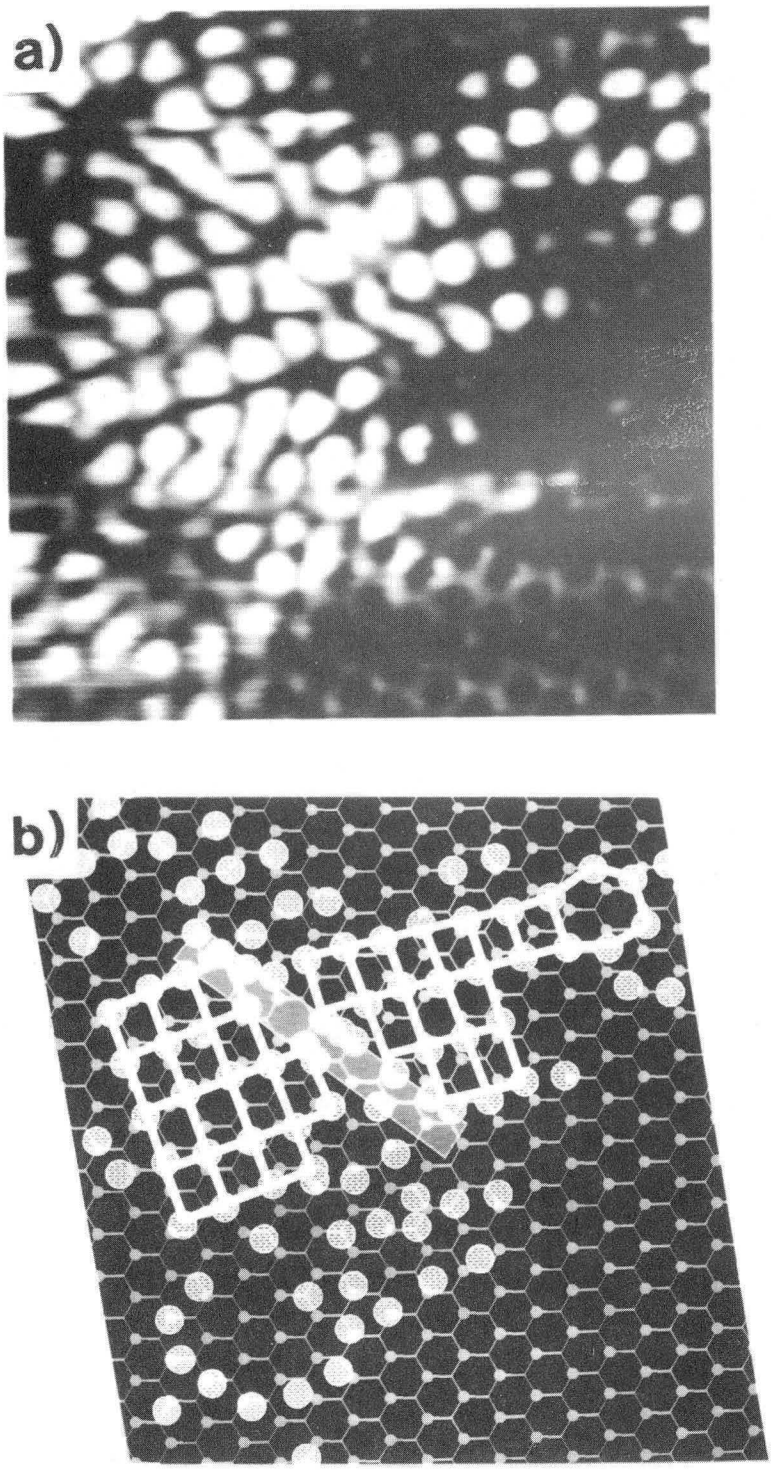

Fig. 8-7 (a) 35 Å X 35 Å current image part of a monolayer Ag island as in Fig. 8-4. The graphite honeycomb lattice is visible at the lower right. (b) Computer model showing the positions of the adatoms (filled circles) on the graphite honeycomb lattice (small dots are at ß-sites). Lines have been drawn to guide the eye. XBB 870-8305

the substrate; otherwise we would expect surface self-diffusion to produce a smooth surface. Drechsler, Metois, and Heyraud[6] have measured the self-diffusion in large gold islands on graphite at elevated temperatures (370K to 700K). With the diffusion constant $D = D_0\, e^{-(\Delta E_s/k_B T)}$, they find $\Delta E_s = 0.34$ eV/atom and $D_0 = 5 \times 10^{-9}$ cm^2/s. If we use these values at room temperature we obtain $D = 6\times10^{-15}$ cm^2/s. This value is large enough to quickly anneal out disorder in our small islands. Thus we conclude that for small Ag islands, the substrate interaction pins the atoms, thus maintaining disorder.

In contrast to the general disorder of the small island in Figure 8-3, atoms in the interior of the larger island of Figure 8-7 form ordered, incommensurate structures suggesting that when the atoms have more nearest neighbors, the Ag-Ag interaction is dominant. Furthermore, as the Ag atoms bind to other Ag atoms, the interaction with the substrate is reduced due to rebonding effects[11].

A portion of a gold island (region A) is shown in Figure 8-8. In the interior of the island, there are two domains, each with its own ordered structure: On the left we observe a rectangular lattice with spacings of (2.47±0.06) Å X (3.9±0.1) Å, and on the right a honeycomb lattice. The whole island is rotated by 3.4 ± 1.4° relative to the substrate.

Figure 8-9 shows three current images from a different part of the same island (region B). The lattice spacings were roughly (2.35±0.1) Å X (3.5±0.1) Å for these images. The island shows both chain-like structures as well as buckled chains (which approach a honeycomb pattern). Figure 8-9(a) shows chains of atoms. On the right

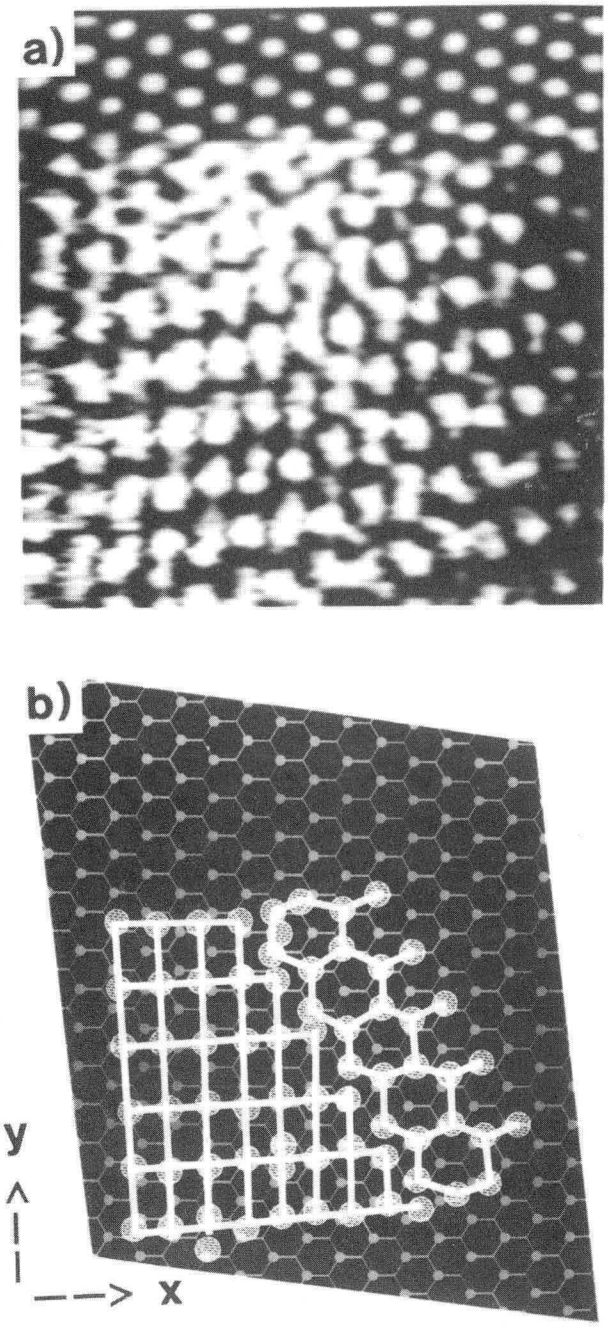

Fig. 8-8 (a) 35 Å X 35 Å current image of region A of a monolayer Au island on graphite. The graphite is imaged as dots at the top of the image. (b) Computer model showing a rectangular lattice on the left, and a honeycomb lattice on the right.

XBB 870-8307

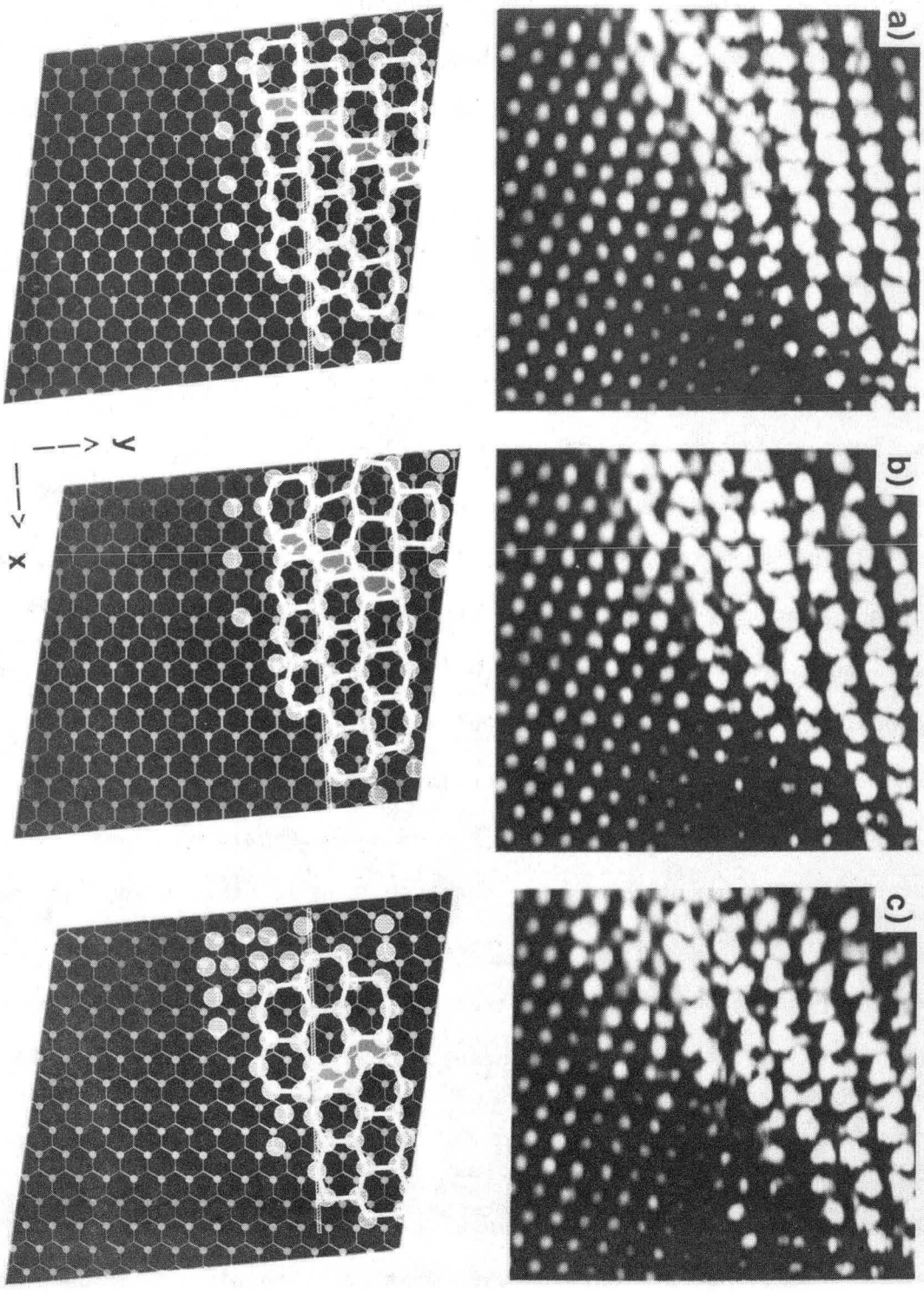

Fig. 8-9 (a) 35 Å X 35 Å current image of another region, B, of the same Au island as in Fig. 8-8 with an image taken (b) 4 sec later, and (c) another image from the same series.

XBB 870-8306

hand side of the image, the chains are buckled forming a honeycomb pattern. In Figure 8-9(b) we see a boundary between buckled down (relative to the dashed line) on the left, and buckled up on the right. In Figure 8-9(c), the boundary runs in a different direction, and so has a different shape. Excess spots visible in the interior of the island are presumably β-sites of the graphite substrate visible through holes in the Au overlayer.

The nearest neighbor spacings observed along the chains of Figures 8-8 and 8-9(a) (2.35 ± 0.1 Å and 2.47 ± 0.06 Å) are surprisingly small. Now, one would certainly expect these values to be smaller than in the bulk: As the dimensionality of a crystal structure is reduced from three-dimensional to two-dimensional to one-dimensional, the bond length is decreased as the number of nearest neighbors is reduced[12], for example, from 2.88 Å for bulk Au[13] to 2.47 Å for a dimer[14]. With appropriate parameters, the model of Tomanek *et al.*[12] gives rough estimates of 2.55 Å for a one-dimensional chain, with two nearest neighbors, and 2.75 Å for a close packed two-dimensional layer with six nearest neighbors. However, the observed bond lengths in the chains are equal to or somewhat smaller than the dimer length, definitely less than the prediction for a one-dimensional chain. This reduction in bond length may arise from the interaction with the substrate.

Neither the Ag nor Au islands exhibit the close packed structure observed in larger and thicker films[2]. We would expect the ground state of an infinite, two-dimensional film to be close-packed in the absence of any interaction with the substrate. Possibly, the observed rectangular structures represent thermal excitations from this ground state. Alternatively, since the islands are rather small in extent,

the effects of surface tension may be important. Yet another possibility is that the rectangular structures arise from the interaction between the adatoms and the substrate, which, while weak, is non-zero. Our images confirm that the interaction is small since the island structures are neither commensurate with nor aligned with the substrate lattice. One can hope to resolve these issues only with a detailed model calculation and further experimental work.

In summary, we have imaged small two-dimensional metal islands atom by atom. We observe a mixture of order and disorder, with rectangular lattice structures in the interiors of the islands, and disorder at the peripheries. We observe grain boundaries in these islands. Finally, the shape of the individual atoms is unique and reproducible, perhaps due to atomic vibration, or alternatively to variations in the local electronic structure of the island.

REFERENCES

1 F. Trager and G. zu Putlitz Eds: "Metal Clusters", (Springer Verlag, New York 1986).

2 R. Kern, J. J. Metois and G. LeLay, Curr. Top. Mater. Sci. 3, 131 (1979).

3 J. J. Metois, J. C. Heyraud and Y. Takeda, Thin Solid Films 51, 105 (1978).

4 J. C. Heyraud and J. J. Metois, Acta Metall. 28, 1789 (1980).

5 J. C. Heyraud and J. J. Metois, J. Crystal Growth 50, 571 (1980).

6 M. Dreschler, J.J. Metois, and J.C. Heyraud, Surf. Sci. 108, 549 (1981).

7 J. J. Metois & J. C. Heyraud, Thin Solid Films 75, 1 (1981).

8 T. P. Darby and C. M. Wayman, J. Crystal Growth 29, 98 (1975).

9 J. M. Bermond and J. A. Venables, J. Crystal Growth 64, 239 (1983).

10 M. de Crescenzi, P. Picozzi, S. Santucci, C. Battistoni, and G. Mattogno, Surf. Sci 156, 352 (1985).

11 P. J. Feibelman, Phys. Rev. Lett. 58, 2766 (1987).

12 D. Tomanek, S. Mukherjee, and K.H. Bennemann, Phys. Rev. B 28, 665 (1983).

13 C. Kittel, "Introduction to Solid State Physics", 5th Ed., p. 32 (John Wiley and Sons, New York 1976).

14 K.S. Krasnov *et al.*, Handbook of Molecular constants of Inorganic Compounds, (Israel program for scientific translations, Jerusalem 1970).

CHAPTER IX

IMAGING OF THREE-DIMENSIONAL METAL ISLANDS ON GRAPHITE

There has been extensive transmission electron microscopy (TEM) work on the morphology and properties of small three dimensional particles on weakly interacting substrates[1,2,3]. TEM is a very powerful and versatile technique, but the STM may prove less intrusive, and should provide better surface sensitivity. In this chapter we present preliminary results for several large particles that we have imaged using the STM.

In Fig 9-1(a) we show a 39 Å X 39 Å current image of a Ag island on graphite. The atoms are not quite resolved, but we can see that the island is disordered. We note that it is relatively difficult to study disordered systems with the STM, because of multiple tip effects and the relatively unknown instrumental resolution. The island in Figure 9-1(a) is quite flat: just one or two atoms thick. It has a dendritic shape, reminiscent of the shapes produced by diffusion limited aggregation[4] [the island of Figure 8-1(a) is also dendritic, but on a larger scale]. In fact, we might expect that this island grew by diffusion limited aggregation (as impinging atoms were captured by the growing island), but it is surprising that self-diffusion did not rearrange the atoms to provide a more compact final form. Thus, the extended profile of the island already suggests that the atoms are pinned to the substrate. Further evidence for this is provided by the fact that during an observation period of 5 minutes, no changes in the atomic features of the island were seen.

To image larger islands, we must use the topographic imaging

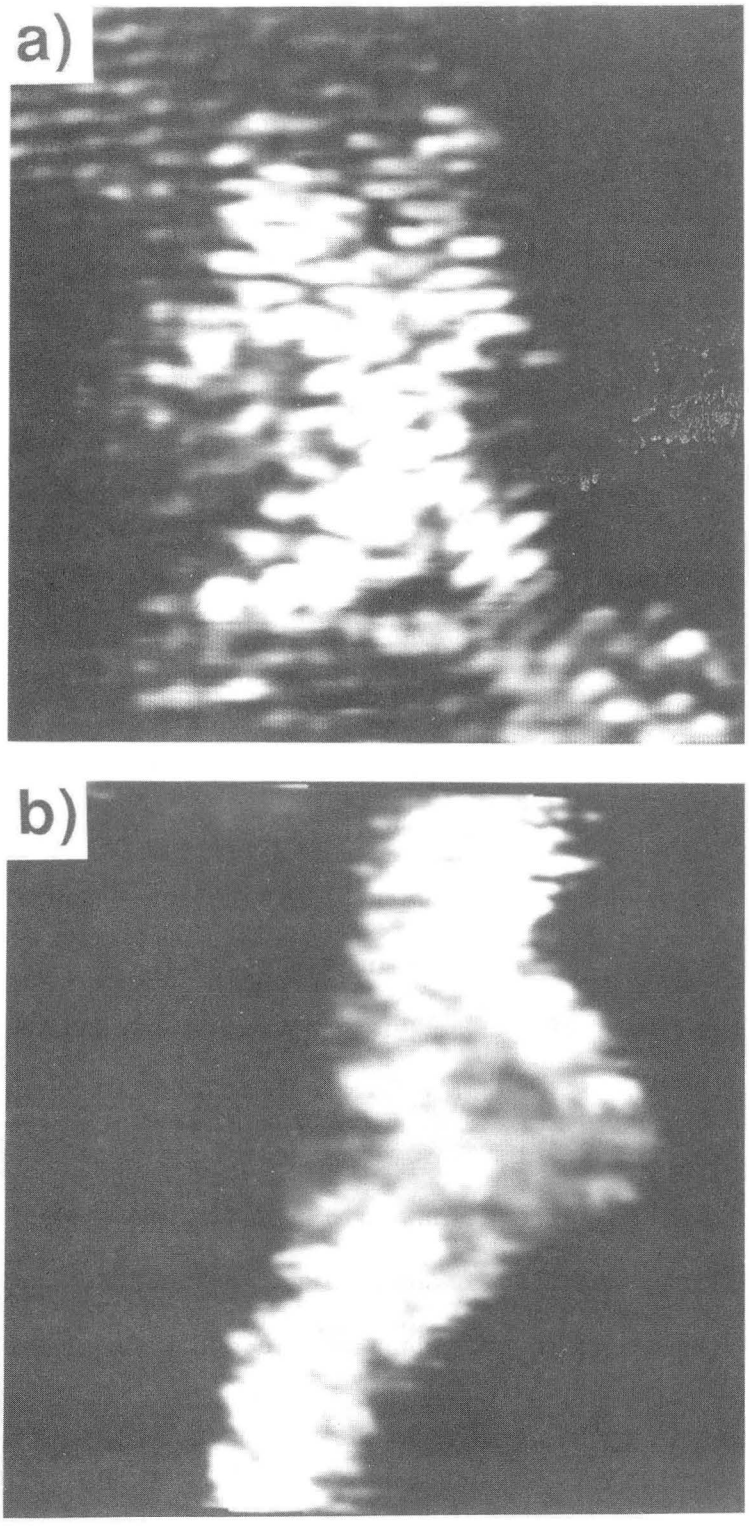

Fig. 9-1 (a) 39 Å X 39 Å current image, and (b) 32 Å X 32 Å topographic image of disordered Ag islands on graphite. XBB 886-6542A

mode. In Figure 9-1(b) we show a 32 Å X 32 Å topographic image of a Ag island. Atomic features are visible at the top of the island. The island is at least two layers thick. The shape of the island and the positions of the visible atoms remained constant during the 30 sec observation period.

Figure 9-2 shows three consecutive topographic images of a 160 Å X 70 Å X 25 Å Cu island. The island is roughly rectangular, and thus is probably a small crystal of Cu. Unfortunately, the individual Cu atoms are not resolved. In Figure 9-2(b), however, a small 15 Å diameter cluster has appeared on top of the crystal. The small feature at the bottom left of the image is probably a second image of the same cluster due to a second effective tunneling tip. The cluster is not visible in Figures 9-2(a) or 9-2(c), images made 8 seconds before and after Figure 9-2(b). A lightsourced, rendered, image of Figure 9-2(b) is shown in Figure 9-3. Similar small crystallite shapes have been observed with TEM when the substrate was heated during the deposition[3,5] (see Figure 8-2). A current image of this same crystal is shown in Figure 9-4. We see that the tip crashes into the cyrstal, giving a very distorted image. Thus, the topographic mode is necessary to image large three-dimensional islands.

In Figure 9-5(a) we show a topographic image of several Cu clusters at a graphite step edge or grain boundary. Either mobile clusters have been captured at this boundary, or else these clusters nucleated and grew at the boundary. The step height is 10 Å, and the clusters are seen to straddle the step. This contrasts with the similar case of Au clusters on alkali halides, where the clusters are observed to sit on the top of the step in order to minimize the elastic

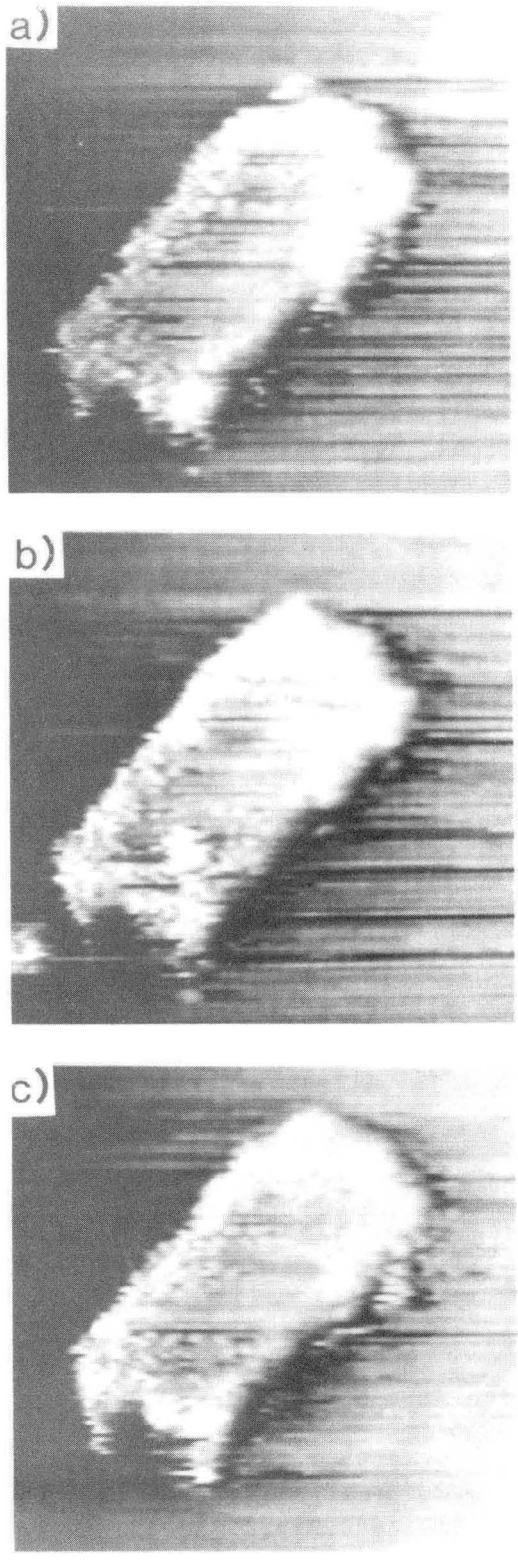

Fig. 9-2 (a), (b), and (c) 3 consecutive 220 Å X 220 Å topographic images of a 170 Å X 60 Å Cu crystal. In (b), a 15 Å diameter cluster is visible on top of the island. XBB 883-2223A

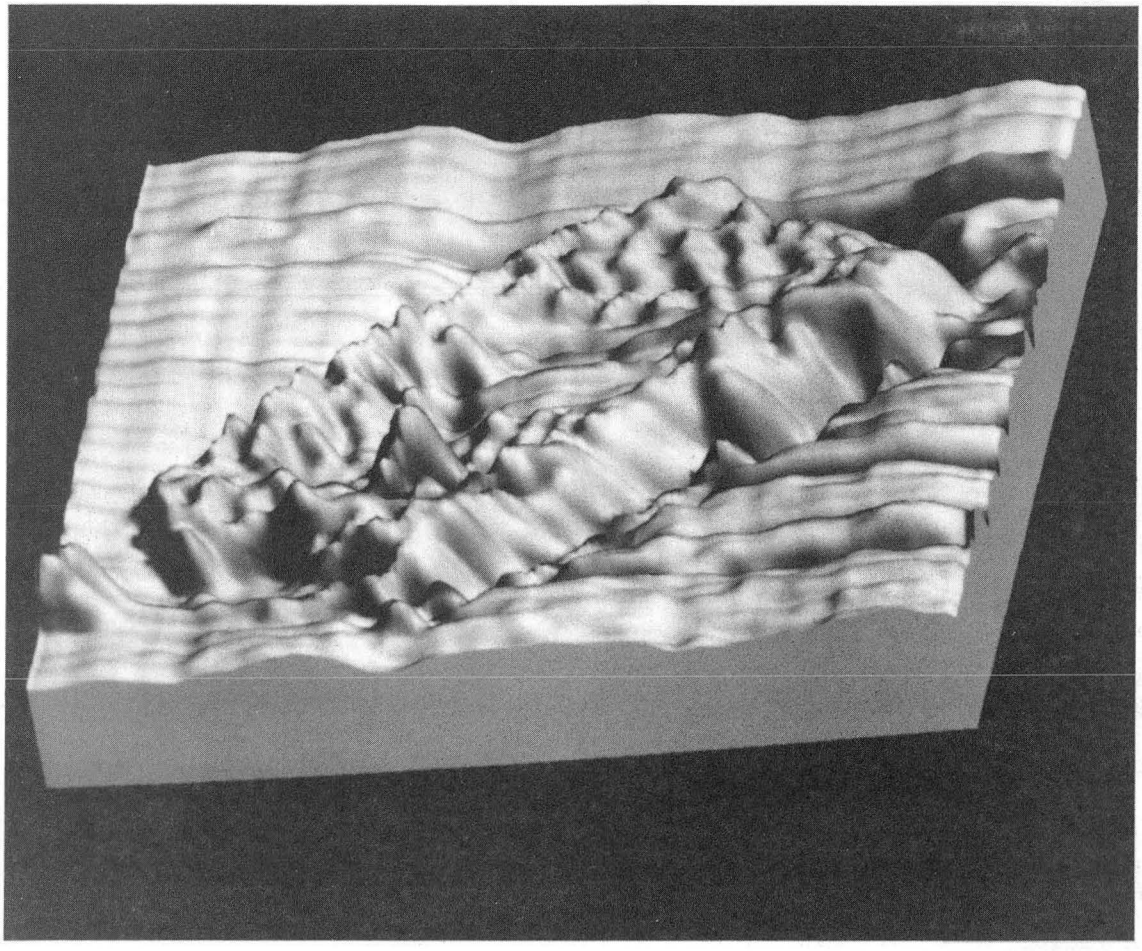

XBB 883-2219

Fig. 9-3 Projected, illuminated image of the Cu crystal of Fig. 9-2(b).

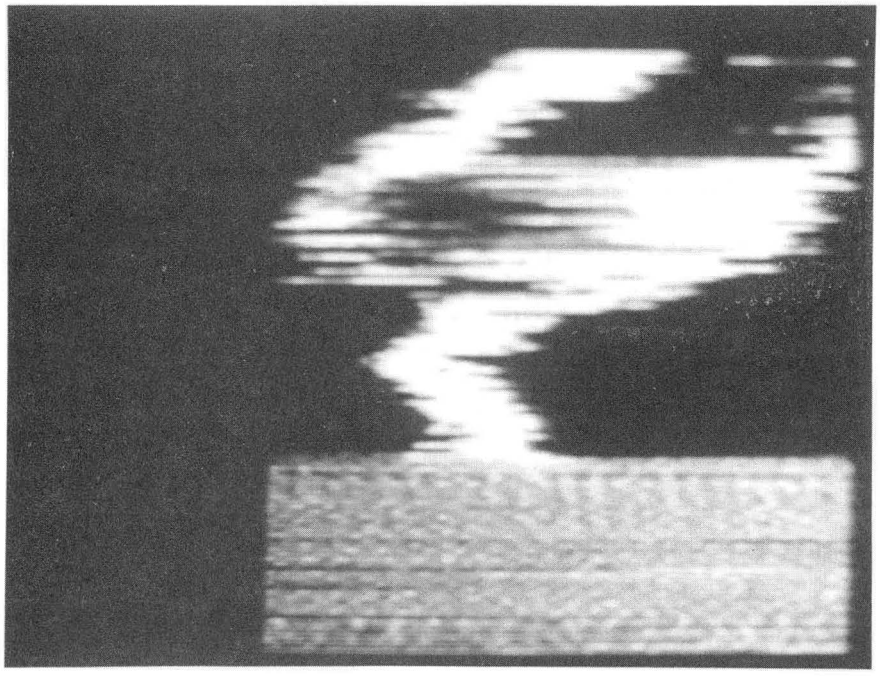

XBB 883-2226

Fig. 9-4 Current image of the Cu crystal.

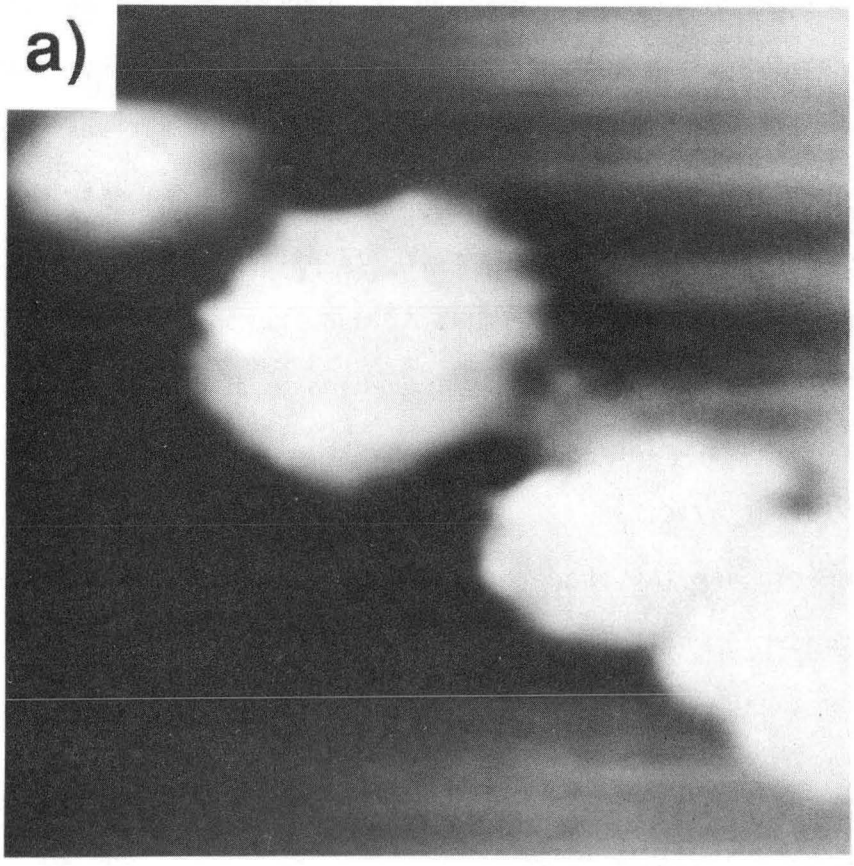

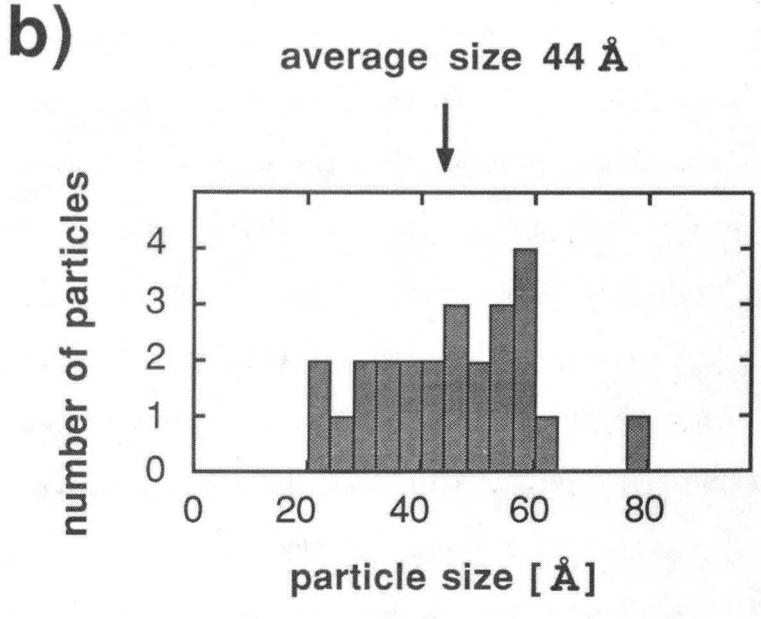

Fig. 9-5 (a) 208 Å X 208 Å topographic image of several Cu clusters at a grain boundary. (b) Size distribution of the Cu clusters. XBB 886-5520A

stress between the substrate and the deposit[5]. The rest of the substrate was found to be clean. We followed this boundary for 5000 Å: The boundary changed direction by 120° three times, and the entire length showed attached clusters. We measured the size of 25 clusters, and plot the histogram of cluster diameters in Figure 9-5(b). We see that the average diameter is 44 Å, and the observed sizes range from 20 Å up to 80 Å. We do not have enough data to determine whether the cluster distribution follows a log-normal distribution as predicted by Granqvist *et al.*[3].

We can see the shape of the particles in Figure 9-6(a), where we have rendered the data. If we look at the particles from a lower viewing angle (Figure 9-6(b)), we can see the gaps between the particles. This reveals the shape of the tip, since the tip must fit down into the gap between two neighboring particles. We caution that deformation of the graphite may amplify the observed height scale by up to a factor of two[6]. The particles are roughly spherical, but, as shown in Figure 9-7, the lower sections of the particles are obscured because the scanning tip is imaging the particles from above. We see that there are several atomic-like features, but the atomic structure of the particles is not resolved.

Figure 9-8 shows a rather unusual feature. At first view, it looks like a sliver of material (it was seen during a Ag run). But on closer inspection [Figure 9-8(b)], we observe a graphite honeycomb with a 2.46 Å periodicity. This suggests that this was a small piece of graphite fiber that was somehow unintentionally deposited onto the substrate.

If we deposit significantly more material onto the surface, we

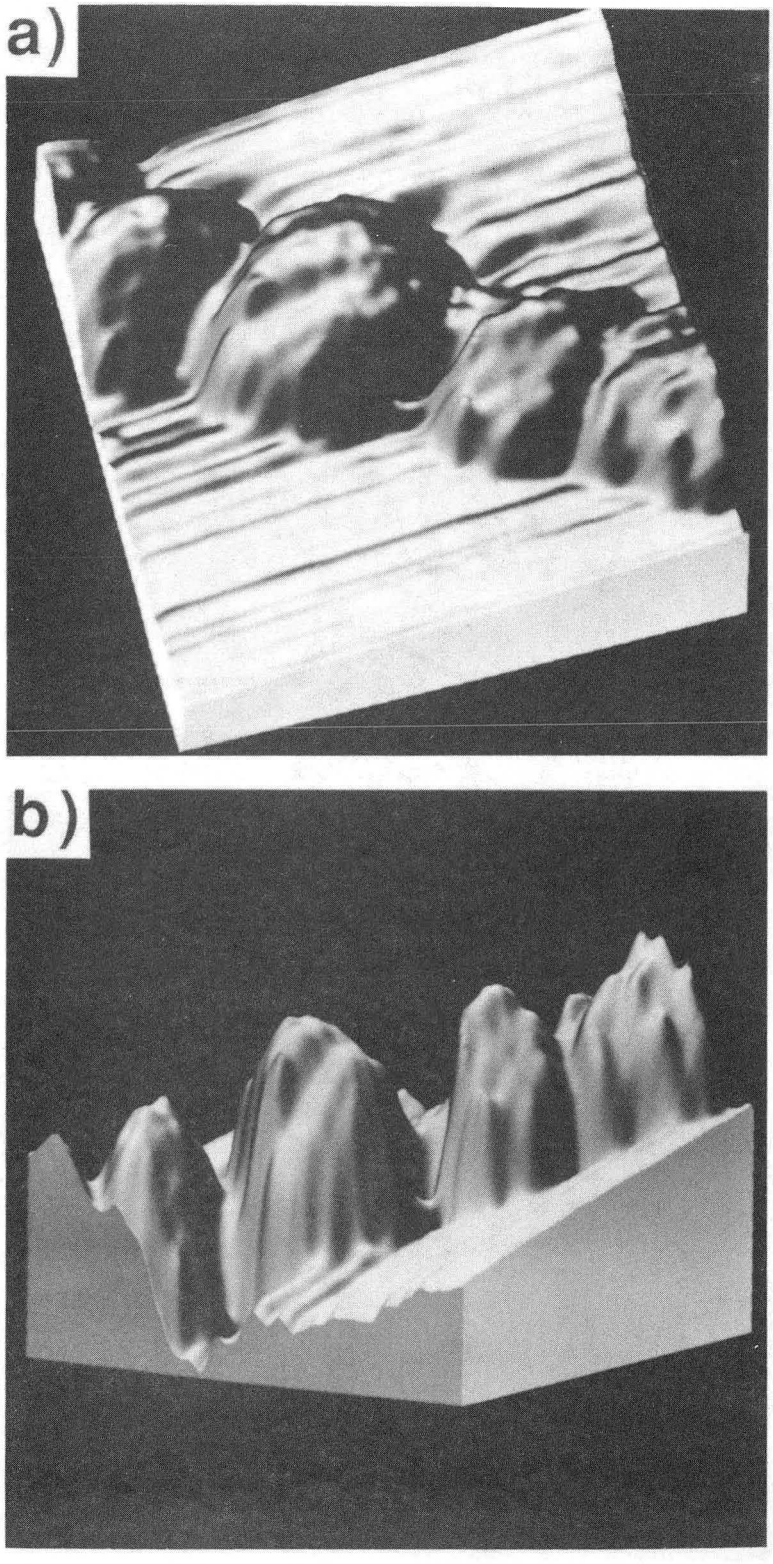

Fig. 9-6 (a) and (b) projected, illuminated views of Fig. 9-5(a).

XBB 886-5521A

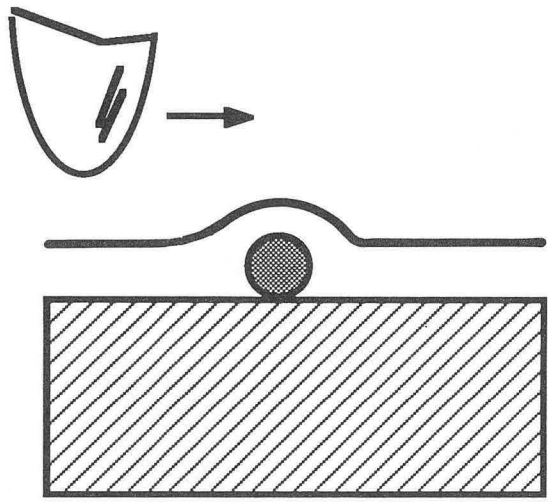

Fig. 9-7 In the topographical imaging mode, as the tip passes over a cluster, the fact that the tip has a non-zero width produces an apparent 'skirt' around the base of the cluster.

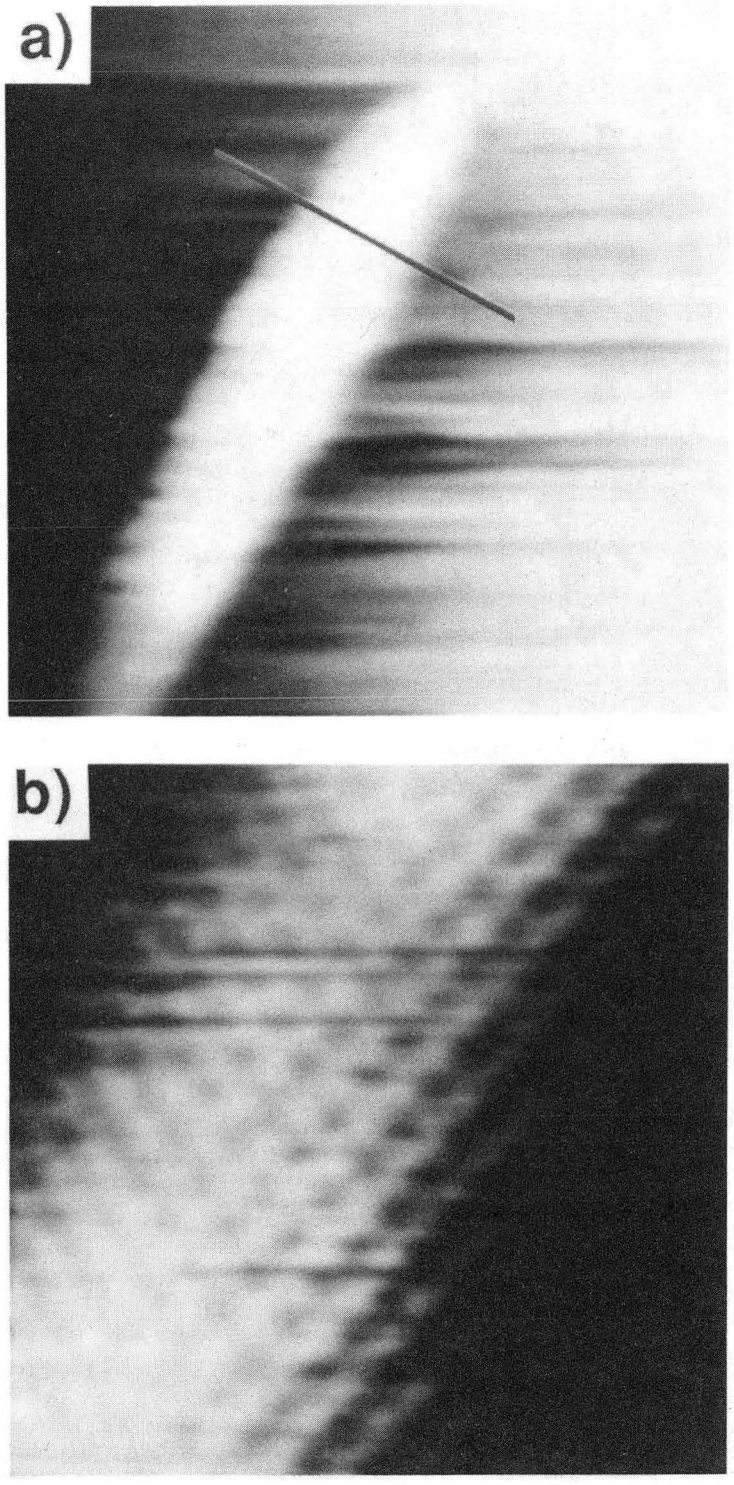

Fig. 9-8 (a) 230 Å X 295 Å topographic image showing a small sliver of material. On closer inspection, this 34 Å X 44 Å topographic image shows a graphite honeycomb structure.

XBB 886-5529A

will cover it with a thin film of metal. Chidsey *et al.*[7] have recently published an STM study of the morphology of gold films on mica under various deposition conditions. They observe granular films on room temperature deposits, with larger crystallites in the films deposited at elevated temperatures.

Figure 9-9 shows a 260 Å X 260 Å topographic image of a thin film of Cu on graphite. Here we observe a very large feature as well as several smaller ones. Figure 9-10(a) shows a topographic image of a thin film of Ag on graphite. The image is 360 Å X 360 Å, and we see that the film is quite granular and rather loosely packed. The grains are roughly 30 to 50 Å in diameter, as are the gaps between the grains. The rendered image of Figure 9-10(b) shows that the tip is not able to probe much below the top of the film. Figure 9-10(c) shows a 260 Å X 260 Å topographic image of a different region from the same Cu thin film in Figure 9-9. Again, this film is quite granular, with particle diameters ranging from 10 to 35 Å.

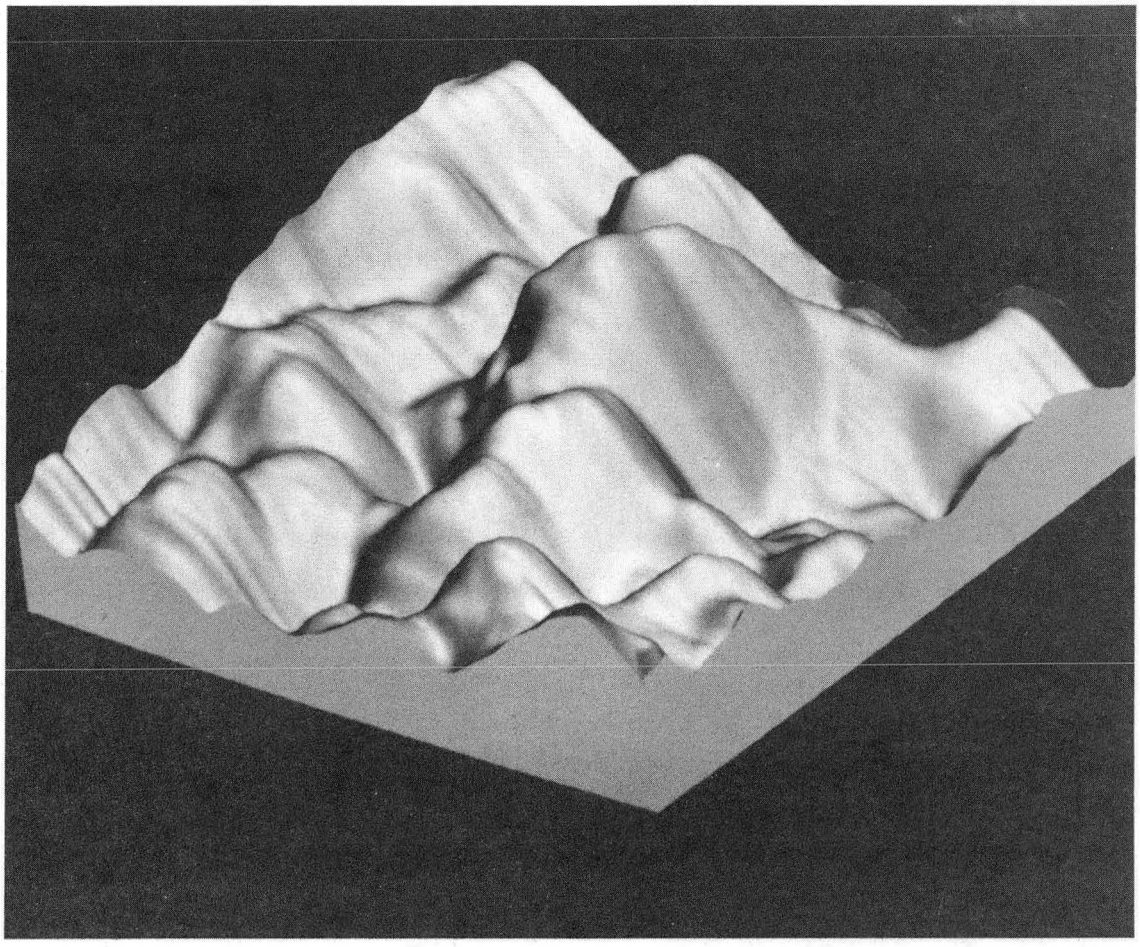

Fig. 9-9 (a) 260 Å X 260 Å topographic image of a thin Cu film on graphite. XBB 883-2218

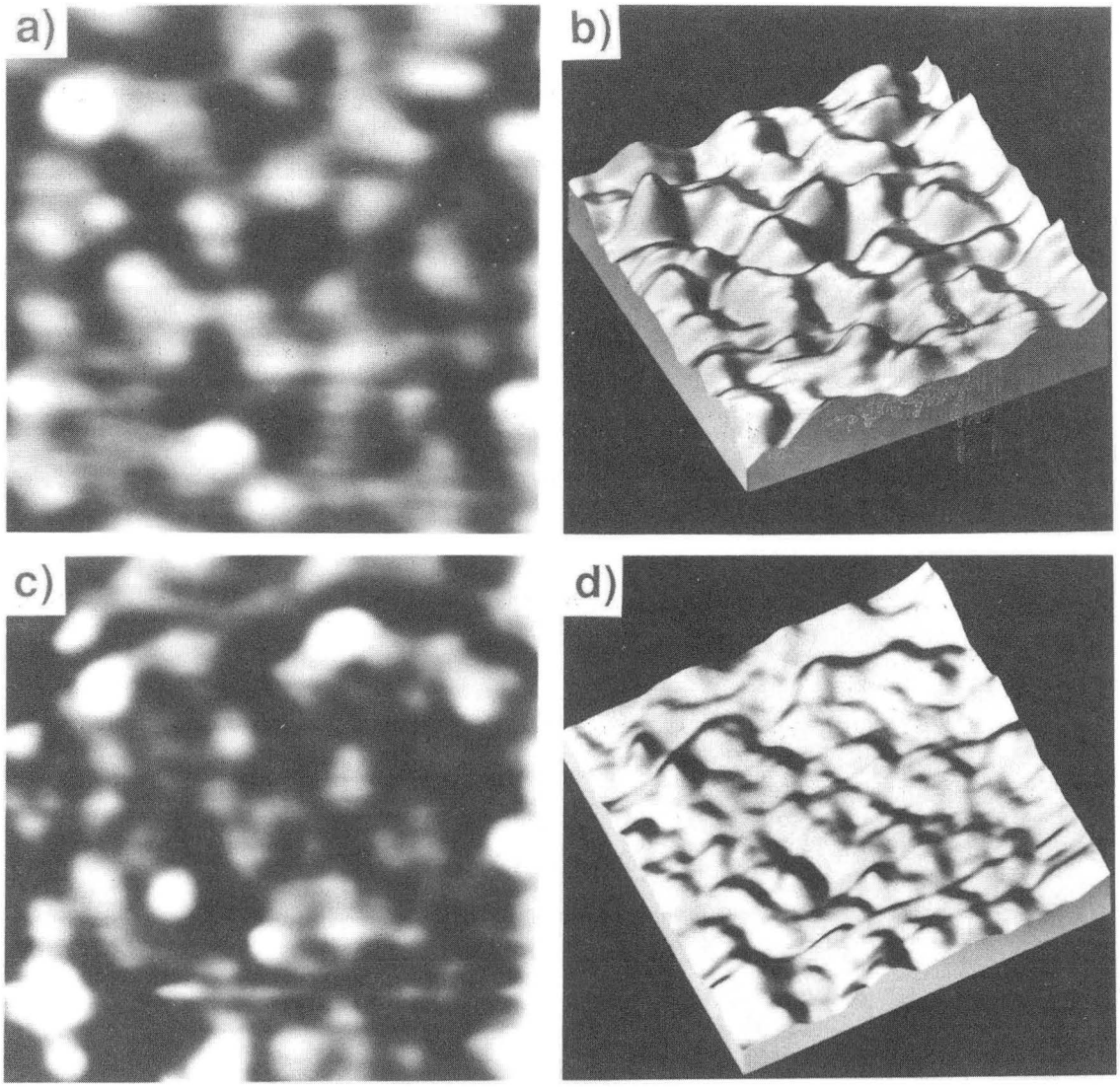

Fig. 9-10 (a) 360 Å X 360 Å top view, and (b) projected, illuminated view of a granular Ag film on graphite. (c) 260 Å X 260 Å top view, and (d) projected, illuminated view of a granular Cu film on graphite.

XBB 886-5698A

REFERENCES

1 M. J. Yacaman, K. Heinemann, and H. Poppa, Chem. and Phys. of Sol. Surf. p. 109, Vanselow and England, Eds. (CRC Press, 1982).

2 L. R. Wallenberg, J.-O. Bovin, and G. Schmid, Surf. Sci. 156, 256 (1985).

3 C. G. Granqvist and R. A. Buhrman, J. Appl. Phys. 47, 2200 (1976).

4 T. Vicsek and F. Family, Phys. Rev. Lett. 52, 1669 (1984).

5 R. Kern, J. J. Metois and G. LeLay, Curr. Top. Mater. Sci. 3, 131 (1979).

6 H. J. Mamin, E. Ganz, D. W. Abraham, R. E. Thomson, and J. Clarke, Phys. Rev. B 34, 9015 (1986).

7 C. E. D. Chidsey, D. N. Loiacono, T. Sleator, and S. Nakahara, Surf. Sci. 200, 45 (1988).

CHAPTER X

DYNAMICS

a) TIME EVOLUTION OF THE STRUCTURE OF ISLANDS

In dynamic systems, processes with time scales of seconds or minutes are most appropriate for study with the STM. In chapter III we discussed our experiments using the scanning tip to make small indentations in gold substrates[1]. We were able to observe a healing effect due to self-diffusion with a time scale of minutes. Recently, this method was extended and refined by Jaklevic and Elie[2] who carefully studied the healing of flat gold substrates over periods of hours. We also were able to deposit small mounds of Au onto the substrate by bringing the tip close to the surface[1]. These mounds were observed to flatten and widen over periods of minutes. A reliable technique for the deposition of small gold mounds in grease on flat gold substrates has been developed by Schneir *et al.*[3] who observed changes in an island over a period of 26 hours. Other STM work on dynamics includes the motion of O_2 on Ni[4] (using noise spikes to identify passing O_2 molecules), changes in the surface of Si in air[5], chemical reactions on Ni[6], and atomic modification of a Ge surface[7].

We have observed two examples of contraction in Au islands. In Figure 10-1 we show three 40 Å X 40 Å current images of a small gold island. The images were obtained at twenty second intervals, and chronicle the contraction of the island. The island remains roughly 25 Å long in the Y direction, while shrinking from 20 Å to 17 Å to 14 Å wide in the X direction. Although it is difficult to resolve the exact atomic structure of the island, it is clearly one to two atoms thick. Presumably, the island was dispersed by a contact with the tip just

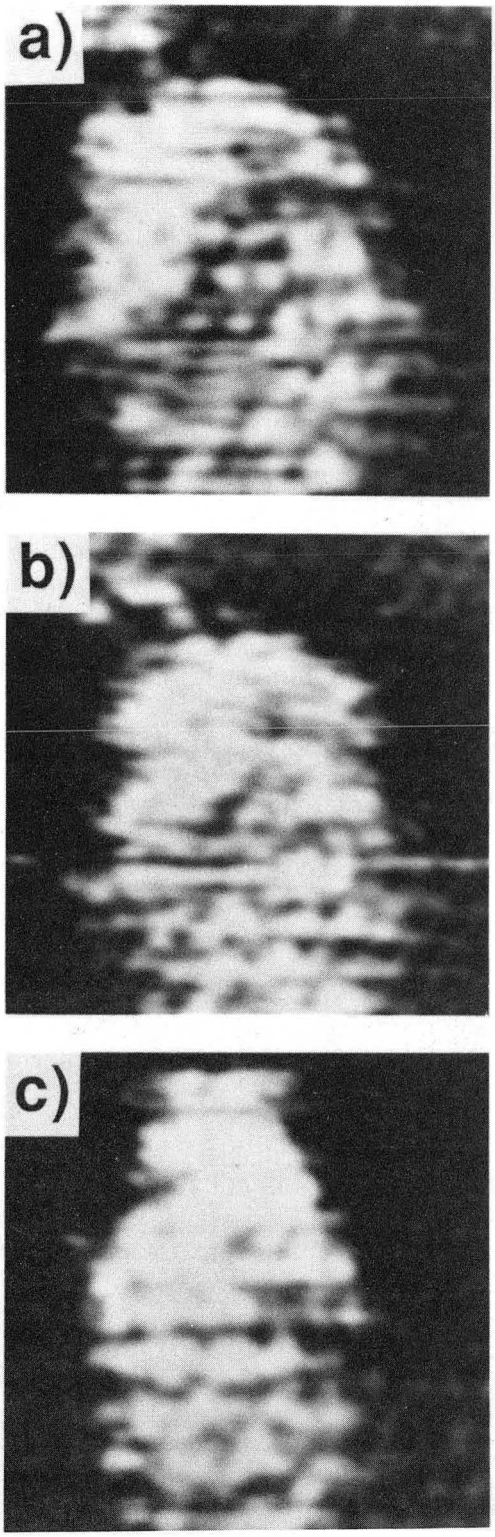

Fig. 10-1 Three subsequent 30 Å X 30 Å current images of a small Au cluster. During the 40 sec of imaging, the cluster width is reduced from 20 Å to 17 Å to 14 Å. XBB 887-6759A

prior to the start of the series.

In fact, the Au island shown in Figs. 8-8 and 8-9 was also observed to shrink. We have analyzed 13 images of region A (Figure 8-8) taken over a period of 90 seconds. We find that the short axis ζ of the rectangular structure remained roughly constant at 2.35±0.15 Å, while the long axis η shrank from 4.05±0.1 Å for the first frames to 3.80±0.1 Å for the last frames of the series. We then moved the STM tip to a region B of the same island (Figure 8-9), where we made a series of 22 images over a period of 10 minutes. We observe that while the value of ζ remains constant at 2.35±0.1 Å, η decreases from 3.8±0.1 Å for the first images to a final value of 3.5±0.1 Å which remains relatively constant. We plot the values of ζ and η for all 35 images in Figure 10-2. The fact that the η axis of the Au lattice was observed to decrease smoothly with time suggests that the Au-graphite coupling is weak, and that there is a shallow minimum in the potential energy as β is varied. We note that in contrast to the mobility of the Au islands, the Ag islands were quite stable.

b) DIFFUSION OF MONOMERS AND CLUSTERS

In fact, in a classic series of experiments, Ehrlich and coworkers[8] studied the diffusion of single metal atoms on small metal facets using field ion microscopy (FIM). By directly imaging the adsorbed atom, they were able to follow the individual jumps on the periodic substrate lattice. They were able to observe the motion of dimers and trimers, but not that of larger clusters. These studies were limited to refractory metals, and the diffusing particle was restricted to motion on a small (60 Å) facet. An article by Tsong[9]

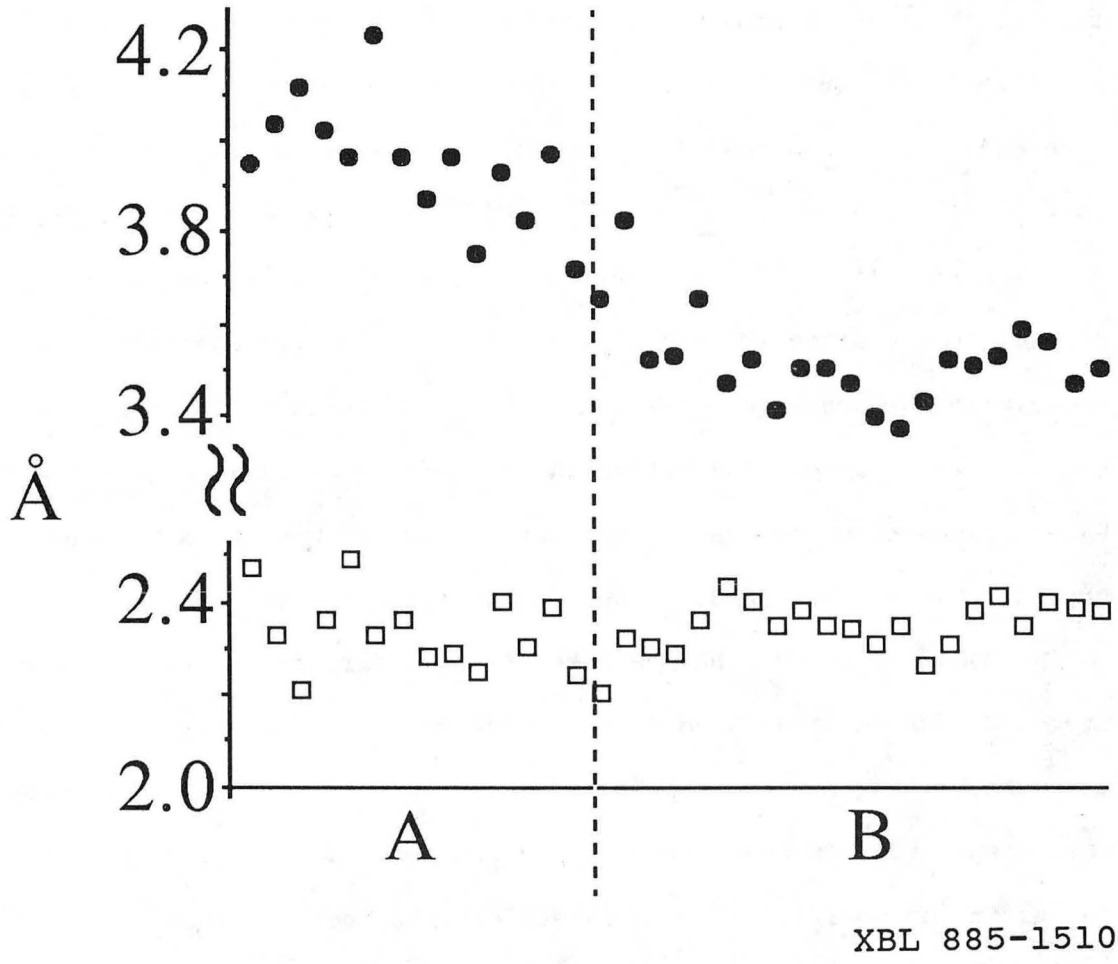

Fig. 10-2 Plot of the short axis, ξ, (open squares) and long axis, η, (filled circles) lattice spacings for the 35 images of regions A and B of the Au island shown in Figs. 8-8 and 8-9. The images were obtained over a period of 1.5 min for region A and 10 min for region B.

reviews recent progress in FIM.

Transmission electron microscopes can also image small clusters[10,11,12]. Dynamic shape changes have been observed in small particles[10,13], but it has been proposed that energy deposited by the high energy electron beam is responsible, and may momentarily melt the particles[14]. There has also been significant work on cluster mobility with TEM[15,16,17,18,19]. In particular, recent work on the model system Au/NaCl suggests the the mobility of clusters is more complicated than the simple law proposed by Kashchiev[20,21] and Lewis[22,23]: that for a cluster with j atoms, the diffusion constant D_j is given by $D_0 j^{-n}$ with D_0 and n positive constants. Therefore, further work will be needed to provide quantitative predictions for cluster mobility.

We begin by discussing the energetics of diffusion. The barrier to atomic diffusion of an atom across a surface, ΔE_d, is generally smaller than the binding energy, ΔE_b, so that diffusion can be important even when evaporation is not. For d-dimensional motion at temperature T, the diffusion coefficient D is related to the free energy of activation ΔF_d by[8]

$$D = (\ell^2/2d)(kT/h) \exp (-\Delta F_d/kT) \quad , \tag{1}$$

where

$$\Delta F_d = \Delta E_d - T\Delta S_d \quad . \tag{2}$$

Here, ℓ is the jump length, k is Boltzmann's constant, h is Plank's constant, and ΔS_d is the entropy of activation for the jump process. Equations (1) and (2) are frequently written as the Arrhenius relation[8]

$$D = D_0 \exp (-\Delta E_d/kT) \quad , \tag{3}$$

with

$$D_0 = \nu \ell^2/2d \tag{4}$$

and

$$\nu = (kT/h) \exp (\Delta S_d/k). \qquad (5)$$

For a one-dimensional random walk[8], the mean square displacement of the particle is

$$<(\Delta x)^2> = N_a \ell^2 = 2Dt \ , \qquad (6)$$

where N_a is the average number of jumps during the diffusion interval of length t. Thus the average time for a single jump is

$$\tau = \ell^2/2D = \nu^{-1} \exp (\Delta E_d/kT). \qquad (7)$$

To estimate ΔE_d we will assume that the attempt frequency $\nu \approx 10^{13}$ s^{-1} (see refs. 15 and 8).

For the monomers of Figure 7-1, we observe $\tau > 1$ sec. From Eq. (7), we find that $\Delta E_d \gtrsim 0.8$ eV, and thus deduce that $\Delta E_b > 0.8$ eV. In contrast, Metois and Heyraud estimated a binding energy $\Delta E_b = 0.26$ eV/atom for large Au islands on graphite[24,25]. However, this value is actually a lower bound for the binding of a single adatom: As groups of adatoms bind to each other, they bind less well to the substrate[26]. We can obtain an upper bound the binding energy from the study of Au on amorphous carbon by Paunov and Harsdorff[27]: They find $\Delta E_b = 1.62 \pm 0.1$ eV and $\Delta E_d = 1.17 \pm 0.1$ eV. Of course, we expect both ΔE_b and ΔE_d to be significantly smaller for Au on the basal plane of graphite than on amorphous carbon, which has dangling bonds. A relatively strong adatom-substrate interaction is also supported by the observation of pinning at the edges of metal islands (see chapter VIII). As mentioned earlier, the strong binding may be due to the presence of defects on the surface, or to the influence of a nearby island.

In addition to the relatively stable monomers of chapter VII (Figure 7-1), we have occasionally observed single Ag adatoms which

appeared only for a single image. These adatoms were typically observed near a larger island. Possibly, the atoms were removed from the nearby island by the scanning tip, which may crash into large objects in the current imaging mode. We note that the two-dimensional vapor pressure of a Ag island is too low to account for the presence of these atoms[15,28]. We can estimate the energy of activation ΔE_d for these isolated adatoms using the Arrhenius relation, Eq. (3). Mobile adatoms were imaged for a period of 3 to 5 scan lines for a total observation time of 15 to 25 msec. With an attempt frequency $\nu = 10^{13}$ s^{-1}, we obtain an estimate $\Delta E_d \approx 0.65$ eV. With a residence time of roughly 20msec, we expect the atoms to make 50 random hops, and thus move out of the imaging area (a distance of roughly 15 Å) before the next scan 1 sec later. We note that this estimate for ΔE_d is a lower bound: If the tip pushes the adatom away, the residence time will be decreased.

We now turn to a discussion of the motion of a Ag_5 cluster. Figure 10-3 shows three consecutive current images with an average tunneling current of 3 nA and a bias voltage of 40 mV. The graphite modulation was 0.75 nA, and the height of the cluster above the graphite was 2.9 nA. The lower part of each image shows the upper terrace of a graphite step, and the cluster is observed on the lower terrace near the step. The tip is scanned in the x-direction, and images are rastered from the bottom of the image to the top (see Figure 10-4). As a result, the area directly below the step is dark (low tunneling current) because, in the current imaging mode, the tip does not follow the step edge as it moves from the upper terrace to the lower (as shown schematically in Figure 10-4). We used a large scan

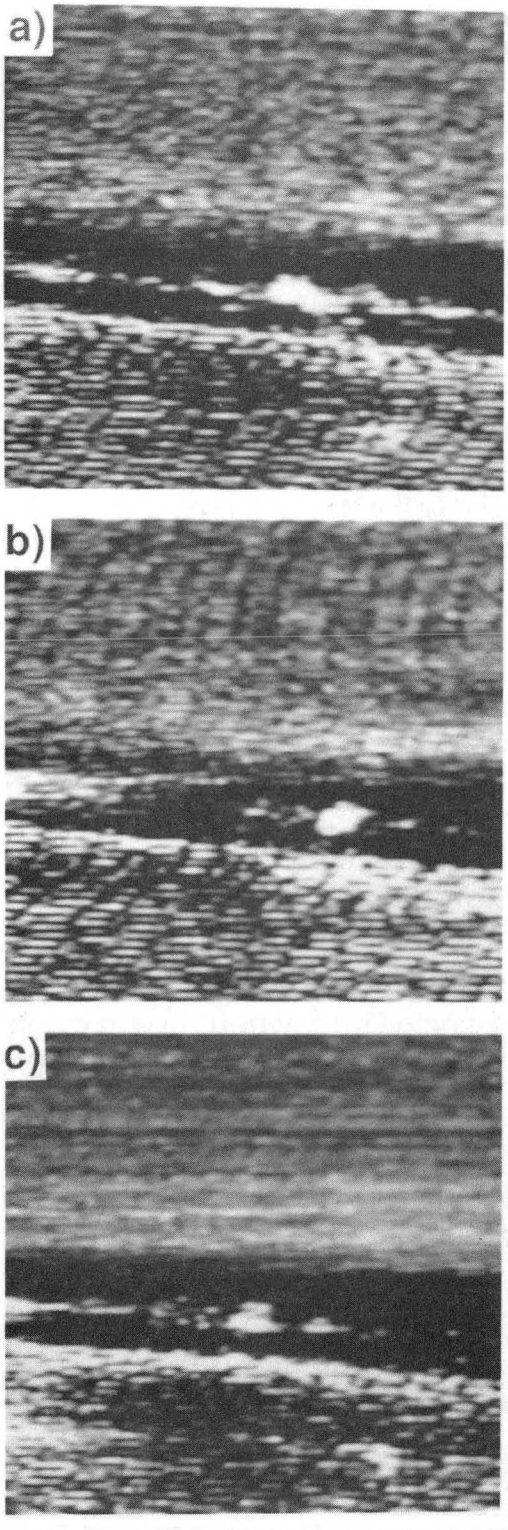

Fig. 10-3 Three consecutive current images of a small Ag_5 cluster (bright white spot) moving along the lower terrace (upper part of image) of a graphite step edge, The images are 130 Å X 130 Å, and were obtained at 2.5 sec intervals.

XBB 885-5671A

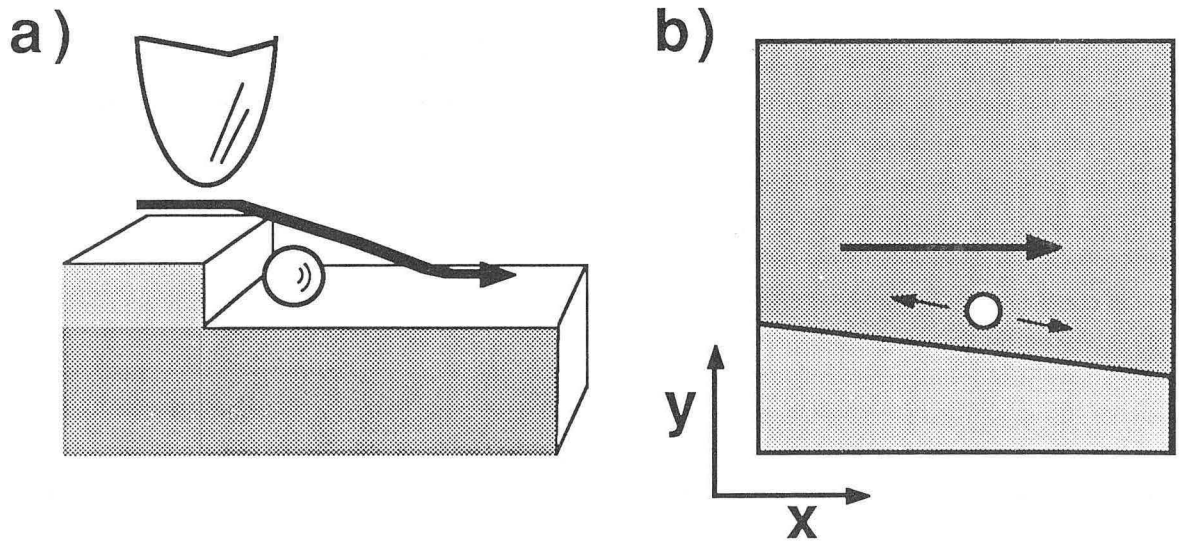

XBL 886-2079

Fig. 10-4 (a) The Ag_5 cluster is on the lower terrace of the step edge. As the tip scans over the surface, the feedback controller keeps the tunneling gap constant with a time constant of about 1 sec. Thus, when the tip crosses the step, the tunneling gap is increased (casting a dark shadow) until the tip has moved down towards the lower terrace. When the tip moves over the particle, the tunneling gap is temporarily reduced, and so the particle appears as a white spot on a black background. (b) Top view of the step and the cluster. The large arrow indicates the direction of tip motion.

size (130 Å) to keep the particle in view; as a result, we were not able to resolve the graphite lattice. However, by computer processing of these images, and by comparison with later calibration runs, we determined that the step edge is aligned along the direction of the β-sites. It is puzzling that the particle does not simply adhere to the step; rather, the center of the particle remains separated from the step edge by 9.8 ± 1.7 Å during its motion. The elastic strain induced in the substrate by the step edge could conceivably be responsible for this offset.

We observed the particle for several minutes, and measured its position along the step for each image. In the 2.5 sec between Figures 10-3(a) and (b), the cluster has moved 11.9 Å to the right. During the next 2.5 sec, the cluster moved 22.7 Å to the left [Figure 10-3(c)]. Thermal drift of the instrument occasionally carried the cluster out of view; we then offset the scanner to reposition the cluster in the center of the image. We chose four series of images, separated by these offsets, and measured the change in the position of the particle from one image to the next within each series. In total, we measured 81 relative displacements. We corrected the data for thermal drift and for creep in the piezoelectric scanner by subtracting out the average motion for each series (0.5 to 1.0 Å in the positive x-direction in each 2.5 sec interval). This drift was comparable to the observed drift of the step edge in the y-direction. Figure 10-5 shows the distribution of relative displacements for all 81 samples. To indicate the magnitude of measurement errors, we have imposed a Gaussian lineshape with a width of 0.8 Å on each data point. The distribution shows that small displacements are very common, although we observe

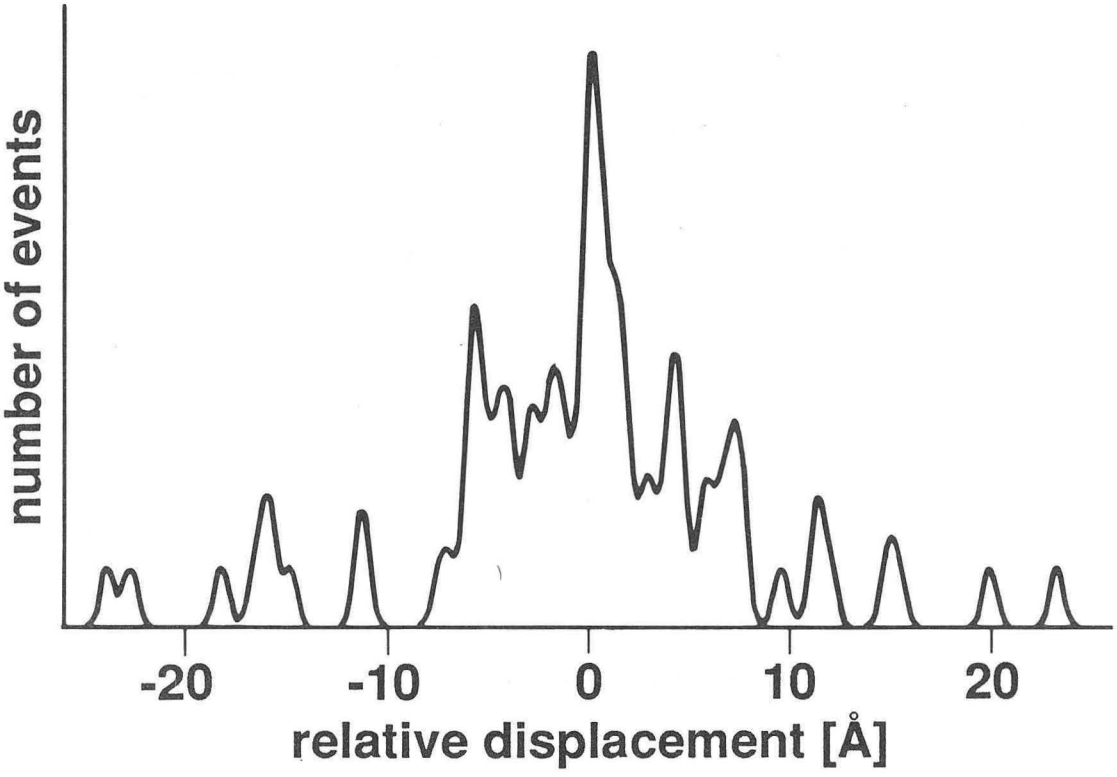

XBL 886-7429

Fig. 10-5 Distribution of Ag_5 particle displacements for 81 observations.

occasional displacements of as much as 24 Å. For lack of a better alternative, in the following analysis we will assume that the particle moves by individual jumps of 2.46 Å (the substrate periodicity), although this periodicity is not evident in Figure 10-5. In contrast to the diffusion of a single atom, however, we expect the motion to be independent of the substrate periodicity for a particle that can rotate and change shape.

In Figure 10-6 we show a histogram of the particle displacements. We assume a step size of 2.46 Å and plot the displacement in units of 2.46 Å steps. From Eq. (4) and the value $\langle(\Delta x)^2\rangle = 58.7$ Å^2, we calculate N_a=10.1 jumps. This value of N_a allows us to plot the predicted[29] random walk jump distribution

$$p(x) = e^{-N} I_x(N) = \sum_N P(N)\, U_x(N) \ , \tag{8}$$

where $I_x(N)$ is the modified Bessel function of the first kind of order x,

$$P(N) = (N_a^{-N} / N!) \exp(-N_a) \tag{9}$$

is a Poisson distribution for the number of jumps, and

$$U_x(N) = \frac{N!}{2^N\, [(N+x)/2]!\ [(N-x)/2]!} \tag{10}$$

is the binomial distribution. We see in Figure 10-6 that the predicted jump distribution fits the data quite well considering the relatively small number of observed displacements.

We note that in Figure 10-6 the four events with the largest displacements seem unlikely to have been the result of a random walk process with a constant step size. These events may have been caused by large individual jumps that spanned several lattice spacings, a

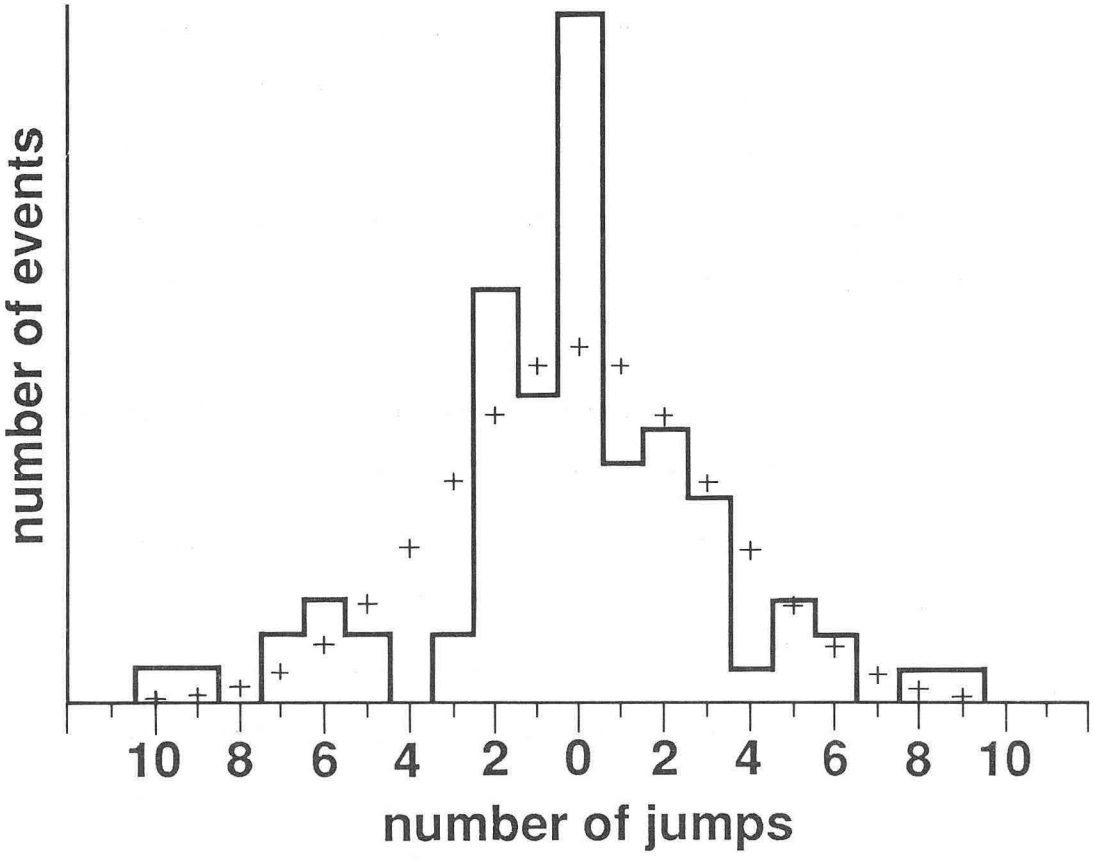

XBL 886-7430

Fig. 10-6 Histogram of Ag_5 particle displacements (to the right or to the left) assuming a 2.46 Å jump distance. We also plot the number of events predicted (crosses) assuming an average of 10.1 jumps per diffusion interval.

mechanism that was proposed by De Lorenzi *et al.*[30] on the basis of a molecular dynamics simulation. These authors suggested this mechanism could enhance the observed diffusion rate. We also observed an unusually large number of events at zero displacement. This could result from a cluster-substrate interaction that depends on the cluster orientation or position. Thus, certain positions may have higher activation energies leading to lower diffusion rates.

From the interval t = 2.5 sec, and the average number of jumps per interval, N_a = 10.1, we find a mean jump frequency f = t/N_a = 4 Hz. Using the mean square displacement $\langle(\Delta x)^2\rangle$ = 58.7 Å^2, we estimate the diffusion constant D = 1.2 X 10^{-15} cm^2/sec at 300K using Eq. (6). Inserting D into Eq. (1), we find the free energy of activation $\Delta F_d \approx$ 0.7 eV at 300K. Neglecting possible changes in entropy (for example, from the rearrangement of particles on the substrate), we can equate ΔF_d with ΔE_d, the activation energy for diffusion.

The STM resolves the particle structure as well as changes in the particle morphology during the diffusion process. In Figure 10-7 we show three enlargements of the image of the particle taken directly from the videotape (which accounts for the horizontal streaks in the image). In Figure 10-7(a), we clearly resolve the five atoms in the cluster. The three atoms on the right side of the particle are aligned with the graphite substrate. The overall size of the particle was (11.0 ± 0.4) Å X (8.6 ± 0.4) Å and remained roughly constant for the entire series. The separation of the atoms in Figure 10-7(a) is (3.4 ± 0.1) Å in the long dimension, and (4.0 ± 0.2) Å in the short dimension. Both the structure and the interatomic spacings are different from those in the bulk or in a free cluster. Bulk Ag has an

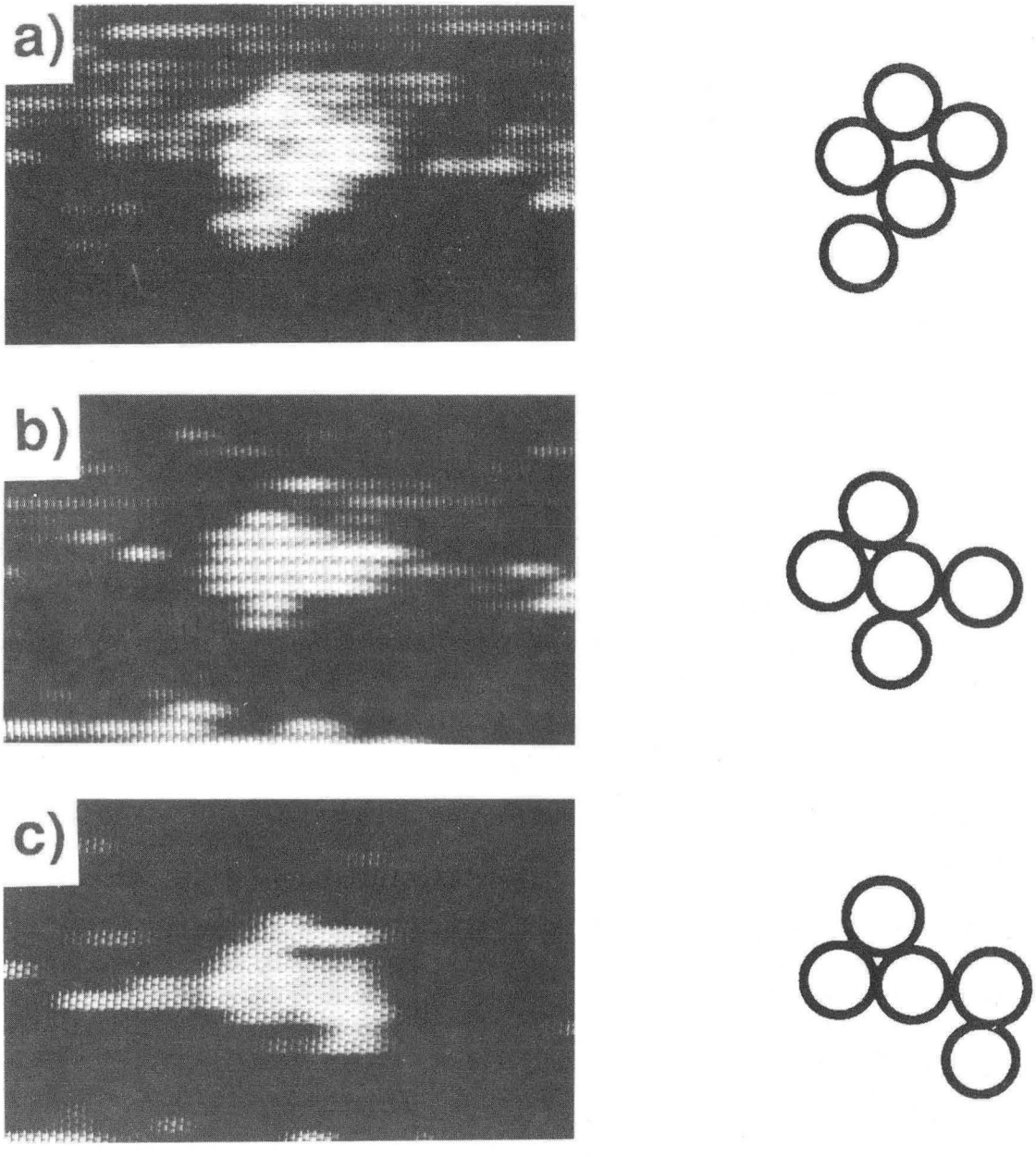

Fig. 10-7 Three enlargements of the Ag_5 particle at various positions during the diffusion. The current images are 35 Å X 22 Å. In (a), the 5 atoms are clearly resolved. (b) and (c) show different particle shapes. To the right, models are drawn to guide the eye. XBB 886-6212

fcc structure with a 2.89 Å nearest neighbor spacing[31], while a free Ag_5 particle is expected to have a tightly packed pyramidal structure[32] with a spacing somewhat smaller than the bulk spacing[33]. In contrast, our Ag_5 cluster has a widely spaced two-dimensional rectangular structure, possibly due to the interaction with the substrate, reminiscent of the structures in chapter VIII.

In Figures 10-7(b) and (c), the individual atoms are not resolved, but the overall shape of the particle is clear, and is seen to vary. We believe that the STM imaging process does not influence the observed diffusion or particle shape. The microscope was operated at low voltages and currents (40 mV and 5 nA), and the tip was several angstroms above the surface. Although large electric fields are certainly present, our earlier work showing reproducible images of small clusters and islands leads us to believe that the influence of the bias voltage is negligible. As shown in Figure 10-4, when the tip is moving to the right, the step edge keeps the tip far above the particle. Because of the non-zero angle between the step edge and the scanning direction, the tip is closer to the lower terrace when moving to the left, and so closer to the particle. Thus, tip-particle interaction would tend to move the particle to the left, in contrast to what we observe. One could perhaps confirm that the STM does not influence the particle motion by varying the temperature of the system to see whether the diffusion obeys the Arrhenius prediction.

Assuming the influence of the tip is negligible, we attribute the different particle shapes of Figure 10-7 to self-diffusion of single Ag atoms in the Ag_5 cluster that occurs without external influence. This motion of the individual Ag atoms makes the particle effectively liquid

at room temperature. We note that the particle does have a well-defined shape in each image, so that the self-diffusion process is not significantly faster than the imaging process. The self-diffusion process is too slow to account for the random walk motion of the particle[15], and so we must treat it as a separate effect.

REFERENCES

1 D. W. Abraham, H. J. Mamin, E. Ganz, and J. Clarke, IBM J. Res. Dev. 30, 492 (1986).

2 R. C. Jaklevic and L. Elie, Phys. Rev. Lett. 60, 120 (1988).

3 J. Schneir, R. Sonnenfeld, O. Marti, P. K. Hansma, J. E. Demuth, and R. J. Hamers, J. Appl. Phys. 63, 717 (1988).

4 G. Binnig, H. Fuchs, and E. Stoll, Surf. Sci. 169, L295 (1986).

5 K. H. Besocke, M. Teske, and J. Frohn, J. Vac. Sci. Tech. A 6, 408 (1988).

6 E. Ritter, R. J. Behm, G. Potschke, and J. Wintterlin, Surf. Sci. 181, 403 (1987).

7 R. S. Becker, J. A. Golovchenko, B. S. Swartzentruber, Nature 325, 419 (1987).

8 K. Stolt, W. R. Graham, and G. Ehrlich, J. Chem. Phys. 65, 3206 (1976).

9 T. T. Tsong, Surf. Sci. Reports 8, 127 (1988).

10 S. Iijima and T. Ichihashi, Phys. Rev. Lett. 56, 616 (1986).

11 J.-O. Bovin, R. Wallenberg, and D. J. Smith, Nature 317, 47 (1985).

12 M. A. Listvan, Surf. Sci. 173, 294 (1986).

13 S. Iijima and T. Ichihashi, Surf. Sci. 192, L872 (1987).

14 P. Williams, Appl. Phys. Lett. 50, 1760 (1987).

15 R. Kern, J. J. Metois and G. LeLay, Curr. Top. Mater. Sci. 3, 131 (1979).

16 J. S. Maa, J. I. Lee and T. E. Hutchinson, Proc. 34th EMSA meeting, p. 648 (1976).

17 B. F. Usher and J. L. Robins, Thin Solid Films 155, 267 (1987).

18 A. Masson, J. J. Metois, and R. Kern, Surf. Sci. 27, 463 (1971).

19 G. A. Basset in "Condensation and Evaporation of Solids", p. 599 Ed: E. Rutner, P. Goldfinger, and J. P. Hirth (Gordon and Breach, New York 1962).

20 D. Kashchiev, Surf. Sci. 55, 477 (1976).

21 D. Kashchiev, Surf. Sci. 86, 14 (1979).

22 B. Lewis, Surf. Sci. 21, 273 (1970).

23 B. Lewis, J. Appl. Phys. 41, 30 (1970).

24 J. C. Heyraud and J. J. Metois, Acta Metall. 28, 1789 (1980).

25 J. C. Heyraud and J. J. Metois, J. Crystal Growth 50, 571 (1980).

26 P. J. Feibelman, Phys. Rev. Lett. 58, 2766 (1987).

27 M. Paunov and M Harsdorff, Z. Naturforsch 29a, 1311 (1974).

28 J. Kolaczkiewicz and E. Bauer, Phys. Rev. Lett. 54, 574 (1985).

29 G. Ehrlich, J. Chem. Phys. 44, 1050 (1966).

30 G. De Lorenzi, G. Jacucci, and V. Pontikis, Surf. Sci. 116, 391 (1982).

31 C. Kittel, "Introduction to Solid State Physics", 5th Ed., p. 32 (John Wiley and Sons, New York 1976).

32 J. A. Howard, R. Sutcliffe, and B. Mile, Surf. Sci. 156, 214 (1985).

33 D. Tomanek, S. Mukherjee, and K.H. Bennemann, Phys. Rev. B 28, 665 (1983).

CHAPTER XI

CONCLUSIONS AND FUTURE DIRECTIONS

IX. CONCLUDING REMARKS

In this thesis, we first described several STM's, and the computing and electronics necessary to run the STM. We then used the STM to modify and examine a Au surface. We were able to make small indentations and scratches in the surface. We also formed 200 Å Au mounds on the surface, and watched them flatten and diffuse over a period of twenty minutes.

We then discussed effects of deformation of the graphite surface, and provided a theoretical prediction for an STM current image of graphite. We discussed the role of tip shape and multiple tips in image production. We then presented early results of metals on graphite imaged in air.

In UHV, we have observed monomers, and clusters of two to four atoms adsorbed onto the basal plane of graphite. These adatoms and small clusters were stable enough to be imaged reproducibly for periods of several seconds to many minutes. Single adatoms were only observed within 10Å of an island: The fact that these single adatoms were stable for periods of seconds is surprising, perhaps indicating bonding to defect sites or the stabilizing influence of the nearby island. The Ag and Al monomers were more usually observed at graphite β-sites, while the one Au monomer we observed was not. We observed small clusters resolved into individual atoms that were near β-sites, as well as

clusters that were not commensurate with the substrate. The presence of a defect may influence the structure of a cluster because of the strong interaction bewteen the defect and the adsorbed atoms. These structures illustrate the very beginnings of nucleation and growth of films on a relatively non-interacting substrate.

We were able to image small two-dimensional islands atom by atom. We observe a mixture of order and disorder, with rectangular lattice structures in the interiors of the islands, and disorder at the peripheries. We also observe grain boundaries in these islands. Further, the shape of the individual atoms is often reproducibly non-circular, possibly due to variations in the local electronic structure of the island, or, alternatively, to atomic vibration. Structures of this kind should provide interesting testing grounds for theories of two-dimensional growth and melting.

Moving on to still larger systems, we used our STM to image small particles and granular films. Although the STM is able to image only the surface of these samples, this does allow us to study the particle size distribution and morphology. We observed a group of Cu clusters which varied in diameter from 20 Å to 80 Å, with an average of 44 Å. The STM should be capable of following growth modes during deposition, and observing the effects of annealing or other post-deposition treatments.

In the last part of the paper, we reported several aspects of the dynamical behaviour of the adsorbed atoms. In Figure 10-1, we observed the contraction of a Au island in roughly 1 min. On an atomic scale, we observed the contraction of the longer axis of a rectangular Au lattice over a period of roughly 10 min. We have been able to make

estimates of the energy barrier for diffusion ΔE_d of Au, Au, and Al monomers from their observed lifetime of more than one sec. Using the Arrhenius relation, we estimate $\Delta E_d \gtrsim 0.8$ eV. We occasionally observed Ag atoms with short lifetimes, and deduced $\Delta E_d \gtrsim 0.65$ eV. The binding energy for these adatoms will be larger than the energy barrier for diffusion. We should point out, however, that we cannot assess the possible influence of the tunneling tip on the lifetime, nor the effect of nearby islands on the binding energy. Finally, in one particularly fortuitous experiment, we observed the one-dimensional surface diffusion of a five-atom Ag cluster along a graphite step, from which we deduce $\Delta E_d \approx 0.7$ eV. We found that the particle-substrate interaction had a strong effect on the particle interatomic spacing, shape, and alignment. In addition to the bodily diffusion of the particle, self-diffusion continuously altered its shape. These changes in structure may have strongly affected the observed diffusion. Finally, the particle diffusion showed an unusually large number of zero displacements, as well as a few unusually large ones. This technique could be used over a wide range of temperatures to test the Arrhenius nature of the diffusion constant. It should be possible to separate the different types of diffusion that are possible, such as self-diffusion, single lattice jumps, or multiple lattice jumps. Furthermore, the method can be applied to a broad range of materials and particle sizes.

These experiments represent a survey of a large number of phenomena associated with adatoms deposited on a relatively inert surface under ultra-high vacuum. Our technique could be improved and extended in several ways. For example, one could cool the substrate to

slow the motion of the adsorbed particles, and study the temperature dependence of their kinetics and the manner in which they form islands. The use of a Knudsen cell would provide a more controlled and uniform deposition of atoms. It would be useful to investigate larger areas of the substrate to gather more statistical information on the distribution of particle sizes. These improvements should make the STM a very powerful tool for the study of a variety of substrates and adsorbates over a wide range of temperature and growth conditions. One should be able to obtain a wealth of information about the static and dynamic behaviour of single atoms and clusters on surfaces and about the growth of thin films on a hitherto unattainable atomic scale.

I had hoped to do several other related experiments. First, it would be interesting to study intercalated materials. These would need to be prepared and cleaved *in situ*, and perhaps should be cooled to 77K as well. A related system is Cs on graphite, which forms ordered two-dimensional arrays at temperatures near 100K[1]. These could be prepared by evaporation onto a cold graphite substrate, evaluated with LEED, and then imaged. If the substrate were then slowly heated, one should be able to study two-dimensional melting with atomic resolution. Preliminary experiments at room temperature gave images that appeared to show (2X2) Cs overlayers on the graphite, but the lattice spacings were not always correct (lateral deformation from thick contamination may be important here), and we were not able to distinguish overlayers from intercalated layers. Cs atoms are quite large, and donate nearly one electron to the substrate. Thus the adatom size may vary considerably depending on the charge donation, and the remaining atoms should be ionized, and thus show long-range Coulomb

interactions.

Another promising candidate for study is doped graphite. For example, at large concentrations, one can fabricate[2] ordered BC_3. Several lattices have been suggested for this compound, and the STM might be able to directly observe the surface order. At low boron concentrations, one could observe the effect of a single substitutional impurity on the graphite electronic structure. We also expect long range interactions between the boron atoms due to elastic strain in the lattice (since the B-C bond is 1.6 Å while the C-C bond is 1.4 Å). Thus, studies of the interaction between annealing and long-range order should be possible. It should be possible to distinguish different impurities, for example N from B, by measuring the decay of adatom signal into the vacuum[3].

Finally, it would be very interesting to study the spectroscopy of these materials, and in particular to observe the small size effects predicted for small metal clusters.

REFERENCES

1 Z. P. Hu, N. J Wu, and A. Ignatiev, Phys. Rev. B33, 7683 (1986).

2 R. B. Kaner, J. Kouvetakis, C. E. Warble, M. L. Sattler, and N. Bartlett, Mat. Res. Bull. 22, 399 (1987) and J. Kouvetakis, Ph.D. Thesis, University of California (1988).

3 H. A. Mizes and W. A. Harrison, J. Vac. Sci. Tech. A6, 300 (1987).

LAWRENCE BERKELEY LABORATORY
CENTER FOR ADVANCED MATERIALS
1 CYCLOTRON ROAD
BERKELEY, CALIFORNIA 94720